

Behaviour of Iron and Titanium Species in Cryolite-Alumina Melts

by

Trond Eirik Jentoftsen

Thesis submitted in partial fulfilment of the
requirements for the degree Doktoringeniør

Norwegian University of Science and Technology
Department of Materials Technology and Electrochemistry

December 2000

Acknowledgements

The work was carried out at the Department of Materials Technology and Electrochemistry at NTNU under the supervision of *Professor Dr. Jomar Thonstad* and *Professor Dr. Geir Martin Haarberg*. I am grateful for their support, advice and active interest in my work.

Dr. Ernest W. Dewing, Kingston, Canada, also showed great interest in my work. His enthusiasm and excellent guidance are highly appreciated.

The experimental results reported in sections 3.3.2 and 7.3.1 were obtained in collaboration with *Dr. Odd-Arne Lorentsen*, with whom I have shared an office for the last three years. I am grateful for his interest, and for all the fruitful discussions we have had during these years.

The industrial measurements were performed at the Hydro Aluminium plant in Årdal. I would like to thank *Mr. Anders Buen*, *Mr. Haakon Haakonsen*, *Mr. Bjørn P. Moxnes* and *Dr. Per A. Solli* for their interest and help. Thanks are also due to *Professor Dr. Åsmund Sterten* for good advice and interesting discussions on this and related matters.

I am grateful to *Dr. Trond Støre* who kindly answered my numerous questions regarding instrumentation and electrochemical techniques.

Thanks are also due to the excellent staff at the Department of Materials Technology and Electrochemistry and at the Electrolysis Group of SINTEF Materials Technology for assistance every time when needed.

Finally, I want to thank the Research Council of Norway and the Norwegian aluminium industry for their financial support of this work as a part of the PROSMAT Primary Aluminium Programme.

Trond Eirik Jentoftsen
Trondheim, December 2000

Contents

Acknowledgements	iii
Table of Contents	v
List of Symbols	vii
Summary	ix
1 Introduction	1
1.1 Primary Aluminium Production	1
1.2 Impurities in the Electrolyte	4
1.3 Aluminium-Alloying Elements	8
1.4 Scope	9
2 Theory	11
2.1 Potential Sweep Techniques	11
2.2 Chronoamperometry	17
2.3 Chronopotentiometry	18
3 Solubility of FeO and FeAl₂O₄ in Cryolite-Alumina Melts	23
3.1 Introduction	23
3.2 Experimental	27
3.2.1 Electrochemical Measurements	27
3.2.2 Chemical Measurements	29
3.3 Results and Discussion	31
3.3.1 Electrochemical Measurements	31
3.3.1.1 Solubility as a Function of Alumina Concentration	31
3.3.2 Chemical Measurements	40
3.3.2.1 Solubility as a Function of Alumina Concentration	40
3.3.2.2 Solubility as a Function of Temperature	46
3.3.2.3 Solubility as a Function of Molar Cryolite Ratio	48
3.3.3 Solubility of Fe ₂ O ₃ in Cryolite-Alumina Melts	53
4 Solubility of TiO₂ in Cryolite-Alumina Melts	61
4.1 Introduction	61
4.2 Experimental	65
4.3 Results and Discussion	66
4.3.1 Solubility as a Function of Alumina Concentration	66
4.3.2 Solubility as a Function of Temperature	77
5 Electrochemistry of Fe(II) in Cryolite-Alumina Melts	81
5.1 Introduction	81
5.2 Experimental	83

5.3 Results and Discussion	84
5.3.1 Reduction of Fe(II)	85
5.3.1.1 Cyclic Voltammetry	85
5.3.1.2 Chronoamperometry	92
5.3.1.3 Chronopotentiometry	95
5.3.1.4 The Diffusion Coefficient	99
5.3.2 Oxidation of Fe(II)	101
5.3.2.1 The Platinum Electrode	101
5.3.2.2 The Gold Electrode	105
5.3.2.3 The Reversible Potential of the Redox Couple Fe(III)/Fe(II)	109
6 Electrochemistry of TiO₂ in Cryolite-Alumina Melts	111
6.1 Introduction	111
6.2 Experimental	115
6.3 Results and Discussion	117
6.3.1 Electrochemical Behaviour of TiO ₂ in Na ₃ AlF ₆ -Al ₂ O ₃ (sat)	117
6.3.2 Electrochemical Behaviour of TiO ₂ in Na ₃ AlF ₆	125
7 Thermodynamic Properties of FeAl₂O₄ and Stability of Iron-Containing Phases	129
7.1 Introduction	129
7.2 Experimental	134
7.3 Results and Discussion	135
7.3.1 Electrochemical Measurements of EMF for Hercynite	135
7.3.2 Thermodynamic Calculations for Hercynite	139
7.3.3 Thermodynamics of Solid Iron Phases in Equilibrium with Cryolite-Alumina Melts	143
7.3.4 Stability of Iron-Containing Ions in Solution	145
7.3.5 The Standard Potential of the Redox Couple Fe(III)/Fe(II)	152
8 Mass Transfer of the Impurities Fe, Si and Ti between Bath and Aluminium in Industrial Hall-Héroult Cells	157
8.1 Introduction	157
8.2 Model	164
8.3 Experimental	167
8.4 Results and Discussion	170
8.4.1 Effect of Cell Type	170
8.4.1.1 Cell Type ETE-I	170
8.4.1.2 Cell Type ETE-II	175
8.4.1.3 Cell Type SBS-I/SBS-II	180
8.4.2 Effect of Current Interruption	187
8.4.3 Effect of Interpolar Distance	191
8.4.4 Mass Transfer Coefficients	197

Major Symbols

The following list includes only the most important symbols. Omitted symbols, subscripts and superscripts are explained where they first appear in the text, unless their meaning is understood from the context.

Symbol	Meaning	Units
A	area	cm ²
a	activity	—
C _p	heat capacity	J K ⁻¹ mol ⁻¹
CE	current efficiency	%
CR	cryolite ratio	—
c [∞]	concentration in the bulk solution	mol cm ⁻³
c ^σ	concentration at the electrode surface	mol cm ⁻³
D	diffusion coefficient	cm ² s ⁻¹
d	diameter	cm
E	potential	V
E [°]	standard potential	V
E _d	decomposition potential	V
E _{dep}	deposition potential in voltammogram	V
E _{i=0}	potential at which i = 0 in voltammogram	V
E _p	peak potential in voltammogram	V
E _{p/2}	half peak potential in voltammogram	V
E _{rev}	reversible potential	V
EMF	electromotive force	V
F	Faraday constant (96487)	C mol ⁻¹
G	Gibbs (free) energy	J mol ⁻¹
G [°]	standard Gibbs (free) energy	J mol ⁻¹
H	enthalpy	J mol ⁻¹
H [°]	standard enthalpy	J mol ⁻¹
h	height	cm
I	current	A
i	current density	A cm ⁻²
i _l	limiting current density in voltammogram	A cm ⁻²
i _p	peak current density in voltammogram	A cm ⁻²
J	flux	mol cm ⁻² s ⁻¹
k	mass transfer coefficient	cm s ⁻¹
k _B	Boltzmann constant (1.3806 × 10 ⁻²³)	J K ⁻¹
M	molecular weight	g mol ⁻¹
n	number of electrons	—
p	partial pressure	bar
R	gas constant (8.3143)	J K ⁻¹ mol ⁻¹

Symbol	Meaning	Units
r	radius	cm
S	entropy	$\text{J K}^{-1} \text{mol}^{-1}$
S°	standard entropy	$\text{J K}^{-1} \text{mol}^{-1}$
T	temperature	K
t	time	s
V	volume	cm^3
w	weight	g
δ	diffusion layer thickness	cm
η	(1) overpotential	V
	(2) viscosity	$\text{kg m}^{-1} \text{s}^{-1}$
v	potential sweep rate	V s^{-1}
ρ	density	g cm^{-3}
τ	transition time in chronopotentiometry	s

Summary

The solubility of divalent iron oxide in cryolite-based melts was studied. Both electrochemical and chemical techniques were employed. To ensure that only divalent iron was present in solution, the melt was contained in an iron crucible under an atmosphere of argon. The experimental work included investigation of the solubility as a function of alumina concentration, temperature and cryolite ratio ($CR = \text{NaF}/\text{AlF}_3$ molar ratio). The solubility at 1020 °C was found to decrease from 4.17 wt% Fe in cryolite to 0.32 wt% Fe in cryolite saturated with alumina. FeO and FeAl_2O_4 were found to coexist as solid phases in equilibrium with the melt at 5.03 wt% Al_2O_3 ; the former being the stable solid phase below this concentration and the latter at high alumina concentrations. The standard Gibbs energy of formation for FeAl_2O_4 from its oxide components at 1020 °C was determined to be $-(17.6 \pm 0.5) \text{ kJ mol}^{-1}$. The solubility of FeAl_2O_4 was found to increase from 0.25 wt% Fe at 981 °C to 0.36 wt% at 1050 °C in alumina-saturated melts. By assuming Henrian behaviour, the apparent partial molar enthalpy of dissolution of FeAl_2O_4 was found to be $(64.8 \pm 2.5) \text{ kJ mol}^{-1}$. Experiments involving varying cryolite ratio in alumina-saturated melts at 1020 °C showed a maximum solubility of 0.62 wt% Fe at a cryolite ratio of five. Modelling indicated that divalent iron species were present as NaFeF_3 in acidic melts ($CR < 3$), while Na_3FeF_5 and/or Na_4FeF_6 dominated in a basic environment ($CR > 3$).

The solubility of TiO_2 in cryolite-alumina melts at 1020 °C was measured. The analytical data showed that the titanium solubility decreased with increasing total oxide concentration, up to a concentration of $\sim 3.5 \text{ wt\% O}$, while it increased at higher concentrations. The solubility was found to be 3.1 wt% Ti and 2.7 wt% Ti, respectively, in cryolite and in alumina-saturated melts. Modelling indicated that the most probable titanium species are TiO^{2+} and TiO_3^{2-} , which coexist in the solution; the former dominating at low alumina concentrations and the latter at high alumina concentrations. Unknown amounts of fluoride may also be associated with the titanium atoms. Determination of the solubility of TiO_2 in alumina-saturated melts as a function of temperature showed that the solubility increased from 1.9 wt% Ti at 975 °C to 2.8 wt% Ti at 1035 °C. The apparent partial molar enthalpy of dissolution of TiO_2 was found to be $(88.3 \pm 4.1) \text{ kJ mol}^{-1}$, provided that Henry's law holds.

The electrochemistry of divalent iron in cryolite-based melts was investigated by voltammetry, chronopotentiometry and chronoamperometry. A working electrode of copper was found to be best suited for the study of the reduction of Fe(II), while gold and platinum gave the best results under oxidising conditions. The reduction of Fe(II) ions was found to be diffusion controlled. The number of electrons involved was determined to be two. A discrepancy was observed between the diffusion coefficients obtained by the different techniques. The diffusion coefficient of Fe(II) in alumina-saturated melts at 1020 °C was found to be $D_{\text{Fe(II)}} = 3.0 \times 10^{-5} \text{ cm}^2 \text{ s}^{-1}$ by voltammetry. Experiments performed in an electrolyte with industrial composition at $\sim 970 \text{ °C}$ gave a

slightly higher value for the diffusion coefficient. The oxidation of Fe(II) on a gold or a platinum wire electrode showed that the process was diffusion controlled, involving one electron. The reversible potential for the redox couple Fe(III)/Fe(II) was found to be more cathodic than the reversible potential for the oxygen evolution by 350 to 400 mV, depending on the solvent composition and on the temperature.

The electrochemistry of TiO₂ in cryolite-alumina melts was studied by voltammetry. The deposition of titanium on tungsten was found to be a three-electron diffusion controlled process. The deposition peak increased with increasing titanium concentration. In alumina-saturated melts two waves were observed prior to the titanium deposition. The potential difference between the cathodic wave closest to the deposition peak and its corresponding oxidation peak indicated a diffusion controlled process that involved a one-electron charge transfer. However, in cryolite melts a single wave was observed prior to the titanium deposition. It is suggested that these cathodic waves might have been caused by underpotential deposition of titanium, and subsequent alloying with tungsten. It cannot be ruled out that redox reactions take place between tetravalent titanium and the titanium alloyed with tungsten, thereby forming trivalent titanium prior to the metal deposition.

In order to determine thermodynamic properties of FeAl₂O₄, a solid electrolyte galvanic cell was used. Cryolite was present in the half-cell containing FeAl₂O₄ to ensure that alumina of the alpha modification was in equilibrium with FeAl₂O₄. An oxygen ion conducting yttria-stabilised zirconia tube served as the solid electrolyte. The EMF was measured in the range 1245 to 1343 K. By using literature data at higher temperatures, thermodynamic properties for the reaction $\text{Fe(s)} + \frac{1}{2}\text{O}_2(\text{g}) + \text{Al}_2\text{O}_3(\text{s}, \alpha) = \text{FeAl}_2\text{O}_4(\text{s})$ could be calculated, *i.e.* $\Delta H^\circ_{1600\text{K}} = -(270615 \pm 1387) \text{ J mol}^{-1}$ and $\Delta S^\circ_{1600\text{K}} = -(56.759 \pm 0.856) \text{ J K}^{-1} \text{ mol}^{-1}$. New thermodynamic data for FeAl₂O₄ were also calculated, and a predominance area diagram for solid iron phases at 1293 K was constructed. The standard potential of the redox couple Fe(III)/Fe(II) as a function of the alumina content was derived from the solubility data of Fe(II) obtained in the present work and literature data for Fe(III). When the standard potentials are put into context of the Hall-Hérault process, the results indicate that neither the CO₂/CO anode gas nor the carbon anode itself can oxidise Fe(II) to Fe(III).

The mass transfer of the impurities Fe, Si and Ti between bath and aluminium in industrial Hall-Hérault cells was investigated. The experiments were performed in several types of cells with prebaked anodes. The impurities were added to the bath in the form of Fe₂O₃, SiO₂ and TiO₂. Bath and metal samples were collected periodically before and after the addition was made. With the criterion that the mass transport was diffusion controlled, a model involving first order reaction kinetics was used to calculate the mass transfer coefficients for transfer into the metal phase. Large scatter were observed in the obtained mass transfer coefficients, but the general trend seemed to be $k_{\text{Fe}} > k_{\text{Si}} > k_{\text{Ti}}$. By averaging the data obtained, it was found: $k_{\text{Fe}} = (10 \pm 3) \times 10^{-6} \text{ m s}^{-1}$, $k_{\text{Si}} = (7 \pm 3) \times 10^{-6} \text{ m s}^{-1}$, and $k_{\text{Ti}} = (5 \pm 2) \times 10^{-6} \text{ m s}^{-1}$.

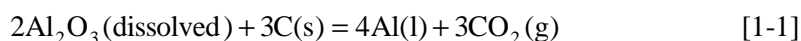
1 Introduction

1.1 Primary Aluminium Production

Aluminium is the most abundant metallic element (8.1 wt%) in the earth's crust. Due to its strong affinity to oxygen, aluminium does not occur in nature in its pure elemental state. Aluminium is present in about 250 different minerals (Grjotheim *et al.* 1982). The most prominent groups of such minerals are the aluminosilicates, and the products of their weathering, the clays. Other important compounds include aluminium oxyhydrates, such as bauxite, the dominating raw material for the production of aluminium at present.

Aluminium cannot be produced by an aqueous electrolytic process because hydrogen is electrochemically much nobler than aluminium. The first commercial aluminium was produced from sodium aluminium chloride, reacting with metallic sodium by an expensive thermic reduction process in the middle of the 19th century. In 1886, however, and independently of each other, Paul Héroult of France and Charles Hall of the USA discovered and patented a process in which alumina was dissolved in molten cryolite and decomposed electrolytically to give liquid aluminium. The Hall-Héroult process is the only method by which aluminium is produced industrially today. Thus, in the Hall-Héroult process liquid aluminium is produced by the electrolytic reduction of alumina (Al_2O_3) dissolved in an electrolyte (bath) mainly containing cryolite (Na_3AlF_6). Cryolite belongs to the technically important halogen compounds of aluminium that occur naturally. Cryolite is used because of its unique and unmatched capacity as a solvent for alumina. The bath is not consumed as such during the electrolytic process, but some losses occur, mainly by vaporisation (NaAlF_4).

In the cell one or several carbon anodes are immersed into the bath, and oxygen from the alumina is discharged electrolytically at the anode, whereby it immediately reacts with the carbon anode and thus gradually consumes it by the formation of gaseous carbon dioxide (CO_2). Underneath the bath there is a pool of liquid aluminium, contained in a preformed carbon lining with insulation materials inside a steel shell. The aluminium is formed at the bath/metal surface, which acts as the cathode. Thus, the overall chemical reaction can be written (Grjotheim and Kvande 1993):



In addition to cryolite as the main component, the bath in modern alumina reduction cells may typically contain 6 - 13 wt% aluminium fluoride (AlF_3), 4 - 6 wt% calcium fluoride (CaF_2), and 2 - 4 wt% alumina. In some cases 2 - 4 wt% lithium fluoride (LiF) and/or magnesium fluoride (MgF_2) may be added. In these cases, the content of aluminium fluoride is usually below 6 - 7 wt% AlF_3 (Grjotheim and Kvande 1993).

The bath temperature during cell operation is typically in the range from 940 - 970 °C. The bath height in the cells does not vary much and is usually close to 20 cm. The interpolar distance, in other words, the vertical distance between the underside of the anode and the surface of the pool of liquid metal, is typically 4 - 5 cm (Grjotheim and Kvande 1993).

It is generally agreed that molten cryolite dissociates completely into sodium cations (Na^+) and hexafluoroaluminate anions (AlF_6^{3-}). The latter ions dissociate partly into tetrafluoroaluminate anions (AlF_4^-), fluoride anions (F^-) and maybe pentafluoroaluminate anions (AlF_5^{2-}) (Grjotheim and Kvande 1993). Sodium ions carry about 99 % of the electric current through the bath, but since sodium has a more negative deposition potential than aluminium, the latter is deposited on the cathode (Grjotheim *et al.* 1982).

Alumina is the actual “raw material” in the process, and is consumed according to the stoichiometric ratio in equation [1-1], which amounts to 1.89 on a mass basis, *i.e.*, 1.89 kg Al_2O_3 gives 1 kg Al. While rather big batches of alumina are added with large time separation in older cells with less sophisticated feeding techniques, alumina is fed to the bath of modern cells more or less continuously by use of automatic “point feeders”. Alumina dissolves in molten cryolite and forms different aluminium oxyfluoride complex anions. The structure of these ions is not completely known at present, but they probably contain two aluminium atoms, one or two oxygen atoms and four, six or eight fluorine atoms, depending on the concentration of dissolved alumina in the bath. These anions provide the oxygen atoms needed for the formation of gaseous carbon dioxide (Grjotheim and Kvande 1993).

There are two basic anode designs, prebaked anodes, see Figure 1.1, and the Söderberg anode, see Figure 1.2. Prebaked anodes are used more extensively, but today about 40 % of the world’s annual aluminium production is still made in cells with Söderberg technology. Prebaked anodes have to be removed at regular intervals, usually after 22 - 26 days, when they have reacted down to about one third or one fourth of their original size. Since most cells have at least 20 prebaked anodes, this means that approximately one anode has to be changed every day in each cell. Söderberg anodes are continuous and self-baking, which in principle is advantageous. Prebaked anodes have the advantage that they significantly reduce anode carbon consumption compared to Söderberg anodes (Grjotheim and Kvande 1993).

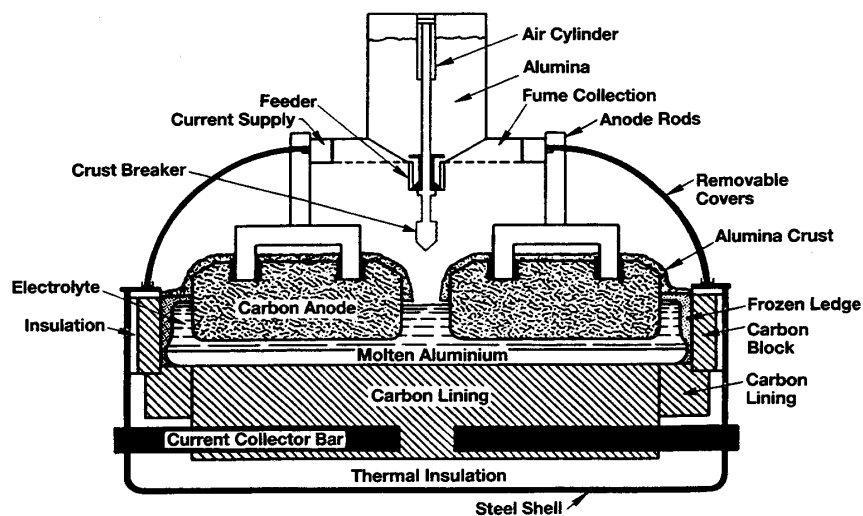


Figure 1.1 Cell with prebaked anodes. From Grjotheim and Kvande (1993).

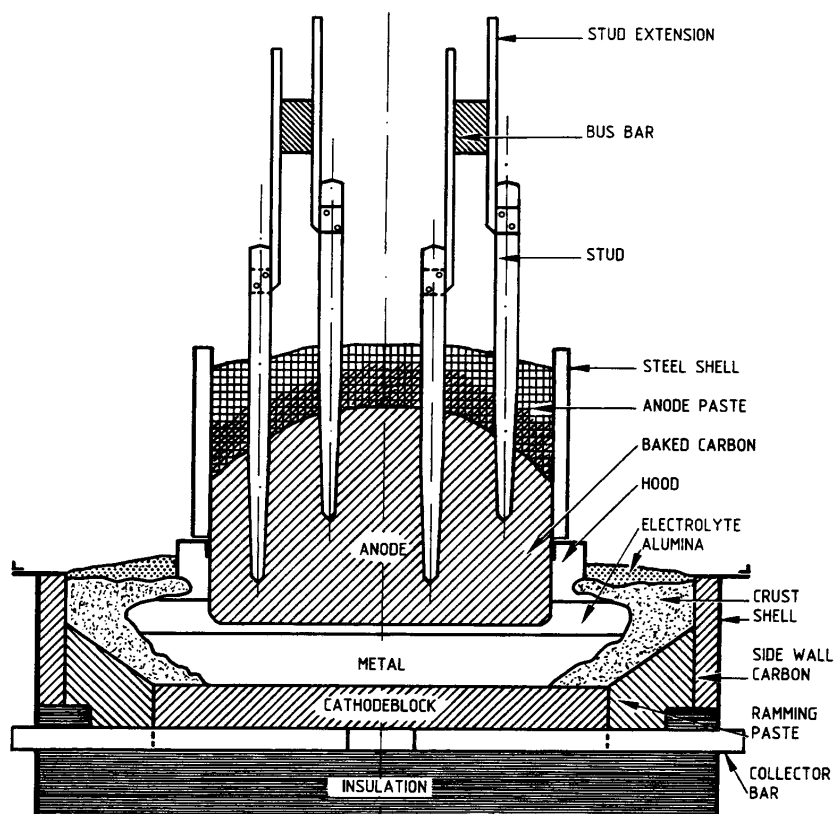
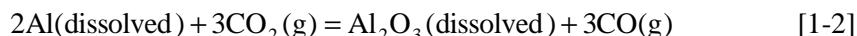


Figure 1.2 Söderberg cell. From Grjotheim and Kvande (1993).

The two main parameters describing the performance of the cell, are current efficiency (CE) and energy consumption. The most modern potlines today operate above 95 % CE. The main reason for the loss in CE is that the metal has a small, but significant solubility in the bath, of the order of 0.1 wt%. The dissolved metal may react with the CO₂ that is formed at the anode, and it is then reoxidised by the back reaction (Grjotheim and Kvande 1993):



This reaction reduces CE because it causes consumption of aluminium, and it also increases anode consumption and accounts for most of the carbon monoxide (CO) gas present in the anode gases during normal cell operation.

Although the Hall-Héroult process still dominates the production of aluminium, other possible methods have attracted considerable interest in recent decades. This has previously especially been the case in time of war, when there has been a shortage of bauxite. As world supplies of bauxite are not inexhaustible, processes will be needed which utilise aluminous ore, *e.g.* aluminosilicates, as the starting material, since these are far more abundant in nature.

The more important disadvantages of the Hall-Héroult process are (Grjotheim *et al.* 1982): (a) the energy efficiency of the electrolysis is fairly low, (b) the production of pure alumina is expensive, and (c) investment cost of an aluminium plant is relatively high, due to the large number of production units, which, for technical and operational reasons, must be limited in size.

The alternatives to the Hall-Héroult process which have been studied in recent years, can be grouped in three categories (Grjotheim *et al.* 1982): (a) thermal reduction of alumina, (b) thermal reduction of aluminous ores followed by refining of the alloy, and (c) non-classical electrolysis processes.

1.2 Impurities in the Electrolyte

Besides the main components (Na₃AlF₆, AlF₃, Al₂O₃) and some additives such as CaF₂, LiF and MgF₂, the electrolyte always contains “foreign” substances (impurities). The additives are usually deliberately added in order to improve the technologically important physico-chemical and electrochemical parameters and the CE. The impurities originate from the raw materials and are continuously introduced to the bath by the alumina feed, anode materials and, to a minor extent, by fluorides used for optimisation of the bath composition. The impurities mainly consist of oxides, phosphates and sulphurous compounds (Grjotheim and Matiasovsky 1983).

All impurities (except possibly B_2O_3 and CaO) are – to a varying degree – deleterious to aluminium electrolysis. Depending on their nature, they may affect the electrolysis in various ways (Grjotheim and Matiasovsky 1983):

1. Reaction of impurities with the components of the electrolyte may change the electrolyte's chemical composition.
2. Impurities may interact with carbon in the bath, anode or carbon lining.
3. Impurities with a lower decomposition potential than alumina may decompose electrolytically or be chemically reduced in the bath. The metals produced thereby will contaminate the aluminium.

The decomposition potentials (E_d) of the impurities in cryolite are of prime importance with respect to their behaviour in the electrolyte. In this context it should be noted that in molten salts no general electrochemical series can be formulated, since the deposition potentials of individual metals vary with the anionic environment. The sequence of the deposition potentials of the individual elements may also vary with temperature. Experimental data collected by Grjotheim and Matiasovsky (1983) are given in Table 1-1 for metal oxides with lower decomposition potential than alumina. In the same table are also presented calculated values of the standard decomposition potential ($E^\circ_{d, 1300\text{ K}}$) of the respective oxides where the standard state of the oxides is the stable form at 1300 K.

When comparing the standard decomposition potentials with experimental values, it should be realised that the latter values are necessarily lower than the calculated ones due to anodic depolarisation when using carbon anodes. Besides, the reported decomposition voltage measurements originate from a wide range of experimental conditions and cell designs. Consequently, reported values are not necessarily comparable, but even trends may be of interest. A comparison of the relative position of the independently determined E_d values of the oxide impurities with that of alumina is of more interest.

According to Grjotheim and Matiasovsky (1983), the impurities can be divided into several groups, depending on their behaviour in the electrolytic process:

- (a) Water.
- (b) Metal oxides with higher decomposition potential than alumina.
- (c) Metal oxides with lower decomposition potential than alumina.
- (d) Non-metallic oxides.
- (e) Sulphurous compounds.

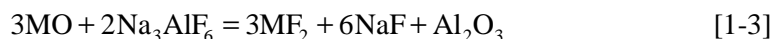
Groups (b) and (c) are most relevant with regard to the present work, and are, therefore, discussed in more detail in the following.

Table 1-1 Theoretical and experimental values of the decomposition potential (in V) of oxide impurities (Grjotheim and Matiasovsky 1983).

Substance	E° _{d, 1300 K}	Experimental E _d values		
Al ₂ O ₃	2.16	1.07	1.45	1.25 to 1.45
BeO	2.45	>1.07		
MgO	2.37	>1.07		
CaO	2.59	>1.07		
BaO	2.20	>1.07		
FeO	0.98	0.23		
NiO	0.65	0.00		
Mn ₃ O ₄	1.21	0.81		
Fe ₃ O ₄	0.91	0.23		
Co ₃ O ₄	0.54	0.14		
Cr ₂ O ₃	1.37	0.75		
SiO ₂	1.80		0.95	1.00 to 1.25
TiO ₂	1.84	0.50		
V ₂ O ₅	1.07	0.08	0.60	
Nb ₂ O ₅	1.39	0.71	0.64	
Ta ₂ O ₅	1.54	0.83	0.91	
MoO ₃	0.75	0.10		
WO ₃	0.89	0.40		

Metal Oxides with Higher Decomposition Potential than Alumina

As can be seen from Table 1-1, the alkali and alkaline earth oxides belong to this group. Theoretically, it might be expected that the impurities of this group would not interfere with the cathode process. They can, however, react with constituents of the electrolyte, *e.g.* by the reaction (Grjotheim and Matiasovsky 1983):



This results in the formation of alumina, NaF and the corresponding fluoride, leading to increased basicity of the electrolyte and eventually to increased consumption of AlF₃. As to their contamination of aluminium, this may be expected to result from a chemical exchange reaction between the metallic ion and aluminium. Increasing concentration of an impurity (*e.g.* Ca, Mg, or Na), however, will reduce the difference between the deposition potentials of the metal and of aluminium, thus making possible the co-deposition of the metal. All these expectations are fully met by calcium, which enters the process from low levels of CaO impurity in the alumina. After some time it attains a steady state concentration in the bath of 4 - 6 wt% CaF₂. It may be assumed that the calcium concentration of aluminium is governed by the equilibrium,

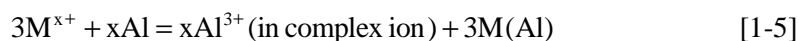


and is determined by the Ca(II) activity in the melt (Grjotheim and Matiasovsky 1983).

According to Grjotheim and Matiasovsky (1983), it can be concluded that alkali and alkaline earth oxides have only a minor influence on the contamination of aluminium, and their negative role in the electrolyte process is mainly confined to an increased consumption of AlF_3 for the adjustment of the electrolyte composition. Alkali metal impurities may, however, have an effect on the lifetime of the carbon cathode lining.

Metal Oxides with Lower Decomposition Potential than Alumina

These impurities are responsible for most aluminium contamination, iron and silicon being the major contaminants with typical concentrations of 800 and 600 ppm, respectively, in aluminium. The metal oxides of this group are reduced at the cathode either electrochemically or chemically by the exchange reaction,



and the reduced metals alloy with and contaminate the aluminium produced (Grjotheim 1985).

Unlike alkali and alkaline earth oxides, the impurities of this group do not accumulate in the electrolyte. During the lifetime of a cell of 1700 days, the concentration of vanadium and titanium in the electrolyte stayed fairly constant, while the calcium fluoride concentration increased (Grjotheim and Matiasovsky 1983). It might be expected that the impurity metal would be quantitatively transferred to the aluminium. This is, however, not the case, and analysis of emissions suggests the reaction of some oxide impurities to form volatile compounds such as SiF_4 , PbF_2 and TiF_4 (Grjotheim and Matiasovsky 1983). In addition impurities may escape as particulates (Thonstad 1999).

The origin and the behaviour of the elements investigated in the present work are discussed below.

Iron

Production equipment (anode studs, gas collecting skirts, cathode bars, burners, spikes, steel tools *etc.*) is the largest source of iron impurities. For instance, in Söderberg cells, sulphur in the anode reacts with the iron studs, producing FeS (Thonstad 1999). According to Sterten *et al.* (1998), dissolved iron compounds reduce the CE by 0.23 % per 0.01 wt% Fe present in the bath. Most of the iron introduced by the raw materials goes into the metal, but some is being recycled with secondary alumina. Iron in the anode increases the carbon consumption (Haarberg *et al.* 1994).

Silicon

Silicon is introduced to the process from alumina, gas collecting skirts, refractory bottom lining and silicon carbide sideling. Some silicon disappears in the exit gas, and this is assumed to be due to volatile SiF_4 which can be formed anodically, in the anode or by reaction in the bath (Thonstad 1999):



Silicon species present in the bath have a negative influence on the CE, *i.e.* 0.31 % per 0.01 wt% Si in solution (Sterten *et al.* 1998).

Titanium

Titanium is introduced mainly through the alumina, but smaller amounts can be assigned to pitch or anodes. Some of the amounts introduced would disappear with the gas, and it is assumed that this is due to formation of volatile TiF_4 (equivalent to reaction [1-6]). Titanium compounds in the bath reduces the CE by 0.24 % per 0.01 wt% Ti (Sterten *et al.* 1998), but due to low contents this effect is small.

1.3 Aluminium-Alloying Elements

Iron

Iron has a high solubility in liquid aluminium. The solubility of iron in the solid state is very low (~0.04 %) and, therefore, most of the iron present in aluminium above this concentration appears as an intermetallic second phase in combination with aluminium and often other elements. Because of its limited solubility, it is used in electrical conductors in which it provides a slight increase in strength and better creep characteristics at moderately elevated temperatures. Although small amounts of iron in aluminium may reduce soldering during die casting, its presence in aluminium-silicon casting alloys is generally undesirable because it forms coarse iron-rich phases that reduce ductility. Iron reduces the grain size in wrought products. Alloys of iron and manganese near the ternary eutectic content, such as 8006 (1.60 % Fe and 0.53 % Mn), can have useful combinations of strength and ductility at room temperature and retain strength at elevated temperatures. The properties are due to the fine grain size that is stabilised by the finely dispersed iron-rich second phase. Iron is added to the aluminium-copper-nickel group of alloys to increase strength at elevated temperatures (Hatch 1984).

Silicon

Silicon is the most common addition in casting alloys. In wrought alloys, silicon is used with magnesium at levels up to 1.5 % to produce Mg_2Si in the 6XXX series of heat treatable alloys. High-purity aluminium-silicon alloys are hot-short up to 3 % silicon, the most critical range being 0.17 to 0.8 % silicon, but additions of silicon (0.5 to 4.0 %) reduce the cracking tendency of aluminium-copper-magnesium alloys. A whole series of aluminium casting alloys containing silicon with copper and/or magnesium are in commercial use. Small amounts of magnesium added to any silicon-containing alloy will render it heat treatable. The mechanical properties of aluminium-silicon casting alloys benefit by modification. Chill casting achieves the same result of refining the silicon eutectic. Up to 12 % silicon is added in wrought alloys used as cladding for brazing sheet. Alloys containing about 5 % silicon acquire a black colour

when anodised and are used for ornamental purposes. A low maximum silicon content is specified in some alloys of the aluminium-magnesium and aluminium-zinc-magnesium groups because silicon in these systems has a deleterious effect on tensile properties (Hatch 1984).

Titanium

Amounts of 10 to 100 ppm titanium are found in commercial aluminium. Titanium depresses the electrical conductivity of aluminium, but its level can be reduced by the addition of boron to the melt to form insoluble TiB_2 . Titanium is used primarily as a grain refiner of aluminium alloy castings and ingots. When used alone, the effect of titanium decreases with time of holding in the molten state and with repeated remelting. The grain-refining effect is enhanced if boron is present in the melt or if it is added as a master alloy containing boron largely combined as TiB_2 . Titanium is a common addition to weld filler wire; it refines the weld structure and prevents weld cracking. It is usually added alone or with TiB_2 during the casting of sheet or extrusion ingots to refine the as-cast grain structure and to prevent cracking (Hatch 1984).

1.4 Scope

The primary objective of this thesis is to contribute to the general understanding of the behaviour of dissolved impurity species in the Hall-Héroult bath. In so doing, the aim was to perform measurements both in the laboratory and in industrial cells to give a better understanding of this complex process.

In order to provide more information about the dissolution reaction of impurity species in the bath, solubility measurements were performed as a function of alumina concentration, temperature and cryolite ratio. In addition to the important solubility data from such measurements, the data can also provide information about the structure of the dissolved impurity species, as well as more fundamental thermodynamic data. The electrochemical behaviour was studied by applying the techniques cyclic voltammetry, chronoamperometry, and chronopotentiometry. These techniques provide information on the type of reaction, the magnitude of diffusion coefficients and the number of electrons taking part in reactions. The aim was to investigate the chemical and electrochemical behaviour of dissolved divalent iron and tetravalent titanium species in cryolite-alumina melts in the laboratory, as described above. Iron was selected because of its importance as the major impurity in the Hall-Héroult bath, as well as a possible constituent in an inert anode. Titanium was chosen because it is an unwanted impurity in aluminium. Titanium may also play an even more important role in the future, if an inert TiB_2 -based cathode will be used.

To obtain reliable information about the mass transport of dissolved impurity species from the bath to the aluminium metal, experiments must be performed in industrial cells. The main reason for this is the difficulty of reproducing the metal flow and the shape of the metal pad in a laboratory cell. The aim was to study the mass transport of

iron, silicon and titanium by adding them as oxides to the bath in industrial cells. By measuring the concentrations of the elements both in the bath and in the produced aluminium, one was able to estimate the mass transfer coefficients and the thickness of the diffusion layer. Silicon was investigated, together with iron and titanium, because it is a major impurity in the Hall-Héroult bath.

References to Chapter 1

- Grjotheim, K. (1985): Nature and Origin of Impurities in the Hall-Héroult Electrolyte and their Effect on Metal Purity, *International Seminar on Refining and Alloying of Liquid Aluminium and Ferro-Alloys*, August 26 - 28, Trondheim, Norway.
- Grjotheim, K., C. Krohn, M. Malinovsky, K. Matiasovsky and J. Thonstad (1982): Aluminium Electrolysis – Fundamentals of the Hall-Héroult Process, 2nd Edition, Aluminium-Verlag GmbH, Düsseldorf, Germany.
- Grjotheim, K. and H. Kvande (1993): Introduction to Aluminium Electrolysis, 2nd Edition, Aluminium-Verlag GmbH, Düsseldorf, Germany.
- Grjotheim, K. and K. Matiasovsky (1983): Impurities in the Aluminium Electrolyte, *Aluminium*, **59**, 687.
- Haarberg, G. M., L. N. Solli and Å. Sterten (1994): Electrochemical Studies of the Anode Reaction on Carbon in NaF-AlF₃-Al₂O₃ Melts, in *Light Metals 1994*, U. Mannweiler, Editor, TMS, Warrendale, PA, p. 227.
- Hatch, J. E. (1984): Aluminum – Properties and Physical Metallurgy, American Society for Metals, Metals Park, Ohio.
- Sterten, Å., P. A. Solli and E. Skybakmoen (1998): Influence of Electrolyte Impurities on Current Efficiency in Aluminium Electrolysis Cells, *J. Appl. Electrochem.*, **28**, 781.
- Thonstad, J. (1999): The Behaviour of Impurities in Aluminium Cells, in *Proceedings of the Tenth International Aluminium Symposium*, Stara Lesna, Slovakia, p. 5.

2 Theory

2.1 Potential Sweep Techniques

A potential sweep technique such as cyclic voltammetry is very widely used, especially in preliminary studies of electrochemical systems. A cyclic voltammogram may be regarded as an electrochemical spectrum containing information about the types of reactions observed in the system and at which potentials they occur. Cyclic voltammetry is not limited to electrochemical reactions, but is probably the most powerful technique available for investigating coupled chemical reactions (Greef *et al.* 1990), where an important feature is its ability to detect and identify reaction intermediates.

One main advantage is that the time scale for these methods can be varied over a wide range, thereby making it possible to study both relatively slow as well as quite fast reactions with one technique. Linear sweep voltammetry is frequently used for measuring diffusion coefficients. Rate constants can in some cases be estimated from cyclic voltammetry, but better techniques probably exist for that purpose (Greef *et al.* 1990).

Linear Sweep Voltammetry

The basis of linear sweep voltammetry (LSV) is to sweep the potential linearly at a constant rate while recording the current:

$$E(t) = E_i \pm vt \quad [2-1]$$

Here E_i is the initial potential at which the sweep starts, and v is the sweep rate. The plus and minus signs indicate sweeping in the anodic or cathodic direction, respectively.

Consider a reversible reduction,



taking place at a planar electrode. According to Fick's first law, the current density is proportional to the concentration gradient of species O at the electrode, *i.e.*

$$i = -nFD_O \left(\frac{\partial c_O}{\partial x} \right)_{x=0} \quad [2-3]$$

where x denotes the distance from the electrode surface. It is therefore not necessary to know the entire concentration profile $c(x, t)$ of O.

Equation [2-3] is valid only if diffusion is the sole mode of mass transport in the system. Migration of O can be neglected by using a large excess of supporting electrolyte. Likewise, convection need not be considered in unstirred solutions on short time scales (<10 s). At longer times, however, natural convection arising from density differences may become important (Greef *et al.* 1990).

Under these conditions the mathematical treatment of transient electrochemical techniques is based on solving Fick's second law,

$$\frac{\partial c_i}{\partial t} = D_i \frac{\partial^2 c_i}{\partial x^2} \quad [2-4]$$

for O and R with appropriate initial and boundary conditions. With just O initially present in solution and assuming $D_O = D_R = D$, the initial and boundary conditions (Greef *et al.* 1990) are,

$$1. \underline{t = 0, x \geq 0} \quad c_O = c_O^\infty \text{ and } c_R = 0 \quad [2-5]$$

$$2. \underline{t \geq 0, x \rightarrow \infty} \quad c_O = c_O^\infty \text{ and } c_R = 0$$

$$3a. \underline{t > 0, x = 0} \quad D_O \left(\frac{\partial c_O}{\partial x} \right) = -D_R \left(\frac{\partial c_R}{\partial x} \right) \text{ and}$$

$$3b. \quad \frac{c_O}{c_R} = \exp \left[\frac{nF}{RT} (E - E^\circ) \right]$$

Conditions 1, 2 and 3a are quite general, whereas 3b holds only for a reversible reaction. The basic assumption is that the electron transfer is so fast that for any change in electrode potential, the ratio c_O/c_R immediately adjusts to the value predicted by this so-called Nernst equation.

This boundary value problem was first solved by Randles and Sevcik (Greef *et al.* 1990), and the peak current density is, therefore, given by the Randles-Sevcik equation:

$$i_p = -0.4463 \frac{(nF)^{3/2}}{(RT)^{1/2}} D_O^{1/2} c_O^\infty v^{1/2} \quad [2-6]$$

Thus, for a reversible reaction, a plot of i_p against $v^{1/2}$ yields a straight line passing through the origin with a slope from which D_O can be calculated.

A convenient diagnostic for a nernstian wave (Bard and Faulkner 1980) is,

$$E_p - E_{p/2} = -2.20 \frac{RT}{nF} \quad [2-7]$$

This difference, referred to as the shape factor, can be used to determine the number of electrons transferred.

Thus far the reduced species has been assumed to be soluble either in the solution or in the electrode. If, however, the product of the reduction forms a solid or liquid deposit, the mathematical treatment becomes somewhat different. Consider a typical metal deposition reaction:



It is convenient to make the simplifying assumption that M is deposited with a constant unit activity. This is true if the electrode surface is immediately covered by at least one monolayer of M once the reversible potential is reached. The problem was first treated by Berzins and Delahay (Delahay 1954), and the peak current density is given by,

$$i_p = -0.6105 \frac{(nF)^{3/2}}{(RT)^{1/2}} D^{1/2} c^\infty v^{1/2} \quad [2-9]$$

The shape factor for a reversible metal deposition (Mamantov *et al.* 1965) is:

$$E_p - E_{p/2} = -0.77 \frac{RT}{nF} \quad [2-10]$$

Comparing the shape factors in equations [2-7] and [2-10], it is evident that the peak is steeper and narrower for a deposition process, as shown in Figure 2.1.

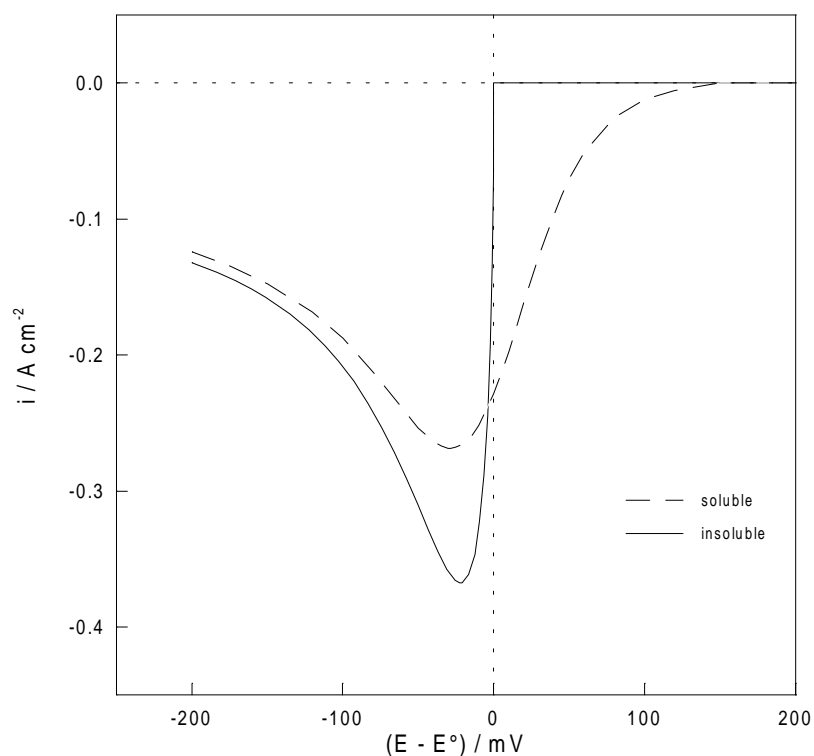


Figure 2.1 Theoretical linear sweep voltammograms for a reversible reduction process with soluble (broken line) and insoluble products (full line). In both cases the following arbitrary parameters are chosen: $n = 1$, $T = 298 \text{ K}$, $c^\infty = 1 \text{ M}$, $D = 10^{-5} \text{ cm}^2 \text{ s}^{-1}$ and $v = 100 \text{ mV s}^{-1}$. The figure is taken from Større (1999).

Cyclic Voltammetry

Experimentally, cyclic voltammetry (CV) is a much more common and versatile method than simple LSV. In the preliminary studies of unknown systems, the method is useful for recognising related cathodic and anodic reactions. Also, when coupled homogenous reactions are involved, CV is an excellent tool for distinguishing between possible reaction mechanisms.

In cyclic voltammetry the potential is varied linearly as in LSV, but when the switching potential E_λ is reached, the sweep is reversed. Normally the same sweep rate is applied for both forward and reverse sweeps. The potential at any time is given by

$$\begin{array}{ll} 0 < t \leq \lambda & E = E_i - vt \\ t \geq \lambda & E = E_i - 2v\lambda + vt \end{array} \quad [2-11]$$

Consider again the reversible reduction of O to R in equation [2-2]. The forward sweep is described in the previous section. On the reverse sweep R is oxidised back to O, and an anodic peak appears with identical shape and size as the cathodic peak. The base line for this anodic peak is the cathodic curve that would have been obtained if there had been no change in direction of the potential sweep (Bard and Faulkner 1980). A typical cyclic voltammogram for a reversible system where both reactant and product are soluble in the solution is shown in Figure 2.2.

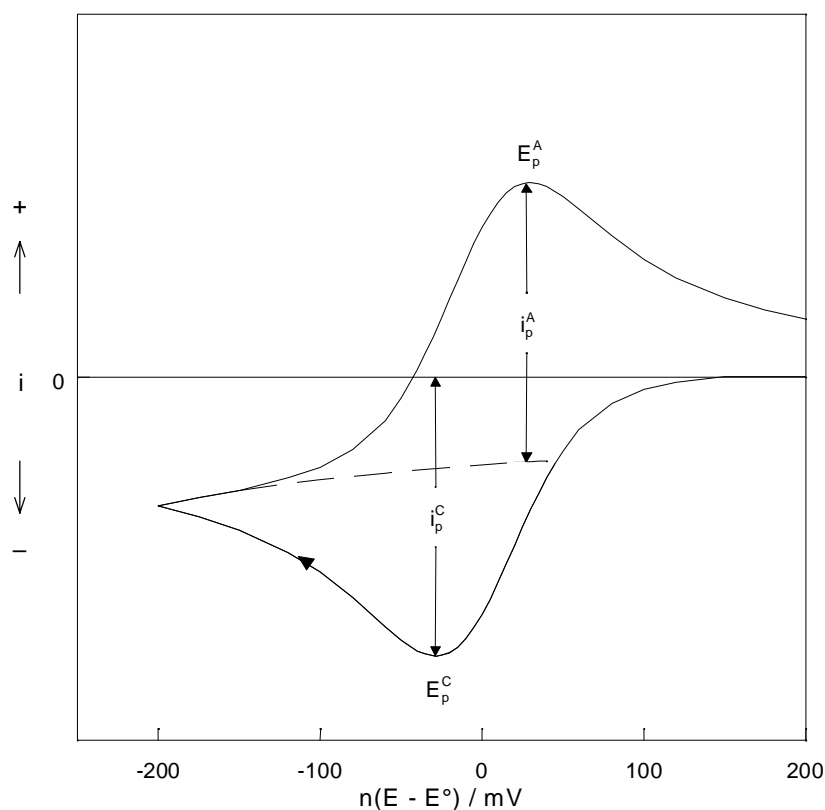


Figure 2.2 Theoretical cyclic voltammogram at 298 K for a reversible reduction process with a soluble product. Note that the anodic peak height is measured to the extension of the cathodic curve, represented by the broken line. At any other temperature, the values on the potential axis must be multiplied by $(T/298 \text{ K})$. The figure is taken from Større (1999).

Table 2-1 contains a number of diagnostic criteria that can be used to test the reversibility of such a system. Failure to satisfy one or more of these criteria implies that the electron transfer in question is not truly reversible on the time scale of the experiment.

Table 2-1 Diagnostic tests for a reversible electron transfer with soluble product (Greef et al. 1990).

1.	$i_p \propto \nu^{1/2}$
2.	$ i_p^A / i_p^C = 1$
3.	E_p independent of ν
4.	$\Delta E_p = E_p^A - E_p^C = \ln 10 \frac{RT}{nF}$
5.	$ E_p - E_{p/2} = 2.2 \frac{RT}{nF}$

A similar cyclic voltammogram for the reversible deposition of an insoluble product, such as a metal, is given in Figure 2.3.

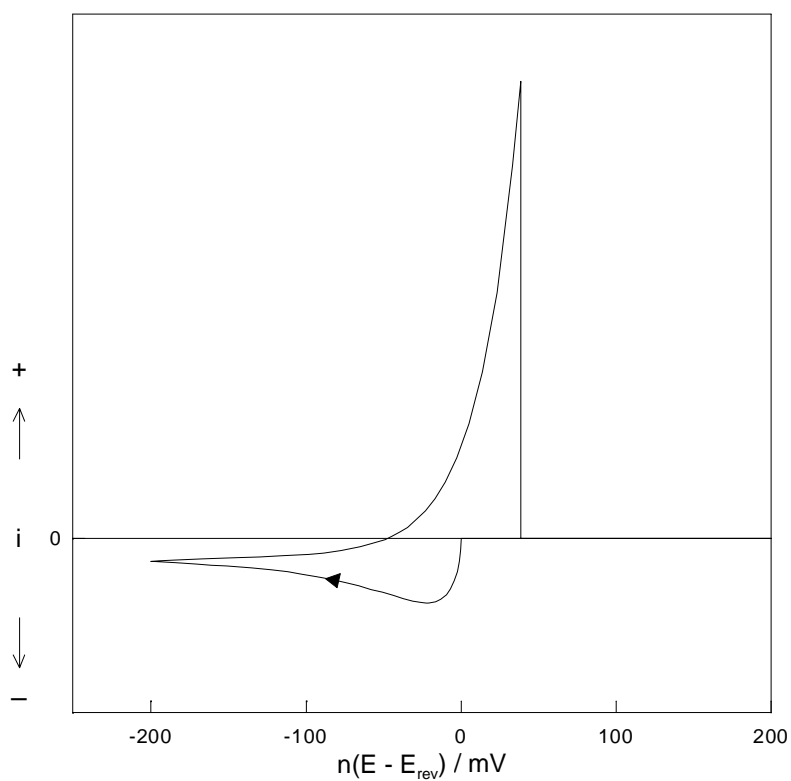


Figure 2.3 Theoretical cyclic voltammogram at 298 K for a reversible reduction process with an insoluble product. At any other temperature, the values on the potential axis must be multiplied by $(T/298 \text{ K})$. The figure is taken from Støre (1999).

2.2 Chronoamperometry

The potential step technique, frequently referred to as chronoamperometry, consists of applying a constant potential to the working electrode and recording the current as a function of time.

Consider a solution with only O initially present. The working electrode is held at a potential E_1 where no reduction of O occurs. At $t = 0$ the potential is instantaneously changed to a value E_2 where the surface concentration of O becomes effectively zero, so that the reaction,



proceeds at a diffusion controlled rate. This is done by choosing E_1 and E_2 well positive and well negative, respectively, of the standard potential of the O/R couple. For a reversible process the electron transfer is fast enough to maintain equilibrium between O and R at the electrode surface. The potential of the working electrode is then related to the surface concentrations of O and R by the Nernst equation,

$$E = E^0 + \frac{RT}{nF} \ln \frac{c_O^\sigma}{c_R^\sigma} \quad [2-12]$$

The activity coefficients are assumed to be unity so that concentrations rather than activities may be used. The mathematics involved in finding an expression for $i(t)$ again reduces to solving Fick's second law,

$$\frac{\partial c_O}{\partial t} = D_O \frac{\partial^2 c_O}{\partial x^2} \quad [2-4]$$

with the boundary conditions (Greef *et al.* 1990),

$$\begin{array}{ll} 1. \underline{t = 0, x \geq 0} & c_O = c_O^\infty \\ 2. \underline{t \geq 0, x \rightarrow \infty} & c_O = c_O^\infty \\ 3. \underline{t \geq 0, x = 0} & c_O = 0 \end{array} \quad [2-13]$$

This boundary value problem is solved by using Laplace transformation (Greef *et al.* 1990). The current density is given by the Cottrell equation (Greef *et al.* 1990):

$$i = -\frac{nFD_O^{1/2}c_O^\infty}{\pi^{1/2}t^{1/2}} \quad [2-14]$$

Thus, if the process is truly diffusion controlled at the applied potential, a plot of i against $t^{-1/2}$ should be linear and pass through the origin. The diffusion coefficient of O can then readily be calculated from the slope.

Since the rate of mass transport is infinite at $t = 0$, the faradaic current is initially kinetically controlled. In theory, the rate constant for the electron transfer could be determined from the value of the current at $t = 0$. Unfortunately, the measured current consists initially of a large nonfaradaic component due to charging of the double-layer capacitance. This phenomenon, which typically lasts a few hundred microseconds (Greef *et al.* 1990), results in a sharp spike that totally conceals the faradaic current at short times. Anyway, owing to limitations imposed by the instrumental equipment, $i_{t=0}$ cannot be measured.

Equation [2-14] is based on the assumption that diffusion is the only mode of mass transport, but as already mentioned, the build-up of density gradients results in natural convection at long times (Bard and Faulkner 1980). The observed current is consequently higher than predicted by the Cottrell equation. The available time range for studying diffusion with the potential step technique is therefore on the order of 1 millisecond to 10 seconds (Greef *et al.* 1990).

2.3 Chronopotentiometry

The galvanostatic experiment analogous to chronoamperometry is known as chronopotentiometry. In this type of experiment the current flowing in the cell is instantaneously stepped from zero to some finite value, *i.e.* the overall reaction rate is fixed, and the potential of the working electrode is then monitored as a function of time. The mathematical problem is identical to the one described in the previous section, with the exception that the third boundary condition is replaced by (Bard and Faulkner 1980):

$$3. \underline{t > 0, x = 0} \quad D_O \left(\frac{\partial c_O}{\partial x} \right) = - \frac{i}{nF} \quad [2-15]$$

A constant concentration gradient is thus established at the electrode. The solution is again readily obtained by the Laplace transform method (Bard and Faulkner 1980). The surface concentration of O decreases continuously with time according to,

$$c_O^s(t) = c_O^\infty + \frac{2it^{1/2}}{\pi^{1/2}nFD_O^{1/2}} \quad [2-16]$$

without disobeying the condition in equation [2-15]. At the so-called transition time $t = \tau$, the surface concentration has dropped to zero, and it is no longer possible to maintain this gradient. Since the flux of O to the electrode is insufficient to sustain the

imposed current, the reduction of O must be accompanied by some other electrode reaction. This could be reduction of another ion in solution, but frequently decomposition of the solvent is the only possibility. One then observes a sudden potential transition to more negative values where the new reaction can take place.

The characteristic transition time, equivalent to the peak current density in voltammetry, is related to the concentration and to the diffusion coefficient of species O by the Sand equation (Bard and Faulkner 1980):

$$i\tau^{1/2} = -\frac{nFD_O^{1/2}\pi^{1/2}c_O^\infty}{2} \quad [2-17]$$

The product $i\tau^{1/2}$, which is independent of the applied current for a diffusion controlled process, can be used to determine either D or c^∞ . This is in fact the basis of the chronopotentiometric method.

The time dependence of the potential is given by,

$$E = E_{\tau/4} + \frac{RT}{nF} \ln \frac{\tau^{1/2} - t^{1/2}}{t^{1/2}} \quad [2-18]$$

where

$$E_{\tau/4} = E^o - \frac{RT}{nF} \ln(D_O / D_R)^{1/2} \quad [2-19]$$

is the so-called quarter-wave potential (Bard and Faulkner 1980). The corresponding expression for a metal deposition (Macdonald 1977) is,

$$E = E_{\text{rev}} + \frac{RT}{nF} \ln \frac{\tau^{1/2} - t^{1/2}}{\tau^{1/2}} \quad [2-20]$$

where E_{rev} is given by the Nernst equation. The shapes of these chronopotentiograms are compared in Figure 2.4.

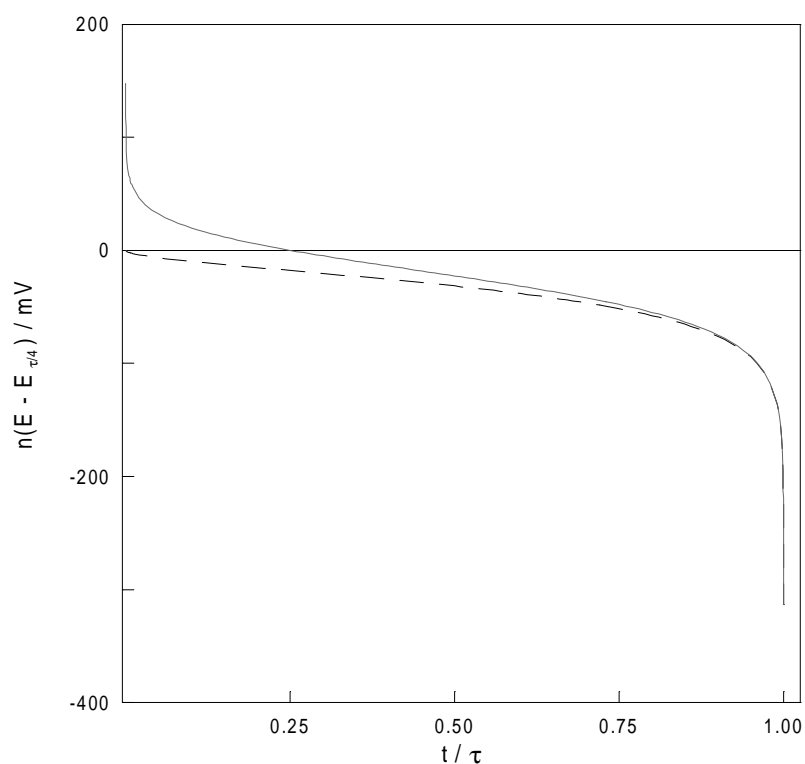


Figure 2.4 Theoretical chronopotentiograms at 298 K for a reversible reduction process with soluble (full line) and insoluble product (broken line). It is assumed that $D_R = D_O$ and $[M^{n+}] = 1\text{ M}$, in which case $E_{v/4} = E^\circ = E_{\text{rev}}$. At any other temperature, the values on the potential axis must be multiplied by $(T/298\text{ K})$. The figure is taken from Større (1999).

The major problem with chronopotentiometry lies in the determination of the transition time. If the potential transition had been instantaneous, *i.e.* $dE/dt \rightarrow \infty$, this would have been a straightforward matter. Unfortunately the situation is complicated by the fact that charging of the double-layer capacitance requires a finite time. In contrast to chronoamperometry, where the potential is held constant, the double-layer charging occurs throughout a chronopotentiometric experiment. Moreover, since the double-layer charging current is proportional to dE/dt (Bard and Faulkner 1980), it is at its largest around the potential transition, which therefore becomes ill-defined. This is a fundamental disadvantage of controlled current methods and the reason for their rather limited popularity.

References to Chapter 2

- Bard, A. J. and L. R. Faulkner (1980): *Electrochemical Methods*, John Wiley & Sons, Inc., New York.
- Greef, R., R. Peat, L. M. Peter, D. Pletcher and J. Robinson (1990): *Instrumental Methods in Electrochemistry*, Ellis Horwood, Chichester, England.
- Delahay, P. (1954): *New Instrumental Methods in Electrochemistry*, Interscience Publishers, Inc., New York, p. 123.
- Macdonald, D. D. (1977): *Transient Techniques in Electrochemistry*, Plenum Press, New York, p. 127.
- Mamantov, G., D. L. Manning and J. M. Dale (1965): Reversible Deposition of Metals on Solid Electrodes by Voltammetry with Linearly Varying Potential, *J. Electroanal. Chem.*, **9**, 253.
- Støre, T. (1999): *Electrodeposition of Metals from Molten Salts*, Doctoral Thesis 1999:18, Department of Electrochemistry, Norwegian University of Science and Technology, Trondheim, Norway.

3 Solubility of FeO and FeAl₂O₄ in Cryolite-Alumina Melts

3.1 Introduction

A study of iron oxide solubility in cryolite-alumina melts is interesting for at least three reasons. Iron is one of the most predominant impurities present in the commercial production of aluminium, the Hall-Héroult process. Since iron compounds have a lower decomposition potential (E_d) than alumina, they contribute to a major part of the contamination in the aluminium metal produced. Contamination as high as ~0.2 wt% iron has been reported according to Thonstad (1999). According to Grjotheim and Matiasovsky (1983) an experimental investigation at 1020 °C gave an E_d of -0.23 V for both FeO and Fe₃O₄ compared to -1.07 V for Al₂O₃ *versus* a carbon anode. The investigation indicated that the decomposition potential of these oxides was independent of the valency of the metal in the oxide added. Calculations by Grjotheim and Matiasovsky (1983) gave theoretical standard decomposition potentials at 1300 K for FeO and Fe₃O₄ as -0.98 V and -0.91 V, respectively. The E_d° for Al₂O₃ was calculated to be -2.16 V. These calculations were based on the assumption that pure metal and oxygen gas were the decomposition products.

According to Sterten *et al.* (1998) dissolved iron compounds may influence the current efficiency (CE) with respect to aluminium. They reported a linear decrease in CE with increasing additions of Fe₂O₃. The lowering in CE was found to be (0.23 ± 0.04) % per 0.01 wt% of Fe(III) added to the melt. Deininger and Gerlach (1979) reported the decrease in CE to be 0.3 % per 0.01 wt% of Fe(III) introduced to the melt.

The use of non-consumable anodes in aluminium electrolysis has been a subject of research and development for several years. So far carbon has been the only applicable anode material in Hall-Héroult cells. For a long time one has been aware of the inherent disadvantages of the carbon anode. It is expensive to produce and it gives considerable pollution of greenhouse gas by emitting CO₂. According to Mannweiler and Keller (1994) approximately 15 - 20 % of the cost of crude aluminium is due to the carbon consumption. The largest disadvantage of carbon anodes is that they are consumable. Prebaked anodes must be changed at regular intervals, and are therefore

very labour intensive. The insertion of a new cold anode represents the biggest operational disturbance of the heat balance of the cell.

If an inert anode material is used, the anode product would be $O_2(g)$ instead of $CO_2(g)$, which is the case when carbon is used. Calculations by Kvande (1999) show an increase of 1.03 V in the decomposition voltage of alumina if/when the new technology is adopted. This disadvantage means an increase in the theoretical minimum energy consumption at 960 °C from 6.34 to 9.26 kWh per kg aluminium.

According to Kvande (1999) the economical advantages of an inert anode are mainly the lower anode cost caused by the elimination of the carbon consumption in the electrolysis process, *i.e.* 160 - 200 USD per ton aluminium. It will be less labour demanding, and improved control and reduction of the interpolar distance will give better anodic current distribution, lower voltage between the anode and the cathode, and hence reduced energy consumption. The environmental advantages will mainly be strongly reduced emissions of PAH components and of the greenhouse gases CO_2 , CF_4 and C_2F_6 .

According to Billehaug and Øye (1981), the physico-chemical requirements for an inert anode may be summarised as follows:

1. Insoluble in a fluoride melt containing dissolved aluminium and sufficiently resistant to accidental contact with the molten aluminium cathode.
2. Resistance towards anodic oxygen.
3. Thermal stability up to 1000 °C with adequate resistance to thermal shock and gradients.
4. Low specific resistivity and low contact resistance to external current conductors. At 1000 °C the specific resistivity should be comparable with or smaller than that of the anode carbon.
5. Low overvoltage of discharge of oxide ions.
6. High overvoltage of undesired anodic reactions, *i.e.* discharge of fluorine.
7. No contamination of the aluminium produced.

It has been shown (Wang and Thonstad 1989) that it is important to avoid low alumina concentrations in order to prevent disintegration (a catastrophic form of corrosion) of the anode material. What happens is that the metal oxide (anode material) reacts with aluminium trifluoride and the metal dissolves as metal fluoride forming alumina. It should be noted that this contradicts criterion 6, *i.e.* discharge of fluorine, which would never take place.

Several materials have been tested with the aim of making an inert anode. Cermets have for a long time been viewed as one of the most promising group of materials. According to Kvande (1999) the material found so far, and the one that perhaps has been the closest to success, is a cermet of the type $NiFe_2O_4$ -18%NiO-17%Cu developed by Alcoa. It showed favourable corrosion and conductivity properties during

experiments in small laboratory cells. By favourable corrosion properties it is meant that the cermet has a limited dissolution rate, and that it is eroded slowly by the melt. This contradicts criterion 1, by Billehaug and Øye (1981), which states that an inert anode should be insoluble. In practice this criterion is unrealistic since all oxides have a certain solubility in cryolite-alumina melts.

To understand the corrosion mechanism of inert anodes, for example NiFe₂O₄, one has to know the solubility of the corrosion products in the electrolyte.

There are numerous studies in the literature on the solubility of iron oxides in cryolite. However, according to Dewing and Thonstad (2000), only a few are interesting since there was no control of the oxygen potential in some of the experiments. Iron has two oxidation states, Fe(II) and Fe(III), and even though the material being dissolved is either Fe(II) or Fe(III), the solution can contain both.

Johansen (1975, 1989) investigated the systems (a) Na₃AlF₆-FeF₂, (b) Na₃AlF₆-FeO, (c) Na₃AlF₆-FeF₃ and (d) Na₃AlF₆-Fe₂O₃ by thermal analysis and chemical analysis. Experiments concerning Fe(II), *i.e.* systems (a) and (b), were conducted in an iron crucible, while those concerning Fe(III), *i.e.* systems (c) and (d), were run in a platinum or graphite crucible. All experiments were made under 1 atm of argon. The results of system (a) showed a simple binary system with a eutectic point at 740 °C and 53 wt% FeF₂. The melting point of pure FeF₂ was found to be 975 °C by thermal analysis. The cryolite-rich part of system (b) was investigated. The eutectic composition was found to be 5.2 wt% Fe_{0.947}O at 983 °C. From the phase diagram the solubility of Fe_{0.947}O at 1020 °C was found to be 5.84 wt%, corresponding to 4.48 wt% iron. System (c) was found to be a simple binary system with a eutectic at 694 °C. The eutectic composition was not reported. Analysis of the solidified melt showed the existence of divalent iron. The cryolite-rich part of system (d) was found to have a eutectic at 1006.5 °C and a composition of 1.1 wt% Fe₂O₃. A solubility of 1.33 wt% Fe₂O₃ (0.93 wt% Fe) at 1020 °C is found from the results. Freezing point depression data gave slopes of ~0.6, ~2, ~1 and ~5 for the systems (a), (b), (c) and (d), respectively. It was concluded that the most probable iron species was FeF₄²⁻ when FeF₂ and FeO were added. By adding FeF₃ and Fe₂O₃ the most likely iron species was found to be FeF₆³⁻, with some FeF₄⁻.

DeYoung (1986) studied the solubility of Fe₂O₃ in the system NaF-AlF₃-CaF₂-Al₂O₃ in the temperature range 800 - 1025 °C, and under an atmosphere of air. The experiments were run at different alumina concentrations and cryolite ratios. A linear relationship was obtained between the logarithm of the iron solubility and the inverse of the temperature ($\log \text{ wt\% Fe} = 4.71 - 7080/T$) for the alumina concentration range 1.5 - 6.5 wt% and CR between 1.4 and 3. Reading from a plot, the iron solubility at 1025 °C and with CR = 2.6 was found to be 0.24, 0.20, 0.19 and 0.19 wt% at the alumina concentrations 0.5, 1.7, 2.5 and 6.5 wt%, respectively. The partial molar enthalpy was reported to be 138 kJ mol⁻¹. No distinct relationship between CR and Fe₂O₃ solubility was observed.

Diep (1998) investigated the solubility of Fe(III) in cryolite melts at 1020 °C under both 1 atm of oxygen and 1 atm of argon, using ferric oxide, Fe_2O_3 , as additive. His results clearly demonstrated the effect of a controlled oxygen potential. The experiments conducted under 1 atm of oxygen consistently gave lower Fe(III) solubility than those run under 1 atm of argon at corresponding alumina concentrations. The solubility of Fe_2O_3 under 1 atm of oxygen and 1020 °C was found to be 0.71 wt% (0.50 wt% Fe) in cryolite, decreasing to 0.24 wt% (0.17 wt% Fe) in cryolite containing 12 wt% alumina. The corresponding solubilities under 1 atm of argon were reported to be 0.75 (0.52 wt% Fe) and 0.27 wt% (0.19 wt% Fe). Diep (1998) also demonstrated that maximum solubility of Fe_2O_3 was found at a cryolite ratio (CR) of three, independent of the alumina content in the melt. The partial molar enthalpy of dissolution was reported to be $(124 \pm 9) \text{ kJ mol}^{-1}$.

Calculations by Dewing and Thonstad (2000) show that at alumina saturation under 1 atm of oxygen, 4 % of the total iron in solution is present as Fe(II), while in an iron crucible under 1 atm of argon only 0.5 % of the total is present as Fe(III). The situation is described in Figure 3.1.

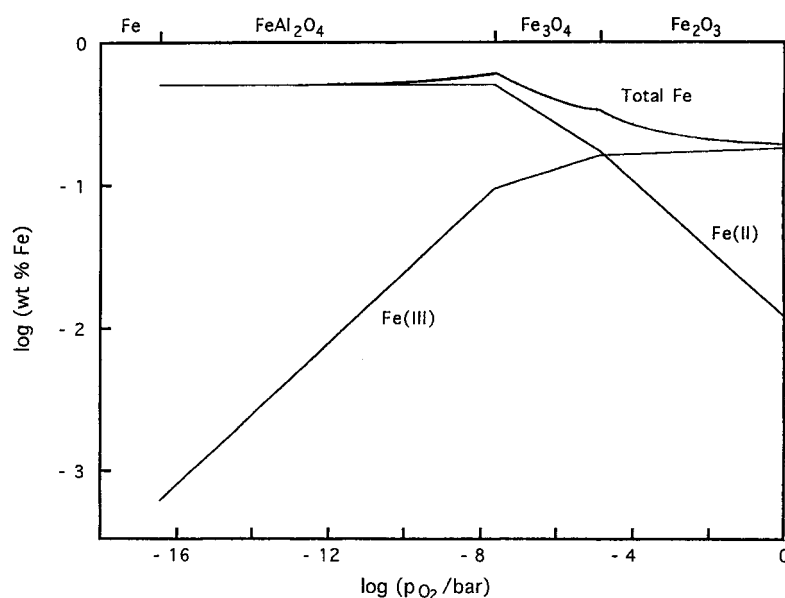
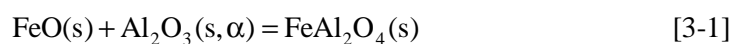
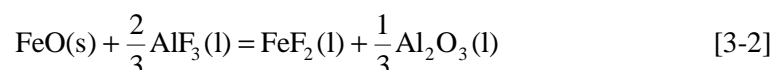


Figure 3.1 Concentrations of Fe(II), Fe(III), and total Fe in solution in cryolite melts saturated with Al_2O_3 at 1020 °C. Dewing and Thonstad (2000).

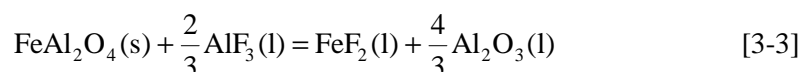
The standard Gibbs energy (ΔG_f°) for the reaction,



has been determined from the electromotive force (EMF) of solid-state cells with oxygen-ion-conducting electrolytes by Rezhukhina *et al.* (1963) and by Chan *et al.* (1973). The implication of their results is that ferrous oxide, FeO, is stable at low alumina concentrations, while at higher alumina concentrations ferrous aluminate, FeAl₂O₄, is stable. As suggested by Johansen (1975) and by Dewing and Thonstad (2000), ferrous oxide probably dissolves in molten cryolite as ferrous fluoride, FeF₂, if we consider neutral species. The scenario would therefore probably be that the dissolution mechanism,



applies at low alumina concentrations, while the dissolution mechanism,



applies at high alumina concentrations.

There are several ways of investigating the solubility of Fe(II) in cryolite melts. In the present work both electrochemical and chemical measurements were performed.

3.2 Experimental

3.2.1 Electrochemical Measurements

Furnace

The experiments were carried out in a standard closed furnace under argon atmosphere (99.99 %). Temperature control within ± 2 °C was achieved with a Eurotherm temperature controller and a calibrated S type thermocouple (Pt-Pt10%Rh) inside the Kanthal heating element. The working temperature was measured with an additional thermocouple protected by a platinum tube inserted into the melt.

Electrodes

A copper wire with a diameter of 0.50 mm served as the working electrode, the iron crucible served as the counter electrode, and an iron wire with a diameter of 2 mm as a reference electrode. Measurements were carried out by galvanostatic deposition of iron on a new copper wire after each addition of ferrous fluoride. The active area of the working electrode was determined after the experiment by visual inspection with a microscope. To avoid the influence of convection, the current applied was of such a magnitude that the transition time in chronopotentiometric measurements was less than 100 ms.

Chemicals

Natural hand-picked cryolite (Na_3AlF_6) from Greenland (Kryolittselskabet) was crushed, and coloured particles were removed before use. Al_2O_3 (Fluka, pro analysi) was stored at 200 °C and FeF_2 (Fluka, 95 %+) was stored in a desiccator to avoid pick-up of moisture. Otherwise the chemicals were used as received.

Cell

The melt (~150 g) was contained in a 70 mm × 46 mm (h × d) iron crucible, which was made by welding together a tube and a disk of low carbon steel. The crucible was sand blasted to remove any mill scale. A suspension made of two nickel wires and several Alsint* tubes (*Product of W. Haldenwanger, Berlin, containing 99.7 % Al_2O_3) positioned the crucible in the middle of the furnace. To minimise the temperature gradient, several evenly spaced radiation shields were placed both below and above the crucible. The connectors to the electrodes or the electrodes themselves were insulated with Alsint tubes. FeF_2 was added to the melt through a quartz tube. The melt was agitated by a platinum stirrer for 15 to 45 minutes after each addition of FeF_2 . All the equipment was brought out through openings in a removable brass lid covering the top of the cell. Figure 3.2 shows a schematic drawing of the cell.

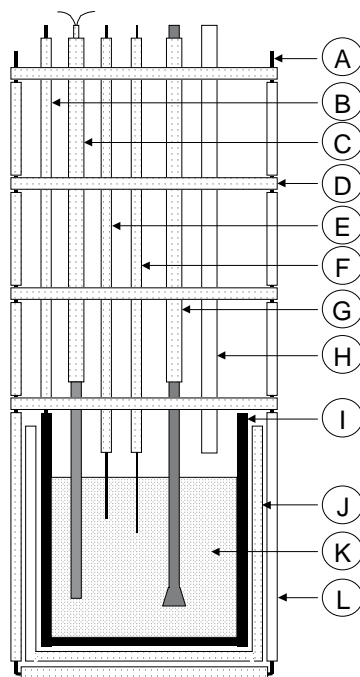


Figure 3.2 Schematic drawing of the experimental cell: (A) Ni wire; (B) Counter electrode connector; (C) Thermocouple; (D) Radiation shield; (E) Fe reference electrode; (F) Cu working electrode; (G) Pt stirrer; (H) Quartz tube for FeF_2 addition; (I) Fe crucible; (J) Alsint crucible; (K) Melt; (L) Alsint insulation.

Instrumentation

The electrochemical measurements were performed with a Radiometer DEA-I digital electrochemical analyser. It comprises a DEA332 potentiostat with a maximum current output of 2 A and an IMT102 electrochemical interface with a response time of less than 3 μ s. Signal imposition and data acquisition were handled by the Windows-based VoltaMaster 2 integrated software. A maximum of 5000 data points per measurement were stored on a PC.

3.2.2 Chemical Measurements

Chemicals

Al₂O₃, FeF₂ and Na₃AlF₆ were prepared as described in section 3.2.1. Aluminium fluoride, AlF₃ (Norzink), was purified in the laboratory by sublimation and dried under argon atmosphere at 400 °C for 10 hours. Sodium fluoride, NaF (Merck, p.a.), was dried under argon atmosphere at 400 °C for 10 hours. Ferrous oxide, FeO, was prepared in the laboratory by mixing and dry grinding ferric oxide, Fe₂O₃ (Aldrich, 99 %+), with excess iron powder (Aldrich, 99 %+) in a ball mill for 28 hours. The mixture was then heated in an iron crucible under argon atmosphere at 1050 - 1100 °C for 48 hours. Ferrous oxide is a non-stoichiometric compound known as wustite, Fe_{0.947}O. Wustite is thermodynamically stable at temperatures above 571 °C (Ullmann's 1989). Below this temperature wustite should disproportionate into magnetite, Fe₃O₄, and iron (eutectoid reaction), but the rate of this disproportionation decreases rapidly with decreasing temperature. At room temperature ferrous oxide is stable for an unlimited period of time. To avoid disproportionation the mixture was quenched by quickly moving the crucible to a colder part of the furnace when the temperature had dropped to around 580 °C. A schematic drawing of the set-up is given in Figure 3.3.

Set-up

Cryolite-alumina melts (~150 g) with excess ferrous oxide powder were contained in a 70 mm \times 46 mm (h \times d) iron crucible. After the solution had melted and the temperature was stabilised, it was agitated for at least one hour with an iron stirrer. The solution was then left without stirring to allow solid particles dispersed in the melt to settle. After 60 minutes a sample was taken with a quartz tube under suction, and subsequently quenched. A schematic drawing of the experimental set-up is given in Figure 3.4.

Analysis

The iron content in the samples was found by an inductively coupled atomic plasma instrument (ICP) of the model AtomScan 16 from Thermo Jarrell Ash. Preparation for the ICP analysis was made by dissolving 1 - 3 g of a crushed sample in 50 ml 30 % AlCl₃·6H₂O. The solutions were kept in teflon vessels at 80 °C for approximately 20 hours before 5 ml 30 % HCl was added. Finally, the solutions were contained in

100 ml polypropylene graduated flasks and filled with deionised water. Calibration of the instrument was done with three standard solutions with different concentrations of iron. It should be noted that the ICP does not differentiate between Fe(II) and Fe(III), but gives the total amount of iron present in the sample.

The oxygen content, and thereby the alumina concentration, was found with an instrument from LECO (RO-336). The sample (~50 mg) is mixed with graphite powder and contained in a graphite crucible. The mixture is reduced carbothermically during heating up to 2300 °C. The CO formed is purged out of the electrode chamber with an inert gas and through an IR cell which detects CO. From the amount of CO the oxygen content in the sample is calculated. The instrument was checked with steel samples of known oxygen content.

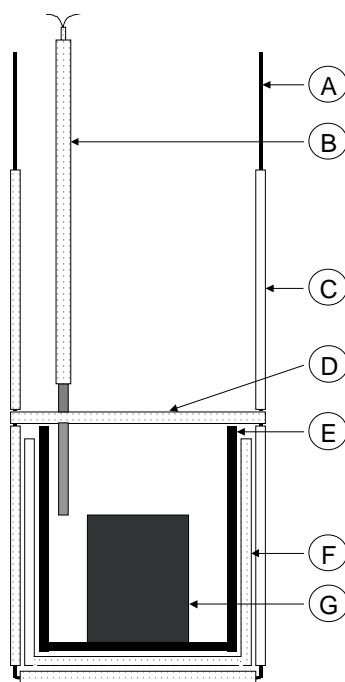


Figure 3.3 Schematic drawing of the experimental set-up: (A) Ni wire; (B) Thermocouple; (C) Alsint tube; (D) Radiation shield; (E) Iron crucible; (F) Alsint crucible; (G) Solid "FeO".

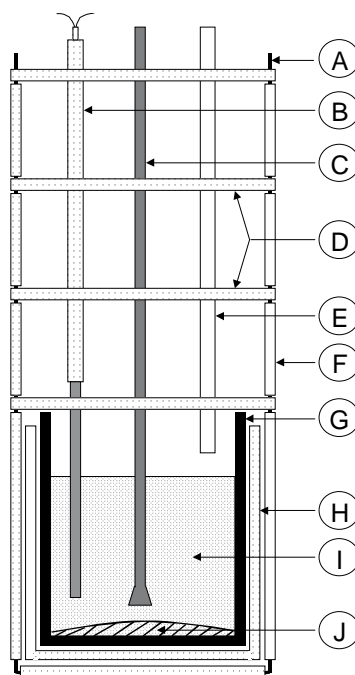


Figure 3.4 Schematic drawing of the experimental set-up: (A) Ni wire; (B) Thermocouple; (C) Iron stirrer; (D) Radiation shield; (E) Quartz tube; (F) Alsint tube; (G) Iron crucible; (H) Alsint crucible; (I) Melt; (J) Excess $\text{FeO}/\text{FeAl}_2\text{O}_4$.

3.3 Results and Discussion

3.3.1 Electrochemical Measurements

3.3.1.1 Solubility as a Function of Alumina Concentration

Ferrous fluoride was used as an additive in these experiments. Since the producer did not give the exact concentration, *i.e.* the purity of the product was given as 95 %+, it had to be analysed. An ICP analysis with respect to iron showed that the product contained 94.7 % ferrous fluoride. It is not known what the rest of the product consisted of, but a major part can probably be related to moisture since ferrous fluoride is known to be hygroscopic. All data presented in this section concerning added ferrous fluoride were corrected with the concentration found by analysis.

Chronopotentiometry was employed in the study of the Fe(II) reduction process, and thereby the study of the solubility of Fe(II) . The potential was monitored as a function of time while applying a constant current. Figure 3.5 contains a series of such

chronopotentiograms. The melt composition and the applied current densities are indicated on the plot.

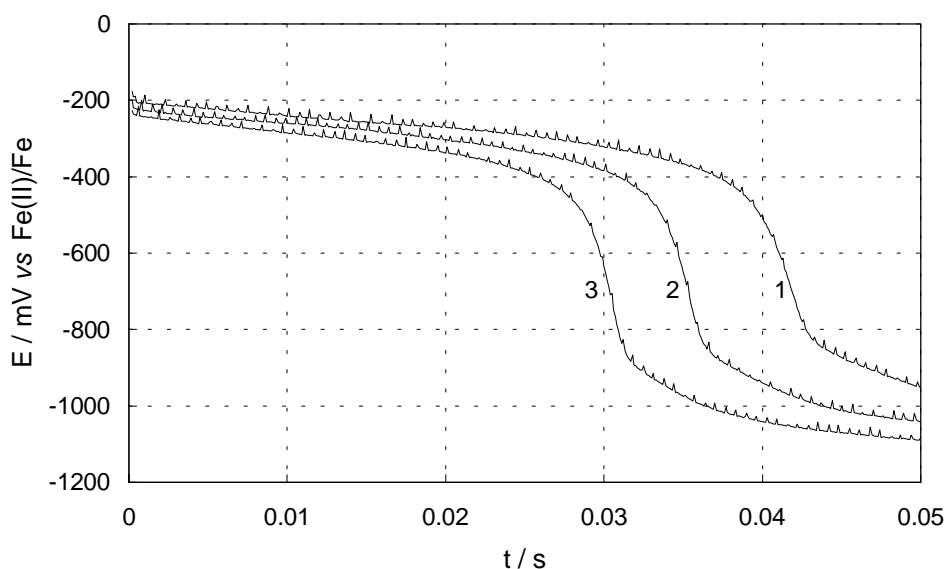


Figure 3.5 Transients resulting from different current densities at 8.56 wt% alumina and 1.47 wt% ferrous fluoride added to cryolite at 1020 °C. $i_1 = -1.83$, $i_2 = -1.98$ and $i_3 = -2.13 \text{ A cm}^{-2}$.

The potential is initially determined by reactions between the copper working electrode and cations present in the melt. The cations governing the working electrode potential would probably be Fe(II), since they are the most noble ions present in the melt. The potential moves gradually to more negative values as the surface concentration of Fe(II) ions decreases. Once the surface concentration at the copper electrode is zero, there is a sudden potential drop to a level where decomposition of the solvent occurs. This reaction is probably the reduction of aluminium ions.

The transition between these two potential plateaus, *i.e.* the plateau for reduction of Fe(II) and the plateau for reduction of Al(III), is clearly not instantaneous. It was discussed in section 2.3 how this sluggishness constitutes an inherent disadvantage of the chronopotentiometric method. Electrochemistry textbooks do not offer any well-established procedure for the determination of transition times in real experiments. Authors of publications rarely describe in detail how τ was measured, but in some cases they have resorted to some graphical method involving tangent lines and inflection points (Delahay 1954, Greef *et al.* 1990). Such a method might also include an element of trial and error with the requirement that the Sand equation (equation [2-17]) be obeyed.

Alternatively the chronopotentiograms can be treated analytically based on the theoretical E-t relationship outlined in section 2.3. With this approach E is plotted against $\ln[1 - (t/\tau)^{1/2}]$ in accordance with equation [2-20]. According to Støre (1999), the transition time is determined by the best linear fit in the interval $\tau/4 < t < 3\tau/4$. The method is illustrated in Figure 3.6 using the chronopotentiogram labelled 3 in Figure 3.5.

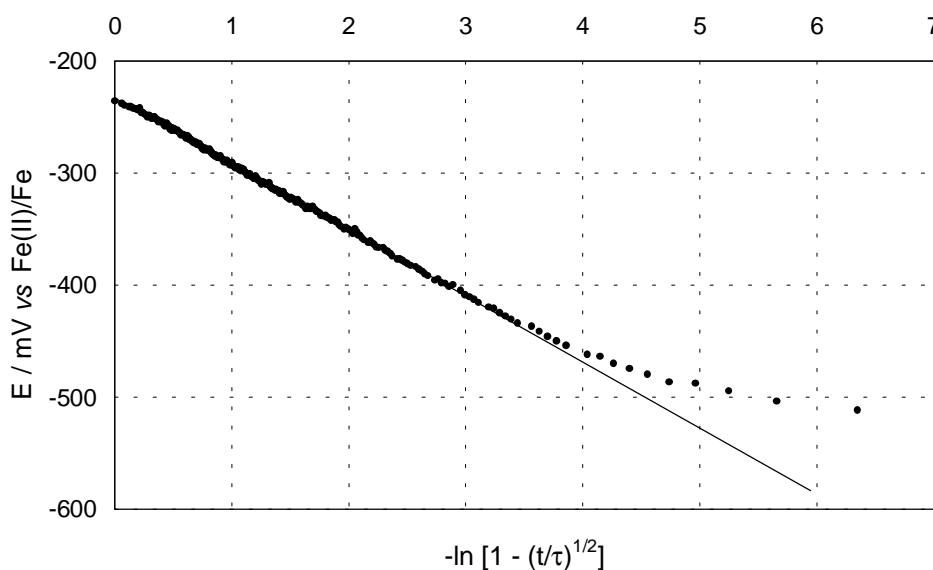


Figure 3.6 Determination of the transition time by best linear fit of the experimental points in the interval $[\tau/4, 3\tau/4]$. n is calculated from the slope of the regression line. See text.

The linear dependence of E on $\ln[1 - (t/\tau)^{1/2}]$ in the interval $0.10\tau < t < 0.90\tau$ verifies that the process is reversible with an insoluble product. The number of electrons involved in the reduction process is readily calculated from the slope of the regression line, as differentiation of equation [2-20] yields the relationship:

$$n = \frac{RT}{F} \frac{1}{dE/d\ln[1 - (t/\tau)^{1/2}]} \quad [3-4]$$

The deviation at long times in Figure 3.6 is probably caused by underpotential deposition of aluminium, *i.e.* deposition at potentials less cathodic than the reversible potential. This is only possible if the activity of the product is less than unity, and it implies that aluminium is forming an alloy with the iron-copper electrode.

Analysis of the chronopotentiograms labelled 1, 2 and 3 in Figure 3.5 yielded -0.3671 , -0.3669 and $-0.3665 \text{ A cm}^{-2} \text{ s}^{1/2}$ for the product $i\tau^{1/2}$, respectively. The corresponding n values were found to be 1.90, 1.86 and 1.89. From the resulting values one sees that the agreement is satisfactory. The product $i\tau^{1/2}$ is independent of the applied current density and proportional to the bulk concentration in accordance with the Sand equation (equation [2-17]). The slopes of the regression lines were close to the theoretical value, 55.7 mV, for a two electron reversible process at 1020 °C, indicating that reduction of Fe(II) is the predominant reaction. From Figure 3.5 it can also be seen that the Fe(III) concentration in the melt must be close to zero, since there is no plateau for the reduction of Fe(III) to Fe(II) at short times. This is in agreement with the calculations by Dewing and Thonstad (2000).

The analytical method outlined above is very time-consuming and not suited when it comes to treatment of the amount of data obtained in the present work, *i.e.* several hundred chronopotentiograms. Initially, some of the chronopotentiograms were analysed as described above. A graphical technique was then adopted based on the experience gained with the analytical method. The graphical technique is demonstrated in Figure 3.7.

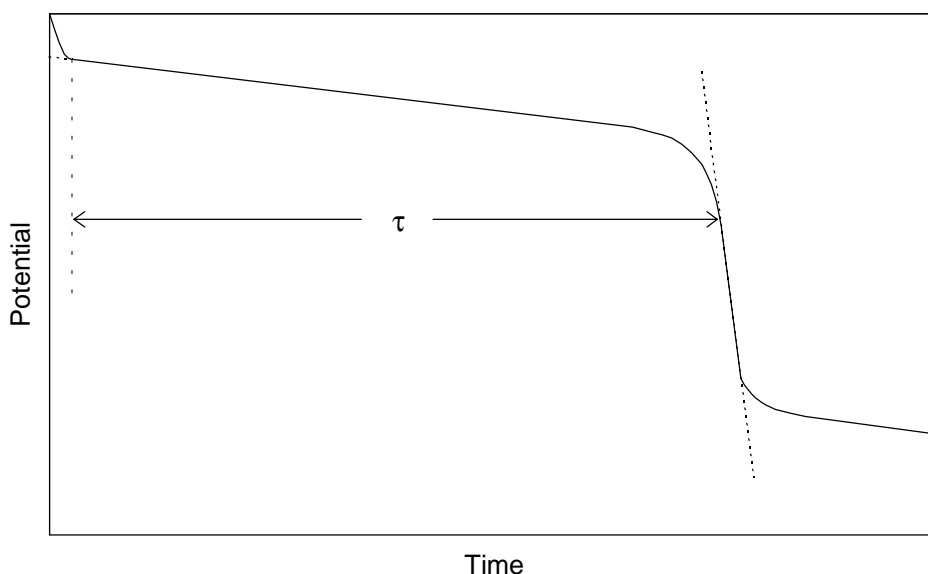
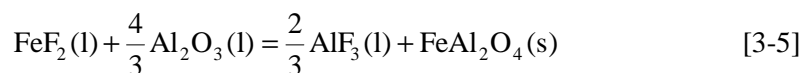


Figure 3.7 Illustration of the graphical technique for determination of the transition time.

From Figure 3.7, one can see that the transition time was determined as the difference between two inflection points. The graphical technique always yielded larger transition times compared with the analytical technique. Deviations of less than 3 % in

determined transition time values were found when a selection of chronopotentiograms was tested with the two techniques.

A typical plot of the ferrous fluoride concentration *versus* $i\tau^{1/2}$ is given in Figure 3.8 for an experiment with a melt below alumina saturation. The experimental points are given as open circles. The solid line consists of two parts separated by a breakpoint (BP), which defines the coexistence of ferrous fluoride and FeO or FeAl₂O₄. The first part, which is a straight line starting at zero concentration of ferrous fluoride, is obtained by regression analysis of the experimental points. In this concentration range the additive is completely dissolved in the electrolyte, and the alumina concentration is considered to be unchanged. One might expect that after the solution is saturated, the value of $i\tau^{1/2}$ would become constant, but Figure 3.8 shows that the line still has an upward slope. At the concentrations used in these experiments, the phase precipitating is FeAl₂O₄. The precipitation reaction is the reverse of reaction [3-3], or,



so that when FeAl₂O₄ is precipitated, not only FeF₂ but also Al₂O₃ is removed from solution. The consequent reduction in alumina concentration increases the solubility of FeAl₂O₄ (see Figure 3.9) and $i\tau^{1/2}$ continues to increase.

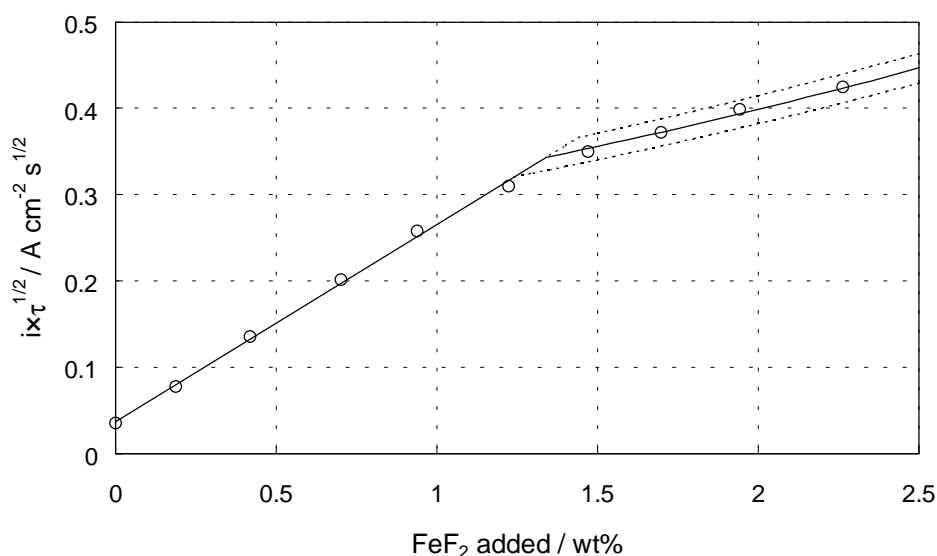


Figure 3.8 Plot of ferrous fluoride added versus $i\tau^{1/2}$ in a chronopotentiometric experiment with 8.56 wt% alumina in a cryolite melt at 1020 °C.

To represent this situation in order to estimate the location of the BP ($c_{\text{FeF}_2}^{\text{BP}}$), a model was made, taking into account the effect of changes in the alumina concentration beyond the BP. The model is described by the following equations:

$$c_{\text{Al}_2\text{O}_3} = c_{\text{Al}_2\text{O}_3}^{\circ} - \left((c_{\text{FeF}_2}^{\text{ADD}} - c_{\text{FeF}_2}^{\text{BP}}) \frac{M_{\text{Al}_2\text{O}_3}}{M_{\text{FeF}_2}} x_i K \right) \quad [3-6]$$

$$c_{\text{FeF}_2}^{\text{DIS}} = c_{\text{FeF}_2}^{\text{BP}} \left(\frac{a_{\text{Al}_2\text{O}_3}^{\circ}}{a_{\text{Al}_2\text{O}_3}} \right)^{x_i} \quad [3-7]$$

$$c_{\text{FeF}_2}^{\text{PRE}} = K(c_{\text{FeF}_2}^{\text{ADD}} - c_{\text{FeF}_2}^{\text{BP}}) \quad [3-8]$$

$$c_{\text{FeF}_2}^{\text{ADD}} = c_{\text{FeF}_2}^{\text{DIS}} + c_{\text{FeF}_2}^{\text{PRE}} \quad [3-9]$$

These equations are valid only for ferrous fluoride concentrations larger than the concentration defined by the BP.

The meaning of the symbols are:

$a_{\text{Al}_2\text{O}_3}$	Al_2O_3 activity corresponding to the estimated concentration.
$a_{\text{Al}_2\text{O}_3}^{\circ}$	Al_2O_3 activity corresponding to the initial concentration.
$c_{\text{Al}_2\text{O}_3}$	Estimated Al_2O_3 concentration / wt%.
$c_{\text{Al}_2\text{O}_3}^{\circ}$	Initial Al_2O_3 concentration / wt%.
$c_{\text{FeF}_2}^{\text{ADD}}$	Total amount of FeF_2 added to the melt / wt%.
$c_{\text{FeF}_2}^{\text{BP}}$	Same as BP, FeF_2 concentration at breakpoint / wt%.
$c_{\text{FeF}_2}^{\text{DIS}}$	Amount of FeF_2 dissolved in the melt / wt%.
$c_{\text{FeF}_2}^{\text{PRE}}$	Amount of iron precipitated as FeO or FeAl_2O_4 / wt%.
K	Constant which represents the fraction of iron that precipitates.
M_i	Molecular weight / g mol^{-1} .
x_i	$= 1/3$ for FeO or $= 4/3$ for FeAl_2O_4 .

Even though no fluoride precipitates, it is written as $c_{\text{FeF}_2}^{\text{PRE}}$ to simplify the calculations since the units are in wt%.

There is no activity data available for the ternary system under investigation, so data for the binary system alumina-cryolite had to be used. The alumina activities were based on the equation,

$$N_{\text{Al}_2\text{O}_3} = \alpha a_{\text{Al}_2\text{O}_3}^{1/3} + \beta a_{\text{Al}_2\text{O}_3}^{2/3} \quad [3-10]$$

given by Dewing and Thonstad (1997a) for the relationship between molar fraction of alumina and alumina activity. The coefficients α and β are 0.0772 ± 0.0025 and 0.159 ± 0.0048 , respectively. Unit alumina activity corresponds to 13.06 wt%.

The iterations were made manually in a simple spreadsheet. By investigating equations [3-6] to [3-9] one can see that BP and K are the only parameters that have to be iterated. After estimating BP, the slope of the experimental points at lower concentrations was calculated by regression analysis. The diffusion coefficient of divalent iron can be derived from the slope. Equations [3-6] to [3-8] were then combined, and K was found by iteration, *i.e.* when equation [3-9] was balanced. This procedure was conducted in steps beyond the guessed BP. The parameter K, which is the fraction of iron precipitated as ferrous oxide or ferrous aluminate, decreased with increasing additions of ferrous fluoride. The estimated amount of dissolved ferrous fluoride for the different additions was then multiplied by the slope of the regression line to obtain $it^{1/2}$ values. It was assumed that the diffusion coefficient of divalent iron remained constant throughout the concentration range. Although this is a simplification since parameters like density and viscosity might be influenced by large additions of ferrous fluoride, Table 3-1 shows that the diffusion coefficient is not very sensitive to composition changes. If the modelled line did not fit the experimental points, a new BP was guessed and the iterations were repeated. The dashed lines in Figure 3.8 are the results of the iterations after guessing the BP to be too low and too high by 0.10 wt%. The first points close to the BP, were emphasised when the experimental points deviated from the model.

Results were obtained only for alumina concentrations greater than 7.68 wt%. The reason was that chronopotentiometry failed at lower alumina concentrations due to the high solubility of ferrous fluoride. It was then not possible to obtain any chronopotentiometric transitions.

The diffusion coefficient of Fe(II) was determined by regression analysis and the Sand equation [2-17] from the slope of the experimental points at the low ferrous fluoride concentrations in Figure 3.8. The results are given as a function of alumina concentration in Table 3-1, together with the solubility of ferrous fluoride and the corresponding Fe(II) concentrations. From Figure 3.8 it can be seen that some divalent iron was initially present in the melt as an impurity since the regression line does not intercept at zero concentration. The initial amount of divalent iron, FeF_2° , was calculated from the regression line, and is included in the tabulated values. Density data for the cryolite-alumina system used to calculate the volume concentrations are taken from Solheim (2000). Analysis of the Greenland cryolite showed that it contained 0.30 wt% alumina, which is included in the tabulated alumina concentrations.

Table 3-1 Diffusion coefficients, initial ferrous fluoride concentration, solubility of ferrous fluoride and Fe(II) as a function of alumina concentration in cryolite-alumina melts at 1020 °C.

Al ₂ O ₃ wt%	10 ⁵ ×D _{Fe(II)} cm ² s ⁻¹	FeF ₂ ^o wt%	FeF ₂ wt%	Fe(II) wt%
7.7	3.7	0.18	1.89	1.12
8.6	3.8	0.16	1.50	0.89
9.3	3.7	0.28	1.23	0.73
10.3	3.8	0.20	0.93	0.55
11.3	3.1	0.22	0.81	0.48
12.3	3.2	0.32	0.76	0.45

The fact that the level of iron impurity goes up with the alumina content of the melt suggests that the alumina may be a source of iron. Certainly the alumina used does not contain that much iron, but it may have adsorbed moisture which has subsequently corroded the iron crucible. The solubility of Fe(II) as a function of the alumina concentration at 1020 °C is shown in Figure 3.9.

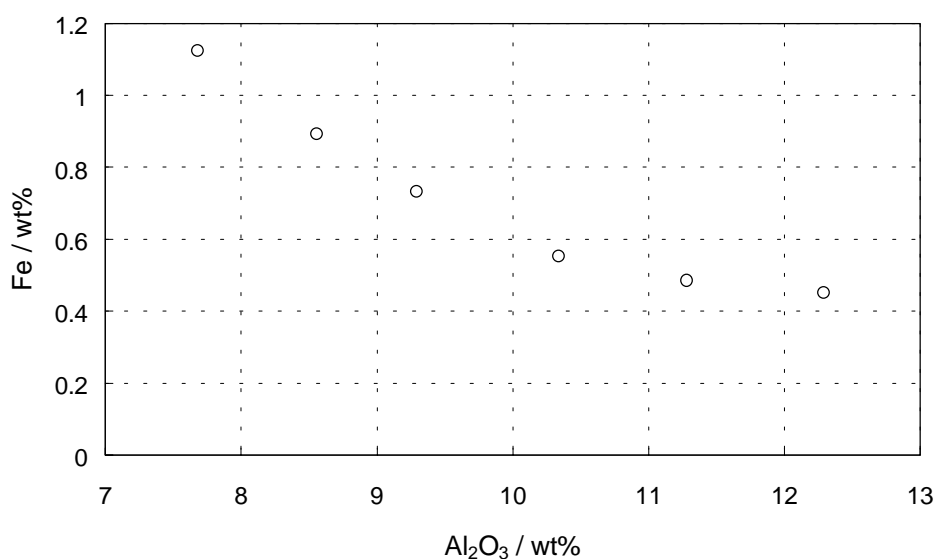


Figure 3.9 Solubility of Fe(II) in cryolite-alumina melts at 1020 °C versus alumina concentration.

According to Dewing and Thonstad (1997b), a logarithmic plot of solubility *versus* alumina activity makes it possible to derive the stoichiometric relationship for the dissolution mechanism, *i.e.*, between alumina and dissolved Fe(II). This is shown in Figure 3.10, where the alumina activities are calculated from equation [3-10].

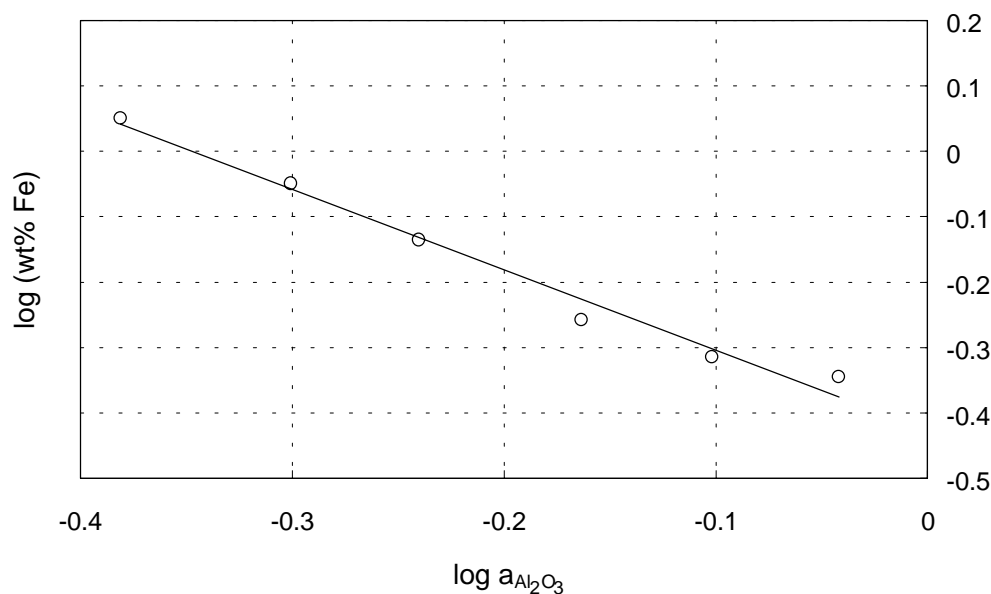


Figure 3.10 Solubility of Fe(II) in cryolite-alumina melts at 1020 °C as a function of alumina activity plotted on a logarithmic scale.

The regression line given by Figure 3.10 is,

$$\log(\text{wt}\% \text{ Fe}) = -(1.23 \pm 0.08) \log a_{\text{Al}_2\text{O}_3} - (0.43 \pm 0.02) \quad [3-11]$$

for the alumina activity range, *i.e.*, 0.41 - 0.91. Equation [3-11] was found to have a standard deviation of ± 0.02 .

The slope given by equation [3-11], which is very close to $-4/3$, indicates that the dissolution reaction is best described by equation [3-3]. This confirms that the stable solid phase is ferrous aluminate, FeAl₂O₄, in the given alumina concentration range.

In one case two samples were taken from the frozen material remaining in the crucible, at the bottom and in the middle, crushed, and submitted to X-ray diffraction (XRD) analysis. This showed that ferrous aluminate was present in the solidified melt, with

higher concentrations of ferrous aluminate close to the bottom of the crucible. This result further supports the conclusion drawn above.

3.3.2 Chemical Measurements

3.3.2.1 Solubility as a Function of Alumina Concentration

Ferrous oxide was used as additive at lower alumina concentrations instead of the more costly ferrous fluoride. This was because of the high Fe(II) solubility in this concentration range. To check the quality of the wustite produced in the laboratory, an XRD analysis was performed. It showed qualitatively that the product contained wustite. The reason for lack of quantitative data was that the sample was not completely crystalline.

A test showed that complete saturation of Fe(II) in the melt was reached within half an hour.

The main factors influencing the uncertainty in the data found by ICP analysis are calibration of the instrument and sample preparation. Since three standards of different concentrations were used, it was easily detected if one of the standards had a wrong concentration. During analysis, checks were performed by analysing the standards at regular intervals to see if the instrument drifted. Typically, these checks showed deviations of less than 3 %. The error connected to sample preparation is hard to estimate. The main uncertainty would probably be the dissolution of the samples, and not errors in the volume of the pipettes used. If the samples did not dissolve properly, the measured concentrations would be too low. An uncertainty of less than 5 % is expected in the iron concentrations measured by ICP analysis.

The uncertainty in the alumina concentrations obtained from LECO analysis is expected to be less than 10 % for the investigated system. The standard steel samples used showed a deviation of around 5 %.

The data obtained from the solubility experiments, *i.e.* solubility of divalent iron at varying alumina concentrations, is given in Table 3-2. Oxygen from iron oxide dissolved in the melt is included in the alumina concentration. The same data are presented graphically in Figure 3.11.

Table 3-2 Solubility of Fe(II) in cryolite with different alumina concentrations at 1020 °C.

Al ₂ O ₃ wt%	Fe wt%	Al ₂ O ₃ wt%	Fe wt%
2.7	4.17	4.8	2.32
3.0	3.54	5.2	2.30
3.0	3.85	5.2	2.40
3.0	3.50	5.6	2.04
3.0	3.43	5.9	1.70
3.0	3.61	7.2	1.12
3.1	3.48	8.1	0.84
3.3	3.19	9.3	0.84
3.6	3.35	9.8	0.60
4.1	3.15	11.2	0.46
4.1	3.27	sat	0.32
4.3	2.60	sat	0.31

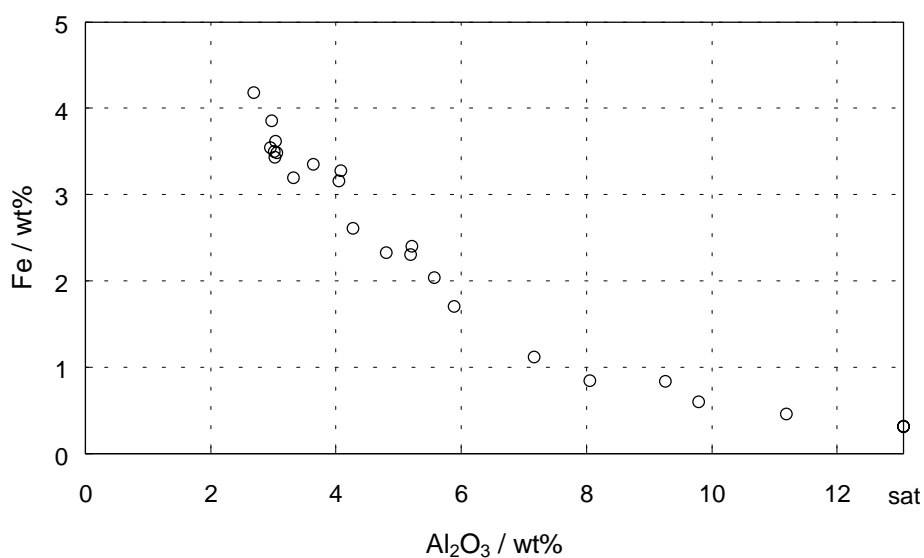


Figure 3.11 Solubility of Fe(II) versus alumina concentration in cryolite melts at 1020 °C.

As mentioned earlier, a logarithmic plot of solubility *versus* alumina activity makes it possible to derive the stoichiometric relationship for the dissolution reaction. This is shown in Figure 3.12, where the alumina activities are calculated from equation [3-10].

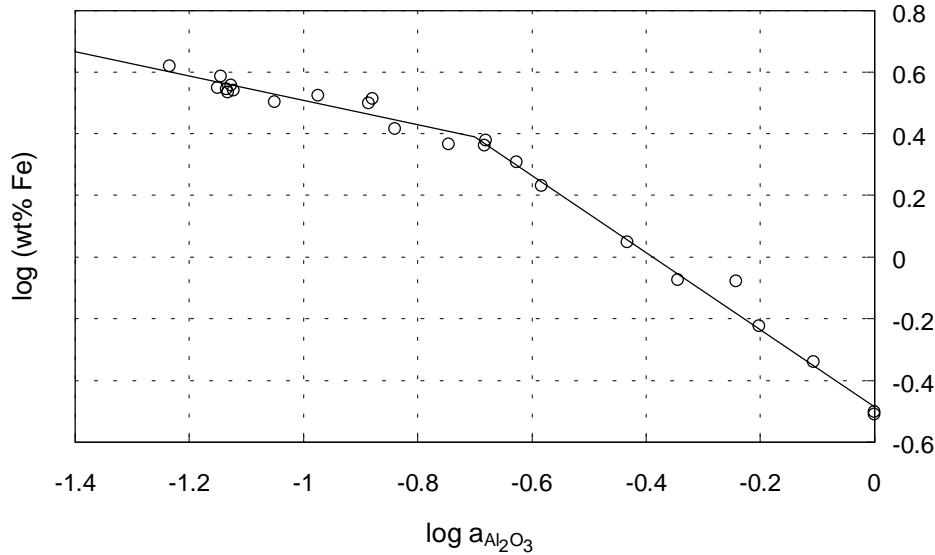


Figure 3.12 Solubility of Fe(II) in cryolite-alumina melts at 1020 °C as a function of alumina activity plotted on a logarithmic scale.

From Figure 3.12 one sees that the experimental points lie on two straight lines with different slopes, indicating different reaction mechanisms. The slope at low alumina content is close to $-1/3$, while it is around $-4/3$ at high alumina concentrations. This suggests that equations [3-2] and [3-3] represent the dissolution mechanisms. With this in mind, the intercept of the two lines was found using the method described by Lorentsen *et al.* (2000). The relation between the slopes of the two lines is used to solve the problem. At low alumina content the dissolution reaction of ferrous oxide can be written,



The slope of the plot will be $-x$. The corresponding dissolution reaction at high alumina content is given by,



with a slope of $-(x+1)$. This will be true provided that Fe(II) in solution exists as monomeric species.

To locate the alumina activity at which the intercept was situated, a procedure had to be made that minimised the error (sum of squares) for all the data. A trial and error procedure was adopted. First a value of the intercept was guessed. The value of the

experimental points at alumina activities less than the intercept were then increased corresponding to a decrease in the slope of minus one, *i.e.* $\log(\text{wt\% Fe})$ was increased by $1 \times (\log a_{\text{Al}_2\text{O}_3}^{\text{intercept}} - \log a_{\text{Al}_2\text{O}_3})$. The procedure is illustrated in Figure 3.13.

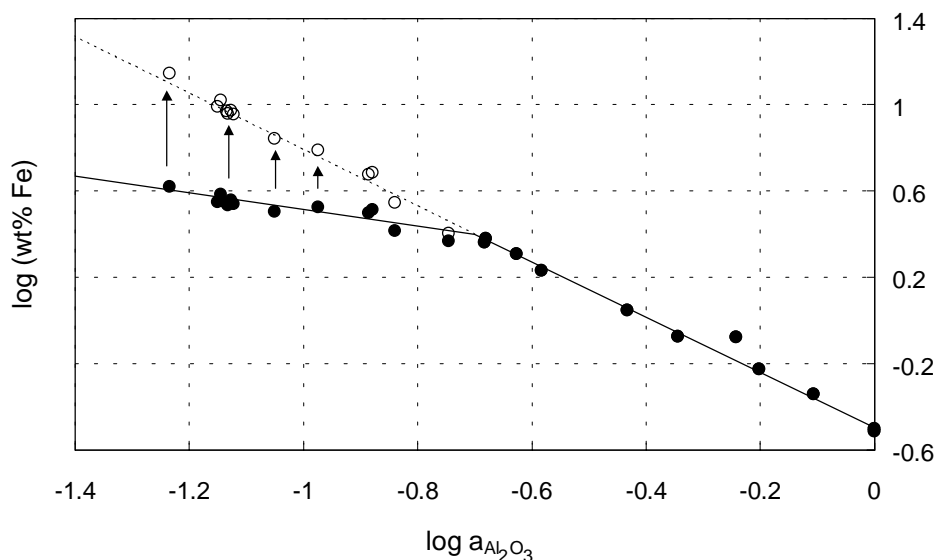


Figure 3.13 Illustration of how all the experimental points at alumina activities below the intercept are transformed to fit a single regression line. See text.

Regression analysis of the corrected data gave a slope and a standard deviation. The procedure was repeated for several possible intercepts until a minimum value was obtained, *i.e.* the regression line with the lowest error by the sum of squares. Figure 3.14 shows the sum of squares error (SS_E) of different regression lines as a function of the alumina activities chosen as intercepts.

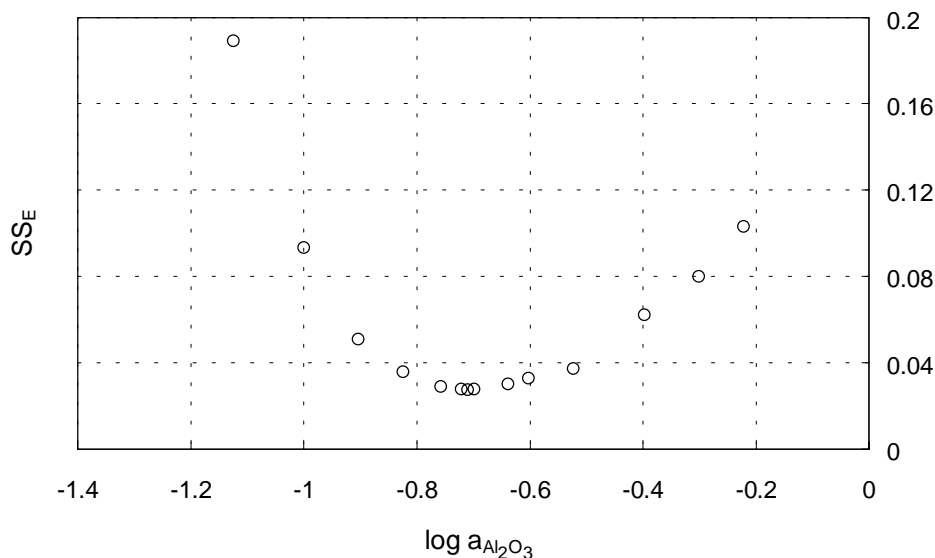


Figure 3.14 Sum of squares error (SS_E) of regression lines as a function of the alumina activity chosen as intercept. See text.

From Figure 3.14 the intercept, *i.e.* the minimum SS_E , is found at -0.710 , a value corresponding to an alumina activity equal to 0.195 ± 0.009 .

The solubilities of Fe(II) when alumina activities are lower and greater than 0.195 , are given by,

$$\log(\text{wt\% Fe}) = -(0.40 \pm 0.06) \log a_{\text{Al}_2\text{O}_3} + (0.11 \pm 0.06) \quad [3-14]$$

and,

$$\log(\text{wt\% Fe}) = -(1.26 \pm 0.04) \log a_{\text{Al}_2\text{O}_3} - (0.49 \pm 0.02) \quad [3-15]$$

respectively. Equations [3-14] and [3-15] were found to have standard deviations of ± 0.03 and ± 0.04 , respectively.

By using the alumina activity at the intercept, the Gibbs energy of formation, ΔG_f° , of ferrous aluminate can be calculated for the reaction given by equation [3-1] according to:

$$\Delta G_f^\circ = -RT \ln \left(\frac{1}{a_{\text{Al}_2\text{O}_3}} \right) \quad [3-16]$$

The standard Gibbs energy of formation for ferrous aluminate from its components (FeO + Al₂O₃) at 1020 °C was calculated to be:

$$\Delta G_{\text{f FeAl}_2\text{O}_4}^0 = -(17.6 \pm 0.5) \text{ kJ mol}^{-1}$$

This value deviates from the ones found by Rezhukhina *et al.* (1963) and Chan *et al.* (1973). The cause of this deviation will be discussed in Chapter 7. A discrepancy is also observed for the measured slopes giving the stoichiometric ratio between alumina and dissolved Fe(II) and the ones predicted by equations [3-2] and [3-3]. There can be several reasons for this. It was assumed that the activities of aluminium trifluoride and sodium fluoride were constant. Another assumption was that the activity coefficient of ferrous fluoride does not vary with the alumina content. None of those conditions are likely to be fulfilled: Sterten and Mæland (1985) found that the activity of both NaF and AlF₃ were smaller in an alumina-saturated melt than in pure liquid cryolite at 1027 °C.

The results obtained from both the electrochemical and the conventional solubility measurements, together with the result of Johansen (1975), are given in Figure 3.15.

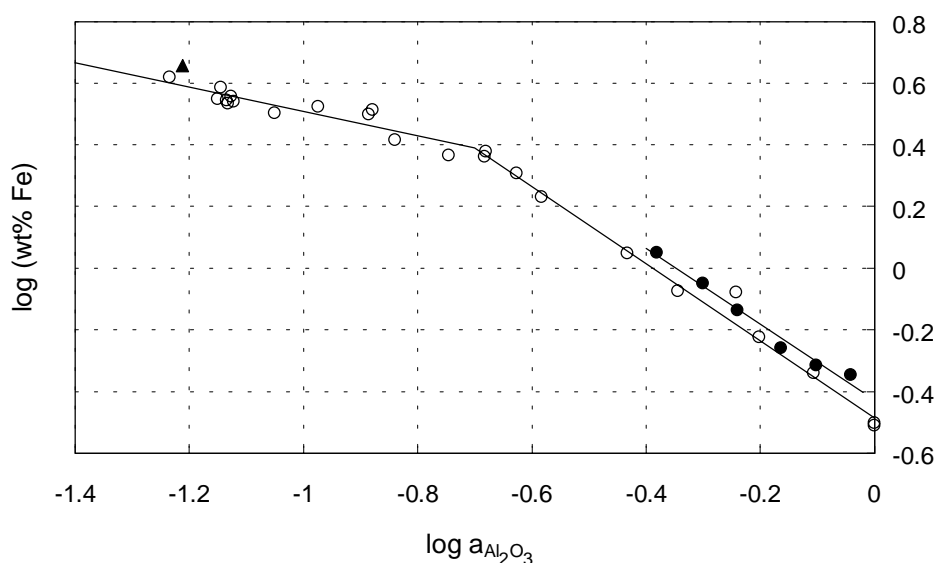


Figure 3.15 Solubility of Fe(II) in cryolite-alumina melts at 1020 °C as a function of the alumina activity plotted on a logarithmic scale: ○ analytical- and ● electrochemical measurements, present work; ▲ Johansen (1975).

Figure 3.15 shows that the agreement between the result of Johansen (1975) and the present work is satisfactory. The results from the electrochemical measurements are somewhat higher (12 - 15 %) than the chemical measurements. There are several possible reasons for this. The additions of ferrous fluoride were made with a quartz tube. Visual inspection of the tube showed that small amounts of ferrous fluoride adhered to the inside wall. It was not possible to determine the loss of ferrous fluoride, but the effect would be that the given solubilities are too high. Another source of error may be the dissolution of the samples when preparing for ICP analysis. If the samples did not dissolve completely, the experimental points from the chemical measurements are too low. Samples from the same experiments were also analysed by LECO. Calibration errors connected to the LECO apparatus would influence the determination of the oxygen content and thereby the calculated alumina activity.

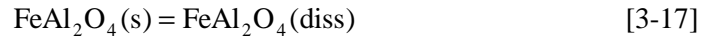
3.3.2.2 Solubility as a Function of Temperature

To investigate the effect of temperature on the Fe(II) solubility, several experiments were performed in the range from 981 to 1050 °C. The system under study was cryolite saturated with alumina. The results, which are presented in Table 3-3, show that the solubility of divalent iron in the melt increased with increasing temperature. Since the measurements were conducted at alumina saturation, the stable solid phase would be ferrous aluminate, FeAl_2O_4 .

Table 3-3 Solubility of Fe(II) in alumina-saturated cryolite melts at different temperatures.

T	Fe	T	Fe
°C	wt%	°C	wt%
981	0.24	1020	0.32
981	0.25	1021	0.32
987	0.27	1030	0.32
990	0.27	1030	0.32
990	0.27	1030	0.32
998	0.29	1040	0.35
1000	0.29	1040	0.34
1000	0.30	1041	0.35
1009	0.30	1050	0.36
1010	0.31	1050	0.36
1011	0.30	1050	0.37
1019	0.31		

The apparent partial molar enthalpy of dissolution, $\Delta\bar{H}^\circ$, of FeAl_2O_4 in the melt can be obtained from the solubility data. At saturation of FeAl_2O_4 we have:



$$\Delta G^\circ = -RT \ln \frac{a_{\text{FeAl}_2\text{O}_4(\text{diss})}}{a_{\text{FeAl}_2\text{O}_4(\text{s})}} \quad [3-18]$$

where the activity of solid FeAl₂O₄ is equal to unity. Since the solubility is low, we can assume Henrian behaviour:

$$a_{\text{FeAl}_2\text{O}_4(\text{diss})} = kx_{\text{FeAl}_2\text{O}_4(\text{diss})} \quad [3-19]$$

where k is Henry's constant and x is the concentration, in this case in wt%.

By introducing the Gibbs-Helmholtz equation, we obtain the following equation,

$$\frac{\partial \ln x_{\text{FeAl}_2\text{O}_4(\text{diss})}}{\partial 1/T} = -\frac{\Delta \bar{H}_{\text{FeAl}_2\text{O}_4}^\circ}{R} \quad [3-20]$$

Therefore, a plot of $\ln(\text{wt\% Fe})$ versus T^{-1} should be linear, provided that the assumption of Henrian behaviour holds and that the partial molar enthalpy of ferrous aluminate is independent of temperature. In Figure 3.16 the solubility data for Fe(II) are plotted in this manner.

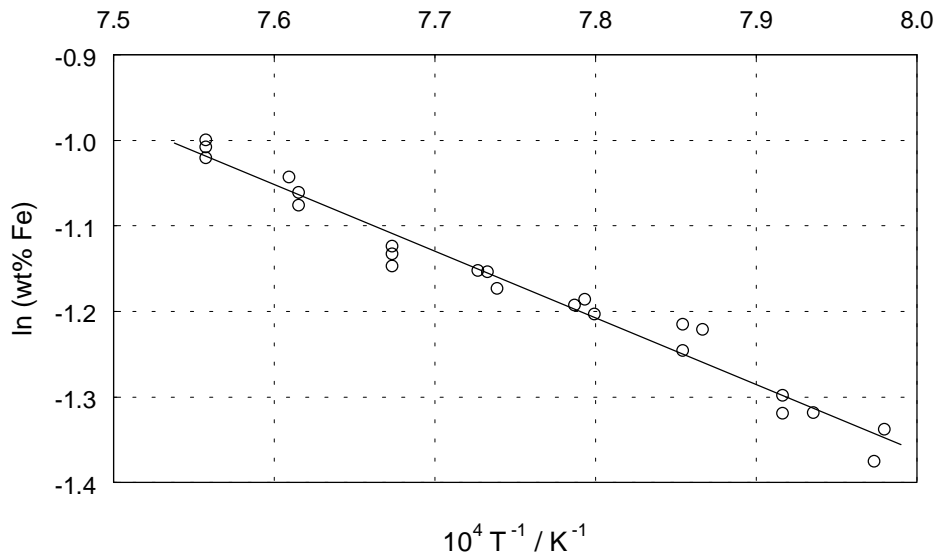


Figure 3.16 Natural logarithm of the Fe(II) solubility as a function of the reciprocal temperature in alumina-saturated cryolite melts.

From Figure 3.16 it is seen that the correlation between concentration and temperature is good. The least-squares equation was found to be,

$$\ln(\text{wt\% Fe}) = -\frac{(7790 \pm 300)}{T} + (4.87 \pm 0.23) \quad [3-21]$$

with a standard deviation of ± 0.02 . The temperature unit is Kelvin.

The apparent partial molar enthalpy of dissolution of FeAl_2O_4 was calculated to be:

$$\Delta \bar{H}_{\text{FeAl}_2\text{O}_4}^0 = (64.8 \pm 2.5) \text{ kJ mol}^{-1}$$

Diep (1998) and DeYoung (1986) reported the partial molar enthalpy of dissolution for ferric oxide to be 124 and 138 kJ mol^{-1} , respectively. Since the solubility of ferrous aluminate is several times higher than that of ferric oxide, the value obtained seems reasonable.

3.3.2.3 Solubility as a Function of Molar Cryolite Ratio

To investigate the effect of varying molar cryolite ratio, CR, on the Fe(II) solubility, experiments were performed with various NaF-AlF₃ compositions. The experiments were made with alumina saturation at 1020 °C. The amount of alumina added prior to the experiments was based on alumina saturation limits for basic baths (CR > 3) as measured by Diep (1998) for the system NaF-AlF₃-Al₂O₃. For acidic melts (CR < 3) the amount of alumina added was calculated using the equation given by Solheim *et al.* (1995). To ensure that the acidic melts were completely saturated, approximately 10 % excess alumina was added. It should be noted that $\alpha\text{-Al}_2\text{O}_3$ is not stable in basic melts.

The results, which are presented in Table 3-4, show that the solubility of divalent iron in the melt varies with CR. Since the measurements were conducted at alumina saturation, the stable solid phase would be ferrous aluminate, FeAl_2O_4 . The results are presented graphically in Figure 3.17.

Table 3-4 Solubility of Fe(II) in alumina saturated cryolite melts at 1020 °C as a function of molar cryolite ratio.

NaF/AlF ₃	Fe
Molar Ratio	wt%
2.00	0.35
2.29	0.34
2.52	0.28
3.00	0.31
3.00	0.32
3.00	0.31
4.00	0.49
4.79	0.59
5.00	0.62
6.50	0.62
8.00	0.60

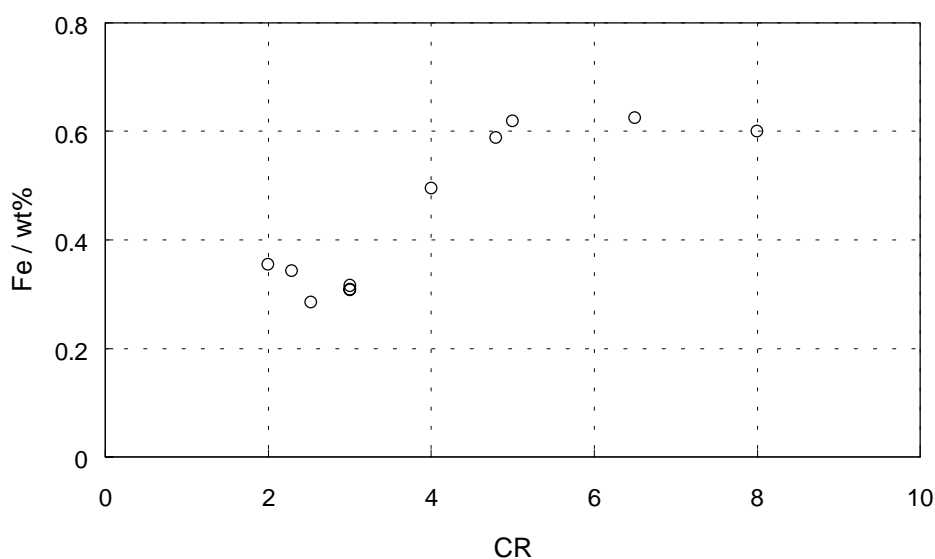
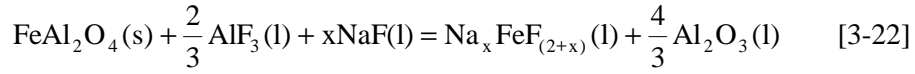


Figure 3.17 Solubility of Fe(II) in alumina-saturated cryolite melts at 1020 °C as a function of molar cryolite ratio.

From the investigation of solubility of Fe(II) as a function of alumina concentration it was found (section 3.3.2.1) that FeO and FeAl₂O₄ dissolve in the melt as FeF₂ species. These species may be associated with a number of sodium fluorides. In the case of ferrous aluminate, the dissolution reaction can be expressed as,



The equilibrium constant for equation [3-22], *i.e.* K_x , can be expressed as,

$$K_x = \frac{a_{\text{Na}_x\text{FeF}_{(2+x)}} a_{\text{Al}_2\text{O}_3}^{4/3}}{a_{\text{AlF}_3}^{2/3} a_{\text{NaF}}^x} \quad [3-23]$$

Equation [3-23] can be expressed in a logarithmic form as,

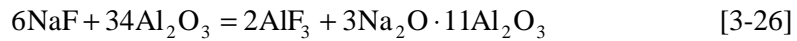
$$\log a_{\text{Na}_x\text{FeF}_{(2+x)}} + \frac{4}{3}\log a_{\text{Al}_2\text{O}_3} - \frac{2}{3}\log a_{\text{AlF}_3} = x \log a_{\text{NaF}} + \text{constant} \quad [3-24]$$

By assuming Henrian behaviour, *i.e.* the solute species has a constant activity coefficient, one can replace the activity of the FeF_2 species with the concentration of divalent iron (in wt%):

$$\log c_{\text{Fe}} + \frac{4}{3}\log a_{\text{Al}_2\text{O}_3} - \frac{2}{3}\log a_{\text{AlF}_3} = x \log a_{\text{NaF}} + \text{constant} \quad [3-25]$$

A plot of the left-hand side of equation [3-25] against the logarithm of the sodium fluoride activity should therefore give a straight line with a slope of x , *i.e.* the number of NaF associated with the FeF_2 species.

In acidic melts saturated with alumina the activity of $\alpha\text{-Al}_2\text{O}_3$ is unity. Since $\beta\text{-Al}_2\text{O}_3$ ($\text{Na}_2\text{O} \cdot 11\text{Al}_2\text{O}_3$) is formed in basic melts for $\text{CR} > \sim 4$ (Foster 1964 and Holm 1966), one has to take the reaction,



into account when calculating the alumina activity in basic melts. The equilibrium constant for equation [3-26] is given as,

$$K = \frac{a_{\beta}^3 a_{\text{AlF}_3}^2}{a_{\alpha}^{34} a_{\text{NaF}}^6} \quad [3-27]$$

where a_{α} and a_{β} are the activities of Al_2O_3 and $\text{Na}_2\text{O} \cdot 11\text{Al}_2\text{O}_3$, respectively. If one rearranges equation [3-27], an expression for the activity of $\alpha\text{-Al}_2\text{O}_3$ is obtained for basic melts, *i.e.* unit activity of beta alumina:

$$a_{\alpha} = \left(\frac{a_{\text{AlF}_3}^2}{a_{\text{NaF}}^6 K} \right)^{1/34} \quad [3-28]$$

According to Sterten *et al.* (1982), alpha alumina converts into beta alumina at a CR of approximately 3.7 when the CR is increased. The equilibrium constant K for equation [3-26] at this point simply becomes,

$$K = \frac{a_{\text{AlF}_3}^2}{a_{\text{NaF}}^6} \quad [3-29]$$

since both alpha and beta alumina have unit activities at exactly this CR. By using the activity data of Sterten *et al.* (1982, 1985) for an alumina-saturated melt at 1020 °C with a CR of 3.7, the equilibrium constant was found to be $2.05 \cdot 10^{-7}$. This value was used for the calculations of the alpha alumina activity at CR's above 3.7.

By using the data given in Table 3-4 and the activity data for AlF₃ and NaF in alumina-saturated melts given by Sterten *et al.* (1982, 1985), equation [3-25] can be plotted as shown in Figure 3.18 to give the number of NaF associated with the FeF₂ species.

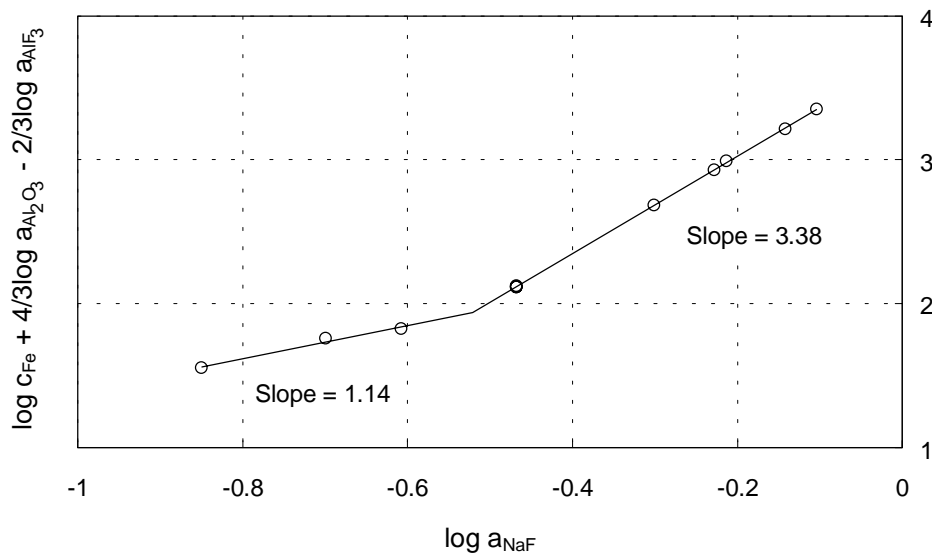


Figure 3.18 Plot to estimate the number of NaF's associated with the FeF₂ species in alumina-saturated cryolite melts at 1020 °C. See text.

From Figure 3.18 a slope of 1.14, *i.e.* $x \cong 1$, is observed at low CR's. This means that the most probable species in this region is NaFeF_3 . At high CR's a slope of 3.38 is found, and indicates that either 3 or 4 NaF 's are associated with the FeF_2 species. The most likely species in this region would, therefore, be either Na_3FeF_5 or Na_4FeF_6 , or possibly a mix of both.

It is also possible to model the most plausible species present in the melts. By rearranging equation [3-23], one can express the relative activity of the FeF_2 species as,

$$a_{\text{Na}_x\text{FeF}_{(2+x)}} = K_x \frac{a_{\text{AlF}_3}^{2/3} a_{\text{NaF}}^x}{a_{\text{Al}_2\text{O}_3}^{4/3}} \quad [3-30]$$

One can then model the different species by testing different values for x and change the corresponding K_x by trial and error until the best fit of the experimental points (in wt%) is obtained. Species with x values from 0 to 4 were modelled, and the result is given in Figure 3.19.

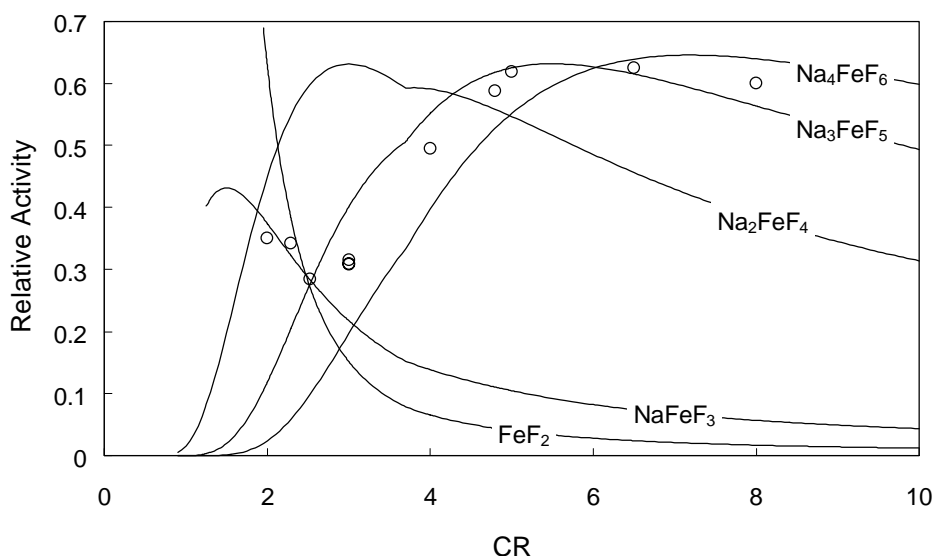


Figure 3.19 Model fitting to determine the number of NaF 's associated with the dissolved FeF_2 species in alumina-saturated cryolite melts at 1020°C . See text.

From Figure 3.19 it is seen that at low CR's the best fit was obtained for NaFeF_3 ($x = 1$ and $K_1 = 270$). At high CR's the best fit was obtained for either Na_3FeF_5 ($x = 3$ and $K_3 = 4300$) or Na_4FeF_6 ($x = 4$ and $K_4 = 6200$), or possibly a mix of both. This is exactly

the same conclusion as found by the first method. The conclusion seems logical since the species suggested in the basic melts which have high contents of NaF contain three or four sodium fluorides, while the one assumed to be present in the acidic melts contains only one.

3.3.3 Solubility of Fe_2O_3 in Cryolite-Alumina Melts

It can be of interest to apply the techniques used for ferrous species on literature data for dissolution of Fe_2O_3 . This should give a more or less complete picture of these systems.

DeYoung (1986) and Diep (1998) measured the solubility of Fe_2O_3 in cryolite-alumina melts, as discussed in section 3.1. Diep (1998) concluded from the solubility measurements in alumina-saturated melts, under 1 atm of oxygen at 1020 °C, as a function of CR, that Na_3FeF_6 was the most important species, besides $\text{Na}_2\text{AlFeOF}_6$, $\text{Na}_6\text{AlFeOF}_{10}$ and $\text{Na}_2\text{AlFeO}_2\text{F}_4$. This means that Fe(III) can substitute Al(III). Diep (1998) gave the alumina concentration in the melts as the concentration before any Fe_2O_3 was added. Since alumina is formed by dissolution of Fe_2O_3 into the melt, this quantity has to be taken into account. This has been done and the results are given in Figure 3.20 together with the results of DeYoung (1986).

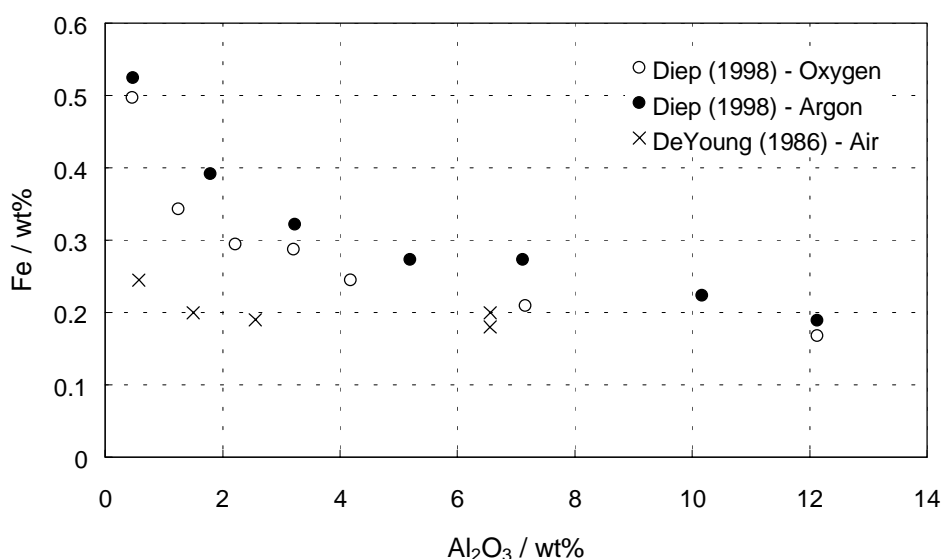


Figure 3.20 Solubility of Fe(III) in cryolite-alumina melts as a function of alumina concentration under different atmospheres. Diep (1998): CR = 3.0 and $T = 1020$ °C. DeYoung (1986): CR = 2.6 and $T = 1025$ °C.

If one uses the data of Diep (1998) obtained under 1 atm of oxygen, given in Figure 3.20, it is possible to derive the stoichiometric relationship for the dissolution reaction for Fe_2O_3 . This is done by making a logarithmic plot of solubility against alumina activity, as shown in Figure 3.21.

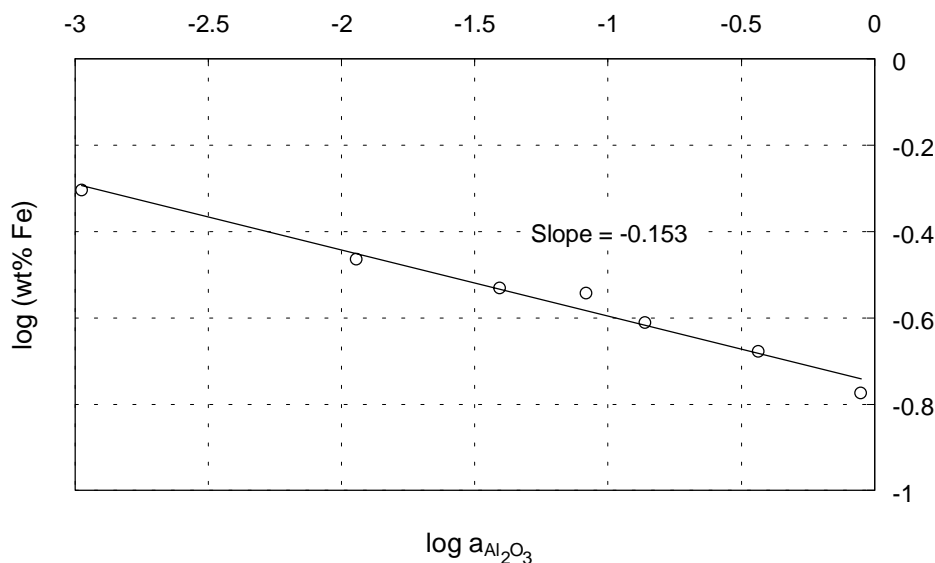


Figure 3.21 Solubility of Fe(III) in cryolite-alumina melts under 1 atm of oxygen at 1020 °C as a function of alumina activity plotted on a logarithmic scale.

Figure 3.21 shows that the correlation between concentration and alumina activity is good. The least-squares equation was found to be,

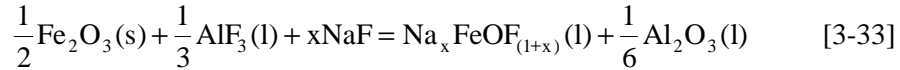
$$\log(\text{wt}\% \text{ Fe}) = -(0.15 \pm 0.01) \log a_{\text{Al}_2\text{O}_3} - (0.75 \pm 0.02) \quad [3-31]$$

with a standard deviation of ± 0.03 .

Equation [3-31] gives a slope which is close to $-1/6$. This means that one Al_2O_3 is formed for every sixth Fe(III) introduced into the melt as Fe_2O_3 , and that all possible Fe(III) species must be associated with exactly one oxygen ion, *i.e.* the basis of the species is FeOF. Two of the species suggested by Diep (1998) ($\text{Na}_2\text{AlFeOF}_6$ where $x = 2$ and $\text{Na}_6\text{AlFeOF}_{10}$ where $x = 6$) fulfil this condition, and can be described by the general dissolution mechanism:



If one takes into consideration that Fe(III) species not associated with aluminium can form, a possible dissolution mechanism may be,



The equilibrium constant for equation [3-33], *i.e.* K_x , can be expressed as,

$$K_x = \frac{a_{\text{Na}_x\text{FeOF}_{(1+x)}} a_{\text{Al}_2\text{O}_3}^{1/6}}{a_{\text{AlF}_3}^{1/3} a_{\text{NaF}}^x} \quad [3-34]$$

Equation [3-34] can be expressed in logarithmic form as,

$$\log a_{\text{Na}_x\text{FeOF}_{(1+x)}} + \frac{1}{6} \log a_{\text{Al}_2\text{O}_3} - \frac{1}{3} \log a_{\text{AlF}_3} = x \log a_{\text{NaF}} + \text{constant} \quad [3-35]$$

By assuming Henrian behaviour, *i.e.* the solute species has a constant activity coefficient, one can replace the activity of the FeOF species with the concentration of trivalent iron (c_{Fe}) (in wt%):

$$\log c_{\text{Fe}} + \frac{1}{6} \log a_{\text{Al}_2\text{O}_3} - \frac{1}{3} \log a_{\text{AlF}_3} = x \log a_{\text{NaF}} + \text{constant} \quad [3-36]$$

A plot of the left-hand side of equation [3-36] against the logarithm of the sodium fluoride activity should, therefore, give a straight line with a slope of x , *i.e.* the number of NaF's associated with the FeOF species. As discussed in section 3.3.2.3, beta alumina has unit activity at CR's above 3.7, while the activity of alpha alumina decreases. The same procedure was used here too. By using the activity data of Sterten *et al.* (1982, 1985) for an alumina saturated melt at 1020 °C with a CR of 3.7, the equilibrium constant given by equation [3-29] was found to be $2.05 \cdot 10^{-7}$. This value was used for the calculations of the alpha alumina activity at CR's above 3.7.

By the use of solubility data of Diep (1998) ($\text{Na}_3\text{AlF}_6\text{-Al}_2\text{O}_3(\text{sat})$, 1 atm O_2 , $T = 1020$ °C) as a function of CR and the activity data for AlF_3 and NaF given by Sterten *et al.* (1982, 1985), equation [3-36] can be plotted as shown in Figure 3.22 to give the number of NaF's associated with the FeOF species.

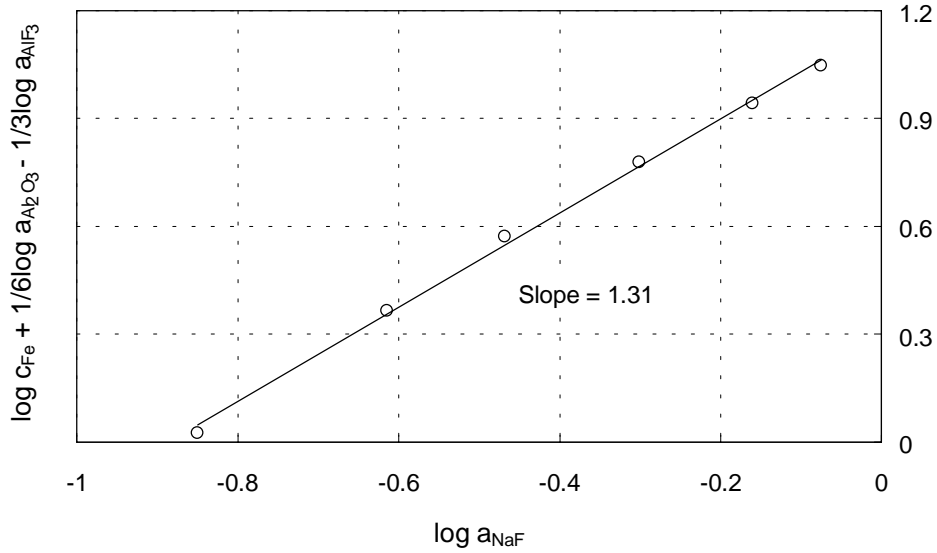


Figure 3.22 Plot to estimate the number of NaF's associated with the FeOF species in alumina-saturated cryolite melts under 1 atm of O₂ at 1020 °C. See text.

From Figure 3.22 a slope of 1.31 is found, which gives $x \cong 1$, and implies that the most probable species is NaFeOF₂ if no aluminium ions are associated with it.

By using the same procedure for possible species associated with one aluminium ion, *i.e.* the dissolution mechanism given by equation [3-32], one obtains the equilibrium constant,

$$K_x = \frac{a_{\text{Na}_x\text{AlFeOF}_{(4+x)}} a_{\text{Al}_2\text{O}_3}^{1/6}}{a_{\text{AlF}_3}^{4/3} a_{\text{NaF}}^x} \quad [3-37]$$

which can be expressed in a logarithmic form as,

$$\log a_{\text{Na}_x\text{AlFeOF}_{(4+x)}} + \frac{1}{6} \log a_{\text{Al}_2\text{O}_3} - \frac{4}{3} \log a_{\text{AlF}_3} = x \log a_{\text{NaF}} + \text{constant} \quad [3-38]$$

By assuming Henrian behaviour one gets,

$$\log c_{\text{Fe}} + \frac{1}{6} \log a_{\text{Al}_2\text{O}_3} - \frac{4}{3} \log a_{\text{AlF}_3} = x \log a_{\text{NaF}} + \text{constant} \quad [3-39]$$

Equation [3-39] is plotted in Figure 3.23 to give the number of NaF's associated with the AlFeOF₄ species.

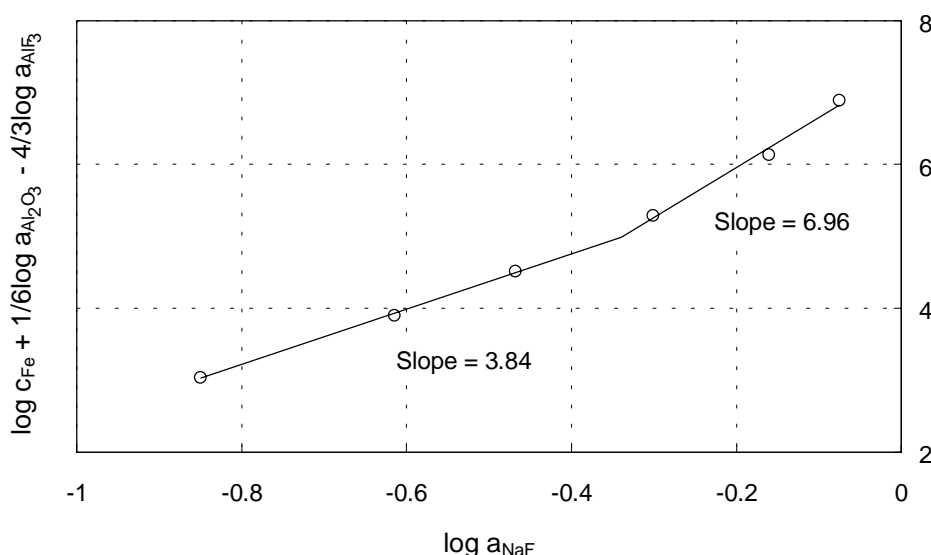


Figure 3.23 Plot to estimate the number of NaF's associated with the AlFeOF₄ species in alumina-saturated cryolite melts under 1 atm of O₂ at 1020 °C. See text.

Figure 3.23 gives slopes of 3.84 and 6.96 in acidic and basic melts, respectively. This means that x is approximately 4 in the acidic melts, and that the most probable species is Na₄AlFeOF₈ in this region. In basic melts $x \cong 7$, and the species present is most likely to be Na₇AlFeOF₁₁.

By using the second method, as described in section 3.3.2.3, the activities of the FeOF and the AlFeOF₄ species can be expressed as,

$$a_{\text{Na}_x\text{FeOF}_{(1+x)}} = K_x \frac{a_{\text{AlF}_3}^{1/3} a_{\text{NaF}}^x}{a_{\text{Al}_2\text{O}_3}^{1/6}} \quad [3-40]$$

and

$$a_{\text{Na}_x\text{AlFeOF}_{(4+x)}} = K_x \frac{a_{\text{AlF}_3}^{4/3} a_{\text{NaF}}^x}{a_{\text{Al}_2\text{O}_3}^{1/6}} \quad [3-41]$$

by rearranging equations [3-34] and [3-37], respectively. The results of the modelling are given in Figure 3.24.

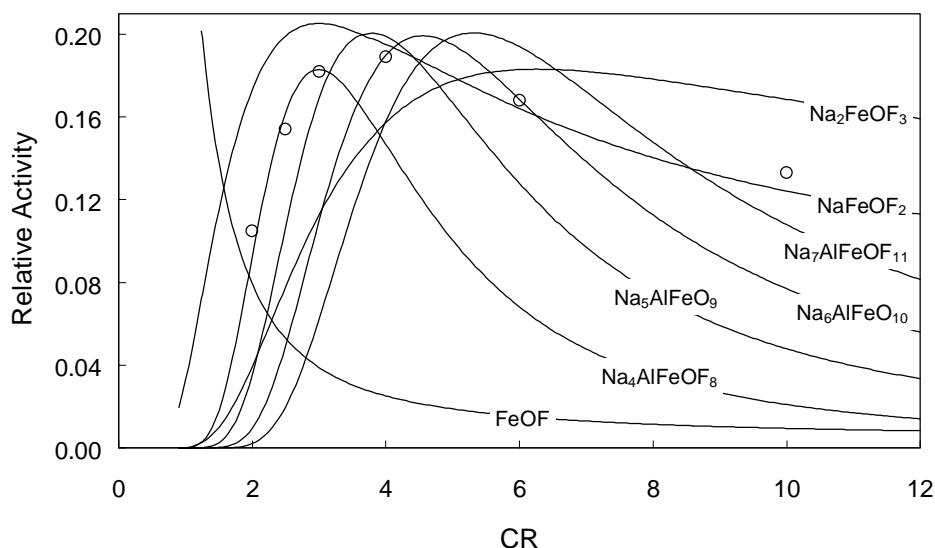


Figure 3.24 Model fitting to determine the number of NaF's associated with the dissolved FeOF and AlFeOF_4 species in alumina-saturated cryolite melts under 1 atm of O_2 at 1020 °C. See text.

From Figure 3.24 it is seen that at low CR's the best fit was obtained for $\text{Na}_4\text{AlFeOF}_8$ (equation [3-41]: $x = 4$ and $K_4 = 2.43 \cdot 10^6$). At high CR's the best fit was obtained for NaFeOF_2 (equation [3-40]: $x = 1$ and $K_2 = 12.39$). Since both FeOF and AlFeOF_4 species were tested against each other by this second method, the outcome is probably more correct. This means that the most probable species are the ones found by means of Figure 3.24, *i.e.* $\text{Na}_4\text{AlFeOF}_8$ in acidic melts and NaFeOF_2 in basic melts. One might expect the opposite to be the case, *i.e.* more sodium fluorides associated with the species in basic melts than in acidic melts, since the activity of NaF increases with increasing CR. It seems difficult to explain why the chosen species seem to form regardless of the NaF activity.

References to Chapter 3

- Billehaug, K. and H. A. Øye (1981): Inert Anodes for Aluminium Electrolysis in Hall-Héroult Cells, *Aluminium*, **57**, 146, and *Aluminium*, **57**, 228.
- Chan, J. C., C. B. Alcock, and K. T. Jacob (1973): Electrochemical Measurement of the Oxygen Potential of the System Iron-Alumina-Hercynite in the Temperature Range 750 to 1600 °C, *Can. Met. Quart.*, **12**, 439.
- Deininger, L. and J. Gerlach (1979): Stromausbeutemessungen bei der Aluminium-oxidreduktionselektrolyse in Laboratoriumszellen, *Metall*, **33**, 131.
- Delahay, P. (1954): New Instrumental Methods in Electrochemistry, Interscience Publishers, Inc., New York, p. 179.
- Dewing, E. W. and J. Thonstad (1997a): Activities in the System Cryolite-Alumina, *Metall. Mater. Trans. B*, **28B**, 1089.
- Dewing, E. W. and J. Thonstad (1997b): Solutions of CeO₂ in Cryolite Melts, *Metall. Mater. Trans. B*, **28B**, 1257.
- Dewing, E. W. and J. Thonstad (2000): Solutions of Iron Oxides in Molten Cryolite, *Metall. Mater. Trans. B*, **31B**, 609.
- DeYoung, D. H. (1986): Solubilities of Oxides for Inert Anodes in Cryolite-Based Melts, in *Light Metals 1986*, R. E. Miller, Editor, TMS, Warrendale, PA, p. 299.
- Diep, Q. B. (1998): Structure and Thermodynamics of Cryolite-Based Melts with Additions of Al₂O₃ and Fe₂O₃, Doctoral Thesis 1998:28, Department of Electrochemistry, Norwegian University of Science and Technology, Trondheim, Norway, p. 79.
- Foster, P. A. Jr. (1964): Phase Equilibria in the Sodium Fluoride Enriched Region of the Reciprocal System Na₆F₆-Al₂F₆-Na₆O₃-Al₂O₃, *J. Chem. Eng. Data*, **9**, 2, 200.
- Greef, R., R. Peat, L. M. Peter, D. Pletcher and J. Robinson (1990): Instrumental Methods in Electrochemistry, Ellis Horwood, Chichester, England, p. 74.
- Grjotheim, K. and K. Matiasovsky (1983): Impurities in the Aluminium Electrolyte, *Aluminium*, **59**, 687.
- Holm, J. L. (1966): Undersøkelser av en del systemer med tilknytning til aluminium-elektrolysen, *Tidssk. Kjemi Bergv.*, **26**, 10, 171.
- Johansen, H. G. (1975): Jern som forurensningselement i aluminium-elektrolysen, Doctoral Thesis, Department of Electrochemistry, Norwegian Institute of Technology, Trondheim, Norway, p. 16.
- Johansen, H. G., Å. Sterten and J. Thonstad (1989): The Phase Diagrams of the Systems Na₃AlF₆-Fe_{0.947}O and Na₃AlF₆-FeF₂ and Related Activities of FeF₂ from Emf Measurements, *Acta Chem. Scand.*, **43**, 417.
- Kvande, H. (1999): Inert Electrodes in Aluminium Electrolysis Cells, in *Light Metals 1999*, C. E. Eckert, Editor, TMS, Warrendale, PA, p. 369.

- Lorentsen, O.-A., E. W. Dewing and J. Thonstad (2000): Solubility of NiO and NiAl_2O_4 in Cryolite-Alumina Melts, in *Proceedings of the Twelfth International Symposium on Molten Salts*, H. C. DeLong, S. Deki, G. R. Stafford and P. C. Trulove, Editors, PV 99-41, The Electrochemical Society Proceedings Series, Pennington, NJ, p. 428.
- Mannweiler, U. and F. Keller (1994): The Design of a New Anode Technology for the Aluminum Industry, *JOM*, **46**, 2, 15.
- Rezukhina, T. N., V. A. Levitskii and P. Ozhegov (1963): Thermodynamic Properties of Iron Aluminate, *Russ. J. Phys. Chem.*, **37**, 358.
- Solheim, A., S. Rolseth, E. Skybakmoen, L. Støen, Å. Sterten and T. Støre (1995): Liquidus Temperature and Alumina Solubility in the System Na_3AlF_6 - AlF_3 - LiF - CaF_2 - MgF_2 , in *Light Metals 1995*, J. E. Evans, Editor, TMS, Warrendale, PA, p. 451.
- Solheim, A. (2000): The Density of Molten NaF - LiF - AlF_3 - CaF_2 - Al_2O_3 in Aluminium Electrolysis, *Alum. Trans.*, **2**, 161.
- Sterten, Å., K. Hamberg and I. Mæland (1982): Activities and Phase Diagram Data of NaF - AlF_3 - Al_2O_3 Mixtures Derived from Electromotive Force and Cryoscopic Measurements. Standard Thermodynamic Data of $\beta\text{-Al}_2\text{O}_3(\text{s})$, $\text{Na}_3\text{AlF}_6(\text{s})$, $\text{Na}_5\text{Al}_3\text{F}_{14}(\text{s})$ and $\text{NaAlF}_4(\text{l})$, *Acta Chem. Scand. A*, **36**, 329.
- Sterten, Å. and I. Mæland (1985): Thermodynamics of Molten Mixtures of Na_3AlF_6 - Al_2O_3 and NaF - AlF_3 , *Acta Chem. Scand. A*, **39**, 241.
- Sterten, Å., P. A. Solli and E. Skybakmoen (1998): Influence of Electrolyte Impurities on Current Efficiency in Aluminium Electrolysis Cells, *J. Appl. Electrochem.*, **28**, 781.
- Støre, T. (1999): Electrodeposition of Metals from Molten Salts, Doctoral Thesis 1999:18, Department of Electrochemistry, Norwegian University of Science and Technology, Trondheim, Norway, p. 67.
- Thonstad, J. (1999): The Behaviour of Impurities in Aluminium Cells, in *Proceedings of the Tenth International Aluminium Symposium*, Stara Lesna, Slovakia, p. 5.
- Ullmann's Encyclopedia of Industrial Chemistry (1989): Vol. 14 A, 5th Edition, VCH Verlagsgesellschaft mbH, Weinheim, Germany, p. 463.
- Wang, H. and J. Thonstad (1989): The Behaviour of Inert Anodes as a Function of some Operating Parameters, in *Light Metals 1989*, P. G. Campbell, Editor, TMS, Warrendale, PA, p. 283.

4 Solubility of TiO_2 in Cryolite-Alumina Melts

4.1 Introduction

There are several reasons for investigating the solubility of titanium oxide in cryolite melts. In most cases titanium is considered to be an unwanted impurity in the Hall-Héroult bath. According to Sterten *et al.* (1998), titanium is present in the bath as a polyvalent species that reduces the current efficiency (CE) by (0.24 ± 0.14) % per 0.01 wt% introduced in the bath. Deininger and Gerlach (1979) found the reduction in CE to be 0.75 % for each 0.01 wt% titanium in the melt. Another reason for an investigation is the possibility of producing aluminium-titanium alloys by electrolysis, as discussed by Qiu *et al.* (1988) and Devyatkin *et al.* (1998). Qiu *et al.* (1988) suggested synthetic rutile, which is a product from iron electric arc furnace slag with a high content (92 %) of TiO_2 , as a potential raw material for the process. Madhavan *et al.* (1971) studied the ternary system $\text{Na}_3\text{AlF}_6\text{-NaCl-TiO}_2$ with regard to a possible application of these mixtures as electrolytes for the electrodeposition of titanium, especially in electroplating.

In aluminium reduction cells carbon materials are used both as anodes and as cathode cell linings. Although having several advantages, carbon has also many shortcomings. When used as cathode, for example, it is not wetted by liquid aluminium, it is penetrated by sodium and molten electrolyte and it reacts with aluminium with the formation of aluminium carbide (Al_4C_3). These problems have stimulated extensive investigations into the possibility of replacing it by other materials better suited to meet the severe conditions of an aluminium cell. According to Makyta *et al.* (1996) titanium diboride (TiB_2) comes closest to meeting the strict requirements for an “ideal” cathode lining material. TiB_2 exhibits a high melting point and hardness, high electronic conductivity, it is wetted by molten aluminium and it is resistant towards chemical attack by both aluminium and cryolite-alumina melts. A possible process for production of TiB_2 is by electrolysis of cryolite electrolytes containing B_2O_3 and TiO_2 . Makyta *et al.* (1996) investigated this system. They found that the prepared coatings of TiB_2 had poor quality, being inhomogeneous and not coherent. Another problem observed was the escape of gaseous BF_3 , leading to a continuous decrease in the boron content. Dionne *et al.* (1999) characterised TiB_2 -carbon composites after immersion in

the bath for various periods of time. They found that TiB_2 particles were partially dissolved by the bath and that dissolution of TiB_2 occurred along specific atomic planes. It was also pointed out that the dissolution of TiB_2 appears to be enhanced by the presence of Al_2O_3 in solution. If TiB_2 dissolves in contact with the melt the solubility of titanium species may be of interest.

The phase diagram for the system $\text{TiO}_2\text{-Al}_2\text{O}_3$ is given in Figure 4.1.

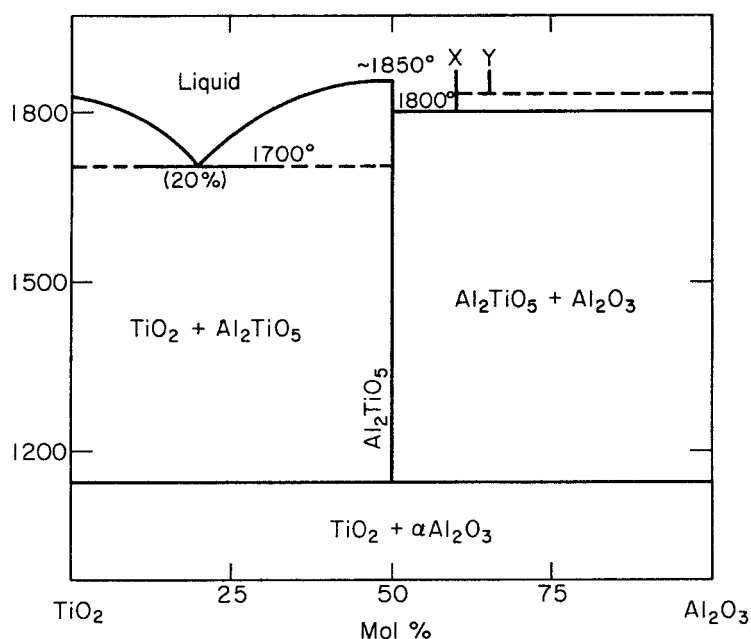


Figure 4.1 Phase diagram for the system $\text{TiO}_2\text{-Al}_2\text{O}_3$. Temperatures are in degrees centigrade. *Phase Diagrams* (1975).

From Figure 4.1 it can be seen that the phase diagram shows no compounds or significant solid solution between titanium dioxide and alumina at temperatures up to 1140 °C. Hence one can treat the TiO_2 activity as unity in this temperature range.

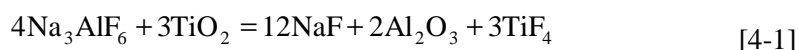
Several investigators have measured the solubility of TiO_2 in Na_3AlF_6 , and in one case in $\text{Na}_3\text{AlF}_6\text{-5 wt\% Al}_2\text{O}_3$. The reported data for TiO_2 solubility are given in Table 4-1.

All data in Table 4-1, except the value found in Qiu *et al.* (1988), are interpolated from phase diagrams.

Table 4-1 Solubility of TiO₂ in molten cryolite and in cryolite-alumina mixtures at 1020 °C reported in the literature.

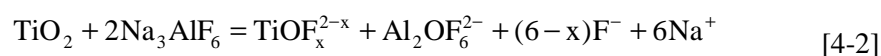
Reference	Na ₃ AlF ₆ wt% TiO ₂	Na ₃ AlF ₆ -5 wt% Al ₂ O ₃ wt% TiO ₂
Belyaev <i>et al.</i> (1956)	5.7	5.0
Hayakawa and Kido (1952)	6.1	-
Madhavan <i>et al.</i> (1971)	5.2	-
Sterten and Skar (1988)	6.5	-
Qiu <i>et al.</i> (1988)	5.3	-

There are very few works in the literature that propose any dissolution mechanisms for TiO₂ in the system under study. Qiu *et al.* (1988) studied the solubility of TiO₂ in molten cryolite at 1020 °C. They suggested that the following reaction may occur:



No standard state for the TiF₄ was given. Calculation (Outokumpu HSC Chemistry[®]) of the standard Gibbs energy change at 1020 °C, assuming gaseous or liquid state, gives 544 or 839 kJ mol⁻¹, respectively. The TiF₄(l) data used in the calculations were found by extrapolation from 285 °C. A temperature of 1020 °C must be way above the critical point for TiF₄, so a liquid state calculation is very doubtful. The positive values for the standard Gibbs energy change indicate that the proposed dissolution mechanism is not probable.

Sterten and Skar (1988) studied the dissolution of TiO₂ in cryolite by means of thermal and chemical analysis. Freezing point depression data indicated that only two new entities were formed at small additions of TiO₂ to Na₃AlF₆. The most probable dissolution process, according to Sterten and Skar (1988) is,



giving rise to two new species in agreement with the freezing point depression data. The positive value for the standard Gibbs energy change for equation [4-1] was also pointed out.

Titanium is known to appear in different oxidation states, Ti(II), Ti(III) and Ti(IV), depending on the oxygen partial pressure and on the system. Electrochemical investigations of Ti(IV) in fluoride electrolytes showed a two-step reduction mechanism for Ti(IV) with Ti(III) as a sole stable intermediate (Makyta *et al.* 1989). In chloride systems a three-step reduction of Ti(IV) was found (Haarberg *et al.* 1993), *i.e.* Ti(IV) → Ti(III) → Ti(II) → Ti(0). In the published works, it often seems that little attention has been paid to controlling the oxygen partial pressure. Only one of the

references in Table 4-1 states under which atmosphere the experiments were conducted. Sterten and Skar (1988) used an argon atmosphere, and it seems likely that the other investigations had a similar experimental set-up. One can assume that a certain oxygen potential is needed to ensure that one is dealing with Ti(IV) only. Chemical reactions that may influence the oxidation state of titanium in the electrolyte are given in Table 4-2 (Outokumpu HSC Chemistry[®]).

Table 4-2 Standard Gibbs energy for some chemical reactions at 1020 °C.

Reaction	ΔG° kJ mol ⁻¹	Eq.
$\text{TiO}_2(\text{s}) = \text{TiO}(\text{s}) + 1/2\text{O}_2(\text{g})$	291	[4-3]
$\text{TiO}_2(\text{s}) = 1/2\text{Ti}_2\text{O}_3(\text{s}) + 1/4\text{O}_2(\text{g})$	128	[4-4]
$\text{TiO}_2(\text{s}) = 1/3\text{Ti}_3\text{O}_5(\text{s}) + 1/6\text{O}_2(\text{g})$	81	[4-5]
$\text{TiO}_2(\text{s}) = 1/4\text{Ti}_4\text{O}_7(\text{s}) + 1/8\text{O}_2(\text{g})$	60	[4-6]
$\text{TiO}_2(\text{s}) + 4/3\text{AlF}_3(\text{l}) = \text{TiF}_4(\text{g}) + 2/3\text{Al}_2\text{O}_3(\text{l})$	39	[4-7]
$\text{TiO}_2(\text{s}) + 4/3\text{AlF}_3(\text{l}) = \text{TiF}_4(\text{l}) + 2/3\text{Al}_2\text{O}_3(\text{l})$	137	[4-8]
$\text{TiO}_2(\text{s}) + 2/3\text{AlF}_3(\text{l}) = \text{TiOF}_2(\text{g}) + 1/3\text{Al}_2\text{O}_3(\text{l})$	219	[4-9]
$\text{TiO}_2(\text{s}) + 1/3\text{Al}_2\text{O}_3(\text{l}) + 4\text{NaF}(\text{l}) = \text{Na}_2\text{TiO}_3(\text{s}) + 2/3\text{Na}_3\text{AlF}_6(\text{l})$	26	[4-10]
$\text{TiO}_2(\text{s}) + 1/2\text{C}(\text{s}) = 1/2\text{Ti}_2\text{O}_3(\text{s}) + 1/2\text{CO}(\text{g})$	15	[4-11]
$\text{TiO}_2(\text{s}) + 1/3\text{Al}(\text{l}) = 1/2\text{Ti}_2\text{O}_3(\text{s}) + 1/6\text{Al}_2\text{O}_3(\text{l})$	-83	[4-12]
$\text{TiO}_2(\text{s}) + 4/3\text{Al}(\text{l}) = \text{Ti}(\text{s}) + 2/3\text{Al}_2\text{O}_3(\text{l})$	-132	[4-13]
$\text{TiO}_2(\text{s}) + 1/3\text{Ti}(\text{s}) = 2/3\text{Ti}_2\text{O}_3(\text{s})$	-66	[4-14]

From Table 4-2 one sees that all the reactions have positive standard Gibbs energies, except for equations [4-12] to [4-14]. This implies that Ti(IV) should be stable as long as neither aluminium nor titanium metal are present in the system. Calculations of the equilibrium pressure of oxygen for the reactions given by equations [4-3], [4-4], [4-5] and [4-6], assuming that TiO, TiO₂, Ti₂O₃, Ti₃O₅ and Ti₄O₇ have unit activity, give $3 \cdot 10^{-24}$, $2 \cdot 10^{-21}$, $2 \cdot 10^{-20}$ and $5 \cdot 10^{-20}$ bar, respectively. Since most of the given data only concern solid phases of titanium compounds, it is hard to predict the necessary oxygen pressure to stabilise Ti(IV) in solution. For this reason the present work was performed under 1 atm of oxygen.

The purpose of the present work was to measure the solubility of TiO₂ as a function of the alumina content in cryolite melts at a constant temperature. From the results obtained the objective was to propose a probable dissolution mechanism for TiO₂, and to indicate the structure of the dissolved titanium complexes.

4.2 Experimental

The chemicals used in the experiments and the pre-treatment of them are given in Table 4-3. The experimental set-up is shown in Figure 4.2.

Table 4-3 Specifications of the chemicals used in the TiO_2 solubility experiments.

Compound	Producer/quality	Pre-treatment
Na_3AlF_6	Hand-picked natural Greenland cryolite	Coloured particles (impurities) were removed manually
Al_2O_3	Merck, anhydrous γ -alumina	Heated to 200 °C before use
TiO_2	Alfa Johnson Matthey, 2 micron, 99 %+ rutile	Heated to 200 °C before use
O_2	AGA, 99.99 %	Used as received

A batch was made up by mixing the desired amounts of cryolite and alumina with an excess of titanium dioxide. The batch (~160 g) was contained in a platinum crucible. The experiments were performed in a standard furnace at 1020 ± 2 °C under oxygen atmosphere. The temperature was recorded using a Pt-PtRh10% thermocouple placed in a platinum tube. When the mixture had melted, it was agitated for at least 60 minutes using a platinum stirrer. The melt was then left without stirring to allow solid particles dispersed in the melt to settle. Minimum settling time was 90 minutes. A sample of the melt was then withdrawn by suction using a quartz tube, and subsequently quenched.

Bath samples (~3 g) taken during preliminary experiments were analysed by ICP. Different solvents were tested to dissolve the bath samples. All solvents failed, leaving a large amount of undissolved material at the bottom of the flask. As a result too low titanium concentrations were analysed by ICP. This observation is in accordance with Gmelins Handbuch (1951) which states that TiO_2 is insoluble in almost all solvents, with the exception of warm 40 % HF and hot concentrated H_2SO_4 , in which it is partly soluble. Subsequently XRF was tested and proved to be successful. The XRF instrument is more demanding when it comes to the amount of sample material needed. To get enough material for several replicates about 20 g was collected. As a result a maximum of three samples were taken during an experiment.

The oxygen content in the samples was found by carbothermic reduction analysis using a LECO apparatus (TC-436). The sample, contained in a tin capsule, was heated together with graphite powder until the oxygen in the sample reacted with the graphite. The CO formed was oxidised to CO_2 , and led out of the electrode chamber and through an IR cell which detected CO_2 . From the amount of CO_2 the oxygen content in the sample was calculated. The samples were analysed by a scan method, *i.e.* the

temperature was gradually increased at $7\text{ }^{\circ}\text{C s}^{-1}$ from 800 to 2700 $^{\circ}\text{C}$. The instrument was calibrated with standard steel samples.

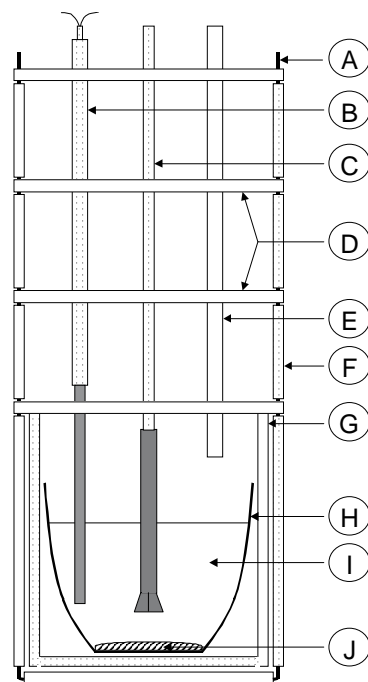


Figure 4.2 Experimental set-up: (A) 3 mm Incolloy wire; (B) Thermocouple (Pt-PtRh10%) placed in platinum; (C) Platinum stirrer; (D) Radiation shields; (E) Quartz sampling tube; (F) Alsint* tubes; (G) Alsint* outer crucible; (H) Platinum crucible; (I) Cryolite-alumina melt; (J) Solid TiO_2 (excess). *Product of W. Haldenwanger (Berlin) containing 99.7 % Al_2O_3 .

4.3 Results and Discussion

4.3.1 Solubility as a Function of Alumina Concentration

Visual inspection of the slowly solidified melt showed that the lower part had become yellow. This indicates that solid rutile is present since it should be golden yellow or rusty yellow as inclusions or thin crystals (<http://mineral.galleries.com>).

The quenched bath samples were white. Three of the samples with varying alumina content were analysed by XRD. Only TiO_2 and Na_3AlF_6 were detected in these samples. The absence of Al_2O_3 in the XRD results is in agreement with the findings of Holm (1963). He showed that it is not possible to detect any Al_2O_3 in a quenched

sample. A diffractogram from the XRD analysis showing that TiO_2 is present in the bath samples is given in Figure 4.3.

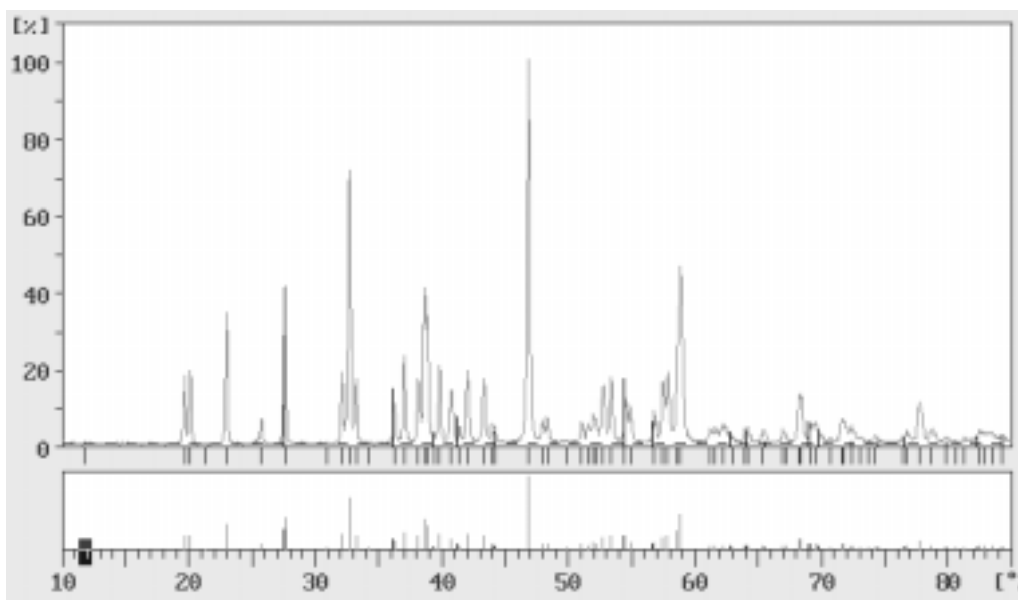


Figure 4.3 A diffractogram from the XRD analysis of a bath sample with regard to TiO_2 .

The total amount of oxygen found at TiO_2 saturation, and the corresponding titanium concentration, using LECO and XRF are given in Table 4-4.

A plot of the titanium concentration versus the total oxygen concentration based on the data in Table 4-4 is given in Figure 4.4. The relation between titanium and total oxygen can be expressed empirically by,

$$[\text{Ti}] = \alpha + \frac{\beta[\text{O}]^2}{[\text{O}] - \gamma} \quad [4-15]$$

for the investigated range. The units of titanium and oxygen are in wt%. The constants α , β , and γ were found by iterations to be 1.8 wt%, 0.092 and 1.7 wt%, respectively. The standard deviation of titanium was found to be ± 0.05 wt%. The relationship given by equation [4-15] is presented as a solid line in Figure 4.4.

Table 4-4 Total oxygen concentration found at TiO_2 saturation, and the corresponding titanium concentration found at 1020 °C.

Oxygen wt%	Titanium wt%	Oxygen wt%	Titanium wt%
1.9	3.1	3.9	2.4
2.0	3.1	5.0	2.5
2.1	2.7	5.0	2.5
2.2	2.7	5.3	2.5
2.2	2.8	5.6	2.5
2.4	2.6	5.6	2.5
2.6	2.5	6.0	2.5
2.7	2.5	6.0	2.6
2.7	2.4	6.3	2.6
3.1	2.4	7.1	2.7
3.7	2.4	8.1	2.7
3.2	2.4	8.1	2.7
3.3	2.3	8.2	2.7
3.5	2.4		

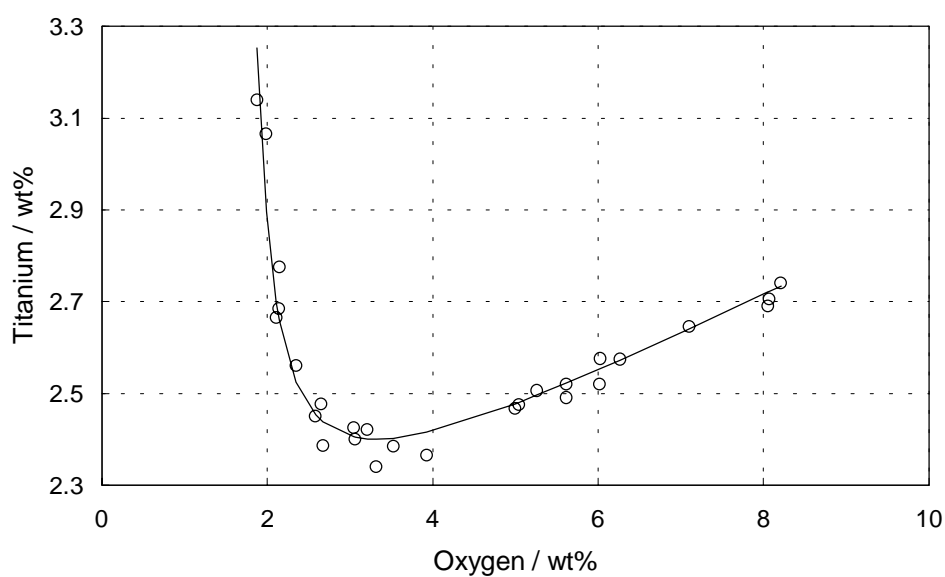


Figure 4.4 Solubility of titanium versus the oxygen content in cryolite-alumina melts at 1020 °C.

The results show that the solubility of TiO_2 in cryolite melts at 1020 °C was found to be 3.1 wt% Ti, *i.e.* 5.2 wt% TiO_2 . This value is in good agreement with the findings of Madhavan *et al.* (1971) and Qiu *et al.* (1988), as can be seen in Table 4-1.

It was expected that the uncertainty in the measured titanium concentrations, using the XRF instrument, should be less than 10 % (Fredheim 2000). A test was performed at 1020 °C with a weighed-in melt composition of 3.0 wt% TiO_2 , 9.0 wt% Al_2O_3 and 88.0 wt% Na_3AlF_6 . The XRF analysis determined about 95 % of the amount of TiO_2 added.

The uncertainty in the determined oxygen concentrations, using LECO, was found to be about 3 % when steel standards were used (Mediaas 2000). Oxygen analysis of the test mentioned above obtained approximately 95 % of the initial concentration. Danek *et al.* (2000) investigated the system $\text{NaF-AlF}_3\text{-Al}_2\text{O}_3$ using the same instrument, *i.e.* LECO TC-436. Their results showed that the ratio between alumina measured and alumina added were 0.870, 0.769 and 0.728 at CR's equal to 2, 3 and 4, respectively. Although the samples of Danek *et al.* (2000) did not contain any titanium, the influence of the CR should be noted. An uncertainty of less than 10 % is expected in the measured oxygen concentrations.

From Table 4-4 one sees that the oxygen content varies from 1.88 - 8.21 wt%. The extremes were found in cryolite and in cryolite at alumina saturation, respectively. The implication is that in the cryolite case all the oxygen was introduced to the system by the titanium dioxide. With increasing oxygen content the titanium dioxide solubility initially decreases until the oxygen concentration becomes ~3.5 wt%, as shown in Figure 4.4. This indicates that the dissolution mechanism in dilute solution produces alumina as suggested by Sterten and Skar (1988) and given by equation [4-2].

According to Dewing and Thonstad (1997b), a logarithmic plot of solubility versus alumina activity makes it possible to derive the stoichiometric relationship for the dissolution mechanism, *i.e.* between alumina and dissolved titanium dioxide. A check was performed to see if the data obtained fitted the mechanism of Sterten and Skar (1988). If we treat the solution as consisting of only neutral complexes, the dissolution mechanism of Sterten and Skar (1988) proposes that titanium is in solution as TiOF_2 . If we assume that oxygen not associated with titanium is in solution as alumina, one oxygen atom per titanium atom is subtracted from the total oxygen to give the alumina concentration. Activity data for the pure system cryolite-alumina are found in the literature. As an approximation the data of Dewing and Thonstad (1997a) were used to convert alumina concentration into alumina activity. The equation for conversion is given by:

$$N_{\text{Al}_2\text{O}_3} = \alpha a_{\text{Al}_2\text{O}_3}^{1/3} + \beta a_{\text{Al}_2\text{O}_3}^{2/3} \quad [4-16]$$

The values of the coefficients α and β are 0.0772 ± 0.0025 and 0.159 ± 0.0048 , respectively.

The relationship obtained between TiOF_2 and alumina activity is given in Figure 4.5.

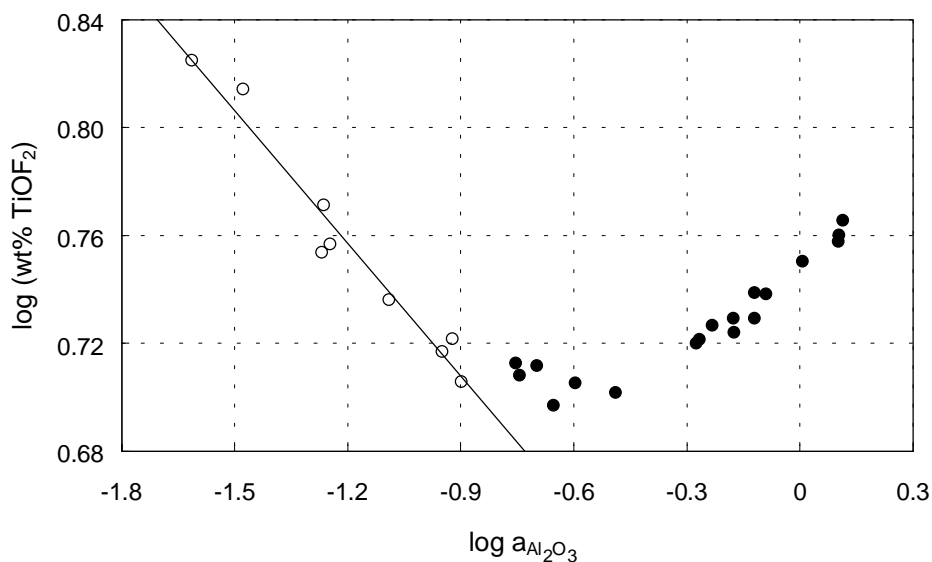
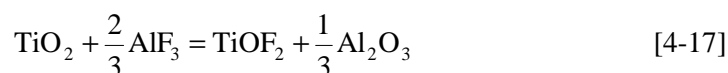


Figure 4.5 Solubility of TiO_2 expressed as TiOF_2 at 1020 °C as a function of alumina activity plotted on a logarithmic scale. The open circles were used in the regression line.

The regression line of the experimental points at low alumina concentration is found to have a slope of -0.164 ± 0.012 and a constant of 0.560 ± 0.015 . Conversion of equation [4-2] (Sterten and Skar 1988) into the simplest possible neutral species gives:

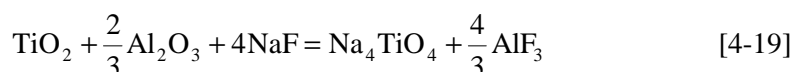
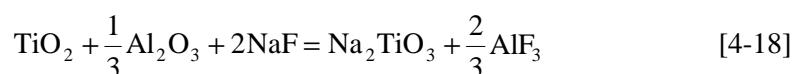


From equation [4-17] one sees that the concentration of TiOF_2 should be proportional to $a_{\text{Al}_2\text{O}_3}^{-1/3}$, corresponding to a slope of $-1/3$ in a plot like Figure 4.5. Comparison of the obtained slope (-0.164) with the theoretical indicates that the part of the system low in oxygen cannot be described by this dissolution mechanism alone.

Beyond ~3.5 wt% oxygen the titanium oxide solubility increases, indicating that the predominant dissolution mechanism consumes alumina. This implies that more than two oxygen atoms are linked to each titanium atom. According to Dewing and Thonstad (1997a) the solubility of alumina in cryolite at 1020 °C is 13.06 wt%. It is known that introduction of new species to a solution changes the solubility, and thereby the activities of the species. Since there is no data reported at high alumina

concentrations for the system under investigation, as a first approximation we use the alumina solubility and activities for the binary cryolite-alumina system (Dewing and Thonstad 1997a). By calculating the molar ratio between the oxygen not related to the 13.06 wt% alumina, and the measured titanium oxide solubility, a value of 2.25 is obtained. This value indicates that there must be a coexistence of at least two titanium species with different numbers of oxygen atoms attached to them.

Based on the information from Figure 4.5 and the work by Sterten and Skar (1988), a model was made assuming that TiO^{2+} was one of the species. To simplify, it was assumed that the solution contained only two titanium species. The most likely second species would be TiO_3^{2-} or TiO_4^{4-} . For simplification it is assumed that the species are present in the solution as neutral compounds. Probable dissolution mechanisms for the formation of TiO_3^{2-} or TiO_4^{4-} are given in equations [4-18] and [4-19], respectively.



A model can now be made for the system $\text{TiOF}_2\text{-Na}_2\text{TiO}_3$. The first assumption is that the reactions given by equations [4-17] and [4-18] are independent of one another, and that both equilibria are satisfied simultaneously. Furthermore, the activities of all compounds except alumina are constant – that of TiO_2 because it is saturated, and that of AlF_3 and NaF because one has a constant solvent composition (except for the fact that the varying alumina affects the activities of AlF_3 and NaF , a second order effect that we will, for the time being, neglect). One then assumes that Henry's law applies and replaces activities of the solute species with concentrations. This leads to the following equations:

$$[\text{TiOF}_2] = K_1 a_{\text{Al}_2\text{O}_3}^{-1/3} \quad [4-20]$$

$$[\text{Na}_2\text{TiO}_3] = K_2 a_{\text{Al}_2\text{O}_3}^{1/3} \quad [4-21]$$

The constants K_1 and K_2 are not true equilibrium constants since they do not contain the activity terms for AlF_3 and NaF , so they are just proportionality constants. Brackets indicate that the units are in mol per 100 g solution. This concentration unit was chosen in preference to wt% to simplify the iterations. The exponents of the alumina activities are seen from equations [4-17] and [4-18]. The exponent $-1/3$ ($+1/3$) is due to the liberation (association) of one alumina molecule per three titanium dioxide molecules introduced to the melt.

The total titanium concentration is given by:

$$[\text{Ti}] = [\text{TiOF}_2] + [\text{Na}_2\text{TiO}_3] \quad [4-22]$$

The ratio between Na_2TiO_3 and TiOF_2 is then found by combining equations [4-20] and [4-21]:

$$\frac{[\text{Na}_2\text{TiO}_3]}{[\text{TiOF}_2]} = \frac{K_2}{K_1} a_{\text{Al}_2\text{O}_3}^{2/3} \quad [4-23]$$

The relationship between the total titanium concentration and alumina activity is found by combining equations [4-20] to [4-22]:

$$[\text{Ti}] = K_1 a_{\text{Al}_2\text{O}_3}^{-1/3} + K_2 a_{\text{Al}_2\text{O}_3}^{1/3} \quad [4-24]$$

On this basis an iteration can be started. All the titanium species contain at least one oxygen atom. Initially, one oxygen atom is subtracted per titanium atom from the reported total alumina (oxygen). A plot of $[\text{Ti}]a_{\text{Al}_2\text{O}_3}^{1/3}$ *versus* $a_{\text{Al}_2\text{O}_3}^{2/3}$ is made. The relationship is found by multiplying equation [4-24] by $a_{\text{Al}_2\text{O}_3}^{1/3}$. Regression analysis of the plot gives the first estimates of K_1 (intercept) and K_2 (slope). Equation [4-23] is then used for each experimental value to estimate how the total titanium concentration is split between TiOF_2 and Na_2TiO_3 . The additional two oxygen atoms contained in the estimated Na_2TiO_3 are then subtracted from the total alumina. The iteration is now repeated – the alumina concentrations are revised, and hence the alumina activities. If, when the iteration has closed, the plot is “reasonably” straight, one has an adequate interpretation of the results. Why only “reasonably” straight lines can be expected is due to the criteria on which the quantitative treatment is based, the criteria being (a) constant activity of AlF_3 , and (b) constant activity coefficients of the titanium species. Since neither of these conditions can be expected to be exactly correct, one can only look for “reasonably” straight lines.

The same iteration procedure is applied for the other possible mechanism, *i.e.* the system $\text{TiOF}_2\text{-Na}_4\text{TiO}_4$. The only difference is that one more oxygen atom has to be subtracted from the alumina due to equation [4-19], leading to an increase of 1/3 in the power of the alumina activity in an equation similar to equation [4-21]. A combination of equations as described above gives that $[\text{Ti}]a_{\text{Al}_2\text{O}_3}^{1/3}$ should be plotted *versus* $a_{\text{Al}_2\text{O}_3}$ instead of $a_{\text{Al}_2\text{O}_3}^{2/3}$.

The plot of $[\text{Ti}]a_{\text{Al}_2\text{O}_3}^{1/3}$ *versus* $a_{\text{Al}_2\text{O}_3}^{2/3}$ for the system $\text{TiOF}_2\text{-Na}_2\text{TiO}_3$ after the iteration had closed is given in Figure 4.6. A similar plot, but *versus* $a_{\text{Al}_2\text{O}_3}$, for the system $\text{TiOF}_2\text{-Na}_4\text{TiO}_4$ is given in Figure 4.7. The work of Dewing and Thonstad (1997a) was used for converting alumina concentrations into activities.

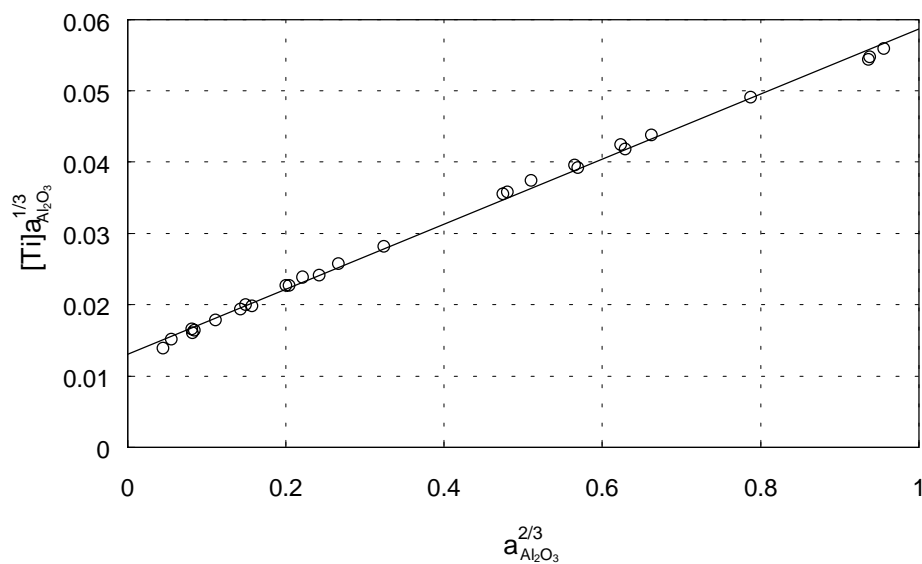


Figure 4.6 Plot of $[\text{Ti}]a_{\text{Al}_2\text{O}_3}^{1/3}$ versus $a_{\text{Al}_2\text{O}_3}^{2/3}$ for the system $\text{TiOF}_2\text{-Na}_2\text{TiO}_3$. The concentration is in mol per 100 g solution. See text.

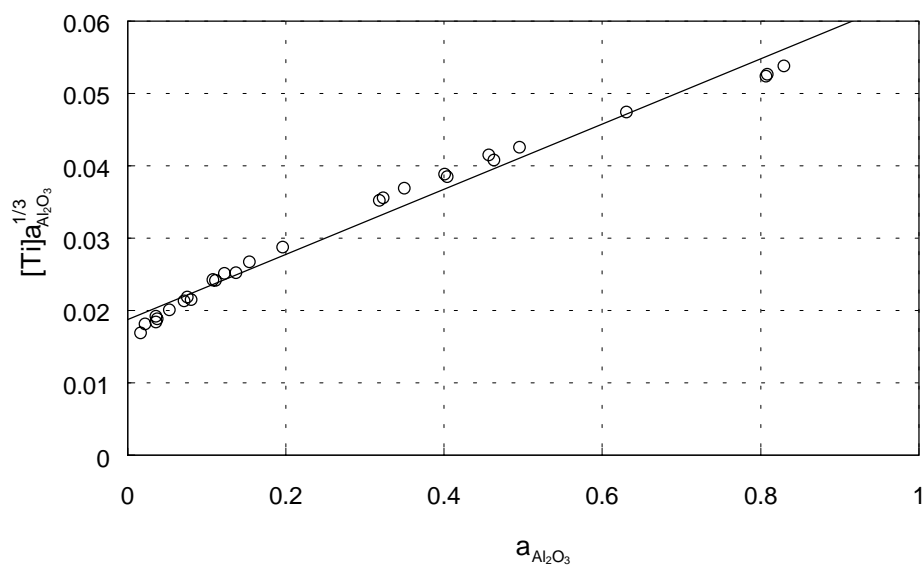


Figure 4.7 Plot of $[\text{Ti}]a_{\text{Al}_2\text{O}_3}^{1/3}$ versus $a_{\text{Al}_2\text{O}_3}$ for the system $\text{TiOF}_2\text{-Na}_4\text{TiO}_4$. The concentration is in mol per 100 g solution. See text.

The relationship between titanium concentration and alumina activity is found by regression analysis of the iterated values in Figures 4.6 and 4.7. The results for the systems $\text{TiOF}_2\text{-Na}_2\text{TiO}_3$ and $\text{TiOF}_2\text{-Na}_4\text{TiO}_4$ are given by equations [4-25] and [4-26], respectively.

$$[\text{Ti}]a_{\text{Al}_2\text{O}_3}^{1/3} = (0.0456 \pm 0.0005)a_{\text{Al}_2\text{O}_3}^{2/3} + (0.0130 \pm 0.0002) \quad [4-25]$$

$$[\text{Ti}]a_{\text{Al}_2\text{O}_3}^{1/3} = (0.0450 \pm 0.0013)a_{\text{Al}_2\text{O}_3} + (0.0187 \pm 0.0005) \quad [4-26]$$

Equations [4-25] and [4-26] were found to have standard deviations of ± 0.0007 and ± 0.0017 , respectively.

From the results of the iterations the calculated concentrations of the different titanium species could be plotted versus alumina activity, as shown in Figures 4.8 and 4.9 for the systems $\text{TiOF}_2\text{-Na}_2\text{TiO}_3$ and $\text{TiOF}_2\text{-Na}_4\text{TiO}_4$, respectively.

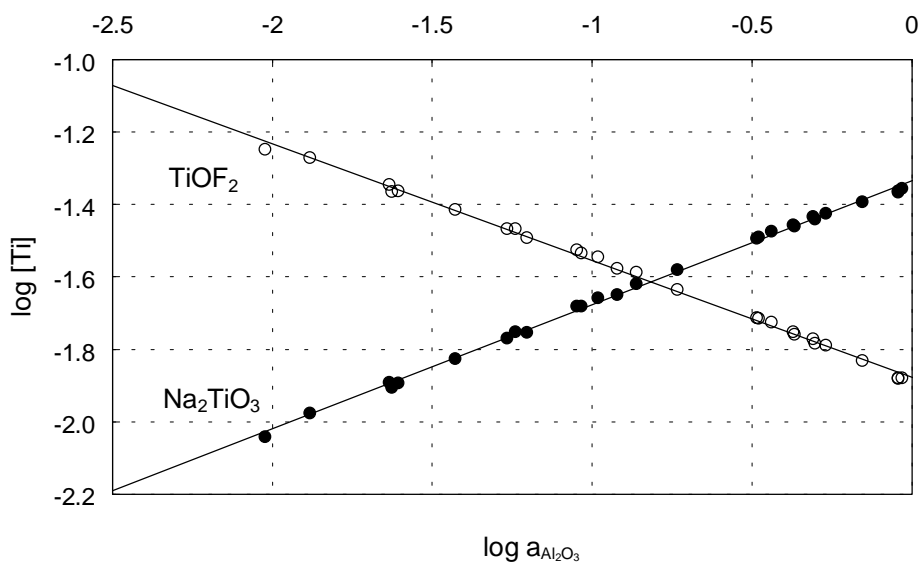


Figure 4.8 Plot of the calculated concentrations of TiOF_2 and Na_2TiO_3 versus alumina activity on a logarithmic scale. The concentration scale is in mol per 100 g solution.

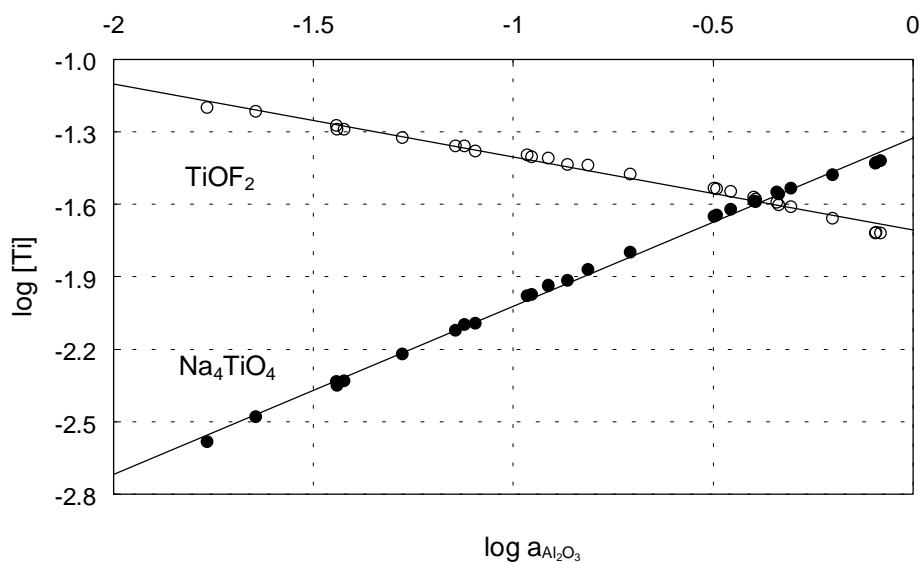


Figure 4.9 Plot of the calculated concentrations of TiOF_2 and Na_4TiO_4 versus alumina activity on a logarithmic scale. The concentration scale is in mol per 100 g solution.

The relationship between the calculated concentrations of TiOF_2 , Na_2TiO_3 and the alumina activity is given by equations [4-27] and [4-28].

$$\log [\text{TiOF}_2] = -(0.322 \pm 0.003) \log a_{\text{Al}_2\text{O}_3} - (1.876 \pm 0.003) \quad [4-27]$$

$$\log [\text{Na}_2\text{TiO}_3] = (0.343 \pm 0.003) \log a_{\text{Al}_2\text{O}_3} - (1.335 \pm 0.003) \quad [4-28]$$

Equations [4-27] and [4-28] were found to have standard deviations of ± 0.010 and ± 0.009 , respectively.

The relationships between the calculated concentrations of TiOF_2 , Na_4TiO_4 and the alumina activity are given by equations [4-29] and [4-30].

$$\log [\text{TiOF}_2] = -(0.303 \pm 0.008) \log a_{\text{Al}_2\text{O}_3} - (1.706 \pm 0.007) \quad [4-29]$$

$$\log [\text{Na}_4\text{TiO}_4] = (0.679 \pm 0.008) \log a_{\text{Al}_2\text{O}_3} - (1.325 \pm 0.007) \quad [4-30]$$

Equations [4-29] and [4-30] were found to have standard deviations of ± 0.020 and ± 0.020 , respectively.

A look at Figure 4.6 and especially at Figure 4.7 shows that the curves are both slightly concave downward. As mentioned earlier, one of the underlying assumptions for the model was that the activities of AlF_3 and NaF remained constant. This was based on a constant solvent composition, *i.e.* cryolite ratio (CR) equal to three, and no internal reactions in the solution involving NaF and AlF_3 . The CR is simply the ratio of NaF/AlF_3 as determined by chemical analysis, and it is not changed by the introduction of TiO_2 to the system. It is often found that the maximum solubility of various species in cryolite melts is at around $\text{CR} = 3$. Xiao *et al.* (1995) investigated the solubility of SnO_2 in the systems $\text{NaF}-\text{AlF}_3$ and $\text{NaF}-\text{AlF}_3-\text{Al}_2\text{O}_3(\text{sat})$. In both cases it was found that the maximum solubility occurred at $\text{CR} = 3$. A study of the solubility of Fe_2O_3 in the systems $\text{NaF}-\text{AlF}_3$ and $\text{NaF}-\text{AlF}_3-\text{Al}_2\text{O}_3(\text{sat})$ by Diep (1998) obtained a similar result.

Examination of equations [4-17] to [4-19] shows that the activities of NaF and AlF_3 are affected by both the alumina concentration and the amount of TiO_2 present in the system. At low alumina concentrations the reaction given by equation [4-17] is predominant. AlF_3 is being “consumed” as TiO_2 dissolves in the melt, and hence the activity of AlF_3 decreases while the activity of NaF increases. At high alumina concentrations the reactions given by equation [4-18] or [4-19] are predominant. In this case NaF is being “consumed” during the dissolution, giving a decrease in its activity and hence an increase in the AlF_3 activity. The implications are that the activities of NaF and AlF_3 are different from what they would be in a ternary $\text{NaF}-\text{AlF}_3-\text{Al}_2\text{O}_3$ mixture without TiO_2 , upon which the model was based. The best fit between the experimental points and the alumina activity data by Dewing and Thonstad (1997a) would, therefore, be at the alumina concentration where the reactions described by equations [4-17] and [4-18] or [4-19] balances, *i.e.* the net change in NaF and AlF_3 is zero. This can be seen as an analogy to the influence of CR on the solubility as discussed above. Therefore, it could be expected that the graphs would be concave downward, and with a “maximum” at some intermediate alumina concentration.

The closed iterations shown in Figures 4.6 and 4.7 give the alumina activities at alumina saturation as 0.934 (12.51 wt%) and 0.830 (11.61 wt%), respectively. The activity data (Dewing and Thonstad 1997a) used in the model stated that the saturation concentration of alumina was 13.06 wt%. It is known that introduction of a new species into the system may change the solubility limits of the species already present. It is therefore not to be expected that the alumina saturation concentration should remain the same as for the binary system $\text{Na}_3\text{AlF}_6-\text{Al}_2\text{O}_3$. There is also some uncertainty associated with the activity data used in the modelling. Insertion of the standard deviations given by Dewing and Thonstad (1997a) into equation [4-16] gives an alumina saturation concentration ranging from 12.60 to 13.52 wt% at unit alumina activity. It is noticed that the first value is very close to the alumina saturation concentration found by iteration for the system $\text{TiOF}_2-\text{Na}_2\text{TiO}_3$.

The criterion for an interpretation of the results was a reasonably straight plot. The standard deviations of the slope, found by regression analysis, for the systems TiOF_2-

Na_2TiO_3 and $\text{TiOF}_2\text{-Na}_4\text{TiO}_4$ are given by equations [4-25] and [4-26], respectively. Calculations give a standard deviation of 1.0 % for the system $\text{TiOF}_2\text{-Na}_2\text{TiO}_3$, and 2.8 % for the system $\text{TiOF}_2\text{-Na}_4\text{TiO}_4$. A reasonable interpretation is that the system $\text{TiOF}_2\text{-Na}_2\text{TiO}_3$ is the more probable.

The modelling and iterations were conducted with the simplification that the species are present in the electrolyte as neutral compounds. The structure of TiO^{2+} was suggested by Sterten and Skar (1988) and given by equation [4-2], *i.e.* TiOF_4^{2-} . It is more difficult to suggest a reasonable structure for the species TiO_3^{2-} , and it cannot be excluded that it is a part of larger complexes including aluminium.

4.3.2 Solubility as a Function of Temperature

To investigate the effect of temperature on the TiO_2 solubility, experiments were performed in the range from 975 to 1035 °C. The system under study was cryolite saturated with alumina. The results, which are presented in Table 4-5, show that the solubility of tetravalent titanium in the melt increased with increasing temperature.

Table 4-5 Solubility of titanium at alumina saturation measured as a function of temperature.

Temperature	Titanium
°C	wt%
975	1.9
985	2.0
995	2.2
1005	2.3
1015	2.4
1025	2.7
1035	2.8

The apparent partial molar enthalpy of dissolution, $\Delta\bar{H}^\circ$, of TiO_2 in the melt can be obtained from the solubility data. At saturation of TiO_2 we have,



$$\Delta G^\circ = -RT \ln \frac{a_{\text{TiO}_2(\text{diss})}}{a_{\text{TiO}_2(\text{s})}} \quad [4-32]$$

where the activity of solid TiO_2 is equal to unity. If the solubility is low we can assume Henrian behaviour:

$$a_{\text{TiO}_2(\text{diss})} = kx_{\text{TiO}_2(\text{diss})} \quad [4-33]$$

where k is Henry's constant and x is the concentration, in this case in wt%.

By introducing the Gibbs-Helmholtz equation, we obtain the following equation,

$$\frac{\partial \ln x_{\text{TiO}_2(\text{diss})}}{\partial 1/T} = -\frac{\Delta \bar{H}_{\text{TiO}_2}^0}{R} \quad [4-34]$$

Therefore, a plot of $\ln(\text{wt\% Ti})$ versus T^{-1} should be linear, provided that the assumption of Henrian behaviour holds and the partial molar enthalpy of dissolution is independent of temperature. In Figure 4.10 the solubility data for tetravalent titanium are plotted in this manner.

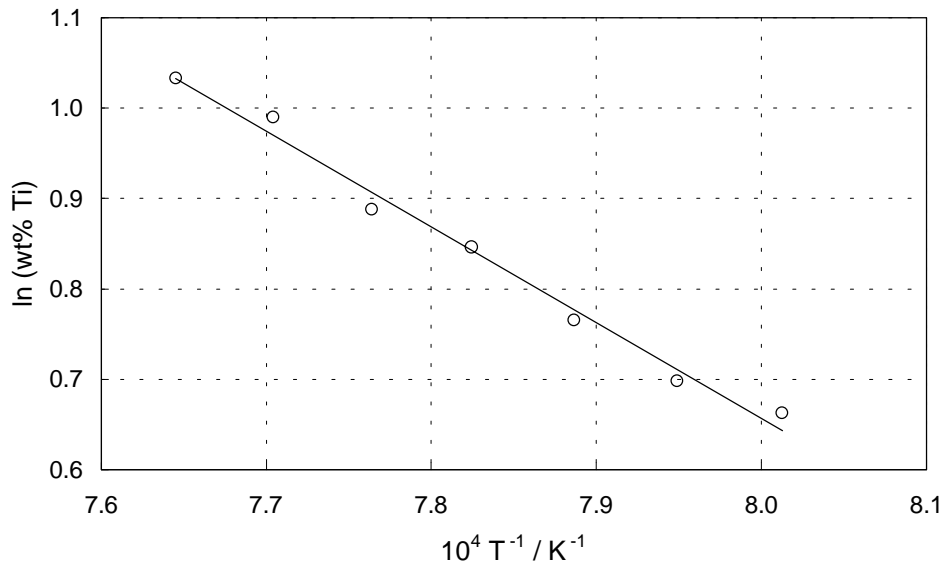


Figure 4.10 Natural logarithm of the Ti(IV) solubility as a function of the reciprocal temperature in alumina-saturated melts.

From Figure 4.10 it can be seen that the correlation between the saturation concentration and the temperature is good. The least-squares equation was found to be,

$$\ln(\text{wt\% Ti}) = - \frac{(10600 \pm 500)}{T} + (9.15 \pm 0.39) \quad [4-35]$$

with a standard deviation of ± 0.02 . The temperature unit is Kelvin.

The apparent partial molar enthalpy of dissolution of TiO_2 was calculated to be:

$$\Delta \bar{H}_{\text{TiO}_2}^{\circ} = (88.3 \pm 4.1) \text{ kJ mol}^{-1}$$

The assumption of Henrian behaviour is questionable since the titanium solubility is of the order of several wt%. Comparison of the solubility data presented in Table 4-4 at alumina saturation, ~2.71 wt%, with the one given by equation [4-35] at 1020 °C, ~2.56 wt%, gives a deviation of 5.5 %. Since the experimental data show such a good linear relationship, it is believed that the deviation is due to a systematic error such as the calibration of the XRF instrument. This is supported by the fact that the data presented in the Tables 4-4 and 4-5 were not analysed at the same time. The observed deviation of 5.5 % is within the assumed uncertainty of 10 %.

References to Chapter 4

- Belyaev, A. I., M. B. Rapoport and L. A. Firsanova (1956): Metallurgie des Aluminiums, Band I, Veb Verlag Technik, Berlin, Germany, p. 84.
- Danek, V., Ø. Gustavsen and T. Østvold (2000): Structure of the MF-AlF₃-Al₂O₃ (M = Li, Na, K) Melts, *Can. Met. Quart.*, **39**, 15.
- Deininger, L. and J. Gerlach (1979): Stromausbeutemessungen bei der Aluminium-oxidreduktionselektrolyse in Laboratoriumszellen, *Metall*, **33**, 131.
- Devyatkin, S. V., G. Kaptay, J.-C. Poignet and J. Bouteillon (1998): Chemical and Electrochemical Behaviour of Titanium Oxide and Complexes in Cryolite-Alumina Melts, *High Temp. Mat. Proc.*, **2**, 497.
- Dewing, E. W. and J. Thonstad (1997a): Activities in the System Cryolite-Alumina, *Metall. Mater. Trans. B*, **28B**, 1089.
- Dewing, E. W. and J. Thonstad (1997b): Solutions of CeO₂ in Cryolite Melts, *Metall. Mater. Trans. B*, **28B**, 1257.
- Diep, Q. B. (1998): Structure and Thermodynamics of Cryolite-Based Melts with Additions of Al₂O₃ and Fe₂O₃, Doctoral Thesis 1998:28, Department of Electrochemistry, Norwegian University of Science and Technology, Trondheim, Norway, p. 79.
- Dionne, M., G. L'Espérance and A. Mirtchi (1999): Wetting of TiB₂-Carbon Material Composite, in *Light Metals 1999*, C. E. Eckert, Editor, TMS, Warrendale, PA, p. 389.

- Fredheim, B. (2000): Hydro Aluminium, N-6882 Øvre Årdal, Norway, Personal communication, February 2000.
- Gmelins Handbuch der Anorganischen Chemie (1951): Titan, **41**, 8. Auflage, Verlag Chemie, GmbH, Weinheim/Bergstrasse, Germany, p. 211.
- Haarberg, G. M., W. Rolland, Å. Sterten and J. Thonstad (1993): Electrodeposition of Titanium from Chloride Melts, *J. Appl. Electrochem.*, **23**, 217.
- Hayakawa, Y. and H. Kido (1952): The Solubility of Substances in Molten Salts (Part 2) – The Solubility of ZnO, CdO and TiO₂ in Molten Cryolite, *J. Electrochem. Soc. Japan*, **20**, 263.
- Holm, J. L. (1963): Undersøkelser av struktur og faseforhold for en del systemer med tilknytning til aluminiumelektrolysen, Thesis, Department of Inorganic Chemistry, Norwegian Institute of Technology, Trondheim, Norway, p. 19.
- <http://mineral.galleries.com/minerals/oxides/rutile/rutile.htm> (January 2000).
- Madhavan, T. P., K. Matiasovsky and V. Danek (1971): Physico-Chemical Properties of the System Na₃AlF₆-NaCl-TiO₂, *Chem. zvesti*, **25**, 253.
- Makytá, M., K. Matiasovsky and V. I. Taranenko (1989): Mechanism of the Cathode Process in the Electrochemical Synthesis of TiB₂ in Molten Salts – I. The Synthesis in an all-Fluoride Electrolyte, *Electrochim. Acta*, **34**, 861.
- Makytá, M., V. Danek, G. M. Haarberg and J. Thonstad (1996): Electrodeposition of Titanium Diboride from Fused Salts, *J. Appl. Electrochem.*, **26**, 319.
- Mediaas, H. (2000): SINTEF Applied Chemistry, N-7465 Trondheim, Norway, Personal communication, February 2000.
- Outokumpu HSC Chemistry[®] for Windows, Chemical Reaction and Equilibrium Software with extensive Thermochemical Database, Version 3.0, Outokumpu Research Oy, Pori, Finland.
- Qiu, Z., M. Zhang, Y. Yu, Z. Che, K. Grjotheim and H. Kvande (1988): Formation of Aluminium-Titanium Alloys by Electrolysis and by Thermal Reduction of Titania in Cryolite-Alumina Melts, *Aluminium*, **64**, 606.
- Phase Diagrams for Ceramists - 1975 Supplement, M. K. Reser, Editor, The American Ceramic Society, Columbus, OH, p. 135.
- Sterten, Å. and O. Skar (1988): Some Binary Na₃AlF₆-M_xO_y Phase Diagrams, *Aluminium*, **64**, 1051.
- Sterten, Å., P. A. Solli and E. Skybakmoen (1998): Influence of Electrolyte Impurities on Current Efficiency in Aluminium Electrolysis Cells, *J. Appl. Electrochem.*, **28**, 781.
- Xiao, H., J. Thonstad and S. Rolseth (1995): The Solubility of SnO₂ in NaF-AlF₃-Al₂O₃ Melts, *Acta Chem. Scand.*, **49**, 96.

5 Electrochemistry of Fe(II) in Cryolite-Alumina Melts

5.1 Introduction

The major role of iron compounds in the Hall-Héroult process was discussed in Chapter 3. The possibility of iron compounds as constituents in an inert anode (cermet and metal anodes) was also mentioned. Very few investigations of the electrochemical behaviour of iron species in the cryolite system have been reported, while several investigations have been reported in molten salts systems. However, since systems not involving cryolite are of minor interest here, only a few will be mentioned.

Boxall *et al.* (1974) investigated the electrochemical behaviour of Fe(III) in molten equimolar $\text{AlCl}_3\text{-NaCl}$ at 175 °C. A tungsten wire served as the working electrode. Using cyclic voltammetry, the Fe(III)/Fe(II) couple was found to be reversible, while the Fe(II)/Fe couple showed typical deposition-stripping behaviour. The potential difference between the two couples was found to be 0.8 V.

Chrysoulakis *et al.* (1978) studied the reduction of iron dissolved in the industrial aluminium refining melt ($\text{NaF-AlF}_3\text{-BaCl}_2$) by cyclic voltammetry and chronopotentiometry. The required solutions were obtained by adding ferrous or ferric fluoride to the electrolyte, which was kept under an argon atmosphere. Platinum, iron and graphite electrodes were used. Chemical analysis showed that the stable valency of dissolved iron species in the melt at 750 °C was two. The reduction of Fe(II) ions was reversible and involved two electrons. The diffusion coefficient of the Fe(II) ions was found to be $D_{\text{Fe(II)}} = (2.8 \pm 0.2) \times 10^{-5} \text{ cm}^2 \text{ s}^{-1}$ at 750 °C.

Inman *et al.* (1978) investigated the reduction of Fe(II) in a eutectic LiCl-KCl melt at 500 °C by chronopotentiometry. The Fe(II) ionic solution was prepared *in situ* by anodic dissolution of the metal. Electroreduction of these Fe(II) ions on a flat polished tungsten cathode yielded n values between 1.87 and 2.01. The diffusion coefficient was found to be $D_{\text{Fe(II)}} = (2.2 \pm 0.2) \times 10^{-5} \text{ cm}^2 \text{ s}^{-1}$.

Hugdahl (1981) investigated cryolite melts saturated with alumina at 1000 °C under a nitrogen atmosphere. After adding FeF_2 or FeF_3 , linear and cyclic voltammetry were

applied with a platinum wire as the working electrode, a silver pad as the counter electrode and an aluminium reference electrode. Several peaks were observed, and by calculating the corresponding number of electrons transferred the following oxidation and reduction steps were suggested:



All steps were reported to be reversible. It was commented that the reduction of Fe(III) directly to iron metal instead of to Fe(II) could be due to alloying with the platinum wire. The diffusion coefficient of the Fe(II) ion was reported to be $D_{\text{Fe(II)}} = 3.4 \times 10^{-5} \text{ cm}^2 \text{ s}^{-1}$.

Stangeland (1981) investigated exactly the same system as Hugdahl (1981) by cyclic voltammetry, coulometry, and limiting current measurements. Stangeland (1981) confirmed the findings of Hugdahl (1981), except for the reduction of Fe(III) given by equation [5-3]. This reduction mechanism was reported to involve a single electron being transferred instead of three, *i.e.*,



The diffusion coefficient for Fe(II) was found to be $D_{\text{Fe(II)}} = 7.4 \times 10^{-5} \text{ cm}^2 \text{ s}^{-1}$ from the limiting current measurements of reaction [5-2].

Diep (1998) studied the electrochemical behaviour of dissolved Fe_2O_3 in molten cryolite by applying cyclic voltammetry. The experiments were performed at 1020 °C, and under an atmosphere of oxygen to ensure that Fe(III) was the stable iron species in the melt. The reduction of Fe(III) was found to follow equation [5-5], *i.e.* a one-electron transfer. However, the shape of the voltammograms implied the possibility of a simultaneous alloying reaction taking place, thereby interfering with the Fe(III)/Fe(II) reduction:



The diffusion coefficient was calculated to be $D_{\text{Fe(III)/Fe(II)}} = (1.7 \pm 0.4) \times 10^{-5} \text{ cm}^2 \text{ s}^{-1}$.

5.2 Experimental

Furnace

The experiments were carried out in a standard closed furnace under argon atmosphere (99.99 %). Temperature control within ± 2 °C was achieved with a Eurotherm temperature controller and a calibrated type S thermocouple (Pt-Pt10%Rh) inside the Kanthal heating element. The working temperature was measured with an additional thermocouple protected by a platinum tube inserted into the melt.

Electrodes

A copper ($\varnothing = 1.5$ mm), gold ($\varnothing = 1.0$ mm), or platinum wire ($\varnothing = 1.0$ mm) was used as working electrode. The iron crucible served as the counter electrode and an iron wire ($\varnothing = 1 - 2$ mm) as a reference electrode. The working electrode was lowered ~ 8 mm after making contact with the electrolyte surface (measured by a multimeter), and the active area was checked after each experiment by visual inspection of the electrode.

Chemicals

Natural hand-picked cryolite (Na_3AlF_6) from Greenland (Kryolittselskabet) was crushed, and coloured particles were removed before use. Al_2O_3 (Fluka, pro analysi) was stored at 200 °C and FeF_2 (Fluka, 95 %+) was stored in a desiccator to avoid pick-up of moisture. Commercial grade AlF_3 (Norzink) was purified in the laboratory by sublimation and dried under argon atmosphere at 400 °C for 10 hours. CaF_2 (J. T. Baker, pro analysis) was used as received.

Cell

The electrolyte (~ 150 g) was contained in a 70 mm \times 46 mm (h \times d) iron crucible. The electrode leads were insulated with Alsint* tubes (*Product of W. Haldenwanger, Berlin, containing 99.7 % Al_2O_3). The electrolyte was agitated by an iron stirrer for 20 minutes after the experimental temperature had stabilised. If necessary, FeF_2 was added to the electrolyte through a quartz tube, and the electrolyte was agitated for 20 minutes. Samples of the electrolyte were taken with a quartz tube applying suction, and subsequently quenched. Figure 5.1 shows a schematic drawing of the cell.

Instrumentation

The electrochemical measurements were performed with a Radiometer DEA-I digital electrochemical analyser. It comprises a DEA332 potentiostat with a maximum current output of 2 A and an IMT102 electrochemical interface with response time less than 3 μs . Signal imposition and data acquisition were handled by the Windows-based VoltaMaster 2 integrated software. A maximum of 5000 data points per measurement were stored on a PC.

Analysis

Quenched melt samples were analysed with respect to the iron concentration with an ICP apparatus.

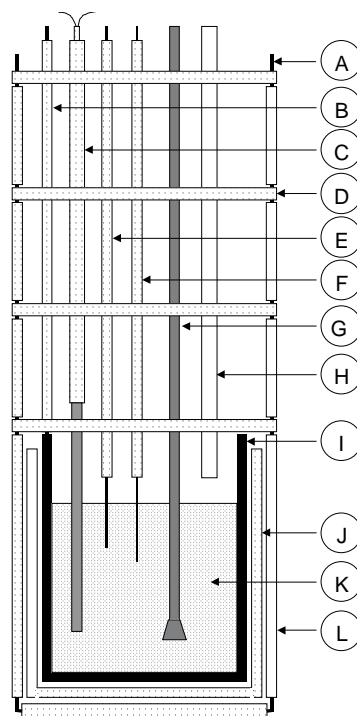


Figure 5.1 Schematic drawing of the experimental cell: (A) Ni wire; (B) Counter electrode connector; (C) Thermocouple; (D) Radiation shield; (E) Fe reference electrode; (F) Working electrode; (G) Fe stirrer; (H) Quartz tube for FeF_2 addition; (I) Fe crucible; (J) Alsint crucible; (K) Melt; (L) Alsint insulation.

5.3 Results and Discussion

Preliminary experiments with cyclic voltammetry showed that neither tungsten nor glassy carbon were suitable as materials for a working electrode. The tungsten electrode dissolved when the potential was positive of the iron reference electrode, *i.e.* tungsten is not sufficiently noble for investigations concerning reduction or oxidation of iron ions in cryolite melts. No clear cathodic peak due to reduction of Fe(II) was obtained at a glassy carbon electrode, while the stripping peak became jagged. This may be explained by a difference of just 0.1 V between the stripping potential of solid iron, *i.e.* the anodic peak potential, and the potential for CO/CO_2 evolution.

Copper was found to be the best material for the investigation of iron deposition due to little alloying compared with gold and platinum in particular. Copper oxidises at potentials where the oxidation of Fe(II) takes place, and could therefore not be used for that purpose. The only satisfactory materials found to work at the potentials for the Fe(II) oxidation were gold and platinum. Gold as well as platinum were used in this study, and both materials gave a large potential window.

All experiments involving cyclic voltammetry or chronoamperometry were performed with ohmic drop compensation. Typically the ohmic resistance was between 0.5 and 1.0 ohm.

5.3.1 Reduction of Fe(II)

The reduction of Fe(II) in cryolite melts was investigated with the electrochemical techniques cyclic voltammetry (CV), chronoamperometry (CA), and chronopotentiometry (CP). The experiments were carried out in both simple binary cryolite-alumina melts as well as in more complex melts with industrial composition ($\text{Na}_3\text{AlF}_6\text{-Al}_2\text{O}_3\text{-AlF}_3\text{-CaF}_2$). Results were obtained in the temperature range from 965 to 1020 °C. A copper wire served as the working electrode. All potentials are referred to the Fe reference electrode and are therefore equivalent to overpotentials. It should be noted that the compositions of the melts are given as wt% of the total. This means that 11 wt% AlF_3 is 11 g per 100 g solution, and not 11 wt% excess AlF_3 related to the cryolite composition.

5.3.1.1 Cyclic Voltammetry

To get an impression of the system under investigation, cyclic voltammograms were recorded before any Fe(II), in the form of FeF_2 , was introduced to the melt. The potential was swept in the cathodic direction from the open circuit potential (~100 mV). The potential was reversed at different potentials (-700, -900, -1000 and -1100 mV) to determine the potential for deposition of aluminium. The cyclic voltammograms are shown in Figure 5.2. From the figure it is seen that a stripping peak occurs at around -900 mV when the potential was reversed at -1000 mV, while it is absent by reversal at -900 mV. The increased current density until the potential is about -950 mV is probably due to alloying of aluminium with the copper electrode. At around -950 mV the copper electrode surface has become an aluminium surface and hence pure aluminium is being produced. Both a cathodic and an anodic peak are observed around zero potential in Figure 5.2. Even though no Fe(II) had been added, the peaks can be related to deposition and stripping of iron. Analysis (ICP) of the melt showed that it contained 0.130 wt% Fe(II). The chemicals and especially the equipment are probably the cause of the relatively high iron content. The stirrer, the counter electrode and the reference electrode were all made of iron. All the equipment will have a surface layer of iron oxide, which will dissolve in the melt. Since the

conditions are such that Fe(II) is the stable ion, the introduction of two Fe(III) will give rise to three Fe(II), *i.e.* an increase of 50 %. Due to the influence of the surroundings on the Fe(II) concentration in the melt, all melts were analysed with respect to Fe ions with ICP. This applies to all the results presented in this chapter.

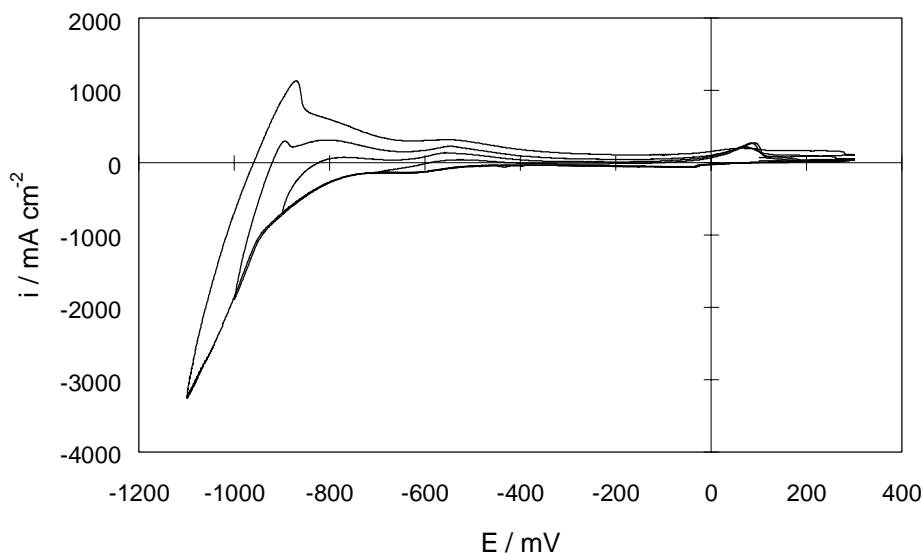


Figure 5.2 Cyclic voltammograms obtained with a copper electrode when the potential was swept in the cathodic direction from the open circuit potential (~ 100 mV). No Fe(II) was added to the system. Sweep rate 200 mV s^{-1} .

Cyclic voltammograms for the deposition and subsequent stripping of iron on a copper electrode were recorded within the potential limits -300 and $+300$ mV. The anodic potential limit was set so that the copper electrode did not oxidise. The cathodic limit was set so that a good deposition peak was obtained, but not so far cathodically to allow for underpotential deposition of aluminium. Typical voltammograms recorded in the system Na_3AlF_6 -3.0 wt% Al_2O_3 with 0.466 wt% Fe(II) at 1020°C are shown in Figure 5.3. The potential was swept with different sweep rates ($v = 100, 200$ and 500 mV s^{-1}) in the cathodic direction from the open circuit potential (~ 100 mV).

A cyclic voltammogram recorded under the same conditions as those in Figure 5.3, but with a lower sweep rate ($v = 20 \text{ mV s}^{-1}$), is given in Figure 5.4.

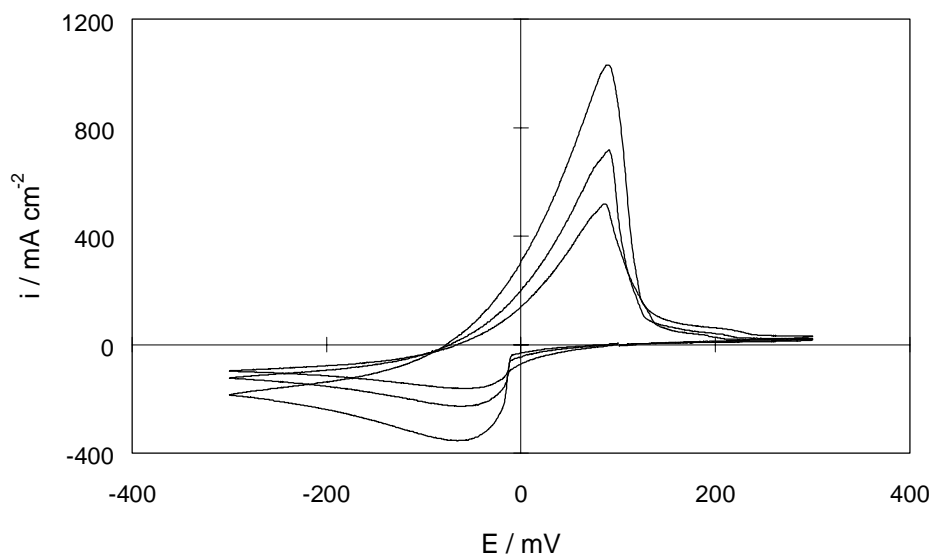


Figure 5.3 Cyclic voltammograms for the deposition of iron on copper in Na_3AlF_6 -3.0 wt% Al_2O_3 with 0.466 wt% Fe(II) at 1020 °C. The potential was swept in the cathodic direction from the open circuit potential (~ 100 mV). Sweep rates 100, 200 and 500 mV s^{-1} .

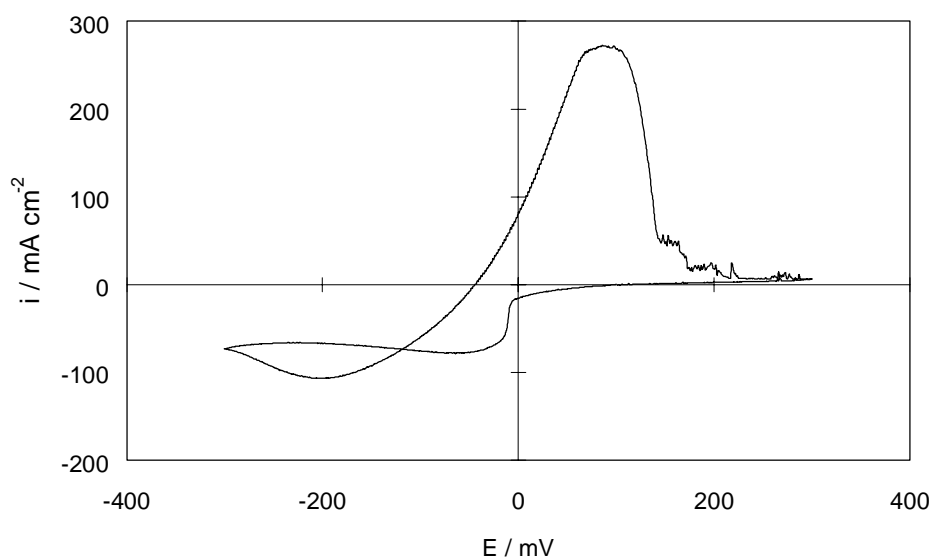


Figure 5.4 As Figure 5.3, but with sweep rate 20 mV s^{-1} .

It is observed in Figure 5.4 that the current density in the cathodic sweep increased just before the switching potential was reached. This could be due to underpotential deposition of aluminium, *i.e.* deposition at potentials less cathodic than the reversible potential. This is only possible if the activity of the product is less than unity. It may occur if the product dissolves in either the electrolyte or in the electrode, or if there is some interaction (adsorption or alloy formation) between the product and the electrode. There is no obvious reason why aluminium dissolution to the melt should vary with sweep rate. The most plausible explanation for the hysteresis in Figure 5.4 seems to be that aluminium dissolves in the iron deposit already covering the electrode. The extended sweep duration increases the amount of iron deposited, and the aluminium underpotential deposition is therefore more pronounced at low sweep rates. Another possible explanation for the increased current density after the potential has been reversed could be an increase in the real surface area.

In Figures 5.3 and 5.4, all the voltammograms show some sort of background current prior to the actual reduction peak. The cause of the cathodic current observed is believed to be underpotential deposition of iron, *i.e.* alloy formation between iron and copper. This is supported by the shoulder appearing immediately after the stripping peak when the potential is swept in the anodic direction. Since it was possible that the underpotential deposition of iron might influence the height of the deposition peak, a check was performed. Firstly, a cyclic voltammogram was recorded, and then enough iron was deposited on the copper electrode to make it an “iron” electrode. Secondly, a linear sweep was performed from the open circuit potential (~ 7 mV) in the cathodic direction. The voltammograms are shown in Figure 5.5.

From Figure 5.5 one sees that the height of the deposition peak obtained on a copper electrode coincides with the one obtained on the “iron” electrode. Based on this information no correction was made with respect to the background current observed prior to the actual deposition peak.

The Fe(II) reduction process was studied over a wide range of sweep rates. A representative selection of voltammograms was displayed in Figures 5.3 and 5.4 for one of the systems investigated (Na_3AlF_6 -3.0 wt% Al_2O_3 with 0.466 wt% Fe(II) at 1020 °C). A number of parameters can be extracted from such *i*-E curves, some of which are included in Table 5-1 for the experiment in question. All calculations throughout this chapter were performed with density data given by Solheim (2000).

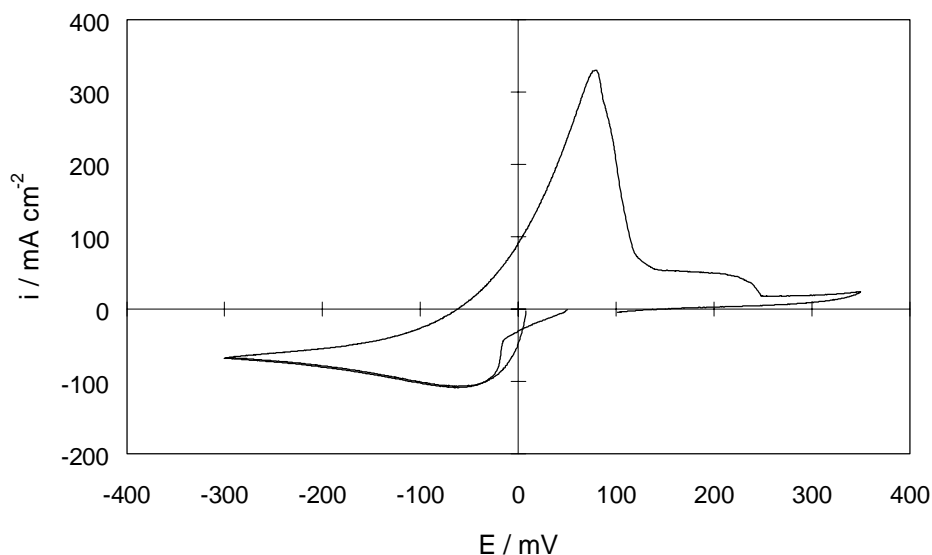


Figure 5.5 Voltammograms that show that alloy formation between iron and copper does not influence the cathodic peak current density.

Table 5-1 Cyclic voltammetric data for reduction of Fe(II) at a copper electrode in Na_3AlF_6 -3.0 wt% Al_2O_3 with 0.466 wt% Fe(II) at 1020 °C. ($c_{\text{Fe(II)}} = 172 \mu\text{mol cm}^{-3}$).

ν mV s^{-1}	i_p^C mA cm^{-2}	E_p^C mV	$E_p^C - E_{p/2}$ mV	n	E_p^A mV	E_{dep} mV	$E_{i=0}$ mV
20	-78.4	-64	-53	1.62	86	-44	-6
30	-99.4	-71	-60	1.43	83	-42	-7
50	-120.9	-54	-43	2.00	82	-49	-9
80	-149.6	-53	-41	2.09	82	-58	-9
100	-162.5	-50	-38	2.26	85	-67	-9
141	-191.2	-51	-38	2.26	89	-70	-10
200	-227.0	-57	-43	2.00	90	-73	-10
303	-277.2	-55	-41	2.09	90	-76	-10
400	-317.8	-56	-41	2.09	90	-76	-11
500	-356.1	-65	-49	1.75	88	-77	-12
1000	-497.1	-64	-47	1.83	91	-78	-13
2000	-700.2	-73	-53	1.62	96	-80	-17
5000	-1084.9	-86	-61	1.41	103	-81	-19

Figure 5.6 shows the sweep rate dependence of the cathodic peak current density. A linear relationship was found between i_p^C and $v^{1/2}$ for $v \leq 5000 \text{ mV s}^{-1}$, indicating a reversible mass transfer controlled reaction. The diffusion coefficient for the Fe(II) ion was calculated from the slope of the regression line and equation [2-9]. The result was $D_{\text{Fe(II)}} = 3.13 \times 10^{-5} \text{ cm}^2 \text{ s}^{-1}$. Another criterion for reversibility is that the straight line should pass through the origin. From Figure 5.6 it is seen that this is almost fulfilled, only a slight deviation is observed. According to equation [2-10], $E_p^C - E_{p/2}$ for a two electron process at 1020 °C is -43 mV . The data in Table 5-1 are in good agreement with this value for all but the two highest and the two lowest sweep rates. Average of all the n values is $n = 1.88 \pm 0.29$.

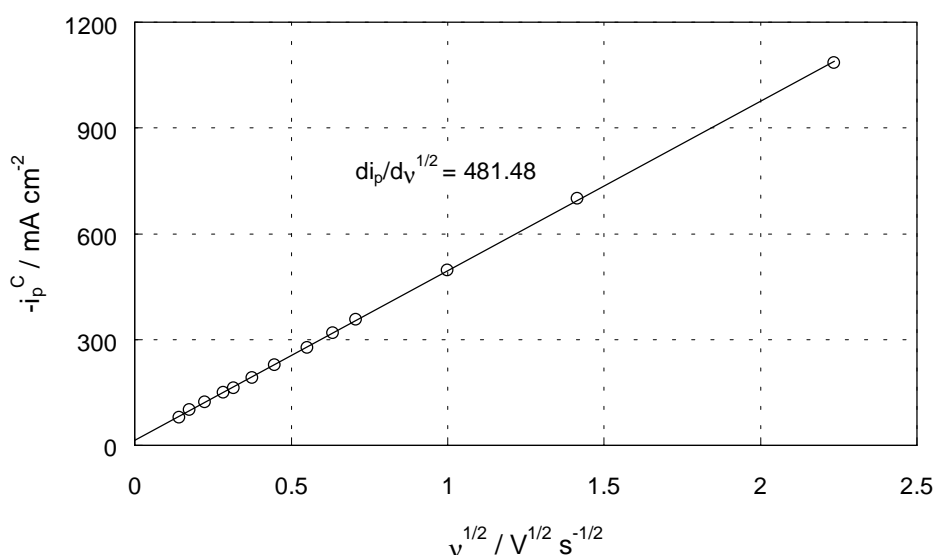


Figure 5.6 Plot of the cathodic peak current density versus the square root of sweep rate. The results were obtained in the system Na_3AlF_6 -3.0 wt% Al_2O_3 with 0.466 wt% Fe(II) at 1020 °C. ($c_{\text{Fe(II)}} = 172 \mu\text{mol cm}^{-3}$). The slope of the regression line is shown in the figure.

The major parameters for the various systems investigated in this study are given in Table 5-2. The average number of electrons involved in the reduction of Fe(II) and the diffusion coefficient (for $n = 2$) were found as described above.

There are several sources that may cause uncertainty in the calculated diffusion coefficients. Firstly, the concentration of Fe(II) in the melt was determined by analysis with ICP. The error associated with this technique is believed to be $\pm 5 \%$ or less. Secondly, when transforming the unit of the Fe(II) concentration from wt% to mol cm^{-3} density data by Solheim (2000) were used. These data (and all other available data)

apply for the systems investigated without any addition of FeF_2 . Although the concentrations are low, 0.308 - 0.750 wt% Fe(II), this approximation may lead to an error in the concentration of Fe(II) when the units are in mol cm^{-3} . Thirdly, the area of the copper electrode was found by measuring the length of the part of the wire immersed into the melt. The accuracy in this technique was ± 0.1 mm. Since the average immersion for all the experiments was around 8 mm, this could in the worst case lead to a deviation of around 2.5 % in the area when comparing two experiments.

Table 5-2 The diffusion coefficient of the Fe(II) ion determined by cyclic voltammetry in different cryolite-based electrolytes in the temperature range 965 - 1020 °C.

Electrolyte composition	T °C	Fe(II) wt%	$c_{\text{Fe(II)}}$ $\mu\text{mol cm}^{-3}$	$di_p/dv^{1/2}$ $\text{mA s}^{1/2} \text{ cm}^{-2} \text{ V}^{-1/2}$	\bar{n}	$10^5 \times D_{\text{Fe(II)}}$ $\text{cm}^2 \text{ s}^{-1}$
$\text{Na}_3\text{AlF}_6\text{-Al}_2\text{O}_3(\text{sat})$	1015	0.308	112	309.89	2.39	3.07
$\text{Na}_3\text{AlF}_6\text{-Al}_2\text{O}_3(\text{sat})$	1020	0.315	114	311.00	1.94	2.98
$\text{Na}_3\text{AlF}_6\text{-Al}_2\text{O}_3(\text{sat})$	1020	0.315	114	307.61	1.94	2.92
$\text{Na}_3\text{AlF}_6\text{-3.0 wt\% Al}_2\text{O}_3$	1020	0.466	172	481.48	1.88	3.13
$\text{Na}_3\text{AlF}_6\text{-3.0 wt\% Al}_2\text{O}_3\text{-}$ $10.9 \text{ wt\% AlF}_3\text{-5.0 wt\% CaF}_2$	965	0.750	280	857.77	1.88	3.60
$\text{Na}_3\text{AlF}_6\text{-2.9 wt\% Al}_2\text{O}_3\text{-}$ $11.0 \text{ wt\% AlF}_3\text{-5.1 wt\% CaF}_2$	970	0.670	250	714.27	1.73	3.15
$\text{Na}_3\text{AlF}_6\text{-3.0 wt\% Al}_2\text{O}_3\text{-}$ $11.0 \text{ wt\% AlF}_3\text{-5.0 wt\% CaF}_2$	970	0.475	177	543.66	1.89	3.64

Table 5-2 indicates that the diffusion coefficient varies somewhat with the melt composition. The trend seems to be $D_{\text{Fe(II)}}(\text{in } \text{Na}_3\text{AlF}_6\text{-Al}_2\text{O}_3(\text{sat})) < D_{\text{Fe(II)}}(\text{in } \text{Na}_3\text{AlF}_6\text{-3.0 wt\% Al}_2\text{O}_3) < D_{\text{Fe(II)}}(\text{in industrial melt})$. Several parameters could possibly cause this variation. The density of the melts differs, *i.e.* $\rho(\text{Na}_3\text{AlF}_6\text{-Al}_2\text{O}_3(\text{sat}) \text{ at } 1020 \text{ }^\circ\text{C}) = 2.022 \text{ g cm}^{-3}$, $\rho(\text{Na}_3\text{AlF}_6\text{-3.0 wt\% Al}_2\text{O}_3 \text{ at } 1020 \text{ }^\circ\text{C}) = 2.065 \text{ g cm}^{-3}$, and $\rho(\text{Na}_3\text{AlF}_6\text{-3.0 wt\% Al}_2\text{O}_3\text{-10.9 wt\% AlF}_3\text{-5.0 wt\% CaF}_2 \text{ at } 965 \text{ }^\circ\text{C}) = 2.088 \text{ g cm}^{-3}$. This means a density difference of approximately 3 % when the extreme values are compared, and it does not account for the difference in the diffusion coefficients.

According to Hertzberg *et al.* (1980) and Tørklep and Øye (1980), the viscosity of the melts increases with increasing concentrations of Al_2O_3 and/or CaF_2 , while it decreases with increasing concentration of AlF_3 . Estimates based on their data show that the viscosity decreases from $\sim 3 \text{ mPa s}$ for the melt composition $\text{Na}_3\text{AlF}_6\text{-Al}_2\text{O}_3(\text{sat})$ at 1020 °C to $\sim 2 \text{ mPa s}$ for the industrial melt at 965 - 970 °C. The Stokes-Einstein equation (Laidler and Meiser 1982) is given by,

$$D = \frac{k_B T}{6\pi r \eta} \quad [5-7]$$

where k_B is the Boltzmann constant, r the ionic radius, and η the viscosity of the melt. Without going into any details, the equation predicts that the diffusion coefficient is proportional to the inverse of the viscosity. It follows that the differences in the magnitude of the diffusion coefficients can be explained by the difference in viscosity. In fact, the Stokes-Einstein equation predicts an even larger variation than the one observed if it is assumed that the Fe(II) species has the same ionic radius in the different systems. According to Støre (1999) one cannot use the Stokes-Einstein equation to quantitatively predict the diffusion coefficient in molten salts systems. Investigation of Pb(II), Zn(II) and Mg(II) in molten KCl-LiCl eutectic gave consistently lower diffusion coefficients than predicted by the Stokes-Einstein equation. Deviations of up to 60 % were observed. This indicates that the Stokes-Einstein equation should be used with caution in molten salts, and only to predict trends.

A last subject that may influence the magnitude of the diffusion coefficient is the kind of species that are actually diffusing. In Chapter 3 it was suggested, based on solubility measurements of Fe(II) as a function of the molar cryolite ratio in alumina-saturated cryolite melts, that the Fe(II) species present in acidic melts were less complexed than those in basic melts. By assuming that a more complexed species has a larger radius, one would expect that the diffusion coefficient would decrease with increasing size of the species.

Based on the discussion regarding experimental errors, it is obvious that the results obtained should not be presented with more than two significant figures. The average number of electrons involved in the reduction of the Fe(II) ion in different cryolite-based melts was calculated disregarding temperature and melt composition. The result was $n = 2.0 \pm 0.2$. The average diffusion coefficient of the Fe(II) ion in the system $\text{Na}_3\text{AlF}_6\text{-Al}_2\text{O}_3(\text{sat})$ at temperatures between 1015 and 1020 °C was found to be $D_{\text{Fe(II)}} = 3.0 \times 10^{-5} \text{ cm}^2 \text{ s}^{-1}$. In the system $\text{Na}_3\text{AlF}_6\text{-3.0 wt\% Al}_2\text{O}_3$ at 1020 °C the result was $D_{\text{Fe(II)}} = 3.1 \times 10^{-5} \text{ cm}^2 \text{ s}^{-1}$, while it was $D_{\text{Fe(II)}} = 3.5 \times 10^{-5} \text{ cm}^2 \text{ s}^{-1}$ in industrial melts between 965 and 970 °C.

5.3.1.2 Chronoamperometry

The electrochemical reduction of Fe(II) on copper was investigated by chronoamperometry over a wide potential range. A typical potentiostatic current transient recorded in the system $\text{Na}_3\text{AlF}_6\text{-3.0 wt\% Al}_2\text{O}_3$ with 0.466 wt% Fe(II) at 1020 °C is displayed in Figure 5.7. The criterion for a truly diffusion controlled process at a given potential is that a plot of i versus $t^{-1/2}$ should be linear and pass through the origin. Such a plot for the potentiostatic current transient displayed in Figure 5.7 is shown in Figure 5.8.

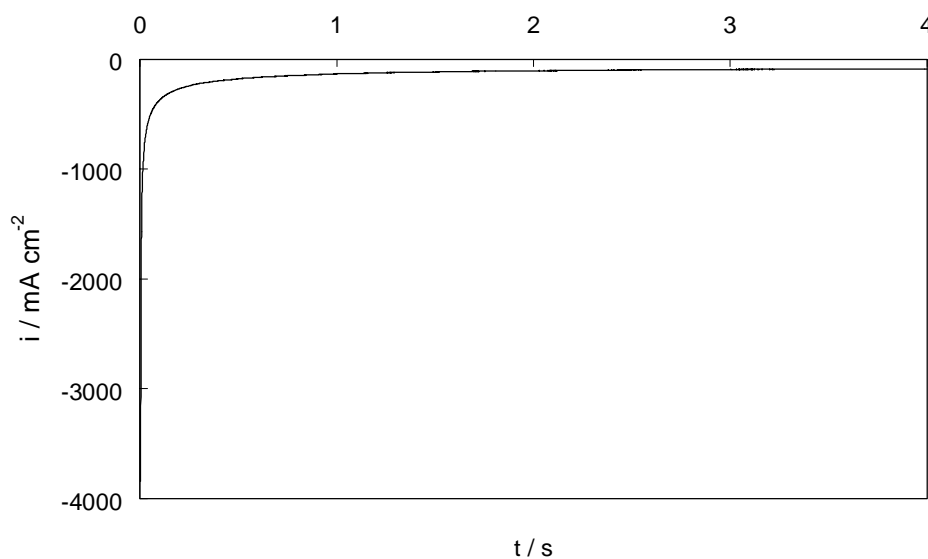


Figure 5.7 Potentiostatic current transient for the deposition of iron on copper in the system Na_3AlF_6 -3.0 wt% Al_2O_3 with 0.466 wt% Fe(II) at 1020 °C. Applied overpotential -200 mV.

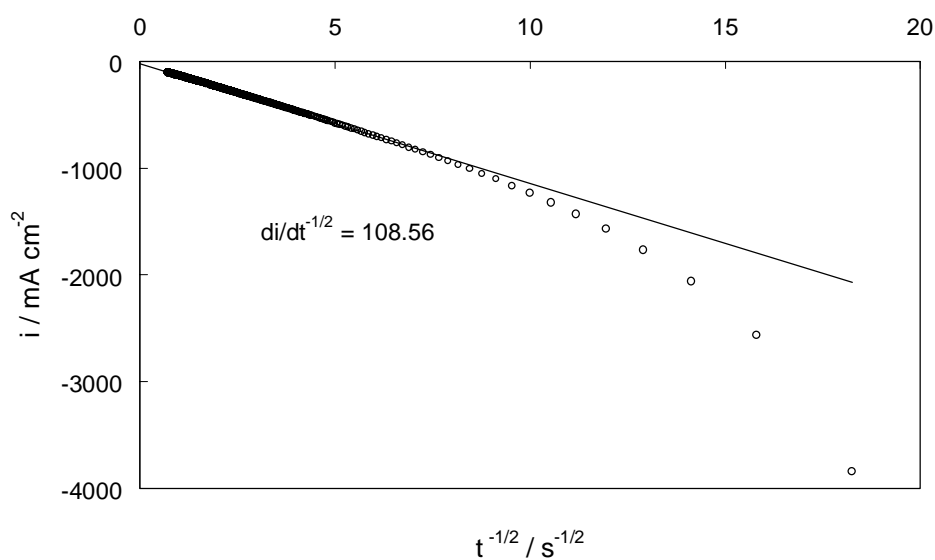


Figure 5.8 Current density versus the inverse square root of time for the potentiostatic current transient given in Figure 5.7.

Figure 5.8 shows that the recorded current density deviates from a straight line at times shorter than 20 ms. This deviation cannot be caused by charging of the double-layer capacitance, which would occur within a few μs , due to the time scale (in ms). A possible explanation is that alloy formation between iron and copper causes the observed deviation from ideality, as discussed in section 5.3.1.1. Regression analysis was performed on the current densities recorded at times longer than 20 ms. The resulting regression line goes straight through the recorded data, and passes practically through the origin. By combining the slope of the regression line with the Cottrell equation (equation [2-14]), the diffusion coefficient for the Fe(II) ion could be calculated. The diffusion coefficient of the Fe(II) ion in the system Na_3AlF_6 -3.0 wt% Al_2O_3 with 0.466 wt% Fe(II) at 1020 °C as a function of applied overpotential is given in Table 5-3.

Table 5-3 Diffusion coefficient as a function of applied overpotential for the deposition of iron on copper in the system Na_3AlF_6 -3.0 wt% Al_2O_3 with 0.466 wt% Fe(II) at 1020 °C as determined by chronoamperometry. ($c_{\text{Fe(II)}} = 172 \mu\text{mol cm}^{-3}$).

η mV	$di/dt^{-1/2}$ $\text{mA cm}^{-2} \text{s}^{-1/2}$	$10^5 \times D_{\text{Fe(II)}}$ $\text{cm}^2 \text{s}^{-1}$
-50	68.09	1.32
-100	93.55	2.50
-150	105.18	3.15
-200	108.56	3.36
-250	109.44	3.42
-300	111.96	3.57
-350	112.22	3.59
-400	112.77	3.63

The data in Table 5-3 suggest that the diffusion coefficient increases at more cathodic overpotentials. It is observed that the values obtained at the overpotentials -50 and -100 mV are very low compared to the other diffusion coefficients. This can be explained by a close look at the cyclic voltammetric data discussed earlier. Table 5-1 shows that the cathodic peak potentials were found between -50 and -86 mV. This implies that an overpotential of -50 mV does not ensure that the surface concentration of Fe(II) reaches zero. The diffusion coefficient of Fe(II) in the system Na_3AlF_6 -3.0 wt% Al_2O_3 with 0.466 wt% Fe(II) at 1020 °C was calculated by taking the average of the values obtained at overpotentials from -150 to -400 mV. The result was $D_{\text{Fe(II)}} = (3.45 \pm 0.18) \times 10^{-5} \text{ cm}^2 \text{s}^{-1}$.

The diffusion coefficient for the Fe(II) ion determined by chronoamperometry in different cryolite-based electrolytes is given in Table 5-4.

Table 5-4 The diffusion coefficient of the Fe(II) ion determined by chronoamperometry in different cryolite-based electrolytes in the temperature range 965 - 1020 °C. The average diffusion coefficient is given in the last column.

Electrolyte composition	T °C	Fe(II) wt%	$c_{\text{Fe(II)}}$ $\mu\text{mol cm}^{-3}$	$10^5 \times D_{\text{Fe(II)}}$ $\text{cm}^2 \text{s}^{-1}$	$10^5 \times \bar{D}_{\text{Fe(II)}}$ $\text{cm}^2 \text{s}^{-1}$
$\text{Na}_3\text{AlF}_6\text{-Al}_2\text{O}_3(\text{sat})$	1015	0.308	112	3.12	3.1
$\text{Na}_3\text{AlF}_6\text{-Al}_2\text{O}_3(\text{sat})$	1020	0.315	114	3.14	
$\text{Na}_3\text{AlF}_6\text{-3.0 wt\% Al}_2\text{O}_3$	1020	0.466	172	3.45	3.5
$\text{Na}_3\text{AlF}_6\text{-3.0 wt\% Al}_2\text{O}_3\text{-}$ $10.9 \text{ wt\% AlF}_3\text{-5.0 wt\% CaF}_2$	965	0.750	280	4.18	4.2
$\text{Na}_3\text{AlF}_6\text{-2.9 wt\% Al}_2\text{O}_3\text{-}$ $11.0 \text{ wt\% AlF}_3\text{-5.1 wt\% CaF}_2$	970	0.670	250	4.12	

The discussion concerning uncertainty in the cyclic voltammetric data also applies for the chronoamperometric results. The data in Table 5-4 confirm the relationship between system and diffusion coefficient found by cyclic voltammetry. The variation of the calculated diffusion coefficient is even more pronounced in the chronoamperometric data. It is noted that the values are somewhat higher than the voltammetric results. Since both cyclic voltammetry and chronoamperometry were performed in the same melts and with the same electrodes, the increased values of the diffusion coefficients can probably be related to the techniques. The average diffusion coefficients were calculated in a similar way as for the voltammetric results. The results are given in Table 5-4.

5.3.1.3 Chronopotentiometry

Chronopotentiometry was employed in a further study of the Fe(II) reduction process. The potential was monitored as a function of time while applying a constant current. Figure 5.9 contains a series of such chronopotentiograms. The potential is initially determined by the Fe(II)/Fe couple. It moves gradually to more negative values as the surface concentration of Fe(II) ions decreases. Once the surface concentration becomes zero there is a sudden potential drop to a level where decomposition of the solvent occurs. This reaction is probably reduction of aluminium ions, since the Al(III)/Al couple has a more positive standard potential than the Na(I)/Na couple (and the Ca(II)/Ca couple) in these melts (Grjotheim *et al.* 1982).

The transition between these two potential plateaus, *i.e.* the plateau for reduction of Fe(II) and the plateau for reduction of Al(III), is clearly not instantaneous, as discussed in section 3.3.1. The transition time was determined, as suggested in section 3.3.1, by plotting E versus $\ln[1 - (t/\tau)^{1/2}]$. This is illustrated in Figure 5.10.

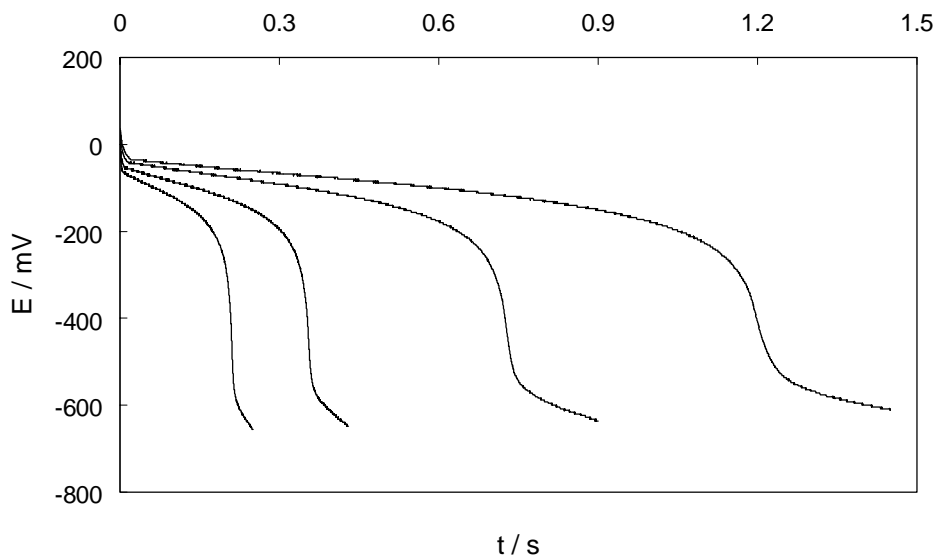


Figure 5.9 Chronopotentiograms for the reduction of Fe(II) at a copper electrode in the system Na_3AlF_6 -3.0 wt% Al_2O_3 with 0.466 wt% Fe(II) at 1020 °C. Applied current densities: 192, 239, 335 and 431 mA cm^{-2} .

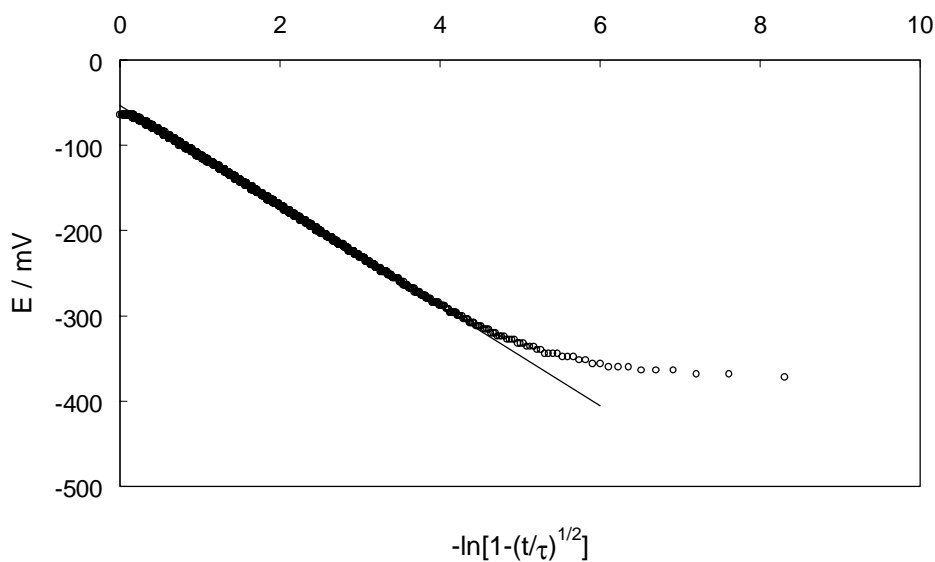


Figure 5.10 Determination of the transition time by best linear fit of the experimental points in the interval $[\tau/4, 3\tau/4]$. n is calculated from the slope of the regression line. Applied current density: 431 mA cm^{-2} .

The linear dependence of E on $\ln[1 - (t/\tau)^{1/2}]$ in the interval $0.10\tau < t < 0.90\tau$ verifies that the process is mass transfer controlled and reversible with an insoluble product. The number of electrons involved in the reduction process is readily calculated from the slope of the regression line in Figure 5.10, as differentiation of equation [2-20] yields the relationship:

$$n = \frac{RT}{F} \frac{1}{dE/d\ln[1 - (t/\tau)^{1/2}]} \quad [5-8]$$

The deviation at long times in Figure 5.10 is probably caused by underpotential deposition of aluminium.

The diffusion coefficient can be calculated by determining the product $i\tau^{1/2}$, which should be independent of the applied current for a diffusion controlled process, and combine with the Sand equation (equation [2-17]). Table 5-5 summarises the results from the chronopotentiometric study of Fe(II) reduction in the system Na_3AlF_6 -3.0 wt% Al_2O_3 with 0.466 wt% Fe(II) at 1020 °C.

Table 5-5 Chronopotentiometric data for the reduction of Fe(II) at a copper electrode in the system Na_3AlF_6 -3.0 wt% Al_2O_3 with 0.466 wt% Fe(II) at 1020 °C. ($c_{\text{Fe(II)}} = 172 \mu\text{mol cm}^{-3}$).

$-i$ mA cm^{-2}	τ s	$-i\tau^{1/2}$ $\text{mA cm}^{-2} \text{s}^{1/2}$	$dE/d\ln[1 - (t/\tau)^{1/2}]$ mV	n	$10^5 \times D_{\text{Fe(II)}}$ $\text{cm}^2 \text{s}^{-1}$
120	4.43	252	82.9	1.34	7.35
144	2.46	226	71.0	1.57	5.88
168	1.609	213	64.8	1.72	5.23
192	1.174	208	63.0	1.77	4.98
216	0.892	204	61.4	1.81	4.79
239	0.704	201	60.3	1.85	4.66
287	0.474	198	59.3	1.88	4.52
335	0.343	196	59.0	1.89	4.45
383	0.257	194	58.5	1.90	4.36
431	0.203	194	58.7	1.90	4.34
479	0.1623	193	58.2	1.92	4.30
567	0.1129	191	58.8	1.89	4.20
680	0.0778	190	58.7	1.90	4.16
907	0.0432	188	59.4	1.87	4.10
1133	0.0272	187	61.4	1.82	4.03

Although $i\tau^{1/2}$ tends to approach a limit at high currents, it is evident from Figure 5.11 that the Sand equation is not being obeyed at low current densities. A good explanation for this apparent departure from diffusion controlled behaviour in this current range has not been found. However, the alloy formation between iron and copper could have a greater impact on the product $i\tau^{1/2}$ at low current densities than at higher ones. As a simplification, the number of electrons involved and the diffusion coefficient were calculated by taking the average of the values obtained at current densities from 192 to 1133 mA cm^{-2} . The results were $n = 1.87 \pm 0.05$ and $D_{\text{Fe(II)}} = (4.41 \pm 0.29) \times 10^{-5} \text{ cm}^2 \text{ s}^{-1}$.

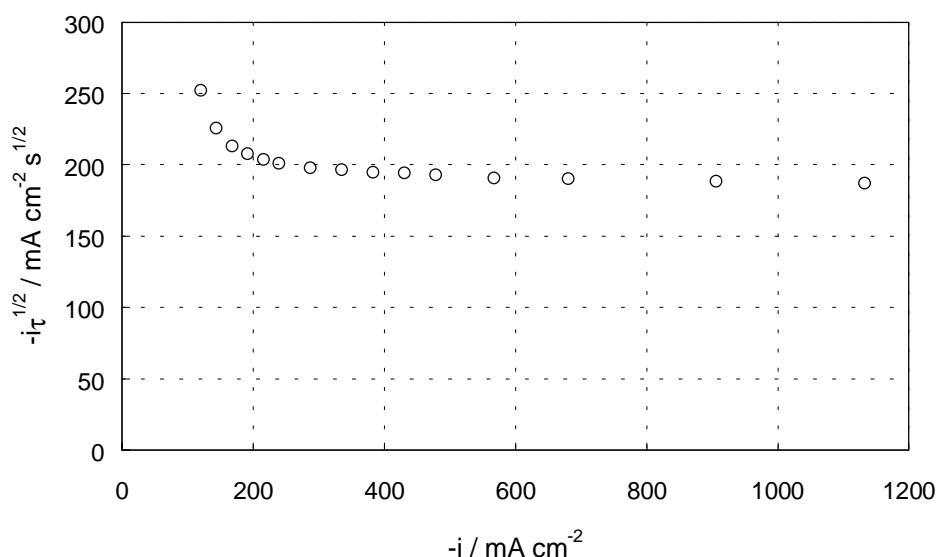


Figure 5.11 Plot of $i\tau^{1/2}$ versus the applied current density for the reduction of Fe(II) at a copper electrode in the system Na_3AlF_6 -3.0 wt% Al_2O_3 with 0.466 wt% Fe(II) at 1020 °C.

Chronopotentiometric data for all the investigated systems are given in Table 5-6.

The discussion concerning uncertainty in the cyclic voltammetric data also applies for the chronopotentiometric results. The data in Table 5-6 confirm the relationship between system and diffusion coefficient found by both cyclic voltammetry and chronoamperometry. The variation in the diffusion coefficients is not as pronounced as for the chronoamperometric data. It is noted that the values are even higher than the chronoamperometric results.

Table 5-6 The diffusion coefficient of the Fe(II) ion determined by chronopotentiometry in different cryolite-based electrolytes in the temperature range 965 - 1020 °C. The average diffusion coefficient is given in the last column.

Electrolyte composition	T °C	Fe(II) wt%	c _{Fe(II)} μmol cm ⁻³	\bar{n}	10 ⁵ × D _{Fe(II)} cm ² s ⁻¹	10 ⁵ × $\bar{D}_{Fe(II)}$ cm ² s ⁻¹
Na ₃ AlF ₆ -Al ₂ O ₃ (sat)	1015	0.308	112	1.70	3.72	4.1
Na ₃ AlF ₆ -Al ₂ O ₃ (sat)	1020	0.315	114	1.89	4.48	
Na ₃ AlF ₆ -3.0 wt% Al ₂ O ₃	1020	0.466	172	1.87	4.41	4.4
Na ₃ AlF ₆ -2.9 wt% Al ₂ O ₃ - 11.0 wt% AlF ₃ -5.1 wt% CaF ₂	970	0.670	250	1.79	4.54	4.5

5.3.1.4 The Diffusion Coefficient

From the discussion above it can be concluded that the reduction of Fe(II) ions in cryolite-based melts is a diffusion controlled two-electron process forming an insoluble deposit. The reaction was also proved to be reversible. However, the results show that the magnitude of the diffusion coefficient varies considerably with the technique used. In Table 5-7 the diffusion coefficients obtained are listed for the electrochemical techniques applied.

Table 5-7 Diffusion coefficients of the Fe(II) ion in different solvents as a function of the electrochemical technique applied.

Electrochemical technique:		CV	CA	CP
Solvent	T °C	10 ⁵ × $\bar{D}_{Fe(II)}$ cm ² s ⁻¹	10 ⁵ × $\bar{D}_{Fe(II)}$ cm ² s ⁻¹	10 ⁵ × $\bar{D}_{Fe(II)}$ cm ² s ⁻¹
Na ₃ AlF ₆ -Al ₂ O ₃ (sat)	1015-1020	3.0	3.1	4.1
Na ₃ AlF ₆ -3.0 wt% Al ₂ O ₃	1020	3.1	3.5	4.4
Na ₃ AlF ₆ -3 wt% Al ₂ O ₃ - 11 wt% AlF ₃ -5 wt% CaF ₂	965-970	3.5	4.2	4.5

Table 5-7 shows that the magnitude of the diffusion coefficient increases in the order CV < CA < CP. The question arises: Which of the techniques is the more reliable? The chronopotentiometric data showed that the product $i\tau^{1/2}$ decreased slightly with the applied current density, and they seemed to approach a steady value. However, a reason for this behaviour has not been found. An average diffusion coefficient, therefore, had to be given. A comparison of the results with those obtained in

Chapter 3 (Table 3-1) shows that the latter are substantially lower, and more in agreement with the results obtained with cyclic voltammetry. The only difference between the two chronopotentiometric experiments was the diameter of the copper electrode, *i.e.* 0.5 mm in Chapter 3 compared to 1.5 mm in this chapter.

The chronoamperometric data showed the same tendency as the chronopotentiometric data, the diffusion coefficient increased with applied overpotential. As for the chronopotentiometric data an average diffusion coefficient had to be calculated. The cyclic voltammetric data, however, showed good consistency between peak current and the square root of the sweep rate. It is therefore believed that the diffusion coefficients obtained by cyclic voltammetry are the more reliable.

As already mentioned, Støre (1999) investigated the electrochemical behaviour of Pb(II), Zn(II) and Mg(II) in KCl-LiCl eutectic with cyclic voltammetry, chronoamperometry and chronopotentiometry. It was concluded that voltammetry gave the more reliable value for the diffusion coefficient. In the case of Zn(II), chronopotentiometry gave a diffusion coefficient twice the value obtained from the voltammetric results.

The diffusion coefficients obtained with cyclic voltammetry in the present work are compared with literature data in Table 5-8.

Table 5-8 Diffusion coefficients for the Fe(II) ion in different solvents.

Authors	Solvent	T °C	$10^5 \times D_{\text{Fe(II)}}$ $\text{cm}^2 \text{s}^{-1}$
This work (CV)	$\text{Na}_3\text{AlF}_6\text{-Al}_2\text{O}_3(\text{sat})$	1015-1020	3.0
This work (CV)	$\text{Na}_3\text{AlF}_6\text{-3.0 wt\% Al}_2\text{O}_3$	1020	3.1
This work (CV)	$\text{Na}_3\text{AlF}_6\text{-3 wt\% Al}_2\text{O}_3\text{-}$ $11 \text{ wt\% AlF}_3\text{-5 wt\% CaF}_2$	965-970	3.5
Chrysoulakis <i>et al.</i> (1978)	$\text{NaF-AlF}_3\text{-BaCl}_2$	750	2.8
Inman <i>et al.</i> (1978)	LiCl-KCl	500	2.2
Hugdahl (1981)	$\text{Na}_3\text{AlF}_6\text{-Al}_2\text{O}_3(\text{sat})$	1000	3.4
Stangeland (1981)	$\text{Na}_3\text{AlF}_6\text{-Al}_2\text{O}_3(\text{sat})$	1000	7.4

Table 5-8 shows that the diffusion coefficients obtained in the present work agree fairly well with the result of Hugdahl (1981). The diffusion coefficient should increase with increasing temperature. With this in mind, the results of both Chrysoulakis *et al.* (1978) and Inman *et al.* (1978) are consistent with the present results. The value of Stangeland (1981) seems rather high compared to the other literature data.

5.3.2 Oxidation of Fe(II)

The oxidation of Fe(II) in cryolite-alumina melts was investigated with cyclic voltammetry. The alumina concentration was either ~3 wt%, or the melt was saturated. The experimental temperature ranged from 970 to 1020 °C. Two different materials were used as working electrodes, either platinum or gold. All potentials are referred to the Fe reference electrode and are therefore equivalent to overpotentials.

5.3.2.1 The Platinum Electrode

A typical cyclic voltammogram obtained with a platinum electrode is shown in Figure 5.12. The potential was swept in the anodic direction from 450 mV. The switching potentials were 1250 and -1100 mV.

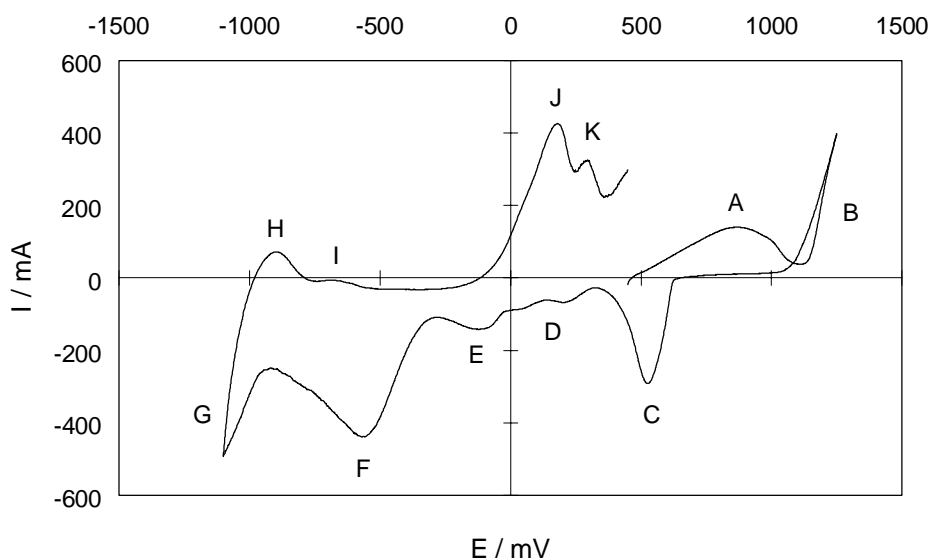


Figure 5.12 Cyclic voltammogram obtained with a platinum electrode in the system $\text{Na}_3\text{AlF}_6\text{-Al}_2\text{O}_3(\text{sat})$ with 0.305 wt% Fe(II) when the potential was swept in the anodic direction from 450 mV. $T = 1020^\circ\text{C}$, and sweep rate 50 mV s^{-1} . See text.

Figure 5.12 shows that several reactions take place when such a wide potential window is investigated. The interpretation of the peaks is as follows: (A) oxidation of Fe(II) to Fe(III); (B) oxygen evolution; (C) reduction of Fe(III) to Fe(II); (D) two small peaks, underpotential deposition of iron, *i.e.* alloying between iron and platinum; (E) reduction of Fe(II) to iron metal; (F) underpotential deposition of aluminium, *i.e.* alloying between aluminium and iron formed on the electrode; (G) reduction of Al(III)

to aluminium metal; (H) stripping of aluminium metal to Al(III); (I) small peak, oxidation of aluminium alloyed with iron to Al(III); (J) stripping of iron metal to Fe(II); and (K) oxidation of iron alloyed with platinum to Fe(II). The number of peaks does not come as a surprise since platinum and iron easily form alloys (Metals Handbook 1973). Therefore, in order to study the oxidation of Fe(II), the cathodic switching potential should be kept as positive as possible to prevent the platinum electrode from being damaged due to alloying with iron. Based on this observation, the potential of the working electrode was never allowed to become less than 350 mV. If needed, a potential of 600 to 700 mV was applied between the runs to avoid alloying.

A cyclic voltammogram with a cathodic switching potential of 350 mV is shown in Figure 5.13. The potential was swept in the anodic direction from 400 mV. Three successive voltammograms were recorded without interruption, *i.e.* the solution was not allowed to equilibrate.

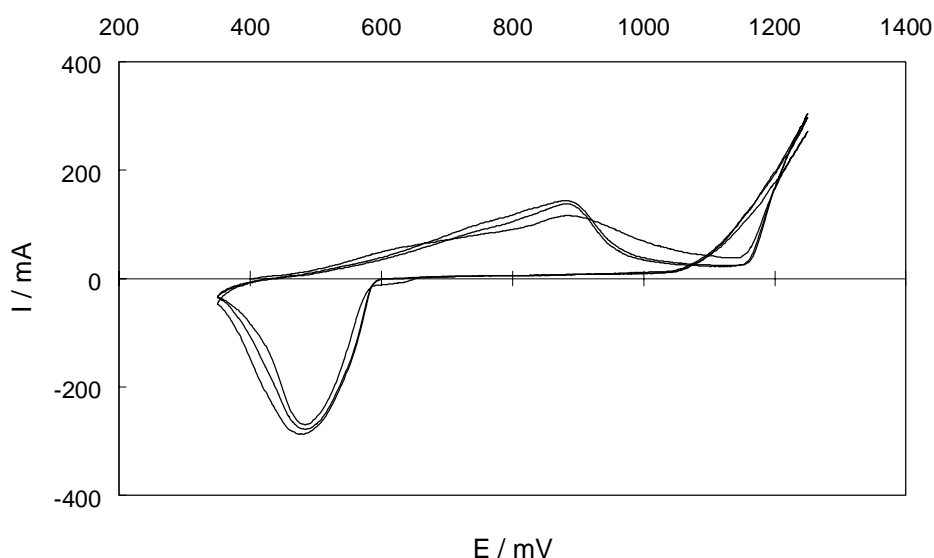


Figure 5.13 Three successive cyclic voltammograms without interruption obtained with a platinum electrode when the potential was swept in the anodic direction from 400 mV. $\text{Na}_3\text{AlF}_6\text{-Al}_2\text{O}_3(\text{sat})$ with 0.248 wt% Fe(II), $T = 970^\circ\text{C}$, and sweep rate 50 mV s^{-1} .

Figure 5.13 shows that both the anodic and the cathodic peak currents increase with increasing time. This could be caused by the oxygen evolution. The solubility measurements in Chapter 3 showed that the solubility of Fe(III) was much less than the solubility of Fe(II) under the same conditions. It is therefore possible that solid Fe_2O_3 forms at the electrode surface above a certain potential by exceeding the solubility

limit of Fe(III). This Fe_2O_3 will then be reduced to Fe(II), together with Fe(III) in solution in the vicinity of the electrode, and cause an increase in the peak current when the sweep is reversed. To optimise the procedure, oxygen evolution should be avoided. The anodic switching potential was therefore set to be 1000 mV.

Typical cyclic voltammograms, within a potential window that avoids underpotential deposition of iron and oxygen evolution, are shown in Figure 5.14. The potential was swept in the anodic direction from 450 mV. Three successive voltammograms were recorded without interruption.

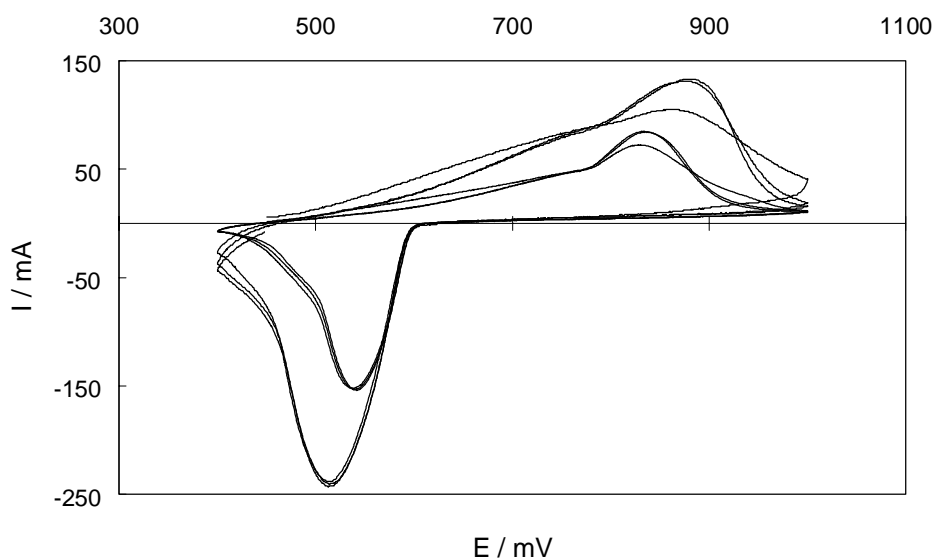


Figure 5.14 Three successive cyclic voltammograms without interruption obtained with a platinum electrode when the potential was swept in the anodic direction from 450 mV. $\text{Na}_3\text{AlF}_6\text{-Al}_2\text{O}_3(\text{sat})$ with 0.248 wt% Fe(II), $T = 970^\circ\text{C}$, and sweep rates 20 and 50 mV s^{-1} .

Figure 5.14 shows that the peak separation increases with increasing sweep rate. This could suggest that the system is irreversible or perhaps quasi-reversible (Greef *et al.* 1990). In the case of a reversible system like the reduction of Fe(II), the charge transfer rates at all potentials are significantly greater than the rate of mass transport, and hence Nernstian equilibrium is always maintained at the electrode surface. When the rate of electron transfer is insufficient to maintain this surface equilibrium, the shape of the voltammogram changes. At low potential sweep rates the rate of electron transfer is greater than that of mass transfer, and a reversible cyclic voltammogram is recorded. As the sweep rate is increased, however, the rate of mass transport increases and becomes comparable to the rate of electron transfer. The most noticeable effect of this

is an increase in the peak separation. If the system were totally irreversible, the reverse peak would be absent. Figure 5.14 shows that this is not the case, and the system is therefore likely to be reversible or quasi-reversible.

Diagnostic tests for a reversible electron transfer with soluble product were given in Chapter 2. One of the tests was that the peak separation, $\Delta E_p = E_p^A - E_p^C$, should be equal to $\ln 10RT/nF$. If the system is, on the other hand, quasi-reversible, then ΔE_p would be greater than $\ln 10RT/nF$ and increase with increasing sweep rate. The voltammetric data obtained at a platinum electrode are given in Table 5-9.

Table 5-9 Cyclic voltammetric data for the oxidation of Fe(II) at a platinum electrode in different cryolite melts. All potentials are given with respect to the Fe(II)/Fe reference electrode.

System	T	ν	E_p^A	E_p^C	ΔE_p	n	$E_{Fe^{3+}/Fe^{2+}}^{rev}$	$E_{O_2/O^{2-}}^{rev}$
	°C	mV s ⁻¹	mV	mV	mV		mV	mV
0.258 wt% Fe(II)- 3.0 wt% Al ₂ O ₃	1000	20	814	626	188	1.34	720	1120
		50	842	618	224	1.13	730	
		100	866	618	248	1.02	742	
		200	874	610	264	0.96	742	
Average						1.11	734	
0.420 wt% Fe(II)- 3.2 wt% Al ₂ O ₃	1000	20	933	633	300	0.84	783	1120
		50	931	611	320	0.79	771	
		100	945	579	366	0.69	762	
						0.77	772	
Average						0.77	772	
0.248 wt% Fe(II)- Al ₂ O ₃ (sat)	970	20	828	542	286	0.86	685	1080
		50	856	517	339	0.73	687	
						0.79	686	
						0.79	686	
0.305 wt% Fe(II)- Al ₂ O ₃ (sat)	1020	20	864	568	296	0.87	716	1070
		50	916	541	375	0.68	729	
		100	886	502	384	0.67	694	
						0.74	713	
Average						0.74	713	

Table 5-9 suggests that the systems studied are quasi-reversible since the peak separation increases with increasing sweep rate. However, it should be clear from the data that the redox couple in question is Fe(III)/Fe(II) (see equation [5-2]), since n is close to unity. It was not possible to utilise the peak currents that could be read off the voltammograms. This was related to the lifetime of the electrode, which turned out to be relatively short. Even with the effort of keeping the electrode potential where it should not alloy with iron (>350 mV), it seemed as if the platinum electrode started to pick up iron once it was immersed into the melt. The consequence was that the quality of the recorded voltammograms started to deteriorate within half an hour or so. This

resulted in unreliable data for several sweep rates. The voltammograms at higher sweep rates were more drawn out, and it was difficult to obtain good and reproducible recordings. This could also be due to irreversibility at higher sweep rates.

The reversible potential for the redox couple Fe(III)/Fe(II) relative to the Fe(II)/Fe reference electrode was determined from the mean value of the anodic and the cathodic peak potentials. The results are given in Table 5-9. It should be noted that the data obtained in the alumina-saturated melts are standard potentials, since these melts were saturated with respect to Fe(II), *i.e.* $a_{\text{Fe(II)}} = 1$ (see section 3.3.2.1).

Even though the peak separation increased with increasing sweep rate, the reversible potential does not seem to be much influenced. To give the reversible potential for the Fe(III)/Fe(II) redox couple relative to the reversible potential for oxygen evolution, the latter had to be determined. Inspection of Figure 5.13 shows that the oxygen evolution started at ~1170 mV when the potential was swept in the anodic direction. When the potential was reversed, however, the recorded current did not cross-over before ~1080 mV. It is believed that this difference indicates that an activation overpotential is needed for the oxygen evolution to take place and that the crossing point gives the reversible potential. The values for the reversible potential of oxygen evolution, given in Table 5-9, were found by taking the average of two or three voltammograms as the one given in Figure 5.13.

Thonstad (1968) investigated the anodic overvoltage on platinum in cryolite-alumina melts. The equilibrium potential of the cell $\text{Al}_{\text{liq}}|\text{Na}_3\text{AlF}_6\text{-Al}_2\text{O}_{3(\text{sat})}|\text{Pt}, \text{O}_2$ was determined from potential-decay curves to be 2.205 V at 1000 °C. A Tafel plot of the anodic overvoltage showed two straight lines with slopes $RT/3F$ and RT/F , indicating a two-step discharge reaction of oxygen. This supports the idea that an activation overpotential is needed for the oxygen evolution to take place.

Sterten *et al.* (1976) studied the behaviour of oxygen and aluminium electrodes by means of EMF measurements in Na_3AlF_6 melts saturated with $\alpha\text{-Al}_2\text{O}_3$ in the temperature range 960 - 1037 °C. The average value of the EMF at 1000 °C for the cell $\text{Al}_{\text{liq}}|\text{Na}_3\text{AlF}_6\text{-Al}_2\text{O}_{3(\text{sat})}|\text{Na}_3\text{AlF}_6\text{-Al}_2\text{O}_{3(\text{sat})}|\text{O}_2(\text{Pt})$ was found to be (2.183 ± 0.003) V. The corresponding value derived from thermodynamic tables was 2.195 V. The results indicated that the electrodes were reversible when they were separated by an $\alpha\text{-Al}_2\text{O}_3$ diaphragm. Both $(\text{Pt})\text{O}_2$ and $(\text{Au})\text{O}_2$ electrodes enclosed in alpha alumina tubes seem to be reversible and reliable electrodes in $\text{Na}_3\text{AlF}_6\text{-Al}_2\text{O}_3$ melts.

5.3.2.2 The Gold Electrode

A typical cyclic voltammogram obtained with a gold electrode is shown in Figure 5.15. The potential was swept in the anodic direction from 450 mV. The switching potentials were 1250 and -1100 mV.

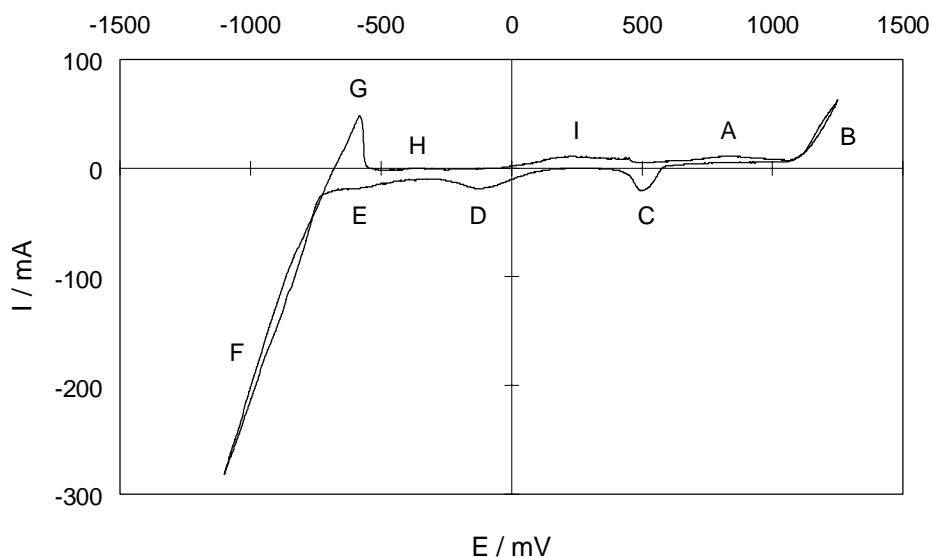


Figure 5.15 Cyclic voltammogram obtained with a gold electrode in the system $\text{Na}_3\text{AlF}_6\text{-Al}_2\text{O}_3(\text{sat})$ with 0.248 wt% Fe(II) when the potential was swept in the anodic direction from 450 mV. $T = 970^\circ\text{C}$, at sweep rate 20 mV s^{-1} .

Figure 5.15 shows that several reactions take place when such a broad potential range is investigated. The interpretation of the peaks is as follows: (A) oxidation of Fe(II) to Fe(III); (B) oxygen evolution; (C) reduction of Fe(III) to Fe(II); (D) reduction of Fe(II) to iron metal; (E) underpotential deposition of aluminium, *i.e.* alloying between aluminium and iron formed on the electrode; (F) reduction of Al(III) to aluminium metal; (G) stripping of aluminium metal to Al(III); (H) small peak, oxidation of aluminium alloyed with iron to Al(III); and (I) stripping of iron metal to Fe(II). It is observed that the voltammogram contains fewer peaks than that recorded at a platinum electrode. This is consistent with the phase diagrams Au-Fe and Pt-Fe, which show that in the latter system more phases are formed at around 1000°C compared to gold and iron (Metals Handbook 1973).

A cyclic voltammogram with a cathodic switching potential of 350 mV is shown in Figure 5.16. The potential was swept in the anodic direction from 400 mV. Three successive voltammograms were recorded without interruption, *i.e.* the solution was not allowed to equilibrate. Figure 5.16 shows that both the anodic and the cathodic peak currents increased with time. It is also observed that the cathodic peak potential shifted to less positive potentials with time. This is probably caused by the oxygen evolution, as discussed above. To optimise the recorded voltammograms, oxygen evolution should be avoided. The anodic switching potential was, therefore, set to 1000 mV.

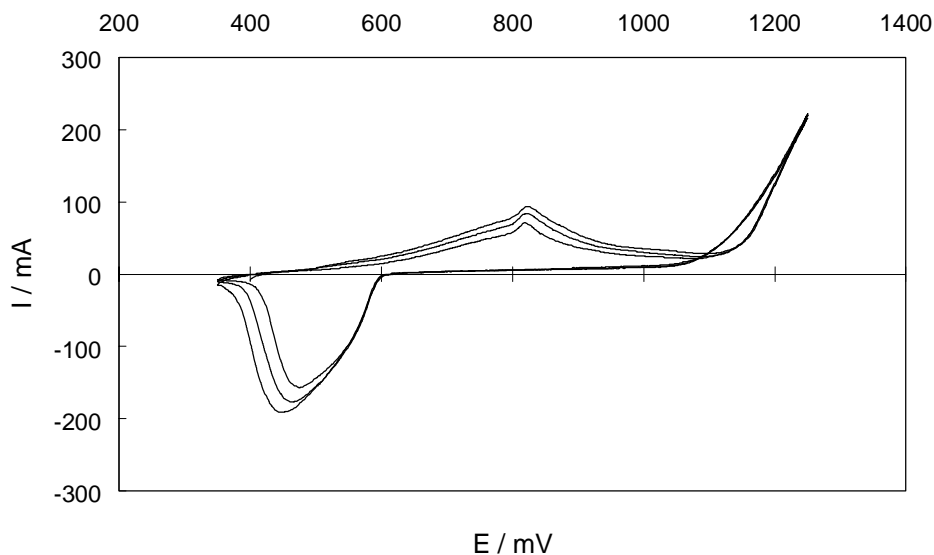


Figure 5.16 Three successive cyclic voltammograms without interruption obtained with a gold electrode when the potential was swept in the anodic direction from 400 mV. $\text{Na}_3\text{AlF}_6\text{-Al}_2\text{O}_3(\text{sat})$ with 0.248 wt% Fe(II), $T = 970^\circ\text{C}$, at sweep rate 20 mV s^{-1} .

A typical cyclic voltammogram recorded with switching potentials 350 and 1000 mV is shown in Figure 5.17. The potential was swept in the anodic direction from 450 mV. Three successive voltammograms were recorded without interruption. Figure 5.17 shows that the cathodic peak potential did not shift with time, as was the case when the voltammograms comprised oxygen evolution (see Figure 5.16). It is observed that the use of gold as electrode material instead of platinum resulted in sharper oxidation and reduction peaks. However, the peaks do not overlap to the same degree as for the peaks with a platinum electrode, *i.e.* the peak currents increase more with time. The voltammetric data obtained with a gold electrode are given in Table 5-10. The different parameters were determined with the same arguments as for those obtained at a platinum electrode.

Table 5-10 shows data similar to those obtained for a platinum electrode, and consequently the discussion and the conclusions remain the same. It should be noted, although the lifetime was approximately the same, that the damage to the gold electrode was more severe than that of the platinum. It was observed that part of the gold electrode disappeared/dissolved. This could be caused by the oxygen evolution, which was necessary to study at the end of an experiment in order to determine its reversible potential. The low melting point of gold (1064°C) could also be a factor influencing the deterioration, and consequently the experimental temperature was kept as low as possible.

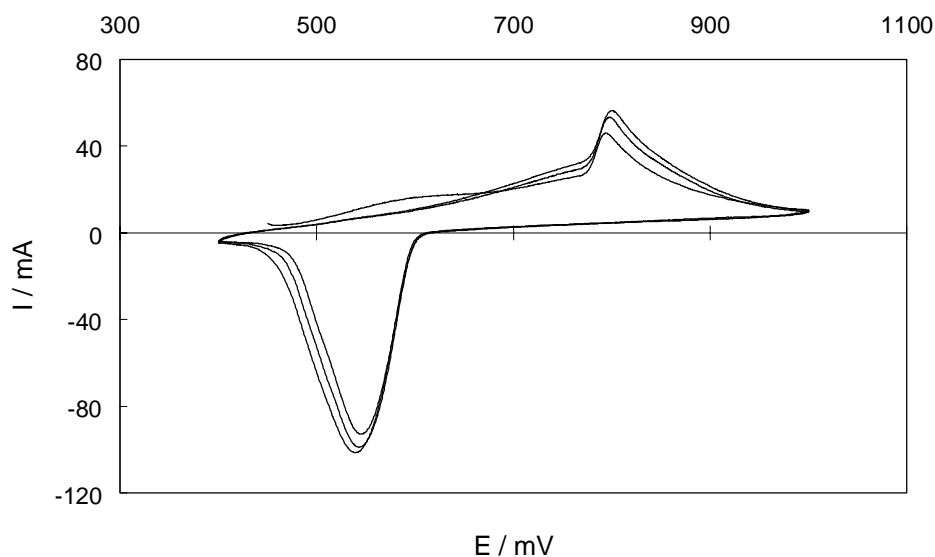


Figure 5.17 Three successive cyclic voltammograms recorded without interruption with a gold electrode when the potential was swept in the anodic direction from 450 mV. $\text{Na}_3\text{AlF}_6\text{-Al}_2\text{O}_3(\text{sat})$ with 0.248 wt% Fe(II), $T = 970^\circ\text{C}$, and sweep rate 20 mV s^{-1} .

Table 5-10 Cyclic voltammetric data for the oxidation of Fe(II) at a gold electrode in different cryolite melts. All potentials are given with respect to the Fe(II)/Fe reference electrode.

System	T °C	v mV s^{-1}	E_p^A mV	E_p^C mV	ΔE_p mV	n	$E_{\text{Fe}^{3+}/\text{Fe}^{2+}}^{\text{rev}}$ mV	$E_{\text{O}_2/\text{O}^{2-}}^{\text{rev}}$ mV
0.420 wt% Fe(II)- 3.2 wt% Al_2O_3	1000	20	945	627	318	0.79	786	1110
		50	927	581	346	0.73	754	
		100	948	534	414	0.61	741	
		200	968	534	434	0.58	751	
		Average				0.68	758	
0.248 wt% Fe(II)- $\text{Al}_2\text{O}_3(\text{sat})$	970	20	793	545	248	0.99	669	1080
		50	819	534	285	0.87	677	
		100	836	495	341	0.72	666	
		Average				0.86	670	

5.3.2.3 The Reversible Potential of the Redox Couple Fe(III)/Fe(II)

The reversible potential for the redox couple Fe(III)/Fe(II) with respect to the reversible potential of oxygen evolution can be calculated from the data in Tables 5-9 and 5-10. When comparing the data found for the two systems studied with both platinum and gold electrodes, one finds that the agreement is quite satisfactory. By using all the data obtained for a system, that includes those obtained on both platinum and gold, an average difference could be calculated. The results are given in Table 5-11.

Table 5-11 Reversible potential of the redox couple Fe(III)/Fe(II) with respect to the reversible potential of O_2/O^{2-} .

System	T °C	$E_{O_2/O^{2-}}^{rev} - E_{Fe^{3+}/Fe^{2+}}^{rev}$ mV
0.258 wt% Fe(II)-Na ₃ AlF ₆ -3.0 wt% Al ₂ O ₃	1000	-387 ± 11
0.420 wt% Fe(II)-Na ₃ AlF ₆ -3.2 wt% Al ₂ O ₃	1000	-350 ± 15
0.248 wt% Fe(II)-Na ₃ AlF ₆ -Al ₂ O ₃ (sat)	970	-404 ± 9
0.305 wt% Fe(II)-Na ₃ AlF ₆ -Al ₂ O ₃ (sat)	1020	-357 ± 17

No data for similar systems have been found in the literature. Boxall *et al.* (1974) reported that the potential difference between the redox couples Fe(III)/Fe(II) and Fe(II)/Fe was 0.8 V in AlCl₃-NaCl melts at 175 °C. This value corresponds well with the potential difference between the two couples obtained in the present work. The reversible potential of the redox couple Fe(III)/Fe(II) in cryolite-alumina melts will be discussed further in Chapter 7.

References to Chapter 5

- Boxall, L. G., H. L. Jones and R. A. Osteryoung (1974): Electrochemical Studies on Ag, Fe, and Cu Species in AlCl₃-NaCl Melts, *J. Electrochem. Soc.*, **121**, 212.
- Chrysoulakis, J., J. Bouteillon and J.-C. Poignet (1978): Electrochemical Behaviour of Pure Iron in the Aluminium Refining Electrolyte, *J. Appl. Electrochem.*, **8**, 103.
- Diep, Q. B. (1998): Structure and Thermodynamics of Cryolite-Based Melts with Additions of Al₂O₃ and Fe₂O₃, Doctoral Thesis 1998:28, Department of Electrochemistry, Norwegian University of Science and Technology, Trondheim, Norway, p. 105.
- Greef, R., R. Peat, L. M. Peter, D. Pletcher and J. Robinson (1990): Instrumental Methods in Electrochemistry, Ellis Horwood, Chichester, England, p. 178.

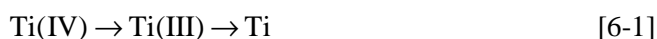
- Grjotheim, K., C. Krohn, M. Malinovsky, K. Matiasovsky and J. Thonstad (1982): Aluminium Electrolysis – Fundamentals of the Hall-Héroult Process, 2nd Edition, Aluminium-Verlag GmbH, Düsseldorf, Germany, p. 370.
- Hertzberg, T., K. Tørklep and H. A. Øye (1980): Viscosity of Molten NaF-AlF₃-Al₂O₃-CaF₂ Mixtures, in *Light Metals 1980*, C. J. McMinn, Editor, TMS, Warrendale, PA, p. 159.
- Hugdahl, A.-L. (1981): Reduksjon/oksydasjon av forurensninger i kryolittsmelter, M.Sc. Thesis, Department of Electrochemistry, Norwegian Institute of Technology, Trondheim, Norway, p. 6.
- Inman, D., J. C. Legey and R. Spencer (1978): A Chronopotentiometric Study of Iron in LiCl-KCl, *J. Appl. Electrochem.*, **8**, 269.
- Laidler, K. J. and J. H. Meiser (1982): Physical Chemistry, The Benjamin/Cummings Publishing Company, Inc., Menlo Park, CA, p. 833.
- Metals Handbook (1973): Metallography, Structures and Phase Diagrams, Vol. 8, American Society for Metals, OH, p. 267 and p. 305.
- Solheim, A. (2000): The Density of Molten NaF-LiF-AlF₃-CaF₂-Al₂O₃ in Aluminium Electrolysis, *Alum. Trans.*, **2**, 161.
- Stangeland, M. (1981): Elektrokjemiske eigenskapar til jern- og vanadium-sambindingar i kryolittsmelter, M.Sc. Thesis, Department of Electrochemistry, Norwegian Institute of Technology, Trondheim, Norway, p. 1.
- Sterten, Å., S. Haugen and K. Hamberg (1976): The NaF-AlF₃-Al₂O₃-Na₂O System – I Standard Free Energy of Formation of α -Aluminium Oxide from EMF Measurements, *Electrochim. Acta*, **21**, 589.
- Støre, T. (1999): Electrodeposition of Metals from Molten Salts, Doctoral Thesis 1999:18, Department of Electrochemistry, Norwegian University of Science and Technology, Trondheim, Norway.
- Thonstad, J. (1968): Anodic Overvoltage on Platinum in Cryolite-Alumina Melts, *Electrochim. Acta*, **13**, 449.
- Tørklep, K. and H. A. Øye (1980): Viscosity of NaF-AlF₃-Al₂O₃ Melt Mixtures, *Electrochim. Acta*, **25**, 229.

6 Electrochemistry of TiO₂ in Cryolite-Alumina Melts

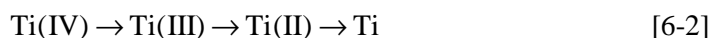
6.1 Introduction

The investigation on the solubility of TiO₂ in cryolite-alumina melts was reported in Chapter 4. In this connection, the presence of titanium compounds in the Hall-Héroult process was discussed, as well as the possibility of titanium as a constituent in an inert cathode (titanium diboride). Although there are several works on the electrochemical behaviour of titanium species in molten salts, few deal with the system cryolite-alumina.

Titanium is known to appear in different oxidation states, Ti(II), Ti(III) and Ti(IV), depending on the system. Electrochemical investigations of Ti(IV) in fluoride electrolytes showed a two-step reduction mechanism for Ti(IV) with Ti(III) as a sole stable intermediate (Makyta *et al.* 1989), *i.e.*,



In chloride systems a three-step reduction of Ti(IV) was found (Haarberg *et al.* 1993), *i.e.*,



Guang-Sen *et al.* (1988) studied the electrochemical reduction of Ti(IV) in an equimolar KCl-NaCl mixture with additions of KF. At low concentrations of fluoride ion, the reduction was found to take place in accordance with reaction scheme [6-2], while the reduction was found to proceed according to equation [6-1] at higher fluoride concentrations.

Delimarskii *et al.* (1979) investigated the electrodeposition of titanium from molten cryolite with varying TiO₂ content at 1050 °C. A three-electrode configuration was used for the linear voltammetry measurements. The cathode was a rod of spectral pure graphite (A = 0.2 cm²). A graphite rod was used as reference electrode, while the

graphite crucible served as the anode. Argon was purged through the cell during the experiments. Their results showed that two plateaus were observed in cryolite melts with varying TiO_2 content, as can be seen from voltammograms (b), (c) and (d) in Figure 6.1. This indicated that Ti(IV) was reduced in a two-step process.

The voltammograms displayed in Figure 6.1 were analysed by use of the Heyrovsky-Ilkovich equation (Mamantov *et al.* 1965),

$$E = E_{1/2} + \frac{2.3RT}{nF} \log \frac{i_l - i}{i} \quad [6-3]$$

where i_l is the limiting current. The second peak (approximately -0.7 V) on voltammograms (b), (c) and (d) was found to correspond to $n = 3$. Although the first plateau (approximately -0.4 V) on the same voltammograms did not agree with $n = 1$, they suggested the following reduction process:

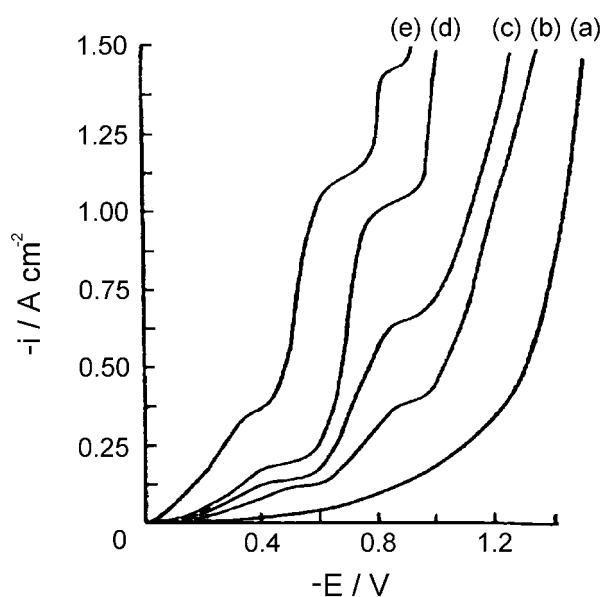


Figure 6.1 Linear voltammograms reported by Delimarskii *et al.* (1979) in: (a) Na_3AlF_6 ; (b) Na_3AlF_6 - 1 wt% TiO_2 ; (c) Na_3AlF_6 - 2 wt% TiO_2 ; (d) Na_3AlF_6 - 3 wt% TiO_2 ; (e) Na_3AlF_6 - 3 wt% TiO_2 - 3 wt% Al_2O_3 . Temperature = 1050°C , working electrode = spectral graphite, counter electrode = graphite, and reference electrode = graphite.

Qiu *et al.* (1988) studied the deposition of titanium with cyclic voltammetry. The working electrode was made of graphite, and the graphite crucible served as the counter electrode. The reference electrode was aluminium contained in a corundum tube, with a molybdenum wire as the current lead. Standard decomposition potentials were calculated for TiO_2 and Al_2O_3 . With a carbon anode and CO_2 as the primary anode product, their calculations yielded $E_d(\text{TiO}_2) = 0.82 \text{ V}$ and $E_d(\text{Al}_2\text{O}_3) = 1.15 \text{ V}$. Experiments were performed in molten cryolite with either (a) Al_2O_3 or (b) TiO_2 as additive. Their results are given in Figure 6.2.

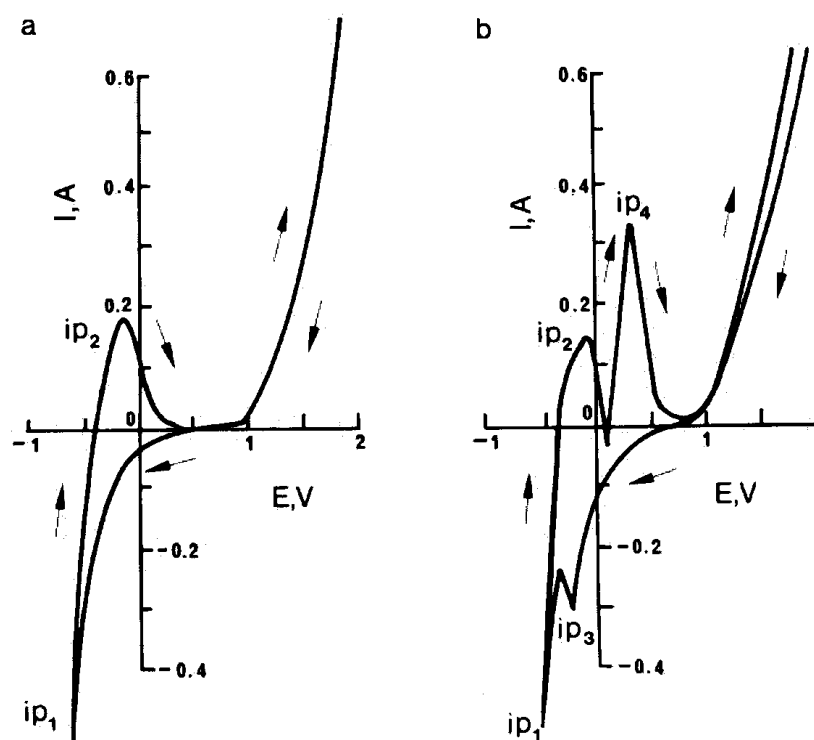


Figure 6.2 Cyclic voltammograms obtained with a working electrode ($A = 0.42 \text{ cm}^2$) and a counter electrode made of graphite, and an Al(III)/Al reference electrode in the systems (a) $\text{Na}_3\text{AlF}_6 - 1 \text{ wt}\% \text{ Al}_2\text{O}_3$ and (b) $\text{Na}_3\text{AlF}_6 - 0.5 \text{ wt}\% \text{ TiO}_2$. $T = 1050 \text{ }^\circ\text{C}$ and $v = 51 \text{ mV s}^{-1}$. From Qiu *et al.* (1988).

The anodic current seen in both voltammograms (a) and (b) at around $\sim 1 \text{ V}$ was caused by CO_2 evolution, while the peak current i_{p1} was assigned to the reaction:



When the potential was reversed in voltammogram (a), an anodic peak appeared. This peak current, i_{p2} , corresponded to the oxidation of aluminium:



When TiO_2 was added instead of Al_2O_3 , two new peaks appeared, as can be seen from voltammogram (b). These peaks were assigned to the reduction of Ti(IV) and the subsequent oxidation of Ti , *i.e.* the peak current i_{p3} corresponded to,



while the peak current i_{p4} corresponded to,

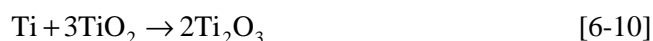


It was pointed out that the potential difference between i_{p1} and i_{p3} was about 0.32 V, *i.e.* close to the difference in the standard decomposition potentials of 0.33 V for Al_2O_3 and TiO_2 .

Raj and Skyllas-Kazacos (1992) carried out electrochemical studies in cryolite-alumina melts at 1050 °C with and without additions of TiO_2 . The working electrode was made of graphite, a tungsten wire was used as a quasi-reference electrode, while the carbon crucible in which the electrolyte was contained, served as the counter electrode. Potential sweep experiments showed that two new current peaks appeared after TiO_2 was added to the melt, *i.e.* one reduction peak and one oxidation peak. These peaks, similar to the current peaks i_{p3} and i_{p4} in Figure 6.2, were assigned to reactions [6-8] and [6-9]. The potential difference between the stripping peaks of aluminium and titanium, which correspond to currents peak i_{p2} and i_{p4} in Figure 6.2, was found to be about 0.3 V. It was commented that this value was close to the difference in the standard decomposition potentials of 0.33 V for Al_2O_3 and TiO_2 discussed above (Qiu *et al.* 1988). When increasing the TiO_2 concentration from 0.2 wt% to 0.5 wt%, i_{p3} and i_{p4} increased. However, when the TiO_2 concentration was increased to 1.0 wt%, the magnitude of i_{p3} and i_{p4} were found to be less than those obtained at the lower TiO_2 concentrations. This result was believed to be related to the concentration limits of the alloying elements in the cathodically deposited aluminium. The magnitude of the cathodic wave i_{p3} was found to be proportional to the square root of the sweep rate, $v^{1/2}$. This indicated that the reaction represented by the current peak was a solution reaction encompassing a diffusion process.

Devyatkin *et al.* (1998) applied cyclic voltammetry to study the electrochemical behaviour of Ti(IV) in cryolite-alumina melts with different additions (TiO_2 , MgTiO_2 or CaTiO_2). The experiments were performed at 1300 K in air. The working electrode was a platinum wire with a surface of 0.15 - 0.2 cm², while $\text{O}_2/\text{O}^{2-}(\text{Pt})$ was used as reference electrode. The counter electrode and the crucible were also made of platinum. Voltammograms recorded in the system $\text{Na}_3\text{AlF}_6\text{-Al}_2\text{O}_3$ showed several

peaks that were assigned to the formation of intermetallic compounds between aluminium and platinum. In the system $\text{Na}_3\text{AlF}_6\text{-Al}_2\text{O}_3\text{-TiO}_2$ two new processes were observed. Based on diagnostic criteria, the first process was found to be a reversible one-electron charge transfer with a soluble product, *i.e.* reaction [6-4]. The second process was believed to be a three-electron transfer with formation of metallic titanium, *i.e.* reaction [6-5]. The deposition of titanium was found to be followed by an irreversible chemical reaction:



When investigating the system $\text{Na}_3\text{AlF}_6\text{-Al}_2\text{O}_3\text{-MgTiO}_3$ a new peak appeared. This process was an irreversible four-electron reaction in accordance with reaction [6-8], followed by an irreversible chemical reaction:



The system $\text{Na}_3\text{AlF}_6\text{-Al}_2\text{O}_3\text{-CaTiO}_3$ gave rise to one new peak. It was concluded that this was in accordance with a reversible four-electron charge transfer with the formation of metallic titanium, *i.e.* reaction [6-8].

6.2 Experimental

Furnace

The experiments were carried out in a standard closed furnace under argon atmosphere (99.99 %). Temperature control within $\pm 2^\circ\text{C}$ was achieved with a Eurotherm temperature controller and a calibrated type S thermocouple (Pt-Pt10%Rh) inside the Kanthal heating element. The working temperature was measured with an additional thermocouple protected by a platinum tube placed in the melt.

Electrodes

A tungsten wire ($\varnothing = 2.0\text{ mm}$) was used as working electrode, while the counter electrode was made of platinum. A wire of either platinum or tungsten served as reference electrode. However, in some experiments a liquid aluminium reference electrode was used. The Al(III)/Al reference electrode consisted of a pool of liquid aluminium in an Alsint* tube (*Product of W. Haldenwanger, Berlin, containing 99.7 % Al_2O_3). A slot was made approximately 5 mm above the metal and a tungsten wire served as electrical lead. The working electrode was lowered 6 - 8 mm after making contact with the electrolyte surface (measured by a multimeter), and the active area was checked after each experiment by visual inspection of the electrode.

Chemicals

Natural hand-picked cryolite (Na_3AlF_6) from Greenland (Kryolittselskabet) was crushed, and coloured particles were removed before use. Al_2O_3 (Fluka, pro analysi) and TiO_2 (Alfa Johnson Matthey, 2 micron, 99 % + rutile) were kept at 200 °C before use.

Cell

The electrolyte (~130 g) was contained in a platinum or an Alsint crucible. The leads to the electrodes or the electrodes themselves were insulated with Alsint tubes. The electrolyte was agitated by a platinum stirrer after the experimental temperature was stabilised. If necessary, TiO_2 was added to the electrolyte through a quartz tube, and the electrolyte was agitated. Figure 6.3 shows a schematic drawing of the cell.

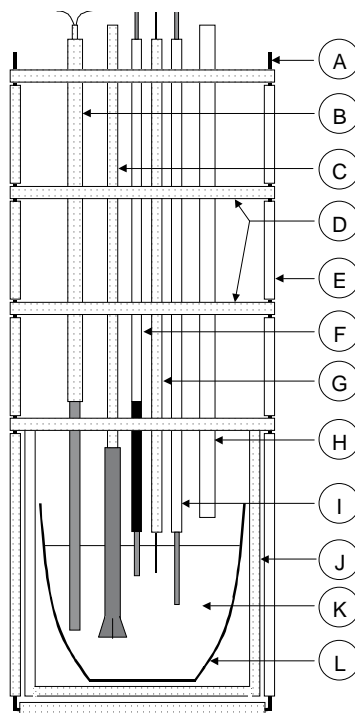


Figure 6.3 Experimental set-up: (A) 3 mm Incolloy wire; (B) Thermocouple (Pt-PtRh10%) sealed in platinum; (C) Platinum stirrer; (D) Radiation shields; (E) Alsint tubes; (F) Tungsten working electrode; (G) Platinum or tungsten reference electrode; (H) Quartz tube; (I) Platinum counter electrode; (J) Alsint crucible; (K) Cryolite-based melt; (L) Platinum crucible.

Instrumentation

The electrochemical measurements were performed with a Radiometer DEA-I digital electrochemical analyser. It comprises a DEA332 potentiostat with a maximum current output of 2 A and an IMT102 electrochemical interface with response time less than 3 μs . Signal imposition and data acquisition were handled by the Windows-based VoltaMaster 2 integrated software. A maximum of 5000 data points per measurement were stored on a PC.

6.3 Results and Discussion

The electrochemical behaviour of TiO_2 , and thereby of Ti(IV) , in cryolite-based melts was investigated by cyclic voltammetry (CV). The solvent consisted of either Na_3AlF_6 or $\text{Na}_3\text{AlF}_6\text{-Al}_2\text{O}_3(\text{sat})$. Preliminary experiments showed that glassy carbon was not appropriate as material for a working electrode. It was not possible to obtain well-developed cathodic peaks, as they were stretched out when the potential was swept in the cathodic direction. A tungsten wire (W) was used as the working electrode, while a platinum wire served as the counter electrode in all experiments. However, different types of reference electrodes were used throughout the experiments, and the material in use is, therefore, stated in the figure legend.

6.3.1 Electrochemical Behaviour of TiO_2 in $\text{Na}_3\text{AlF}_6\text{-Al}_2\text{O}_3(\text{sat})$

Typical voltammograms obtained before adding TiO_2 are shown in Figure 6.4. The sweep rate (v) was 200 mV s^{-1} . An Al(III)/Al reference electrode was used in this particular experiment, so zero potential should correspond with the deposition of liquid aluminium. The potential was swept in the cathodic direction from the open circuit potential ($\sim 1000 \text{ mV}$). The potential was reversed at 0 mV and -100 mV to determine the deposition potential of aluminium. The voltammograms show that the cathodic current slowly increased with decreasing potential until the potential became close to zero. This is believed to be due to alloying between the tungsten wire and aluminium. However, when the potential became negative, a steep increase in the cathodic current was observed. This was very likely caused by deposition of liquid aluminium on the tungsten wire. When the potential was reversed at -100 mV , a typical stripping peak was observed at $\sim 50 \text{ mV}$. This confirmed that aluminium was deposited below zero potential. The anodic peak at $\sim 350 \text{ mV}$, which was observed both when the potential was reversed at 0 mV and at -100 mV , does probably correspond to the oxidation of aluminium alloyed with tungsten. However, it is seen from Figure 6.4 that no cathodic peaks occur prior to the aluminium deposition.

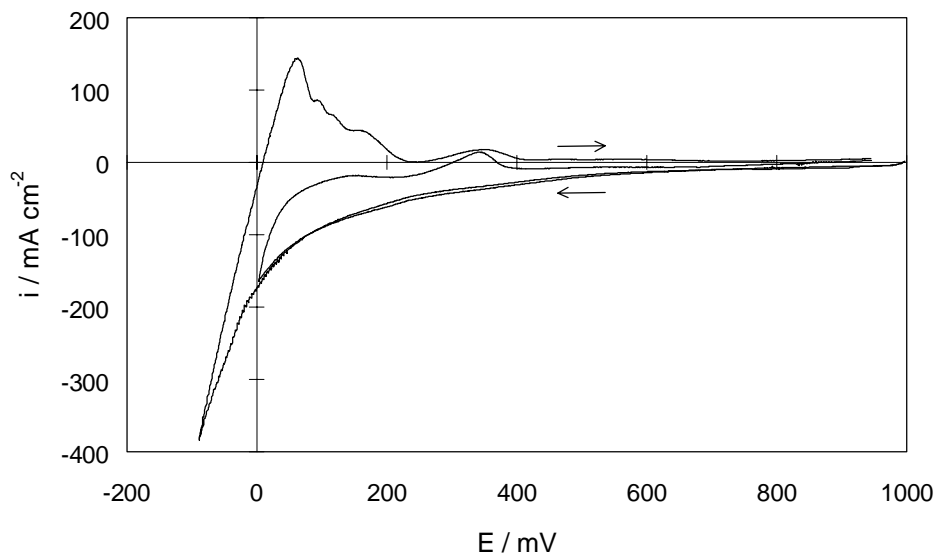


Figure 6.4 Cyclic voltammograms ($v = 200 \text{ mV s}^{-1}$) obtained with a tungsten electrode in the system $\text{Na}_3\text{AlF}_6\text{-Al}_2\text{O}_3(\text{sat})$ at 980°C . Reference electrode = Al(III)/Al .

Figure 6.5 shows voltammograms recorded with constant sweep rate, but with varying switching potential. The electrolyte contained 1.01 wt% TiO_2 , and a tungsten wire served as reference electrode. The figure shows that the cathodic current increased gradually to approximately -660 mV (region A^{C}). When the potential was reversed above -600 mV , no anodic peaks occurred, but a slowly increasing anodic current was observed (region A^{A}). Below region A^{C} a steep increase in the cathodic current was observed (peak B^{C}). The voltammogram that was reversed at -700 mV shows that the cathodic peak B^{C} was correlated with the anodic peak B^{A} . When the potential was swept more cathodic, *i.e.* region C^{C} , a new anodic peak C^{A} appeared. The shape of the peak B^{C} is consistent with a metal deposition, while the corresponding peak B^{A} indicates a stripping peak. Since the solvent does not give rise to any peaks prior to aluminium deposition (see Figure 6.4), peak B^{C} must be due to deposition of titanium. This means that C^{C} and C^{A} correspond with underpotential deposition of aluminium, and subsequently stripping of aluminium from the produced alloy. However, the interpretation of the regions A^{C} and A^{A} are more difficult.

To check if the various reactions were diffusion controlled, cyclic voltammograms were recorded with different sweep rates. Such voltammograms are displayed in Figure 6.6.

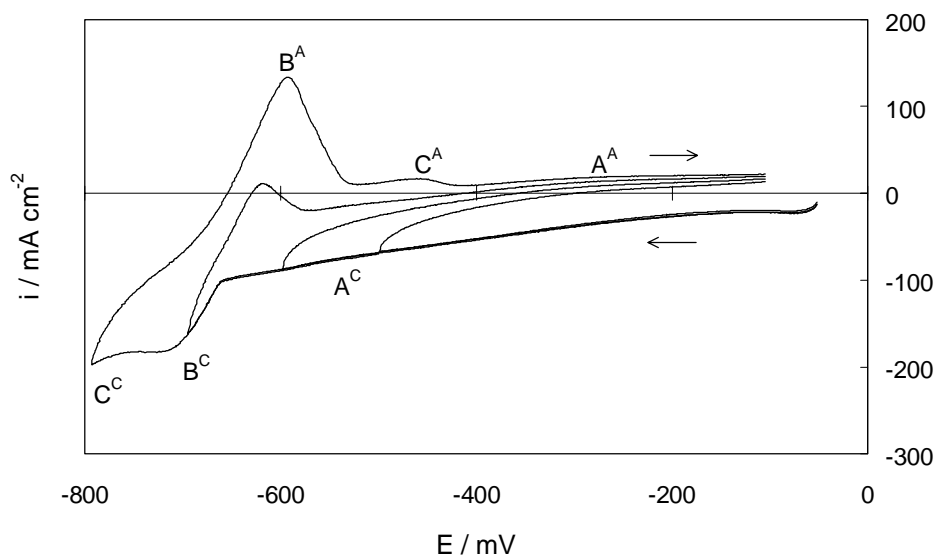


Figure 6.5 Cyclic voltammograms ($v = 200 \text{ mV s}^{-1}$) obtained with a tungsten electrode in $\text{Na}_3\text{AlF}_6\text{-Al}_2\text{O}_3(\text{sat})$ with 1.01 wt% TiO_2 at 1020°C . Reference electrode = W.

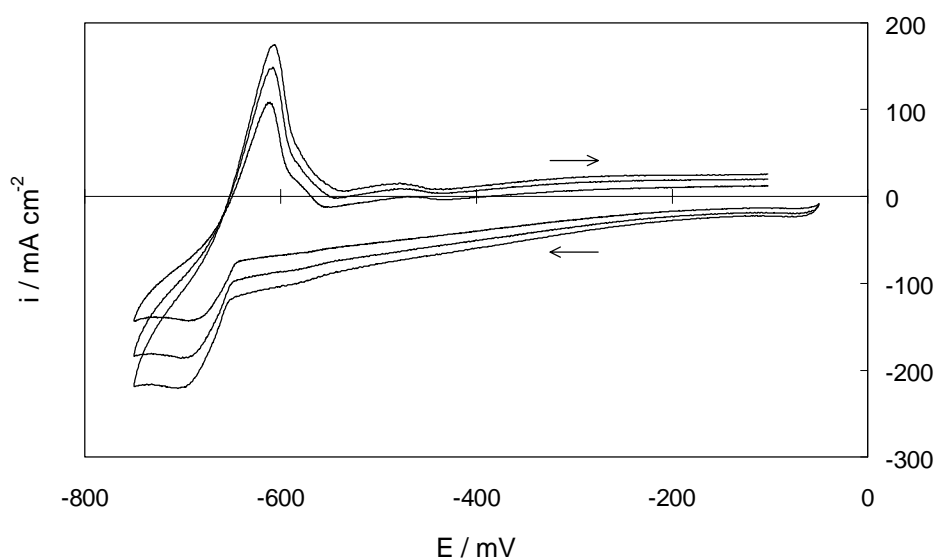


Figure 6.6 As Figure 6.5, but with sweep rates 100, 200 and 303 mV s^{-1} .

Figure 6.6 shows that both the cathodic and the anodic currents increased with increasing sweep rates. This indicates some degree of diffusion control in the reactions involving titanium species. To check if the deposition of titanium (peak B^C) was diffusion controlled, the pertinent data were read off the voltammograms. These data are given in Table 6-1. The cathodic background current (i_b^C) was found by extrapolating the relatively constant cathodic current observed prior to B^C to the cathodic peak potential (E_p^C) for the titanium deposition.

Table 6-1 Cyclic voltammetric data for reduction of Ti(IV) at a tungsten electrode in Na₃AlF₆-Al₂O₃(sat) with 1.01 wt% TiO₂ at 1020 °C.

v	i_p^C	i_b^C	E_p^C	$E_p^C - E_{p/2}$	n
mV s ⁻¹	mA cm ⁻²	mA cm ⁻²	mV	mV	
50	-110	-61	-691	-31	2.77
80	-131	-72	-695	-33	2.60
100	-143	-80	-694	-32	2.68
141	-162	-88	-696	-31	2.77
200	-190	-106	-701	-34	2.52
303	-221	-127	-705	-33	2.60
400	-249	-142	-707	-32	2.68
500	-273	-162	-713	-34	2.52

A plot of the cathodic peak current density (i_p^C) versus the square root of the sweep rate ($v^{1/2}$) is shown in Figure 6.7. A plot of the corrected cathodic peak current density, *i.e.* $i_p^C - i_b^C$, is also displayed in Figure 6.7. As can be seen from the figure, both plots display a linear relationship, thereby indicating that the deposition of titanium is diffusion controlled. The shape factor for a reversible metal deposition is given by equation [2-10], and thereby the number of electrons (n) involved can be determined since the expression $E_p^C - E_{p/2}$ is easily found from the voltammograms. Values for $E_p^C - E_{p/2}$ and the corresponding number of electrons are displayed in Table 6-1. As can be seen from Table 6-1, the average number of electrons involved in the titanium deposition was found to be 2.64, *i.e.* n = 3. This result is in agreement with the findings of Delimarskii *et al.* (1979), who obtained n = 3 when applying the Heyrovsky-Ilkovich equation on their voltammograms. Devyatkin *et al.* (1998) also believed that the observed titanium deposition involved a three-electron charge transfer, since the preceding reaction was found to be a one-electron transfer. It is, therefore, believed that the corresponding peaks B^C and B^A are due to the reaction:



According to the binary phase diagram aluminium-titanium (Metals Handbook 1973), aluminium and titanium form alloys at ~1000 °C. The corresponding peaks C^C and C^A

are, therefore, likely to be due to deposition of aluminium, and subsequent alloying with titanium, *i.e.* the reaction:

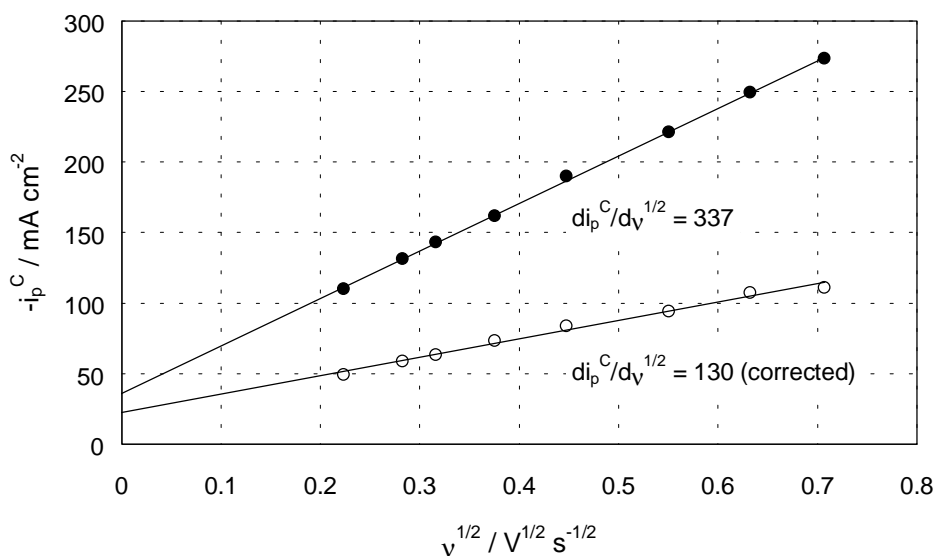
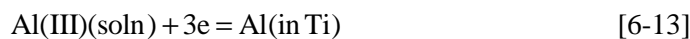
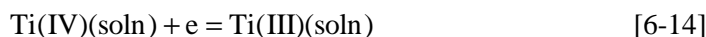


Figure 6.7 Plots of the cathodic peak current density versus the square root of sweep rate. The background current has been subtracted from the peak current for the data marked "corrected". The results were obtained in the system $\text{Na}_3\text{AlF}_6\text{-Al}_2\text{O}_3(\text{sat})$ with 1.01 wt% TiO_2 at 1020 °C.

As mentioned earlier, the interpretation of what kind of reactions that take place in the regions A^{C} and A^{A} in Figure 6.5 is difficult. Since the titanium deposition was found to involve a three-electron charge transfer, *i.e.* reaction [6-12], it seems plausible that the preceding reaction must involve a one-electron charge transfer since the valency of the added titanium was four, *i.e.*,



However, according to the binary phase diagram titanium-tungsten (Metals Handbook 1973), the solid phases of titanium and tungsten exhibit complete miscibility at around 1000 °C. It is, therefore, possible that some sort of underpotential deposition of titanium and subsequent alloying with tungsten takes place in the region A^{C} . Inspection of Figure 6.5 supports this idea; the voltammogram with switching potential -700 mV

gave rise to a cathodic current beyond the stripping peak B^A – implying that the proposed alloying reaction went on when the potential was moving in the anodic direction.

To check if the titanium concentration influenced the results, voltammograms were recorded under the same conditions as those displayed in Figure 6.5, but with twice as much titanium present. Figure 6.8 shows the voltammograms obtained in alumina-saturated cryolite melts with 2.00 wt% TiO_2 .

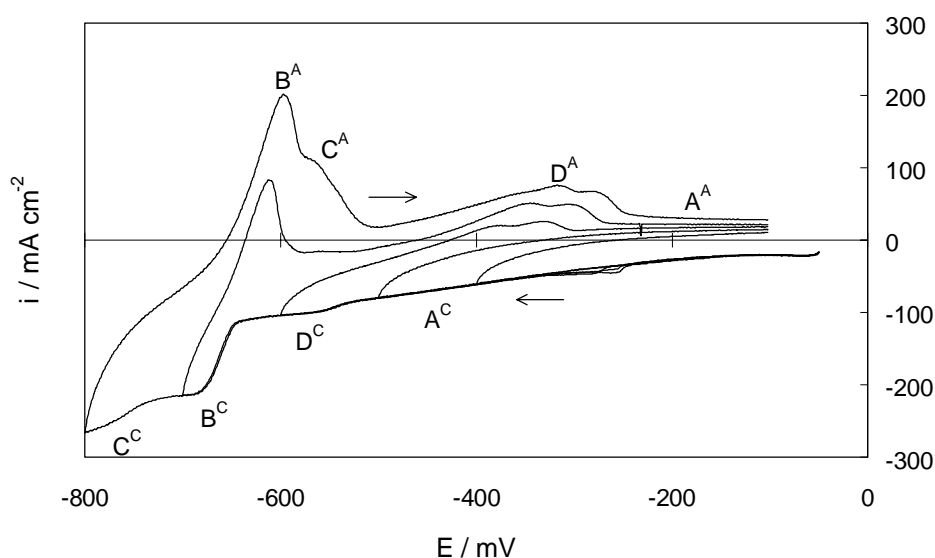


Figure 6.8 Cyclic voltammograms ($v = 200 \text{ mV s}^{-1}$) obtained with a tungsten electrode in $Na_3AlF_6\text{-}Al_2O_3(\text{sat})$ with 2.00 wt% TiO_2 at 1020°C . Reference electrode = W.

Figure 6.8 shows that two new peaks appeared when the concentration of TiO_2 was doubled, *i.e.* D^C and D^A . This is easily seen from Figure 6.9 where voltammograms, with switching potential -750 mV , obtained in alumina-saturated cryolite melts with 1.01 and 2.00 wt% TiO_2 , respectively, are compared. One of the diagnostic tests given in Chapter 2 for a reversible electron transfer with soluble product was:

$$\Delta E_p = E_p^A - E_p^C = \ln 10 \frac{RT}{nF} \quad [6-15]$$

By inserting numerical values into equation [6-15], one finds that $\Delta E_p = (257/n) \text{ mV}$ at 1020°C . Inspection of Figures 6.8 and 6.9 shows that the potential difference between

D^C and D^A is 250 - 300 mV, indicating that the number of electrons involved was equal to one. Similar results were obtained by Delimarskii *et al.* (1979) and by Devyatkin *et al.* (1998). This means that the peaks D^C and D^A correspond to reaction [6-14].

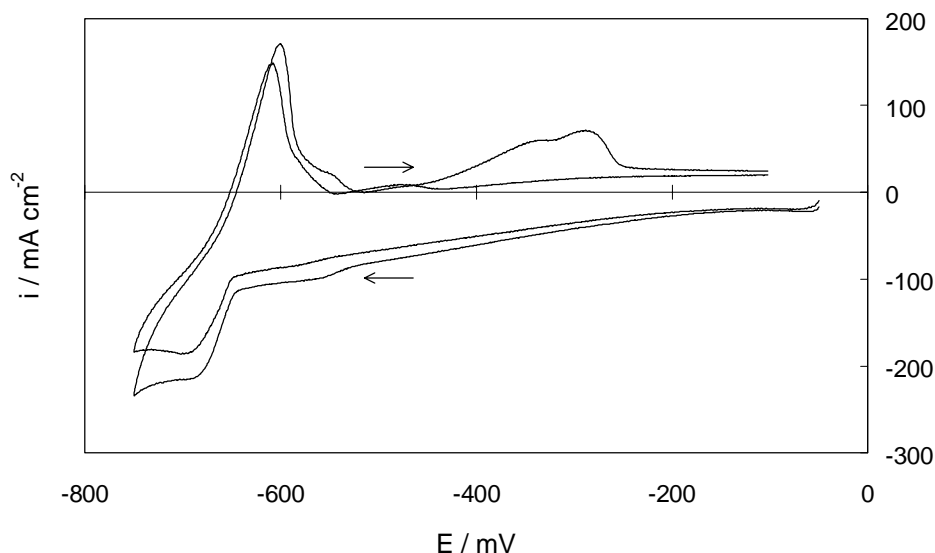


Figure 6.9 Cyclic voltammograms ($\nu = 200 \text{ mV s}^{-1}$) obtained with a tungsten electrode in $\text{Na}_3\text{AlF}_6\text{-Al}_2\text{O}_3(\text{sat})$ with 1.01 wt% and 2.00 wt% TiO_2 at 1020 °C. Reference electrode = W.

To check if peak B^C was diffusion controlled, voltammograms were recorded as a function of the sweep rate. The voltammetric data obtained in the system $\text{Na}_3\text{AlF}_6\text{-Al}_2\text{O}_3(\text{sat})$ with 2.00 wt% TiO_2 at 1020 °C are displayed in Table 6-2, while plots of i_p^C and $i_p^C - i_b^C$ versus $\nu^{1/2}$ are shown in Figure 6.10.

Figure 6.10 shows that both plots obey a linear relationship, thereby indicating that the deposition of titanium, as well as the reaction that causes the background current, are diffusion controlled. It is also seen that the slope of the regression lines increased with increasing TiO_2 concentration. From Table 6-2, the average number of electrons involved in the deposition is found to be 2.78. This corresponds to $n = 3$, being consistent with the findings above. Since the concentration of Ti(III) in the electrolyte is unknown, it is not possible to calculate the diffusion coefficient $D_{\text{Ti(III)}}$.

Table 6-2 Cyclic voltammetric data for reduction of Ti(IV) at a tungsten electrode in $\text{Na}_3\text{AlF}_6\text{-Al}_2\text{O}_3(\text{sat})$ with 2.00 wt% TiO_2 at 1020 °C.

v mV s^{-1}	i_p^C mA cm^{-2}	i_b^C mA cm^{-2}	E_p^C mV	$E_p^C - E_{p/2}$ mV	n
50	-123	-70	-685	-29	2.96
80	-148	-82	-690	-31	2.77
100	-161	-88	-693	-33	2.60
141	-184	-100	-693	-31	2.77
200	-215	-117	-694	-30	2.86
303	-261	-144	-702	-34	2.52
400	-293	-165	-698	-29	2.96
500	-326	-186	-704	-31	2.77

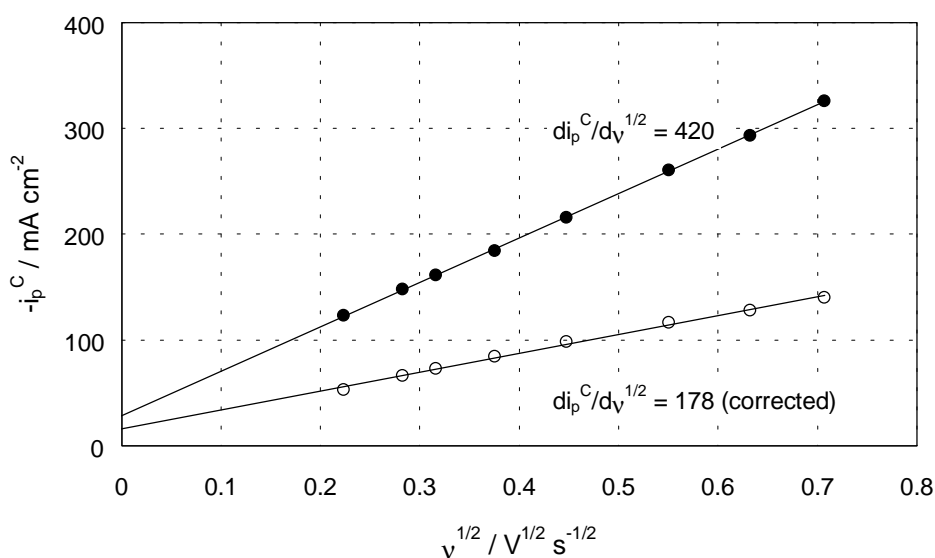
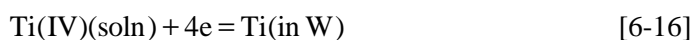
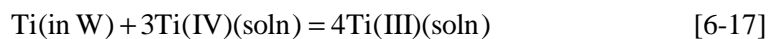


Figure 6.10 Plots of the cathodic peak current density versus the square root of sweep rate. The background current has been subtracted from the peak current for the data marked “corrected”. The results were obtained in the system $\text{Na}_3\text{AlF}_6\text{-Al}_2\text{O}_3(\text{sat})$ with 2.00 wt% TiO_2 at 1020 °C.

If the regions A^C and A^A are consistent with some sort of underpotential deposition, *i.e.*,



then it is also possible that Ti(III) could have been formed in region A^C due to a redox reaction of the type:



However, it should be emphasised that reactions [6-16] and [6-17] merely are suggestions.

6.3.2 Electrochemical Behaviour of TiO_2 in Na_3AlF_6

Cyclic voltammograms were recorded as a function of the sweep rate in cryolite with 1.05 wt% TiO_2 at 1020 °C. A platinum wire served as the reference electrode. Some of the obtained voltammograms are displayed in Figure 6.11.

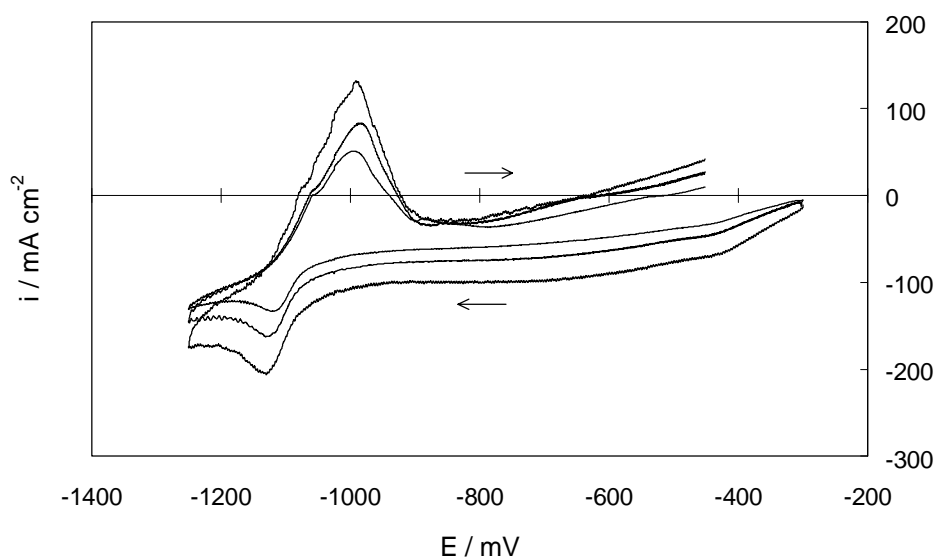


Figure 6.11 Cyclic voltammograms obtained with a tungsten electrode in Na_3AlF_6 with 1.05 wt% TiO_2 at 1020 °C. Reference electrode = Pt. Sweep rates 50, 100 and 200 mV s^{-1} .

Figure 6.11 shows that the cathodic current increased with increasing sweep rate. It is also observed that the cathodic current increased slowly with decreasing potential until around -1100 mV. At approximately -1100 mV a cathodic peak appeared, the shape of which seems to be consistent with a metal deposition, *i.e.* deposition of titanium. When the potential was reversed an anodic peak occurred that looks very much like a

stripping peak. Beyond the stripping peak a negative current is observed before it becomes anodic again. This is in accordance with the observations in Figures 6.5 and 6.8, which was believed to be due to some sort of underpotential deposition of titanium and subsequent alloying with the tungsten electrode.

The voltammetric data that were read off the curves are displayed in Table 6-3, together with the number of electrons involved in the titanium deposition. Plots to check whether the metal deposition was diffusion controlled or not, *i.e.* i_p^C and $i_p^C - i_b^C$ versus $v^{1/2}$, are shown in Figure 6.12.

Table 6-3 Cyclic voltammetric data for reduction of Ti(IV) at a tungsten electrode in Na_3AlF_6 with 1.05 wt% TiO_2 at 1020 °C.

v mV s^{-1}	i_p^C mA cm^{-2}	i_b^C mA cm^{-2}	E_p^C mV	$E_p^C - E_{p/2}$ mV	n
50	-133	-69	-1117	-33	2.60
80	-145	-73	-1104	-32	2.68
100	-159	-77	-1112	-30	2.86
141	-179	-86	-1110	-29	2.96
200	-205	-99	-1120	-30	2.86
303	-239	-117	-1125	-30	2.86
500	-293	-144	-1138	-35	2.45
1000	-395	-201	-1177	-41	2.09

Figure 6.12 shows that the titanium deposition was diffusion controlled since the data obey linear relationships. Table 6-3 shows that the average number of electrons involved in the metal deposition is 2.67. This implies that $n = 3$, and it means that the titanium deposition takes place in accordance with reaction [6-12].

If one compares the slopes $di_p^C/dv^{1/2}$ for the experiment displayed in Figure 6.7, *i.e.* in $\text{Na}_3\text{AlF}_6\text{-Al}_2\text{O}_3(\text{sat})$ with 1.01 wt% TiO_2 , with the slopes derived from the present experiment (Figure 6.12), one might expect to find similar values since the titanium concentration was approximately the same. This is the case for the uncorrected slopes, $di_p^C/dv^{1/2} = 337$ in Figure 6.7 while Figure 6.12 gives $di_p^C/dv^{1/2} = 342$. However, the value of the corrected slopes are rather different for the two systems, *i.e.* $di_p^C/dv^{1/2} = 130$ and $di_p^C/dv^{1/2} = 169$ in Figures 6.7 and 6.12, respectively. This indicates that more Ti(III) was formed in the solvent cryolite than in the solvent alumina-saturated cryolite prior to the titanium deposition. Assuming that the reduction of Ti(IV) to Ti(III) is diffusion controlled, disregarding the possibility that Ti(III) might have been produced according to reaction [6-17], it looks as if the diffusion coefficient $D_{\text{Ti(IV)}}$ might be different in the two solvents.

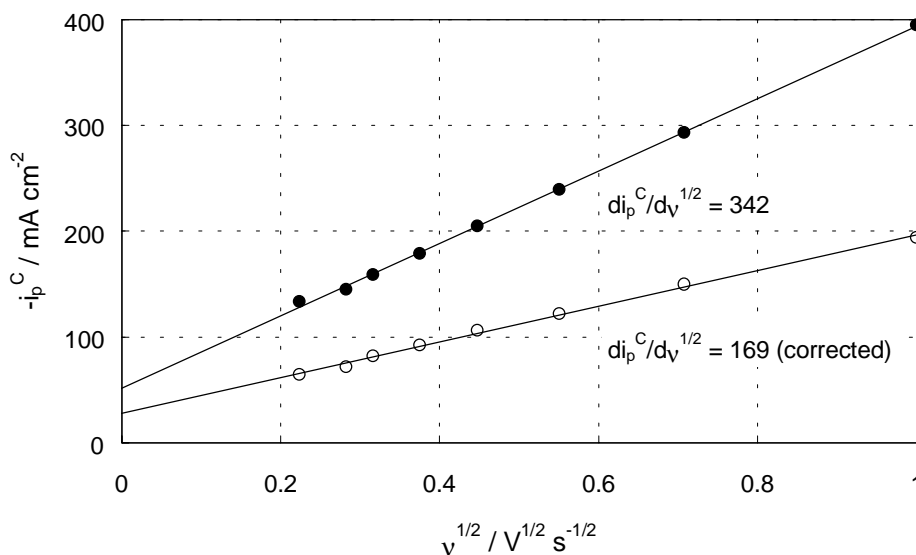


Figure 6.12 Plots of the cathodic peak current density versus the square root of sweep rate. The background current has been subtracted from the peak current for the data marked "corrected". The results were obtained in the system Na_3AlF_6 with 1.05 wt% TiO_2 at 1020 °C.

In Chapter 4, the solubility of TiO_2 in cryolite-alumina melts at 1020 °C was investigated. The modelling of the data obtained suggested that the major titanium species in cryolite melts low in alumina was TiO^{2+} , while TiO_3^{2-} was suggested to be the major titanium species in alumina-rich melts. From the size of the two species, one would expect the diffusion coefficient of Ti(IV) to be larger in cryolite than in cryolite saturated with alumina – that is if these ions are the electroactive species. This is in accordance with the findings above, provided that the assumption of diffusion controlled one-electron charge transfer holds.

References to Chapter 6

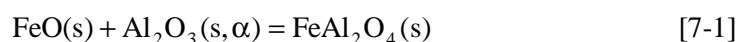
- Delimarskii, Yu. K., A. P. Krymov, V. F. Makogon, V. I. Shapoval and V. V. Nerubashchenko (1979): Electrodeposition of Aluminium and Titanium from Oxy-Fluoride Melts, *Ukr. Khim. Zh.*, **45**, 803.
- Devyatkin, S. V., G. Kaptay, J.-C. Poignet and J. Bouteillon (1998): Chemical and Electrochemical Behaviour of Titanium Oxide and Complexes in Cryolite-Alumina Melts, *High Temp. Mat. Proc.*, **2**, 497.
- Guang-Sen, C., M. Okido and T. Oki (1988): Electrochemical Studies of Titanium in Fluoride-Chloride Molten Salts, *J. Appl. Electrochem.*, **18**, 80.

- Haarberg, G. M., W. Rolland, Å. Sterten and J. Thonstad (1993): Electrodeposition of Titanium from Chloride Melts, *J. Appl. Electrochem.*, **23**, 217.
- Makytá, M., K. Matiasovsky and V. I. Taranenko (1989): Mechanism of the Cathode Process in the Electrochemical Synthesis of TiB_2 in Molten Salts – I. The Synthesis in an all-Fluoride Electrolyte, *Electrochim. Acta*, **34**, 861.
- Mamantov, G., D. L. Manning and J. M. Dale (1965): Reversible Deposition of Metals on Solid Electrodes by Voltammetry with Linearly Varying Potential, *J. Electroanal. Chem.*, **9**, 253.
- Metals Handbook (1973): Metallography, Structures and Phase Diagrams, Vol. 8, American Society for Metals, OH, p. 264 and p. 337.
- Qiu, Z., M. Zhang, Y. Yu, Z. Che, K. Grjotheim and H. Kvande (1988): Formation of Aluminium-Titanium Alloys by Electrolysis and by Thermal Reduction of Titania in Cryolite-Alumina Melts, *Aluminium*, **64**, 606.
- Raj, S. C. and M. Skyllas-Kazacos (1992): Electrochemical Studies of the Effect of TiO_2 and B_2O_3 Additions on the Aluminium Deposition Reaction in the Molten Cryolite Bath, *Electrochim. Acta*, **37**, 1787.

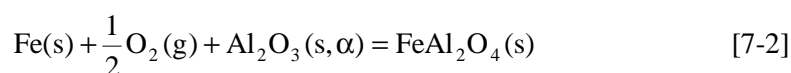
7 Thermodynamic Properties of FeAl₂O₄ and Stability of Iron-Containing Phases

7.1 Introduction

In Chapter 3 the standard Gibbs energy of formation of hercynite, FeAl₂O₄, at 1020 °C (1293 K) was found to be $\Delta G_f^\circ = -(17600 \pm 500) \text{ J mol}^{-1}$. This ΔG_f° value applies for the reaction,

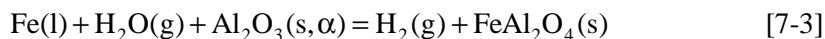


As mentioned in section 3.3.2 this value differed from the values reported by others in this temperature range, *i.e.* Rezhukhina *et al.* (1963) and Chan *et al.* (1973). Several investigations have been performed by different methods at various temperatures in order to determine the ΔG_f° of hercynite. All results from these different methods have been calculated in terms of the ΔG° for the reaction,



When nothing else is stated, the auxiliary data used in the calculations were taken from Barin (1995). The temperature in Kelvin is being used throughout this chapter since it contains several thermodynamic calculations.

Floridis (1957) investigated the reaction,



at 1823 K. Liquid iron was held in a pure corundum (*i.e.* Al₂O₃(s,α)) crucible in an atmosphere of water vapour and hydrogen of controlled composition for a prolonged time, and then the crucible and its content was quenched and the iron was analysed for oxygen. The presence of hercynite was determined by inspection of the crucible after

the run. The oxygen pressure in the gas was determined by the steam/hydrogen ratio, which also controls the oxygen concentration in the metal. Floridis (1957) reported that the highest steam/hydrogen ratio at which there was no formation of hercynite (*i.e.* the crucible remained white) was 0.274. At a ratio of 0.288 hercynite was formed and the crucible turned black. By using the average value, corresponding to a steam/hydrogen ratio of 0.281, the ΔG° for reaction [7-2] was calculated to be $-165200 \text{ J mol}^{-1}$ at 1823 K. The difference between the average steam/hydrogen ratio and the extremes corresponds to $\pm 400 \text{ J mol}^{-1}$.

Pillay *et al.* (1960) studied the same system as Floridis (1957), *i.e.* reaction [7-3], but at 1973 K. The experiments and the analysis were performed in exactly the same way as Floridis (1957). The results show clearly that the authors had been able to determine with high precision the steam/hydrogen ratio at which hercynite was formed, *i.e.* 0.31. ΔG° for the reaction [7-2] was calculated to be $-157600 \text{ J mol}^{-1}$ at 1973 K.

Rezukhina *et al.* (1963) investigated the reaction [7-1] with the solid state cell,



in the range 1235 - 1323 K. Mixed crystals of $\text{ThO}_2\text{-La}_2\text{O}_3$ served as the electrolyte in the cell. The following linear equation with respect to temperature was fitted to the experimental EMF data (with an accuracy of $\pm 0.0007 \text{ V}$) by the least-squares method:

$$E^\circ = 0.2342 - 0.00008857T \quad [7-5]$$

By using equation [7-5] and the relation,

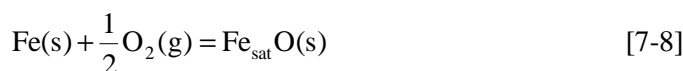
$$\Delta G^\circ = -nFE^\circ \quad [7-6]$$

with $n = 2$, the standard Gibbs energy for reaction [7-1] can be given as,

$$\Delta G^\circ = -45190 + 17.09T \quad [7-7]$$

Rezukhina *et al.* (1963) give the uncertainty in ΔG° as $\pm 150 \text{ J mol}^{-1}$.

Holmes *et al.* (1986) have made a thorough investigation of the reaction,



by the use of galvanic cells with oxygen-specific solid electrolytes made of calcia-stabilised zirconia. Although $\text{Fe}_{0.947}\text{O}$ was used as the reference composition, wustite was denoted $\text{Fe}_{\text{sat}}\text{O}$ due to its temperature dependent stoichiometry. They give a linear

relationship between ΔG° and temperature for reaction [7-8] in the temperature range 800 - 1644 K as,

$$\Delta G^\circ = -264147 + 65.090T \quad [7-9]$$

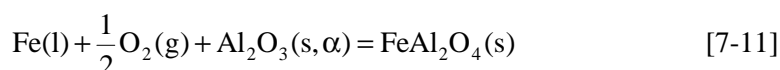
with a standard deviation of $\pm 155 \text{ J mol}^{-1}$. By adding reactions [7-1] and [7-8], *i.e.* combining equations [7-7] and [7-9], ΔG° for reaction [7-2] was found to be,

$$\Delta G^\circ = -309337 + 82.18T \quad [7-10]$$

for the temperature range 1235 - 1323 K.

Brokloff *et al.* (1965) studied the same system as Floridis (1957) and Pillay *et al.* (1960), *i.e.* reaction [7-3]. They equilibrated mixtures of iron, alumina and hercynite with water vapour-hydrogen gas mixtures at different temperatures. At the end of an experiment, reflected light microscopy and X-ray analysis were used to identify the reaction products. The steam/hydrogen ratios for hercynite formation at 1773 and 1808 K were found to be between 0.226 and 0.237 and between 0.231 and 0.258, respectively. By using the average values, *i.e.* 0.232 and 0.245, the ΔG° for reaction [7-2] was calculated to be $-(172609 \pm 343) \text{ J mol}^{-1}$ at 1773 K and $-(167885 \pm 855) \text{ J mol}^{-1}$ at 1808 K.

McLean and Ward (1966) investigated the reaction,



at temperatures between 1823 and 2023 K. Iron was melted, under a helium atmosphere, in an alumina crucible, on the base of which hercynite was compacted. The crucible and contents were held at constant temperature until equilibrium was established between the melt and the two solid phases, alumina and hercynite. At the end of all the experiments, the crucible and its content melt was quenched in a stream of helium, and the oxygen content of samples of the solidified melt was determined by vacuum fusion analysis. The ΔG° for reaction [7-11] was reported as,

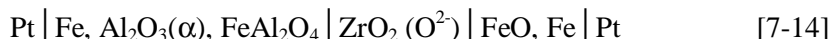
$$\Delta G^\circ = -267400 + 52.47T \quad [7-12]$$

with an uncertainty of $\pm 2100 \text{ J mol}^{-1}$. By using equation [7-12], the ΔG° for reaction [7-2] can be given as,

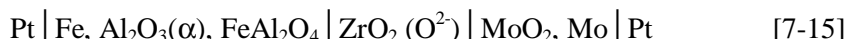
$$\Delta G^\circ = -253600 + 44.84T \quad [7-13]$$

for the temperature range 1823 - 2023 K.

Chan *et al.* (1973) investigated reactions [7-1] and [7-11] from 1023 to 1873 K with calcia-stabilised zirconia as the solid electrolyte. The EMF for the cells,



and,



was measured for both increasing and decreasing temperatures between 1023 and 1663 K at approximately 50 K intervals after sufficient time (between 2 and 10 hours) had elapsed to ensure that equilibrium was attained. Purified argon was used as the inert gas flowing through the two separate individually-gettered electrode compartments. The best line through the experimental points, after converting the results of [7-15] into the form of [7-14], was given as,

$$E^\circ = 0.1444 - 0.000017T \quad [7-16]$$

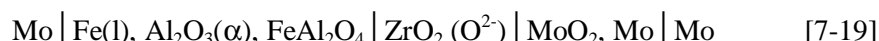
for reaction [7-1], and with an uncertainty of ± 0.004 V. By using equation [7-6] and $n = 2$, ΔG° for reaction [7-1] can be given as,

$$\Delta G^\circ = -27865 + 3.28T \quad [7-17]$$

By adding equations [7-17] and [7-9], ΔG° for reaction [7-2] was found to be,

$$\Delta G^\circ = -292012 + 68.37T \quad [7-18]$$

at temperatures between 1023 and 1663 K. The EMF for the cell,



at 1873 K was obtained by dipping a CaO-ZrO₂ tube into a hercynite-liquid iron mixture which was held under an argon atmosphere and contained in an alumina crucible. An EMF of (308 ± 10) mV for $n = 2$ was obtained for periods of up to 45 minutes. This EMF corresponds to a ΔG° of $-163000 \text{ J mol}^{-1}$ for reaction [7-11]. Calculation gave a ΔG° of $-163500 \text{ J mol}^{-1}$ at 1873 K for reaction [7-2].

The ΔG° of $-(17600 \pm 500) \text{ J mol}^{-1}$ at 1293 K for reaction [7-1], found in section 3.3.2, could be used to calculate the corresponding ΔG° for reaction [7-2]. The corresponding ΔG° for reaction [7-2], after combining it with equation [7-9], was found to be $-197600 \text{ J mol}^{-1}$ at 1293 K.

The standard Gibbs energy for reaction [7-2], based on literature data and experimental data given in section 3.3.2, are plotted against temperature in Figure 7.1.

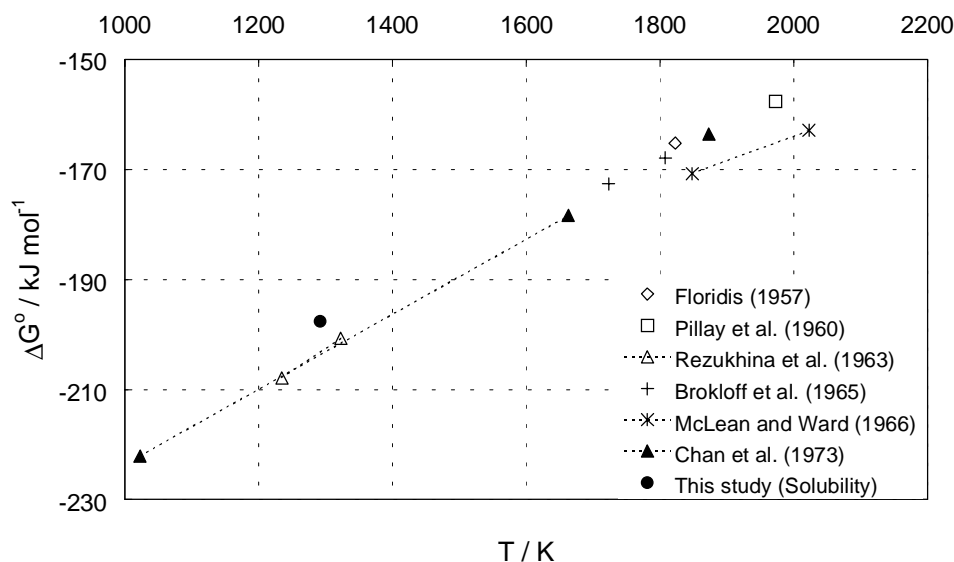


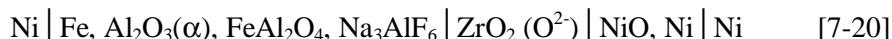
Figure 7.1 Standard Gibbs energy, obtained from solubility measurements and calculated from literature data, for the reaction $\text{Fe(s)} + 1/2\text{O}_2(\text{g}) + \text{Al}_2\text{O}_3(\text{s}, \alpha) = \text{FeAl}_2\text{O}_4(\text{s})$ versus temperature.

The literature review shows that only Rezukhina *et al.* (1963) and Chan *et al.* (1973) have performed measurements in the temperature range at around 1293 K. From Figure 7.1 it is observed that their results deviate from the present value (see section 3.3.2). The discrepancy in the standard Gibbs energy was calculated as 5.5 and 6.0 kJ mol^{-1} , respectively. Both Rezukhina *et al.* (1963) and Chan *et al.* (1973) used alpha alumina in their preparation of hercynite, as well as alumina of the alpha modification in their experiments with solid state cells. They have therefore, and without any discussion, assumed that the alumina, which is taking part in reaction [7-1] or [7-2], is of the alpha modification.

According to Wefers and Misra (1987) metastable intermediate modifications of alumina are transformed to alpha alumina at temperatures above 1273 K, depending on the conditions. It is therefore possible that the reaction studied by both Rezukhina *et al.* (1963) and Chan *et al.* (1973) did not involve alpha alumina, but another crystal modification. Small amounts of fluoride are reported to drastically reduce the temperature of transformation to alpha alumina according to Wefers and Misra (1987). Kachanovskaya *et al.* (1971) showed that when gamma alumina was added to a cryolite melt, the alumina was transformed to alpha within one minute. It is therefore evident that the results obtained in the present work apply for reaction [7-1], *i.e.* alpha alumina took part in the reaction. All the other works presented in the literature review were performed above the melting point of iron, 1808 K, or close to it. It is believed

that such high temperatures ensured that alpha alumina was the stable state of the alumina.

The object of the investigation was to measure the standard Gibbs energy of formation for hercynite by the solid electrolyte cell:



Cryolite was present in the half-cell containing hercynite to ensure that alumina of the alpha modification was in equilibrium with hercynite.

7.2 Experimental

Furnace

The experiments were carried out in a standard closed furnace under argon atmosphere (99.99 %). Temperature control within ± 2 K was achieved with a Eurotherm temperature controller and a calibrated type S thermocouple (Pt-Pt10%Rh) inside the Kanthal heating element. The working temperature was measured with an additional thermocouple close to the cell.

Chemicals

Natural hand-picked cryolite (Na_3AlF_6) from Greenland (Kryolittselskabet) was crushed, and coloured particles were removed before use. Al_2O_3 (Fluka, pro analysi) was stored at 473 K, while nickel powder (Alfa, 99.999 %, Puratronic) and nickel(II) oxide (Alfa, green, 99 %) were used as received. Hercynite was prepared in the laboratory by mixing and dry grinding ferric oxide, Fe_2O_3 (Aldrich, 99 %+), with excess iron powder (Aldrich, 99 %+) and excess alumina in a ball mill for 14 hours. The mixture was then heated in an iron crucible under argon atmosphere at 1323 - 1373 K for 48 hours, see Figure 3.3.

Cell

A schematic drawing of the cell is given in Figure 7.2. The electrolyte consisted of the hercynite-alumina mixture with about 10 wt% cryolite, contained in an iron crucible ($d = 350$ mm, $h = 600$ mm). The NiO/Ni reference electrode was contained in an oxygen ion conducting $\text{ZrO}_2\text{-}8\%\text{Y}_2\text{O}_3$ tube (Frealit-Degussit FZY, 10/6 mm) which served as a solid electrolyte. Nickel wires served as leads to both electrodes to avoid the Thomson effect. The cell was heated slowly (<10 K min^{-1}) to prevent the zirconia tube from cracking. The EMF was measured for several hours after a stable temperature was obtained.

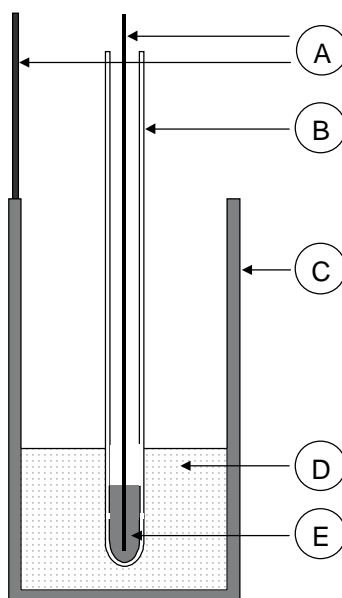


Figure 7.2 Schematic drawing of the cell [7-20]: (A) Ni wires; (B) Zirconia tube; (C) Fe crucible; (D) $\text{Al}_2\text{O}_3 + \text{FeAl}_2\text{O}_4 + 10 \text{ wt}\% \text{ Na}_3\text{AlF}_6$; (E) $\text{Ni} + \text{NiO}$.

7.3 Results and Discussion

7.3.1 Electrochemical Measurements of EMF for Hercynite

A typical plot of the EMF for the cell given by equation [7-20], against time after the temperature had stabilised at 1293 K, is shown in Figure 7.3. It is observed that the EMF seemed to decrease towards a limiting value. A plot of the change in EMF *versus* the EMF is given in Figure 7.4. The stable EMF was found as the intercept of the regression line, found by least-squares error, with the EMF axis. The same procedure was applied for all the measurements.

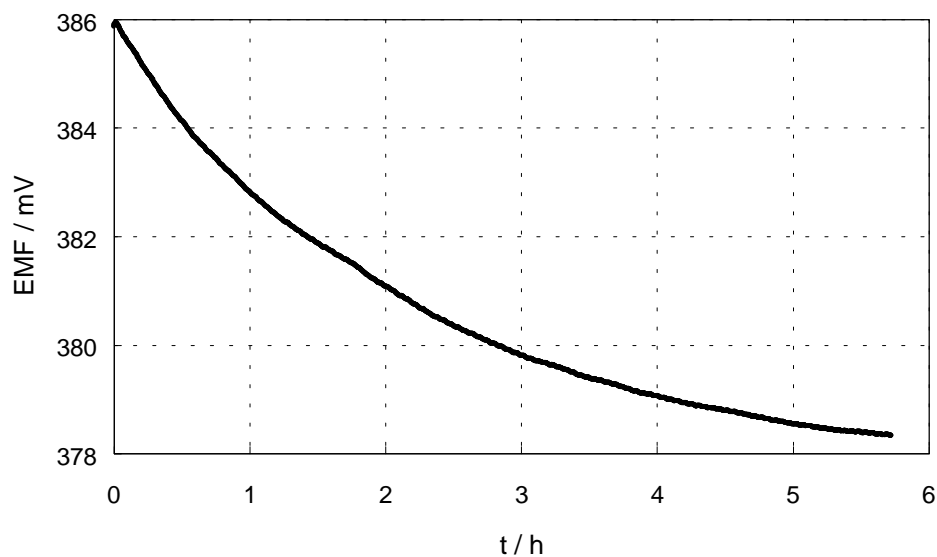


Figure 7.3 EMF versus time after the temperature had stabilised at 1293 K.

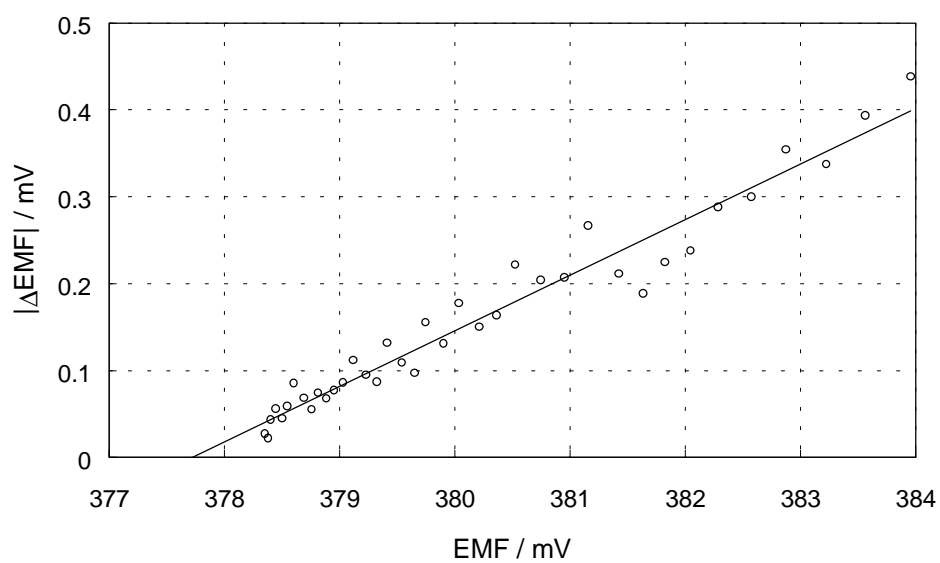
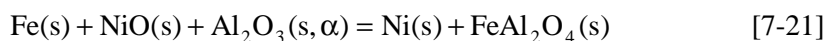


Figure 7.4 $|\Delta EMF|$ versus EMF at 1293 K. The EMF was found to be 377.7 mV.

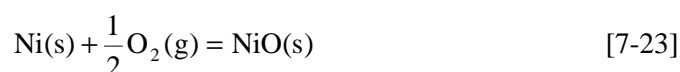
Due to the use of a NiO/Ni reference electrode, instead of an FeO/Fe reference electrode, the measured EMF's apply for the reaction,



Holmes *et al.* (1986) have, as mentioned earlier, made a thorough investigation of reaction [7-8]. In addition to the linear relationship given by equation [7-9] for 800 - 1644 K, they gave a more accurate equation for the temperature range between 1184 and 1644 K:

$$\Delta G_{\text{Fe}_{\text{sat}}\text{O}}^{\circ} = -275770 + 13.841T - 8.4742T \ln T \quad [7-22]$$

The standard deviation of equation [7-22] is only $\pm 1 \text{ J mol}^{-1}$. In the same work also the following reaction was investigated,



They gave the relationship between ΔG° and temperature for reaction [7-23] in the temperature range 900 - 1600 K as,

$$\Delta G_{\text{NiO}}^{\circ} = -239885 + 122.350T - 4.584T \ln T \quad [7-24]$$

and with a standard deviation of $\pm 2 \text{ J mol}^{-1}$.

Reaction [7-1] is obtained by combining reactions [7-8], [7-21] and [7-23]. The corresponding ΔG° for reaction [7-1] is then given by,

$$\Delta G^{\circ} = -2FE_{\text{cell}} + \Delta G_{\text{NiO}}^{\circ} - \Delta G_{\text{Fe}_{\text{sat}}\text{O}}^{\circ} \quad [7-25]$$

since $n = 2$.

Reaction [7-2] is obtained by adding reactions [7-21] and [7-23], and the corresponding ΔG° is then calculated from,

$$\Delta G^{\circ} = -2FE_{\text{cell}} + \Delta G_{\text{NiO}}^{\circ} \quad [7-26]$$

The measured EMF's at different temperatures and the corresponding standard Gibbs energies for reactions [7-1] and [7-2] are tabulated in Table 7-1. The uncertainty in the measured EMF values was believed to be $\pm 0.1 \text{ mV}$.

Table 7-1 Measured EMF values at different temperatures for reaction [7-21], and the corresponding standard Gibbs energies for reactions [7-1] and [7-2].

T / K	EMF / mV	ΔG° [7-1] / J mol ⁻¹	ΔG° [7-2] / J mol ⁻¹
1245	367.2	-16006	-199080
1245	364.8	-15543	-198617
1293	377.7	-17110	-197026
1294	375.3	-16628	-196478
1294	373.4	-16261	-196111
1343	380.1	-16606	-193247

The standard Gibbs energy of reaction [7-2] found by EMF measurements are plotted in Figure 7.5 together with the data found in the literature and the single point obtained during the solubility experiments (see Figure 7.1).

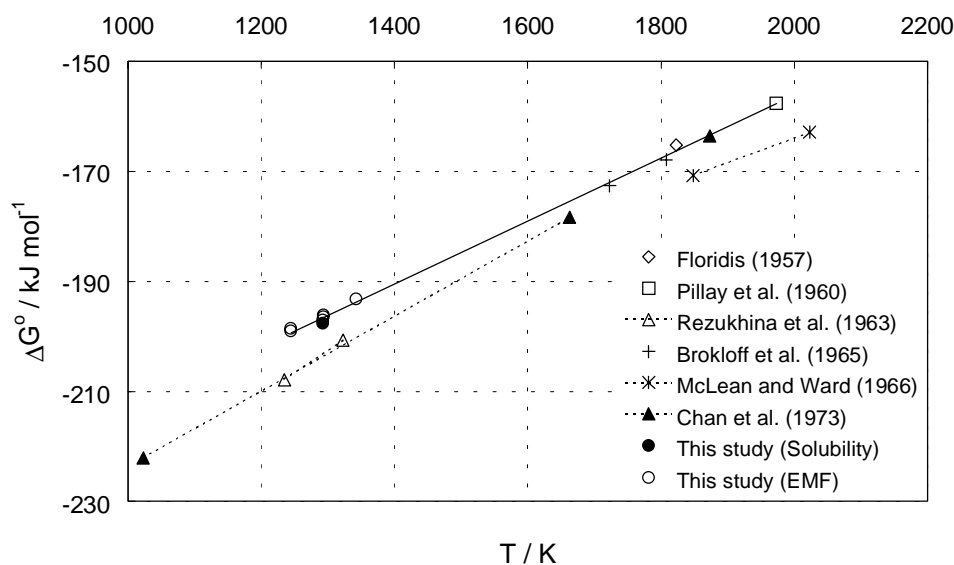


Figure 7.5 Standard Gibbs energies versus temperature, obtained from solubility and EMF measurements, and calculated from literature data, for the reaction $\text{Fe}(s) + 1/2\text{O}_2(g) + \text{Al}_2\text{O}_3(s, \alpha) = \text{FeAl}_2\text{O}_4(s)$.

It is observed from Figure 7.5 that the agreement between the value for the standard Gibbs energy derived from the solubility measurements and the values found by measuring the EMF is very good. Since both methods tested in this investigation give

approximately the same values, under experimental conditions promoting the stability of alpha alumina, it is believed that the equilibrium studied by both Rezhukhina *et al.* (1963) and by Chan *et al.* (1973) did not involve alpha alumina only.

A linear relationship between ΔG° and temperature for reaction [7-2] was found by regression analysis of the data of Floridis (1957), Pillay *et al.* (1960), Brokloff *et al.* (1965), Chan *et al.* (1973) (the measurement at 1873 K), and those obtained in this investigation:

$$\Delta G^\circ = -270615 + 56.759T \quad [7-27]$$

This gives $\Delta H^\circ_{1600\text{K}} = -(270615 \pm 1387) \text{ J mol}^{-1}$ and $\Delta S^\circ_{1600\text{K}} = -(56.759 \pm 0.856) \text{ J K}^{-1} \text{ mol}^{-1}$, respectively. The choice of 1600 K as a representative temperature seems reasonable since it is in the middle of the temperature range for the data on which equation [7-27] is based, *i.e.* 1245 - 1973 K.

7.3.2 Thermodynamic Calculations for Hercynite

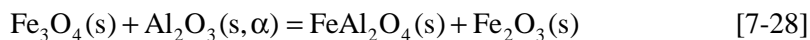
With the information obtained from the solubility and the EMF measurements, a comparison with the data on hercynite compiled by Barin (1995) can be made. The necessary data for calculations are given in Table 7-2.

Table 7-2 Thermodynamic data for different elements. From Barin (1995).

Element	$C^\circ_{p, 298.15\text{K}}$ $\text{J K}^{-1} \text{ mol}^{-1}$	$C^\circ_{p, 1600\text{K}}$ $\text{J K}^{-1} \text{ mol}^{-1}$	$S^\circ_{298.15\text{K}}$ $\text{J K}^{-1} \text{ mol}^{-1}$	$S^\circ_{1600\text{K}}$ $\text{J K}^{-1} \text{ mol}^{-1}$	$H^\circ_{1600\text{K}}$ J mol^{-1}
$\text{Al}_2\text{O}_3(\alpha)$	79.038	133.375	50.936	240.935	-1520003
Fe(s)	24.978	37.364	27.280	86.661	49320
$\text{Fe}_2\text{O}_3(\text{s})$	103.866	144.490	87.404	319.817	-638218
$\text{Fe}_3\text{O}_4(\text{s})$	150.730	199.302	146.147	483.821	-851472
$\text{FeAl}_2\text{O}_4(\text{s})$	123.544	191.616	106.299	377.033	-1774961
$\text{O}_2(\text{g})$	29.376	36.797	205.147	260.434	44266

The change in standard entropy, ΔS° , of reaction [7-2] at 1600 K was calculated to be $-80.780 \text{ J K}^{-1} \text{ mol}^{-1}$ when the data in Table 7-2 were used. Comparison of this value with the one obtained in the present work, *i.e.* $\Delta S^\circ_{1600\text{K}} = -57.222 \text{ J K}^{-1} \text{ mol}^{-1}$, gives a deviation of $23.558 \text{ J K}^{-1} \text{ mol}^{-1}$. If one assumes that the data for the elements Fe(s) , $\text{O}_2(\text{g})$, and $\text{Al}_2\text{O}_3(\text{s}, \alpha)$ are correct, a new standard entropy for hercynite can be calculated at 1600 K, *i.e.* $S^\circ_{1600\text{K}} = 400.591 \text{ J K}^{-1} \text{ mol}^{-1}$. To check if the new value is

more probable than the $S^\circ_{1600\text{K}}$ of hercynite given in Table 7-2, the following reaction can be considered:



Since there is no major structural changes involved in this reaction, it is expected that the change in standard entropy should be close to zero. When the data in Table 7-2 are used, a $\Delta S^\circ_{298.15\text{K}}$ of $-3.380 \text{ J K}^{-1} \text{ mol}^{-1}$ and a $\Delta S^\circ_{1600\text{K}}$ of $-27.906 \text{ J K}^{-1} \text{ mol}^{-1}$ are found for reaction [7-28]. The value at 298.15 K seems reasonable, while the one at 1600 K does not comply with the criterion that the ΔS° should be close to zero. If the same calculations are performed with $S^\circ_{1600\text{K}} = 400.591 \text{ J K}^{-1} \text{ mol}^{-1}$ for hercynite, a $\Delta S^\circ_{1600\text{K}}$ of $-4.348 \text{ J K}^{-1} \text{ mol}^{-1}$ is found for reaction [7-28]. This value is of the same order as the one found at 298.15 K, and it is therefore believed that the new data are more correct. The thermodynamic data have, therefore, been recalculated.

To recalculate the thermodynamic data an expression for the standard molar heat capacity, C_p° , for hercynite must be found. Typically it is given as,

$$C_p^\circ = a + bT + cT^{-2} \quad [7-29]$$

With three unknown constants, a , b and c , one must know three boundary conditions to solve equation [7-29]:

$$C_p^\circ(T_1 = 298.15\text{K}) = a + bT_1 + cT_1^{-2} = 123.544 \text{ J K}^{-1} \text{ mol}^{-1} \quad [7-30]$$

$$C_p^\circ(T_2 = 1600\text{K}) = a + bT_2 + cT_2^{-2} = 188.187 \text{ J K}^{-1} \text{ mol}^{-1} \quad [7-31]$$

$$\begin{aligned} S^\circ_{T_2=1600\text{K}} - S^\circ_{T_1=298.15\text{K}} &= \int_{T_1}^{T_2} \frac{C_p^\circ}{T} dT = a \ln\left(\frac{T_2}{T_1}\right) + b(T_2 - T_1) - \frac{c}{4}(T_2^{-4} - T_1^{-4}) \\ &= 294.292 \text{ J K}^{-1} \text{ mol}^{-1} \end{aligned} \quad [7-32]$$

The first boundary condition is taken from Barin (1995). According to Barin (1995) both H° and S° have been determined at 298.15 K, so that the C_p° could be estimated. The second boundary condition was found by assuming that the ΔC_p° for reaction [7-28] is equal to zero at 1600 K. When inserting the data given in Table 7-2 for the elements $\text{Al}_2\text{O}_3(\text{s}, \alpha)$, $\text{Fe}_2\text{O}_3(\text{s})$ and $\text{Fe}_3\text{O}_4(\text{s})$, the C_p° for hercynite at 1600 K was calculated to be $188.187 \text{ J K}^{-1} \text{ mol}^{-1}$. The third boundary condition was calculated by subtracting the standard entropy at 298.15 K, see Table 7-2, from the standard entropy of hercynite at 1600 K that was calculated earlier.

By combining equations [7-30] to [7-32], the constants a , b and c in equation [7-29] were calculated to be $161.512 \text{ J K}^{-1} \text{ mol}^{-1}$, $0.0176097 \text{ J K}^{-2} \text{ mol}^{-1}$ and $-3841843 \text{ J K mol}^{-1}$, respectively. That is, the relationship between the standard molar heat capacity of hercynite and temperature was found to be:

$$C_p^\circ = 161.512 + 0.0176097T - 3841843T^{-2} \quad [7-33]$$

One is now able to make a thermodynamic table for hercynite. The standard molar heat capacity, C_p° , is given by equation [7-33], and the standard entropy, S° , is easily calculated by,

$$\begin{aligned} S^\circ &= S_{298.15\text{K}}^\circ + \int_{298.15\text{K}}^T \frac{C_p^\circ}{T} dT \\ &= S_{298.15\text{K}}^\circ + a \ln\left(\frac{T}{298.15\text{K}}\right) + b(T - 298.15\text{K}) - \frac{c}{4}(T^{-4} - 298.15\text{K}^{-4}) \end{aligned} \quad [7-34]$$

since $S_{298.15\text{K}}^\circ$ is known.

The difference $H^\circ - H_{298.15\text{K}}^\circ$ is given by the relationship,

$$\begin{aligned} H^\circ - H_{298.15\text{K}}^\circ &= \int_{298.15\text{K}}^T C_p^\circ dT \\ &= a(T - 298.15\text{K}) + \frac{b}{2}(T^2 - 298.15\text{K}^2) - c(T^{-1} - 298.15\text{K}^{-1}) \end{aligned} \quad [7-35]$$

Equation [7-27] gives the change in standard enthalpy for reaction [7-2] at 1600 K, *i.e.* $\Delta H_{1600\text{K}}^\circ = -270615 \text{ J mol}^{-1}$. Combination of $\Delta H_{1600\text{K}}^\circ$ for reaction [7-2] and the standard enthalpies of Fe(s) , $\text{O}_2(\text{g})$ and $\text{Al}_2\text{O}_3(\text{s}, \alpha)$, given in Table 7-2, gives the standard enthalpy of hercynite at 1600 K, *i.e.* $H_{1600\text{K}}^\circ = -1719165 \text{ J mol}^{-1}$. The standard enthalpy at 298.15 K, $H_{298.15\text{K}}^\circ$, of hercynite is then calculated by subtracting the term $H_{1500\text{K}}^\circ - H_{298.15\text{K}}^\circ$, derived from equation [7-35]. This gives $H_{298.15\text{K}}^\circ = -1940703 \text{ J mol}^{-1}$. H° is then easily found by adding the terms $H^\circ - H_{298.15\text{K}}^\circ$ and $H_{298.15\text{K}}^\circ$. The standard Gibbs energy of hercynite, G° , is calculated from H° and S° . The expression $-(G^\circ - H_{298.15\text{K}}^\circ)/T$ is then calculated from $H^\circ - H_{298.15\text{K}}^\circ$ and S° . The results of the calculations are given in Table 7-3. Thermodynamic data for hercynite taken from Barin (1995) are listed in Table 7-4 for comparison.

Table 7-3 Revised thermodynamic data for FeAl_2O_4 .

T K	C_p° ← J K ⁻¹ mol ⁻¹ →	S° J K ⁻¹ mol ⁻¹	$-(G^\circ - H^\circ_{298.15\text{K}})/T$ →	H° ← J mol ⁻¹ →	$H^\circ - H^\circ_{298.15\text{K}}$ J mol ⁻¹	G° →
298.15	123.544	106.299	106.299	-1940703	0	-1972396
300.00	124.108	107.331	106.567	-1940473	229	-1972673
400.00	144.545	155.556	121.068	-1926907	13795	-1989130
500.00	154.950	193.357	135.721	-1911885	28818	-2008563
600.00	161.406	224.565	150.137	-1896046	44657	-2030785
700.00	165.998	251.223	164.026	-1879664	61038	-2055521
800.00	169.597	274.551	177.271	-1862878	77824	-2082520
900.00	172.618	295.336	189.848	-1845764	94938	-2111566
1000.00	175.280	314.114	201.778	-1828367	112336	-2142480
1100.00	177.708	331.268	213.099	-1810716	129987	-2175111
1200.00	179.976	347.083	223.856	-1792831	147872	-2209330
1300.00	182.132	361.772	234.096	-1774724	165978	-2245027
1400.00	184.206	375.502	243.862	-1756407	184296	-2282110
1500.00	186.219	388.406	253.195	-1737885	202817	-2320494
1600.00	188.187	400.591	262.130	-1719165	221538	-2360110
1700.00	190.119	412.143	270.700	-1700249	240454	-2400893
1800.00	192.024	423.136	278.936	-1681142	259561	-2442787
1900.00	193.906	433.630	286.862	-1661845	278858	-2485741
2000.00	195.771	443.675	294.504	-1642361	298342	-2529711

Table 7-4 Thermodynamic data for FeAl_2O_4 taken from Barin (1995).

T K	C_p° ← J K ⁻¹ mol ⁻¹ →	S° J K ⁻¹ mol ⁻¹	$-(G^\circ - H^\circ_{298.15\text{K}})/T$ →	H° ← J mol ⁻¹ →	$H^\circ - H^\circ_{298.15\text{K}}$ J mol ⁻¹	G° →
298.15	123.544	106.299	106.299	-1995070	0	-2026992
300.00	124.025	107.064	106.301	-1995070	229	-2027189
400.00	141.874	145.503	111.421	-1981666	13633	-2039867
500.00	151.540	178.287	121.602	-1966956	28343	-2056100
600.00	157.986	206.517	133.457	-1951463	43836	-2075373
700.00	162.910	231.255	145.697	-1935409	59890	-2097287
800.00	167.024	253.283	157.794	-1918907	76392	-2121534
900.00	170.667	273.170	169.526	-1902020	93279	-2147873
1000.00	174.017	291.327	180.811	-1884784	110515	-2176110
1100.00	177.176	308.062	191.629	-1867223	128076	-2206091
1200.00	180.204	323.609	201.987	-1849353	145946	-2237683
1300.00	183.141	338.149	211.908	-1831185	164114	-2270779
1400.00	186.012	351.827	221.418	-1812727	182572	-2305284
1500.00	188.833	364.757	230.547	-1793984	201315	-2341119
1600.00	191.616	377.033	239.322	-1774961	220338	-2378214
1700.00	194.371	388.732	247.769	-1755662	239637	-2416507
1800.00	197.103	399.920	255.777	-1736088	259211	-2455943
1900.00	199.817	410.649	263.777	-1716242	279057	-2496475
2000.00	202.480	420.967	271.380	-1696125	299174	-2538059

7.3.3 Thermodynamics of Solid Iron Phases in Equilibrium with Cryolite-Alumina Melts

With the newly obtained thermodynamic data for hercynite, it is possible to make a predominance area diagram for the solid iron phases in equilibrium with the solutions. There are two key parameters: the oxygen potential and the activity of alumina. The latter enters since hercynite is stable if the alumina activity is above a given alumina activity. Dewing and Thonstad (2000) have already published such a diagram ($T = 1293 \text{ K}$). The standard Gibbs energies of formation of wustite ($\text{Fe}_{0.947}\text{O}$), magnetite (Fe_3O_4) and hematite (Fe_2O_3) were taken from JANAF (1985), while Dewing and Thonstad (2000) used data by Rezhukhina *et al.* (1963) and by Chan *et al.* (1973) for hercynite (FeAl_2O_4). The standard Gibbs energy of formation of hercynite corresponds to the average value of equations [7-10] and [7-18] at 1293 K. For comparison, the original data by Dewing and Thonstad (2000) were used throughout these calculations. All their data, together with the standard Gibbs energy of formation of hercynite found in this work (equation [7-27]), are presented in Table 7-5.

Table 7-5 Standard Gibbs energy of formation at 1293 K.

Compound	$\Delta G^\circ / \text{J mol}^{-1}$	Reference
$\text{Fe}_{0.947}\text{O}$	-180299	JANAF (1985)
Fe_3O_4	-703897	JANAF (1985)
Fe_2O_3	-489299	JANAF (1985)
FeAl_2O_4	-203344	Rezhukhina <i>et al.</i> (1963) and Chan <i>et al.</i> (1973)
FeAl_2O_4	-197226	This work

To construct the predominance area diagram the oxygen pressure and the activity of iron have to be calculated for each equilibrium. If the data in Table 7-5 are used, the equilibrium $\text{Fe}_3\text{O}_4\text{-Fe}_2\text{O}_3$ would be represented by the equations [7-36] and [7-37],

$$3 \log a_{\text{Fe}} + 2 \log p_{\text{O}_2} = -28.435 \quad [7-36]$$

$$2 \log a_{\text{Fe}} + \frac{3}{2} \log p_{\text{O}_2} = -19.766 \quad [7-37]$$

By combining these two equations, the equilibrium oxygen pressure and the activity of iron are found. As seen from the equations, these values will be independent of the alumina activity. On the other hand, the equilibrium $\text{FeAl}_2\text{O}_4\text{-Fe}_3\text{O}_4$ would be represented by equations [7-36] and [7-38] if the newly obtained data for hercynite are used.

$$\log a_{\text{Fe}} + \frac{1}{2} \log p_{\text{O}_2} + \log a_{\text{Al}_2\text{O}_3} = -7.968 \quad [7-38]$$

If equations [7-36] and [7-38] are combined, the following relationship is obtained:

$$\log p_{\text{O}_2} = -9.232 + 6 \log a_{\text{Al}_2\text{O}_3} \quad [7-39]$$

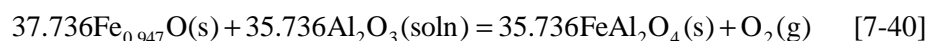
The equilibrium $\text{FeAl}_2\text{O}_4\text{-Fe}_3\text{O}_4$ is, therefore, dependent of the alumina activity. By using the standard Gibbs energies given in Table 7-5, equilibrium oxygen pressures and activities of iron were calculated for all possible combinations. The results are given in Table 7-6. Activity data for alumina were taken from Dewing and Thonstad (1997).

Table 7-6 Equilibrium oxygen pressures and iron activities at 1293 K.

Equilibrium	$\log(p_{\text{O}_2})$	$\log(a_{\text{Fe}})$	$\log(a_{\text{Fe}} p_{\text{O}_2}^{1/2})$	$\log(a_{\text{Fe}} p_{\text{O}_2}^{3/4})$
1. $\text{Fe-Fe}_{0.947}\text{O}$	-14.567	0.000	-7.283	-10.925
2. $\text{Fe}_{0.947}\text{O-Fe}_3\text{O}_4$	-12.887	-0.887	-7.330	-10.552
3. $\text{Fe}_3\text{O}_4\text{-Fe}_2\text{O}_3$	-4.856	-6.241	-8.669	-9.883
4. $\text{Fe}_2\text{O}_3\text{-O}_2$	0.000	-9.883	-9.883	-9.883
5. $\text{Fe-FeAl}_2\text{O}_4$ ($a_{\text{Al}_2\text{O}_3} = 1$)	-16.454	0.000	-8.227	-12.340
6. $\text{FeAl}_2\text{O}_4\text{-Fe}_3\text{O}_4$ ($a_{\text{Al}_2\text{O}_3} = 1$)	-7.646	-4.381	-8.204	-10.115
7. $\text{Fe-FeAl}_2\text{O}_4$ ($a_{\text{Al}_2\text{O}_3} = 1$)	-15.879	0.000	-7.940	-11.910
8. $\text{FeAl}_2\text{O}_4\text{-Fe}_3\text{O}_4$ ($a_{\text{Al}_2\text{O}_3} = 1$)	-9.232	-3.324	-7.940	-10.248

The values given for the equilibria 1 to 6 in Table 7-6 are consistent with those calculated by Dewing and Thonstad (2000), while the values for the equilibria 7 and 8 correspond to the new thermodynamic data obtained for hercynite in the present work. The predominance area diagram for solid iron phases at 1293 K is shown in Figure 7.6.

Figure 7.6 shows that the equilibrium between $\text{Fe}_{0.947}\text{O}$ and FeAl_2O_4 is not represented by a vertical line. The reason for this is that $\text{Fe}_{0.947}\text{O}$ is non-stoichiometric, and, hence, this equilibrium becomes dependent of the partial oxygen pressure:



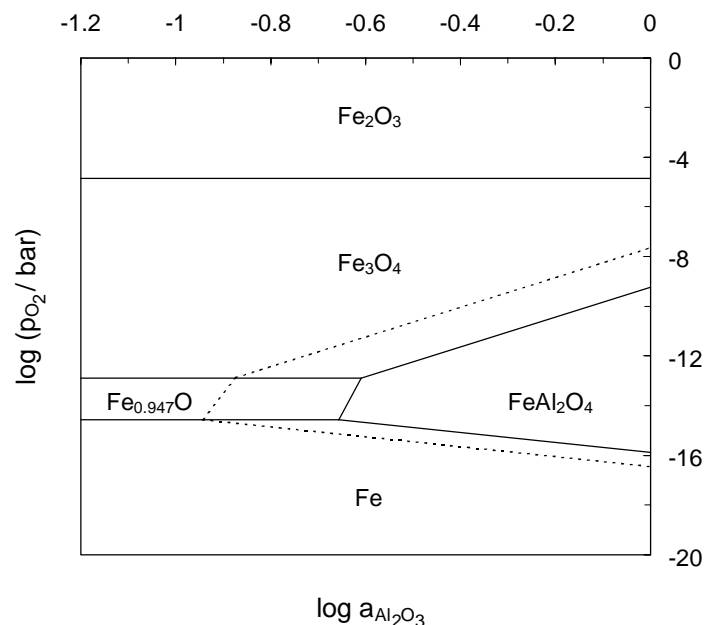
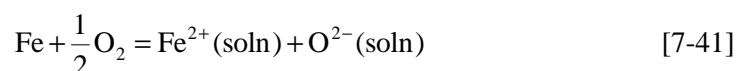


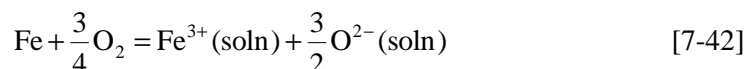
Figure 7.6 Predominance area diagram for solid iron phases at 1293 K. The original calculations by Dewing and Thonstad (2000) are indicated by the dotted lines.

7.3.4 Stability of Iron-Containing Ions in Solution

In the most general case one may expect that solutions of iron oxides in molten cryolite will contain both Fe(II) and Fe(III) species. Since solubility data for both Fe(II) and Fe(III) species in cryolite-alumina melts are available, it should be possible to derive the relationship between the iron ion with the predominant valency (*e.g.* Fe(II)) and its opposing valency (*e.g.* Fe(III)) at a given alumina activity, if we assume that Henry's law holds. Dewing and Thonstad (2000) have derived a procedure for such calculations. It is convenient to take the partial pressure of oxygen as the fundamental independent parameter since, once it is specified, the solid phase in equilibrium is defined and the remaining parameter, the activity of iron, can be calculated. One can then treat the two dissolution reactions as,



and,



It should be noted that these two equations are purely formal; nothing is assumed about the chemical environment in which either the iron ions or the oxide ions find themselves. Then, for a fixed composition of solvent,

$$[\text{Fe}^{2+}] = K_1 a_{\text{Fe}} p_{\text{O}_2}^{1/2} \quad [7-43]$$

and,

$$[\text{Fe}^{3+}] = K_2 a_{\text{Fe}} p_{\text{O}_2}^{3/4} \quad [7-44]$$

Square brackets indicate concentrations (conveniently in wt%), and the K 's are constants. Since pressures are in bar, the dimensions of K_1 and K_2 are $\text{wt}\% \text{ bar}^{1/2}$ and $\text{wt}\% \text{ bar}^{3/4}$, respectively. For all practical purposes an experiment performed in the laboratory under normal atmospheric pressure may be regarded as being at one bar. Specification of a fixed solvent composition, *i.e.* a fixed NaF/AlF_3 ratio and a fixed concentration of alumina, is important since AlF_3 may be involved in the dissolution reaction, and the alumina concentration controls the activity of O^{2-} ion. It is only if the activities of AlF_3 and Al_2O_3 are held constant, that the above simple relations can be expected to hold.

The solubility of Fe(III) in cryolite-alumina melts at 1293 K was discussed in section 3.3.3. The data by Diep (1998) (obtained under one atmosphere of oxygen) gave the following relationship:

$$\log(\text{wt}\% \text{ Fe}) = -0.15 \log a_{\text{Al}_2\text{O}_3} - 0.75 \quad [7-45]$$

Similarly, the solubilities of iron (obtained in an iron crucible and under one atmosphere of argon) were found (section 3.3.2) to be, when alumina activities are lower and greater than 0.195, respectively,

$$\log(\text{wt}\% \text{ Fe}) = -0.40 \log a_{\text{Al}_2\text{O}_3} + 0.11 \quad [7-46]$$

and,

$$\log(\text{wt}\% \text{ Fe}) = -1.26 \log a_{\text{Al}_2\text{O}_3} - 0.49 \quad [7-47]$$

Melts saturated with alumina and with a NaF/AlF_3 ratio of three satisfy the above condition. Equation [7-45] gives the solubility in an alumina-saturated melt under one atmosphere of oxygen as 0.178 wt% Fe. In a similar melt, but in an iron crucible, equation [7-47] gives the solubility as 0.324 wt% Fe. Figure 7.6 shows that the

equilibrium solid phase would have been Fe_2O_3 when an atmosphere of oxygen was applied, while it would have been FeAl_2O_4 in the case where an iron crucible was used. Values of $a_{\text{Fe}}(\text{pO}_2)^{1/2}$ and $a_{\text{Fe}}(\text{pO}_2)^{3/4}$ can be taken from Table 7-6, and equations [7-43] and [7-44] can be solved simultaneously for K_1 and K_2 as shown in Table 7-7.

Table 7-7 Iron solubilities in alumina-saturated melts at 1293 K.

	Fe(II)	+	Fe(III)	=	Total Fe
1 atm O_2 :	$1.309 \times 10^{-10} K_1$	+	$1.309 \times 10^{-10} K_2$	=	0.178
Fe crucible:	$1.149 \times 10^{-8} K_1$	+	$1.231 \times 10^{-12} K_2$	=	0.324
$K_1 = 2.80 \times 10^7$			$K_2 = 1.33 \times 10^9$		

One then finds that under one atmosphere of oxygen, 2.06 % of the total iron in solution is present in the form of Fe(II), while in the iron crucible 0.51 % of the total is present as Fe(III). Similar calculations, *i.e.* to solve for K_1 and K_2 at a fixed alumina concentration, were performed in steps of 0.5 wt% alumina for the entire range. The results are shown in Figure 7.7.

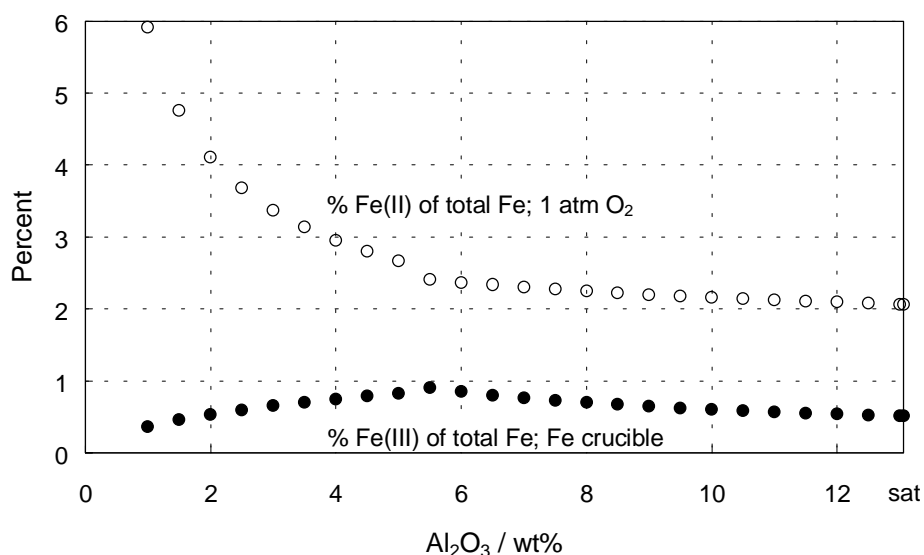


Figure 7.7 Influence of the alumina concentration on the stabilities of Fe(II) and Fe(III) species at 1293 K.

Figure 7.7 shows that there is a discontinuity between the calculated points at 5.0 and 5.5 wt% alumina. Equation [7-45] was used to calculate the iron solubility under one atmosphere of oxygen, while the solubility of iron in an iron crucible was given by equation [7-46] if the alumina activity was less than 0.195 (= 5.03 wt% Al_2O_3), or equation [7-47] if the alumina activity was greater. As can be seen, neither equation [7-46] nor equation [7-47] have slopes in exact accordance with theory, *i.e.* $-0.40 \neq -1/3$ and $-1.26 \neq -4/3$. The difference between the empirical slopes is only 0.86 compared with the theoretical value of one. A discontinuity is therefore inevitable when calculations based upon theoretical principles are performed with empirical equations.

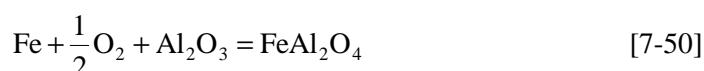
With values for K_1 and K_2 one can now calculate the equilibrium quantities of Fe(II) and Fe(III) in melts with fixed alumina concentrations at all oxygen pressures (*i.e.* along a vertical line in Figure 7.6). Equations [7-43] and [7-44] on a logarithmic form give,

$$\log[\text{Fe}^{2+}] = \log a_{\text{Fe}} + \frac{1}{2} \log p_{\text{O}_2} + \log K_1 \quad [7-48]$$

and,

$$\log[\text{Fe}^{3+}] = \log a_{\text{Fe}} + \frac{3}{4} \log p_{\text{O}_2} + \log K_2 \quad [7-49]$$

The formation reaction of FeAl_2O_4 is simply given by,



Transformation of this equation into a logarithmic expression gives,

$$\log a_{\text{Fe}} + \frac{1}{2} \log p_{\text{O}_2} = \log K \quad [7-51]$$

where K is the equilibrium constant at a given alumina concentration. When equation [7-51] is combined with equations [7-48] and [7-49], the following relationships are found between the partial oxygen pressure and the concentrations of Fe(II) and Fe(III) in the FeAl_2O_4 region:

$$\log[\text{Fe}^{2+}] = \log(K_1 K) \quad [7-52]$$

$$\log[\text{Fe}^{3+}] = \frac{1}{4} \log p_{\text{O}_2} + \log(K_2 K) \quad [7-53]$$

This means that in the FeAl₂O₄ region, or the 'FeO' (= Fe_{0.947}O) region depending on the alumina concentration, the concentration of Fe(II) is constant but the concentration of Fe(III) goes up as the oxygen pressure is raised. Similar deductions can be made for the Fe₃O₄ and Fe₂O₃ regions. The formation reaction of Fe₃O₄ gives,

$$3 \log a_{\text{Fe}} + 2 \log p_{\text{O}_2} = \log K \quad [7-54]$$

and when combined with equation [7-48] and equation [7-49], the following relationships are found:

$$\log[\text{Fe}^{2+}] = -\frac{1}{6} \log p_{\text{O}_2} + \log(K_1 K) \quad [7-55]$$

$$\log[\text{Fe}^{3+}] = \frac{1}{12} \log p_{\text{O}_2} + \log(K_2 K) \quad [7-56]$$

The formation reaction of Fe₂O₃ gives,

$$2 \log a_{\text{Fe}} + \frac{3}{2} \log p_{\text{O}_2} = \log K \quad [7-57]$$

and when combined with equation [7-48] and equation [7-49], the following relationships are found:

$$\log[\text{Fe}^{2+}] = -\frac{1}{4} \log p_{\text{O}_2} + \log(K_1 K) \quad [7-58]$$

$$\log[\text{Fe}^{3+}] = \log(K_2 K) \quad [7-59]$$

This means that in the Fe₂O₃ region the Fe(III) is constant and the Fe(II) goes down as the oxygen pressure is raised, while in the Fe₃O₄ region both vary. Figures 7.8 to 7.11 show the situation in melts with alumina concentrations 1.5 wt%, 4.5 wt%, 6.5 wt% and alumina saturation. On log-log plots such as these the lines for the concentrations of Fe(II) and Fe(III) are straight within the stability range of any one solid phase, so that the figures are easily constructed from the data in Table 7-6.

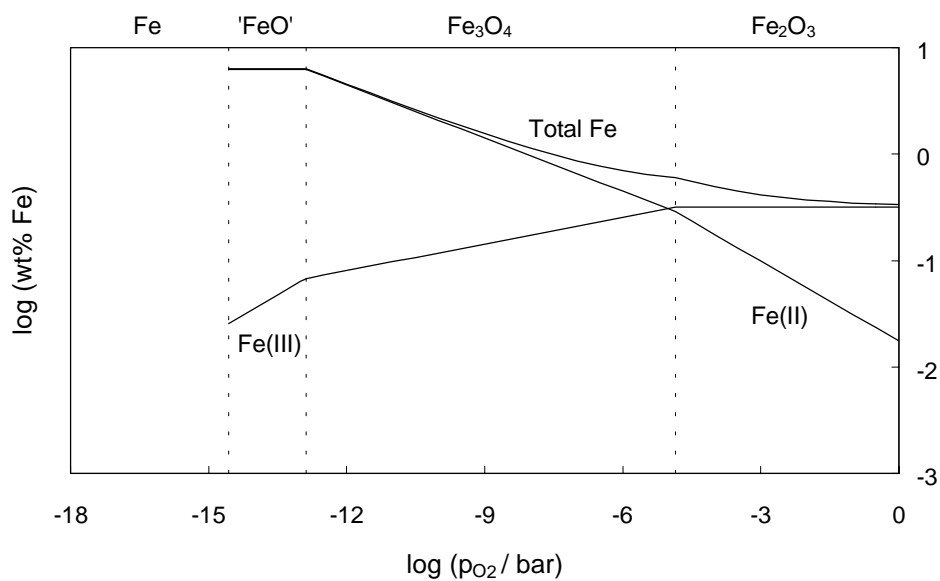


Figure 7.8 Concentrations of Fe(II), Fe(III), and total Fe in solution in melts at 1293 K containing 1.5 wt% Al_2O_3 .

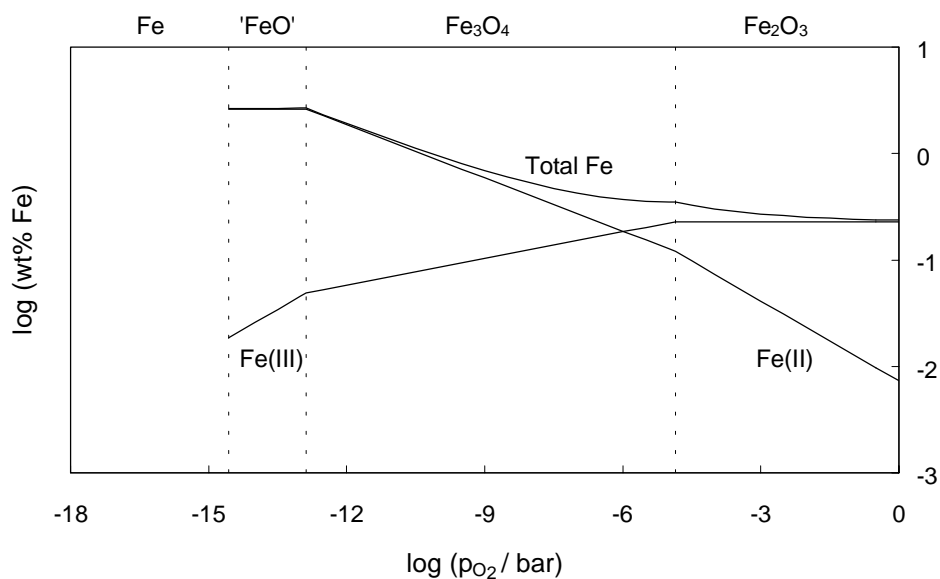


Figure 7.9 Concentrations of Fe(II), Fe(III), and total Fe in solution in melts at 1293 K containing 4.5 wt% Al_2O_3 .

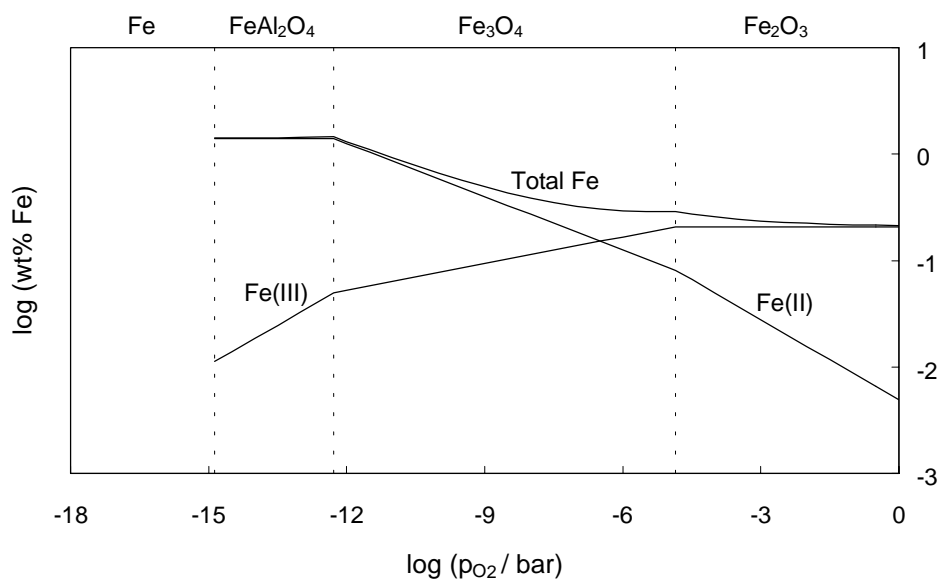


Figure 7.10 Concentrations of Fe(II) , Fe(III) , and total Fe in solution in melts at 1293 K containing 6.5 wt% Al_2O_3 .

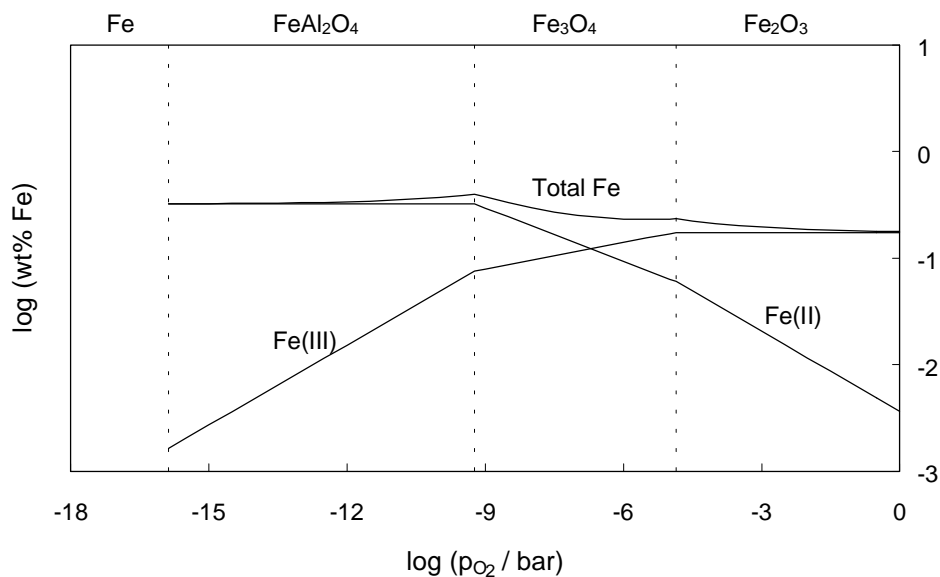


Figure 7.11 Concentrations of Fe(II) , Fe(III) , and total Fe in solution in melts at 1293 K saturated with Al_2O_3 .

7.3.5 The Standard Potential of the Redox Couple Fe(III)/Fe(II)

The standard potential for the Fe(III)/Fe(II) redox reaction can be derived from the intercept at which the two concentrations are equal in Figures 7.8 to 7.11. By combining equations [7-43] and [7-44] one gets,

$$K_1 a_{\text{Fe}} p_{\text{O}_2}^{1/2} = K_2 a_{\text{Fe}} p_{\text{O}_2}^{3/4} \quad [7-60]$$

Rearrangement gives,

$$p_{\text{O}_2}^{1/4} = \frac{K_1}{K_2} \quad [7-61]$$

The standard potential with respect to a reversible oxygen electrode ($n = 4$) for the reaction,



would therefore be given by,

$$E^\circ = \frac{RT}{nF} \ln(p_{\text{O}_2}) = \frac{RT}{F} \ln\left(\frac{K_1}{K_2}\right) \quad [7-63]$$

when combined with equation [7-61]. The standard potential was calculated as a function of alumina activity in steps of 0.5 wt% alumina, and the result is displayed in Figure 7.12.

Figure 7.12 shows that the standard potential of the redox couple Fe(III)/Fe(II) with respect to a reversible oxygen electrode decreases with increasing alumina concentration. Again, as discussed above, the discontinuity observed between the alumina concentrations 5.0 and 5.5 wt% is caused by use of equations [7-46] and [7-47] for the solubility of iron in cryolite-alumina melts contained in iron crucibles.

The reversible potential of the redox couple Fe(III)/Fe(II) with respect to a reversible oxygen electrode was determined by cyclic voltammetry (see section 5.3.2). The experiments were performed in molten cryolite-alumina melts at different temperatures (1243 - 1293 K). The alumina concentrations were varied from 3.0 wt% to saturation. Since the alumina activity data given by Dewing and Thonstad (1997) only apply at 1293 K, the alumina concentrations were transformed into activities with data taken from Solheim and Sterten (1999). These results are incorporated in Figure 7.12. Although some of the reversible potentials were obtained at temperatures slightly lower than 1293 K, the agreement is satisfactory.

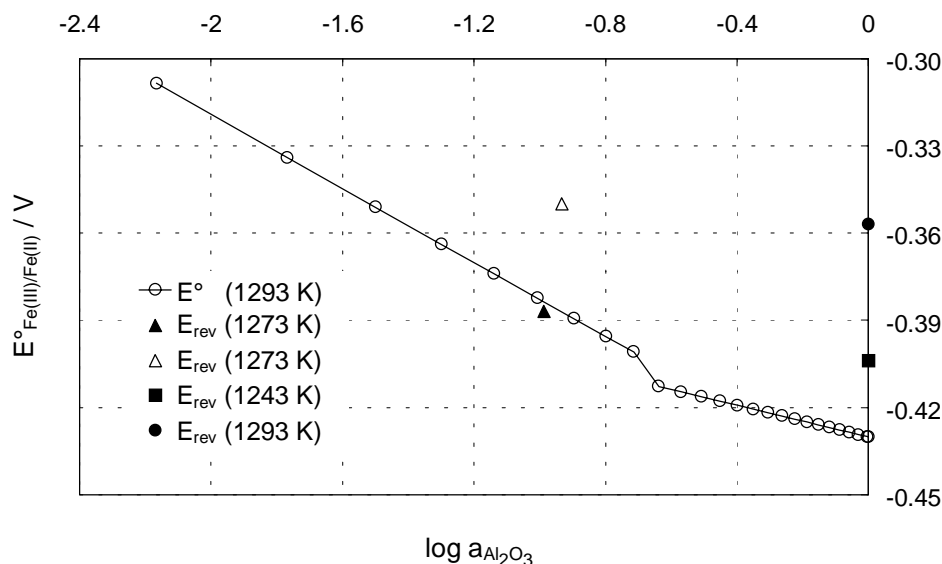
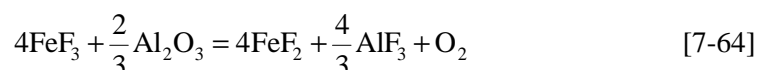
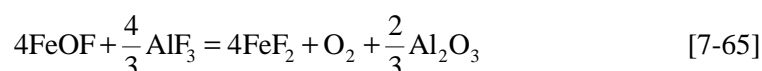


Figure 7.12 Standard potential (E°) for the Fe(III)/Fe(II) redox couple with respect to a reversible oxygen electrode at 1293 K as a function of the alumina activity. Reversible potentials (E_{rev}) found by cyclic voltammetry at different temperatures are also indicated in the plot.

Dewing and Thonstad (2000) obtained a shift of the standard potential for Fe(III)/Fe(II) to a more negative value (lower oxygen pressure) at a lower alumina activity. This is consistent with Fe(II) and Fe(III) both being present as fluorides. If the equilibrium is,



one would expect $\partial \log(p_{\text{O}_2}) / \partial \log(a_{\text{Al}_2\text{O}_3})$ to be $2/3$; their value was 0.72. It was commented by Dewing and Thonstad (2000) that it was impossible to make any assessment of its accuracy since the value 0.72 was being based on only two points. A closer look at Figure 7.12 shows that a negative value is obtained in the present work for the relation $\partial \log(p_{\text{O}_2}) / \partial \log(a_{\text{Al}_2\text{O}_3})$, in contrast to the positive value of Dewing and Thonstad (2000). This implies that one of the iron species is associated with oxide (O^{2-}), and it is consistent with the results obtained in Chapter 3, *i.e.* Fe(III) is associated with one oxide ion while Fe(II) is not. If the equilibrium is (assuming the simplest possible species),



one would expect $\partial \log(p_{\text{O}_2})/\partial \log(a_{\text{Al}_2\text{O}_3})$ to be $-2/3$. If the standard potentials given in Figure 7.12 are used, a slope of -0.87 is obtained. Taking into account the problem with the discontinuity as discussed above, the agreement is satisfactory.

To put the results for the standard potential of the Fe(III)/Fe(II) equilibrium in the context of the Hall-Héroult process is not entirely straightforward. The commercial process operates at a temperature some 60 degrees lower than that at which these calculations were made, and the commercial electrolyte normally contains CaF_2 and some additional AlF_3 . However, Figure 7.13 shows what should be a reasonable approximation to the situation.

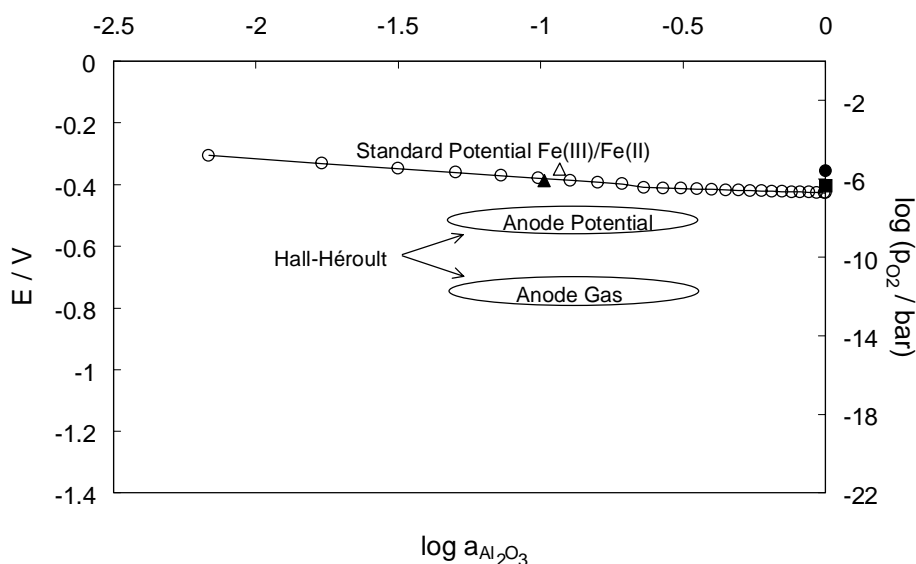
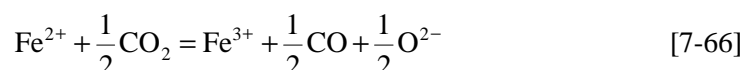


Figure 7.13 Operating region of the Hall-Héroult cell referred to the oxygen electrode, with the data given in Figure 7.12 incorporated.

The reversible C/CO_2 potential lies 1 V below the reversible O_2 potential (Outokumpu HSC Chemistry[®]), but a carbon anode working at around 1 A cm^{-2} current density operates at an overpotential of about 0.55 V (Dewing 1991), and hence it lies at -0.45 V with respect to oxygen. There is some uncertainty regarding this value, and it will become more positive at low alumina contents in the electrolyte (Thonstad 1970). The escaping anode gas, consisting of CO_2 with 10 - 20 % CO , has an equilibrium oxygen potential of -0.76 to -0.81 V (Outokumpu HSC Chemistry[®]). With the standard Fe(III)/Fe(II) potential at around -0.3 to -0.4 V , it looks as if the anode gas cannot be an effective oxidant of Fe(II) in solution, although the anode itself may cause some oxidation. The additional AlF_3 in a commercial electrolyte will push the

reversible Fe(III)/Fe(II) potential in the positive direction (equation [7-65]) making it even harder to oxidise Fe(II).

Sterten (1991) and Sterten and Solli (1995) proposed a model with detailed descriptions of the chemical reactions and transport processes leading to loss in current efficiency with respect to aluminium. They suggested that polyvalent impurity species are involved in cyclic redox reactions in the electrode and in the gas boundary layers. Using iron as an example, the reaction,



was suggested to take place within the electrolyte/anode gas boundary layer (*i.e.* with CO and CO_2 dissolved in the cryolitic melt). Based on the discussion above, the question whether there is a significant contribution to the observed loss of faradaic efficiency from Fe(III)/Fe(II) redox cycle thus remains open, but on the basis of the available information, this seems unlikely. If one had a stable anode generating oxygen, however, the chance of establishing such a cycle would appear to be high, although the ultimate loss of faradaic efficiency might not be significant, since the amount of iron which could be tolerated in solution would be low for other reasons.

References to Chapter 7

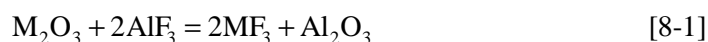
- Barin, I. (1995): Thermochemical Data of Pure Substances, 3rd Edition, VCH Verlagsgesellschaft mb-H, Weinheim, Germany.
- Brokloff, J. E., L. H. Van Vlack and R. A. Flinn (1965): Iron-Alumina Reactions at Steel Casting Temperatures, *Cast Metals Res. J.*, **1**(3), 43.
- Chan, J. C., C. B. Alcock and K. T. Jacob (1973): Electrochemical Measurement of the Oxygen Potential of the System Iron-Alumina-Hercynite in the Temperature Range 750 to 1600 °C, *Can. Met. Quart.*, **12**, 439.
- Dewing, E. W. (1991): The Chemistry of the Alumina Reduction Cell, *Can. Met. Quart.*, **30**, 153.
- Dewing, E. W. and J. Thonstad (1997): Activities in the System Cryolite-Alumina, *Metall. Mater. Trans. B*, **28B**, 1089.
- Dewing, E. W. and J. Thonstad (2000): Solutions of Iron Oxides in Molten Cryolite, *Metall. Mater. Trans. B*, **31B**, 609.
- Floridis, T. P. (1957): Activity of Oxygen in Liquid Iron Alloys, D.Sc. Thesis, Massachusetts Institute of Technology. Sited by Pillay *et al.* (1960).

- Holmes, R. D., H. St. C. O'Neill and R. J. Arculus (1986): Standard Gibbs Free Energy of Formation for Cu_2O , NiO , CoO , and Fe_xO : High Resolution Electrochemical Measurements Using Zirconia Solid Electrolytes from 900 - 1400 K, *Geochim. Cosmochim. Acta*, **30**, 2439.
- JANAF Thermochemical Tables (1985): 3rd Edition, *J. Phys. Chem. Ref. Data*, vol. 14, Suppl. no 1.
- Kachanovskaya, I. S., V. I. Osovik and T. N. Kukhotkina (1971): Phase Transformations and Alumina Dissolution in Cryolite, *Sov. J. Non Ferrous Met.*, **12**(10), 44.
- McLean, A. and R. G. Ward (1966): Thermodynamics of Hercynite Formation, *J. Iron Steel Inst.*, **204**, 8.
- Outokumpu HSC Chemistry[®] for Windows, Chemical Reaction and Equilibrium Software with extensive Thermochemical Database, Version 3.0, Outokumpu Research Oy, Pori, Finland.
- Pillay, T. C. M., J. D'Entremont and J. Chipman (1960): Stability of Hercynite at High Temperatures, *J. Am. Chem. Soc.*, **43**, 583.
- Rezukhina, T. N., V. A. Levitskii and P. Ozhegov (1963): Thermodynamic Properties of Iron Aluminate, *Russ. J. Phys. Chem.*, **37**, 358.
- Solheim, A. and Å. Sterten (1999): Activity of Alumina in the System $\text{NaF-AlF}_3\text{-Al}_2\text{O}_3$ at NaF/AlF_3 Molar Ratios Ranging from 1.4 to 3, in *Light Metals 1999*, C. E. Eckert, Editor, TMS, Warrendale, PA, p. 445.
- Sterten, Å. (1991): Redox Reactions and Current Loss in Aluminium Reduction Cells, in *Light Metals 1991*, E. L. Rooy, Editor, TMS, Warrendale, PA, p. 445.
- Sterten, Å. and P. A. Solli (1995): Cathodic Process and Cyclic Redox Reactions in Aluminium Electrolysis Cells, *J. Appl. Electrochem.*, **25**, 809.
- Thonstad, J. (1970): The Electrode Reaction on the C, CO_2 Electrode in Cryolite-Alumina Melts – I. Steady State Measurements, *Electrochim. Acta*, **15**, 1569.
- Wefers, K. and C. Misra (1987): Oxides and Hydroxides of Aluminium, Alcoa Technical Paper No. 19, Revised, Alcoa Laboratories.

8 Mass Transfer of the Impurities Fe, Si and Ti between Bath and Aluminium in Industrial Hall-Héroult Cells

8.1 Introduction

Impurities are always present in the electrolyte (bath) in industrial Hall-Héroult cells, iron and silicon being the major metallic impurities. These impurities originate from raw materials and are continuously introduced to the bath by the alumina feed, anode materials, equipment and silicon carbide sideling. The major source is the alumina, and in that case the impurities are introduced to the process as metal oxides, and they may dissolve according to a scheme like,

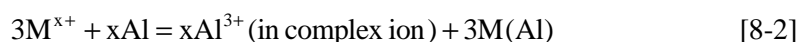


which applies for a trivalent cation (Thonstad 1999). The concentration of impurities in the bath is normally well below their solubility limits (Metson 1997).

There are several reasons for investigating the behaviour of impurities such as iron, silicon and titanium in industrial Hall-Héroult cells:

- (a) They are responsible for most of the aluminium contamination.
- (b) They have a negative effect on the current efficiency (CE).
- (c) Impurity concentrations in the bath have increased due to the use of dry scrubbers.
- (d) Little data have been found in the literature on the mass transfer of impurities between bath and aluminium metal in industrial cells.

The bath impurities iron, silicon and titanium contaminate the produced aluminium metal because their oxides have a lower decomposition potential than alumina. According to Grjotheim (1985), these metal oxides are reduced at the cathode either electrochemically or chemically by the exchange reaction:



For most elements this reaction is shifted far to the right (Thonstad 1999).

The influence on the CE by impurities present in the bath has been investigated in laboratory cells under argon atmosphere both by Deininger and Gerlach (1979) and by Sterten *et al.* (1998). The elements were added as Fe_2O_3 , Ga_2O_3 , P_2O_5 , SiO_2 , TiO_2 , V_2O_5 and ZnO . Both investigations showed that these impurity elements have a negative effect on the CE. Table 8-1 shows how the CE is influenced by the presence of impurities in the bath.

Table 8-1 Reduction in CE (in %) by addition of 0.01 wt% of impurity cations: (1) Sterten *et al.* (1998) and (2) Deininger and Gerlach (1979).

Impurity	$\Delta\text{CE}(1)$	$\Delta\text{CE}(2)$
Fe	0.23 ± 0.04	0.3
Ga	0.14 ± 0.08	-
P	0.68 ± 0.18	0.95
Si	0.31 ± 0.12	-
Ti	0.24 ± 0.14	0.75
V	0.26 ± 0.04	0.65
Zn	0.13 ± 0.03	-

The pollution control system most frequently employed in the aluminium industry is the dry scrubbing system (Grjotheim *et al.* 1982). This system exerts an emission control mainly through the ability of alumina to absorb gaseous hydrogen fluoride. The alumina, however, will retain other constituents in the cell off-gas as well, such as SO_2 , various polyaromatic hydrocarbons (PAH's) and heavy metals in the form of solid particles or gaseous complex molecules. The efficiency of a dry scrubber depends on the design details, operating conditions and above all on the properties of the alumina used.

The dry scrubber alumina (secondary alumina) is fed back to the cells. Although these systems have proved beneficial in diminishing the fluoride pollution problem, an increasing concern has been expressed over the fact that the secondary alumina gives rise to an increasing concentration of impurities in the bath. In this context the distribution of impurities between the metal, the bath and the gas phase is of prime interest.

Ishihara and Mukai (1965, 1966) have made a thorough investigation on the distribution of impurities in the major constituents entering the electrolytic process. Their findings are presented in Table 8-2. To correlate their results with the overall mass balance of the process, the values of concentrations of impurities in the raw materials should be multiplied by a factor of 1.9 for alumina, since 1.89 kg Al_2O_3 gives

1 kg Al, and 0.40 - 0.45 for carbon anodes, since 0.40 - 0.45 kg C is consumed per 1 kg Al produced (Grjotheim *et al.* 1982).

Table 8-2 *Dependence of the concentration of impurities in aluminium metal on the impurities in alumina and in carbon material. From Ishihara and Mukai (1965, 1966).*

Element	Concentration (ppm) in		
	Alumina	Petroleum coke	Cell metal
B	<1	1	2
Ca	72	120	11
Cr	3	1	4
Cu	1	1	16
Fe	56	290	1330
Ga	51	14	99
Mg	5	110	24
Mn	<1	4	11
Na	3500	200	60
Ni	<1	230	10
Pb	6	3	6
Si	61	210	630
Sn	10	0.2	24
Ti	32	10	66
V	2	220	104
Zn	9	9	34

Böhm *et al.* (1976) derived data for the fraction of impurities, which followed the gas stream from three 125 kA cells. They operated a dry scrubber pilot plant with Venturi reactor and electrostatic precipitators to collect the alumina. The most effective system was obtained when placing an electrostatic precipitator in front of the reactor, in order to separate the particulates in the gas stream. It was claimed that up to 90 % of the impurities could be removed in this way. A mass balance was made, covering some of the most important impurities, as shown in Table 8-3.

Table 8-3 Mass balance of impurities in 125 kA industrial cells (concentrations in ppm). From Böhm *et al.* (1976).

Element	Fe	Ga	P	Si	Ti	V	Zn
INPUT							
Alumina	348	131	16	123	67	24	60
Anode carbon	227	2	4	173	3	33	1
Electrolyte	31	-	5	19	1	2	-
TOTAL	606	135	25	315	71	59	61
OUTPUT							
Metal	451	65	3	473	25	20	48
Potgas	378	66	18	42	41	38	12
TOTAL	829	131	21	515	66	58	60

The influence of secondary alumina on the aluminium contamination has been investigated by Thonstad *et al.* (1978) for several elements, as shown in Table 8-4. The results show that use of dry scrubbers, and thereby feeding with secondary alumina, leads to more contaminated metal.

Table 8-4 Trace element concentrations (in ppm) in raw materials, bath and metal and the increase in metal contamination caused by dry scrubbing. From Thonstad *et al.* (1978).

Element	Fe	V	Ni	Cu	Pb	Ga
Primary alumina	80	30	22	72	13	50
Secondary alumina	500	105	250	160	70	60
Anodes	600	140	-	-	-	-
Bath	40	10	5	25	6	7
Metal without secondary alumina	500	52	14	28	20	62
Metal with secondary alumina	860	95	44	55	42	85

According to Thonstad *et al.* (1978), at least four different mechanisms can be envisaged for the transfer of trace elements from the raw materials to the pot gas:

- Evaporation from raw materials, *i.e.* alumina and anodes.
- Evaporation of trace elements (compounds) dissolved in the bath.
- Chemical reactions yielding gaseous species.
- Entrainment of solid particles (alumina, carbon).

Thonstad *et al.* (1978) concluded that the transfer of the elements in Table 8-4 cannot be accounted for by evaporation from the bath only, with the exception of Pb, and entrainment of dust seemed to be important. By performing small-scale tests, they

found that the impurity level in secondary alumina could be substantially reduced by magnetic separation, or by separation of the finest fraction.

Sturm and Wedde (1998) tested an impurity stripper in order to reduce the amount of impurities in the secondary alumina, and thereby the aluminium contamination. In this context they reported the difference in metal quality produced either from primary or secondary enriched alumina, as shown in Table 8-5. By analysing the secondary alumina fine dust with respect to P_2O_5 , they found that it would only be required to separate sharply the very fine fraction below 45 μm to remove more than 70 % of the impurities. The results from laboratory tests showed a removal efficiency of 49 % of the Fe- and 67 % of the P-impurities with a fine fraction of 0.9 % of the total alumina throughput.

Table 8-5 *Impurities in the metal produced from primary and secondary alumina. From Sturm and Wedde (1998).*

Element	Impurity content in metal (wt%)		Enrichment (%)
	Primary alumina	Secondary alumina	
Cr	0.0002	0.0004	100
Fe	0.05	0.10	100
Ga	0.013	0.016	20
Ni	0.0015	0.003	100
Pb	0.0021	0.0038	80
Si	0.03	0.04	30
Ti	0.0028	0.0050	70
V	0.0026	0.0064	150

Øye (1995) calculated typical fractions of impurity elements exiting with pot emissions based on data by Thonstad *et al.* (1978) and by Augood (1980). The results are given in Table 8-6.

Table 8-6 *Typical fractions of impurity elements exiting with pot emissions. From Øye (1995).*

Element	Fe	Ga	Ni	P	Si	Ti	V	Zn
Fraction	0.50	0.50	0.40	0.88	0.08	0.59	0.80	0.20

There are few industrial investigations concerning the mass transfer between bath and aluminium. Johansen *et al.* (1977) studied the mass transfer of iron between bath and aluminium by adding Fe_2O_3 or $FeSO_4$ to a 105 kA Söderberg cell. According to them, the distribution of iron between the bath and the aluminium metal can be discussed in

terms of equation [8-2]. The equilibrium constant for equation [8-2] can, therefore, be written:

$$K = \frac{a_{\text{Fe(Al)}}^3 a_{\text{AlF}_3}^2}{a_{\text{FeF}_2}^3} \quad [8-3]$$

The equilibrium constant for equation [8-3] was reported to be $1.2 \cdot 10^{29}$ when liquid FeF_2 and solid AlF_3 were taken as standard states. This implies that if equilibrium is established, the iron content in the bath should be well below the detection limit. The transfer of iron from bath to metal was shown to be mass transfer controlled. It was found that the pick-up of iron into the metal followed an exponential curve typical for mass transfer control, as shown in Figure 8.1. The mass transfer coefficient was found to be $k = 1.25 \times 10^{-5} \text{ m s}^{-1}$.

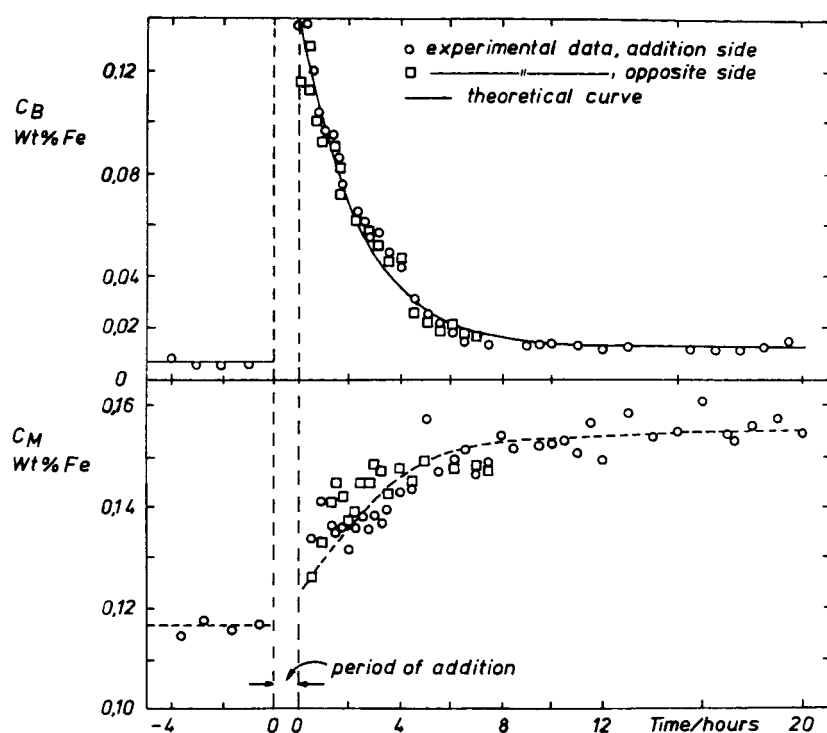


Figure 8.1 Iron content of bath (c_B) and metal (c_M) as a function of time after addition of 10 kg Fe_2O_3 to the bath of a 105 kA Söderberg cell. The figure is taken from Johansen et al. (1977).

Ten hours after an addition was made, Johansen *et al.* (1977) found that the c_M (see Figure 8.1) had increased corresponding to the transfer of 85 to 90 % of the added iron compounds. It was concluded that practically all the iron in the raw materials is recovered in the metal. The valency of the iron cations in the bath was also investigated. When FeSO_4 was added, 88 % of the iron present in the bath was found to be divalent, while 70 % was found to be divalent when Fe_2O_3 was added.

Based on the results of Johansen *et al.* (1977), one might then jump to the conclusion that we have the simple case of complete dissolution of impurities in the bath, and subsequently mass transfer controlled transport to the metal. The relatively high impurity levels in the bath could then be explained by a continuous supply of impurities coupled with slow mass transfer. However, as shown in the following, it is not that simple (Thonstad 1999).

Goodes and Algie (1989) studied the partition of trace metal impurities, including iron, nickel, silicon, titanium, and vanadium, between aluminium, bath and gaseous phases in laboratory tests. Cryolite-based baths were doped with these impurities, in their oxide form, and brought in contact with samples of high purity aluminium contained in graphite crucibles at 1050 °C. The transfer of impurities from bath to metal was far from complete after 26 hours tests, *i.e.* it was very far from chemical equilibrium according to equation [8-2]. Shaking the crucible made no difference. Element concentrations in bath and metal after 26 hours are given in Table 8-7. Fe, Ni, Ti, and V were detected in the fumes above the melt. After 2 - 4 hours the volatilisation seemed to cease.

Table 8-7 Steady state concentrations of impurities in bath and metal 26 hours after pure aluminium was introduced to bath doped with impurities. From Goodes and Algie (1989).

Bath/Metal Mass Ratio		Fe	Ni	Si	Ti	V
1:1	Bath (ppm)	1000	80	1800	80	120
	Metal (ppm)	410	38	800	45	65
2:1	Bath (ppm)	875	60	1220	60	90
	Metal (ppm)	925	80	1100	100	140

Sillinger and Horvath (1990) made similar studies as Goodes and Algie (1989), keeping contaminated bath (0.10 % Fe_2O_3 , 0.14 % SiO_2) in graphite crucibles in contact with aluminium with and without running electrolysis. The impurity concentrations in the bath were stabilised within two to three hours of electrolysis, with iron and silicon concentrations of 0.008 - 0.020 % and 0.006 - 0.016 %, respectively. The dust collected with the off-gas contained 0.2 - 0.5 % iron and 0.8 - 1.5 % silicon. Bubbling of gas through the bath did not reduce the concentration of iron impurities in the bath, while it did so in the case of silicon.

Chin *et al.* (1996) investigated the transfer of oxides of Cu, Fe, and Ni from an alumina-saturated cryolite melt to molten aluminium. The transfer of Cu, Fe, and Ni was found to be incomplete, 13, 63, and 55 %, respectively, were reduced and alloyed with aluminium in non-electrolysis experiments. Analysis of the distribution of the elements revealed that a majority of the Fe and Ni not found in the aluminium remained in the bulk of the melt. Essentially all the Cu that remained in the melt was found in a 1 - 2 mm thick “skim” layer around the metal.

Thonstad (1999) has written a thorough review on the behaviour of impurities in aluminium cells. He reached the following conclusions:

- (a) Impurities contained in the raw materials will upon contact with the bath tend to dissolve, probably forming fluoride (equation [8-1]) or oxy-fluoride species.
- (b) Some impurities may be caught by the gas stream even before entering the bath and be carried away as particulates.
- (c) In contact with dissolved metal or the metal cathode, the impurities may be reduced to the elemental state.
- (d) Carbon particles dispersed in the bath (carbon dust) may act as nucleation sites for these impurities.
- (e) The more abundant impurities, such as iron, may act as a getter for other impurities, *e.g.* vanadium and gallium.
- (f) Carbon particles, although being dispersed all over the bath, tend to accumulate at the surface of the bath, for density reasons. They can then easily be thrown out of the bath as the gas bubbles coming from the anode, burst and entrain a mist of bath in the process.

The object of the present work was to investigate the mass transfer of the impurities iron, silicon and titanium in industrial Hall-Héroult cells by adding them to the bath in their oxide form. In this context, one would try to verify a model given by Johansen (1975) for mass transport of impurity elements from bath into the aluminium metal based on the assumption that the transport was diffusion controlled.

8.2 Model

In an aluminium cell a continuous mass transport between bath and metal will take place. A species M^{n+} will transfer from the bath into the metal by either a chemical or an electrochemical reaction. The cathode reaction can be divided into several steps:

- (a) Transport of M^{n+} through a laminar layer in the bath towards the phase boundary bath/metal.
- (b) Reduction of M^{n+} to a metallic compound M.
- (c) Transport of M through a laminar layer in the metal phase.

Johansen (1975) concluded in his analysis that (a) is the rate determining step for iron. In the following this assumption is believed to apply for the species studied.

The flux of a species transported from the bulk to the boundary surface in a solution with forced convection is given by the expression:

$$J = Ak(c_{\text{bulk}} - c_{\text{boundary}}) \quad [8-4]$$

Here J is the mass flux of species, k is the mass transfer coefficient, c_{bulk} is the concentration of the M^{n+} species in the bulk, and c_{boundary} is the concentration of the M^{n+} species at the boundary. The mass transfer coefficient k is defined by:

$$k = \frac{D}{\delta} \quad [8-5]$$

D is the diffusion coefficient and δ is the thickness of the diffusion layer. The flux J_1 of M^{n+} out of the bath is then given by,

$$J_1 = Ak_{\text{bath}}(c_{\text{bath}} - c_{\text{boundary}(1)}) \quad [8-6]$$

while the flux J_2 of M into the aluminium metal is given by,

$$J_2 = Ak_{\text{metal}}(c_{\text{boundary}(2)} - c_{\text{metal}}) \quad [8-7]$$

A is the boundary surface area between the bath and the aluminium metal. k_{bath} and k_{metal} are the mass transfer coefficients for the species M^{n+}/M in bath and metal. c_{bath} and c_{metal} are the bulk concentrations of the species M^{n+}/M in the bath and in the aluminium metal. $c_{\text{boundary}(1)}$ and $c_{\text{boundary}(2)}$ are the concentrations at the boundary surface in bath and metal.

The relation $J_1 = J_2$ must apply since the flux of species out of the bath and the flux of species into the metal are equal.

Johansen (1975) found the following relation for iron species:

$$\frac{N_{\text{Fe(Al)}}}{N_{\text{FeF}_2}} = \frac{c_{\text{boundary}(2)}}{c_{\text{boundary}(1)}} \approx 10^{16} \quad [8-8]$$

Equation [8-8] suggests that a good approximation would be to set $c_{\text{boundary}(1)}$ equal to zero. Equation [8-6] then becomes:

$$J_1 = Ak_{\text{bath}} c_{\text{bath}} \quad [8-9]$$

This can be written as,

$$I_1 = nFAk_{\text{bath}} c_{\text{bath}} \quad [8-10]$$

since $J = I_1/nF$. I_1 is the total current for co-deposition of the species M^{n+} , n is the number of electrons involved in the reaction, and F is the Faraday constant.

The change of concentration in the electrolyte as a function of time can, therefore, be expressed as:

$$J_1 = -V \frac{dc_{\text{bath}}}{dt} = Ak_{\text{bath}} c_{\text{bath}} \quad [8-11]$$

Combined and integrated this gives:

$$c_{\text{bath}}(t) = c_{\text{added}} e^{-AV^{-1}k_{\text{bath}} t} \quad [8-12]$$

c_{added} is the concentration of M^{n+} added to the bath when the concentration of M in the bath is raised by adding a salt with M cations. Since most of the impurities are continuously being fed to the process through raw materials, a relatively constant background concentration c_{bc} will be established. Equation [8-12] must, therefore, be written as:

$$c_{\text{bath}}(t) = c_{\text{bc}} + c_{\text{added}} e^{-AV^{-1}k_{\text{bath}} t} \quad [8-13]$$

c_{added} can also be given as the difference between the concentration in the electrolyte immediately after addition and just before, *i.e.* $c_{\text{added}} = c_{\text{start}} - c_{\text{bc}}$. The model for transport of the species M^{n+} applies when the following conditions are satisfied:

- (a) First order reaction kinetics with respect to concentration.
- (b) Impurity elements are reduced into the metal.
- (c) Co-deposition of the element is diffusion controlled.
- (d) Other transport processes that can lower the concentration in the electrolyte are ignored.

8.3 Experimental

The measurements were performed on four different types of cells with prebaked anodes. Two were end-to-end cells, while two were side-by-side cells. The end-to-end cells will be referred to as ETE-I and ETE-II, while the side-by-side cells will be referred to as SBS-I and SBS-II. Figures 8.2 to 8.4 show sketches of the ETE-I cell, the ETE-II cell, and the SBS-I/SBS-II cell. The cell types SBS-I and SBS-II are almost identical, and are, therefore, presented together.

ETE-I is a 160 kA cell with both ends entry (Kobbeltvedt 1997). It has 20 anodes and two feeders. The horizontal anode dimensions are 140 cm \times 70 cm. The cell has no real centre channel, as the width of the gaps between the anodes lengthways is the same as for the narrow gaps between the anodes crosswise. The cell has two transverse channels where the feeders are located. The width of the transverse channels with new anodes is 23 cm. ETE-I was fed with primary alumina. The aluminium metal is collected in the position (A), *i.e.* the tapping hole.

ETE-II is a 170 kA cell with both ends entry (Kobbeltvedt 1997). It is equipped with 22 anodes and three feeders. The horizontal anode dimensions are 140 cm \times 70 cm. ETE-II was fed with primary alumina. The tapping hole is located in position (A).

SBS-I is a 230 kA cell, while SBS-II is a 250 kA cell. Both cells have 30 anodes, and the tapping hole is located in position (A). Secondary alumina was used as feed in both cell types.

The procedure for introducing the impurities to the bath was as follows: Firstly, the crust was broken at convenient positions, whereupon carbon dust and/or bits of the carbon anode were removed. Secondly, the impurities were carefully sprinkled on the exposed bath surface. The addition was always made in the tapping hole, but sometimes the additive was introduced simultaneously at one or several other positions to improve the distribution of the element. The impurities were introduced to the bath in their natural oxide form, *i.e.* Fe₂O₃ (Alfa, powder, 99.5 %), SiO₂ (Alfa, <325 mesh, 99.5 %) and TiO₂ (Alfa, rutile, 2 micron, 99 %+).

Bath and metal samples were collected before and during the experiments. A sampling device made of either iron or brass was used for the bath samples, while the metal samples were collected with a ladle made of iron. The element concentration in the bath samples was found by analysis on an ICP or on an XRF instrument. The metal samples were analysed by the use of an optic emission spectrograph.

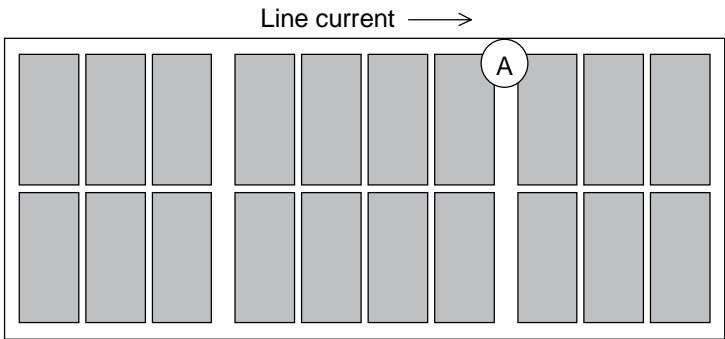


Figure 8.2 Sketch of the ETE-I cell. (A) shows the location of the tapping hole.

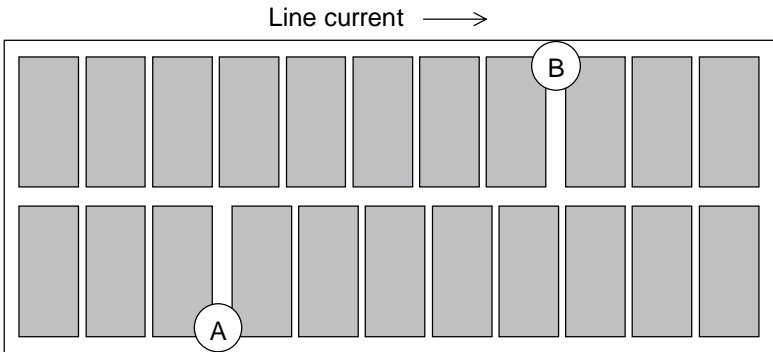


Figure 8.3 Sketch of the ETE-II cell. (A) shows the location of the tapping hole.

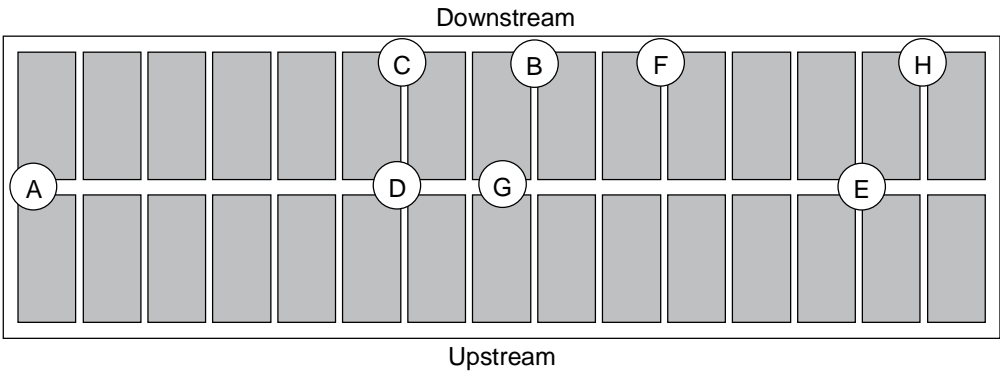


Figure 8.4 Sketch of the SBS-I/SBS-II cell. (A) shows the location of the tapping hole. The other positions are explained in Table 8-9.

Table 8-8 gives the amount of additives in the different experiments.

Table 8-8 Weight of additives in the different experiments.

Experiment	Fe ₂ O ₃	SiO ₂	TiO ₂
	kg	kg	kg
ETE-Ia	2.392	0.900	-
ETE-Ib	1.196	0.450	0.599
ETE-IIa	6.698	1.000	0.402
ETE-IIb	6.196	1.029	0.599
SBS-Ia	7.609	1.498	1.000
SBS-Ib	10.150	5.001	2.010
SBS-Ic	10.571	5.195	2.029
SBS-IIa	7.391	1.502	1.000

The positions where the impurities were added and the bath and metal samples were collected are given in Table 8-9. The analysis techniques applied on the bath samples are also included in Table 8-9.

Table 8-9 Design of the different experiments, and the analysis techniques applied on the bath samples.

Experiment	Addition position	Bath sampling position	Metal sampling position	Analysis technique
ETE-Ia	A	A	A	ICP
ETE-Ib	A	A	A	ICP
ETE-IIa	A	A, B	A	ICP
ETE-IIb	A	A, B	A	ICP
SBS-Ia	A, B	A, B	A	ICP/XRF
SBS-Ib	A, F, G	A	A	XRF
SBS-Ic	A, G, H	A	A	XRF
SBS-IIa	A, C, D, E	A, C	A	ICP/XRF

8.4 Results and Discussion

The analytical techniques used in the present work (ICP and XRF) cannot be used to distinguish between different oxidation states of an element. The reported concentration of *e.g.* iron in the bath would, therefore, be an unknown mix of Fe(II), Fe(III) and perhaps some Fe(0). This means that the obtained mass transfer coefficients apply for the element as present in the bath, and not for a specific valency.

8.4.1 Effect of Cell Type

8.4.1.1 Cell Type ETE-I

Experiments were performed on two different cells of type ETE-I by adding the chemicals to the bath in position (A) (see Figure 8.2). Position (A) was also used for bath and aluminium metal sampling. The bath samples were collected with a pair of steel tongs. The metal samples were collected with a steel ladle, and then poured into a brass-lined steel mould. Bath samples were analysed by ICP, while the content of the investigated impurities in the metal samples was found with an optic emission spectrograph. Metal samples were only collected on a day to day basis.

Figures 8.5 and 8.6 show the bath concentration of the added elements as a function of time for experiments ETE-Ia and ETE-Ib, respectively. The symbols are bath analysis data, while the solid lines are best fits according to equation [8-13].

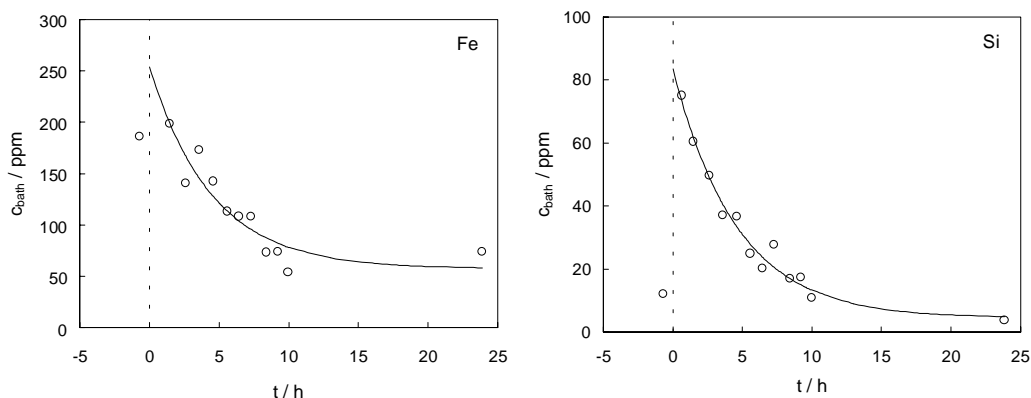


Figure 8.5 Concentrations of iron and silicon in the bath as a function of time for experiment ETE-Ia. The batch added consisted of 2.392 kg Fe_2O_3 and 0.900 kg SiO_2 .

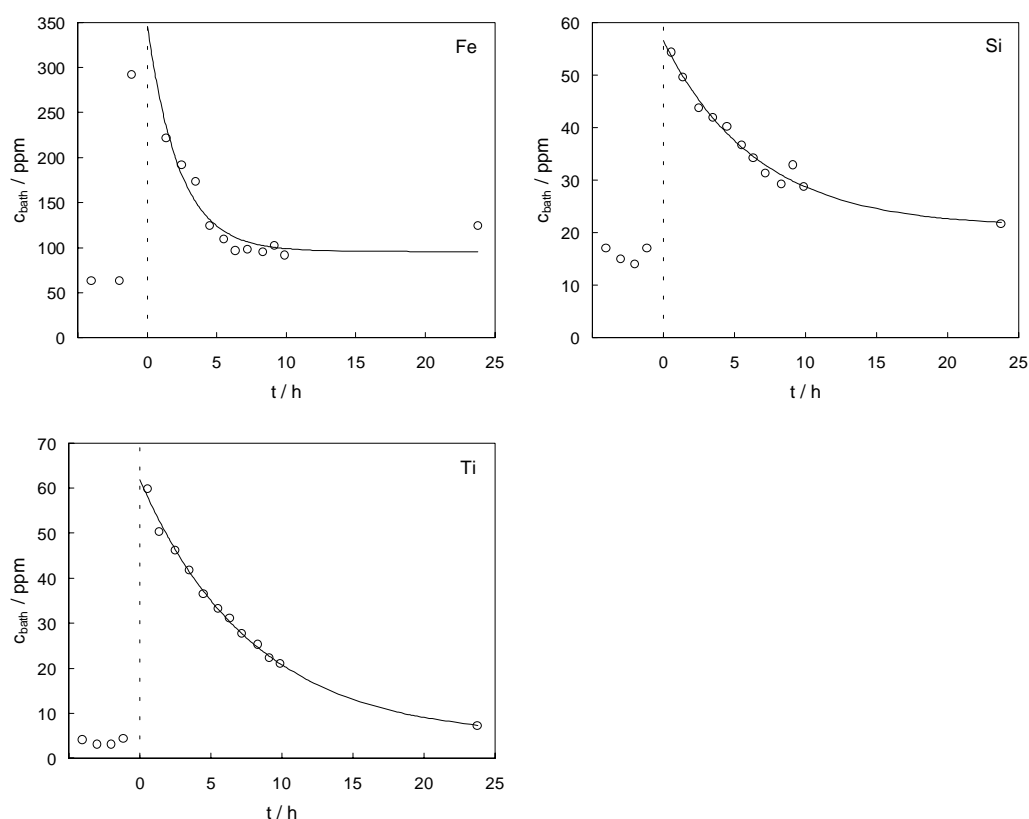


Figure 8.6 Concentrations of iron, silicon and titanium in the bath as a function of time for experiment ETE-Ib. The batch added consisted of 1.196 kg Fe_2O_3 , 0.450 kg SiO_2 and 0.599 kg TiO_2 .

The concentration at $t = 0$ (c_{start}), the background concentration (c_{bc}), and the argument of the exponential function in equation [8-13] ($-kAV^{-1}$) were found by iteration (criterion: least-squares method). Alternatively, the background concentration could have been set equal to the average concentration obtained from bath samples taken before the addition was made. However, the data were often few and scarce, especially for iron, so the procedure of finding the background concentration by iteration was adopted.

The results for experiments ETE-Ia and ETE-Ib are given in Tables 8-10 and 8-11. The uncertainty in the data is given as the mean percent deviation (ϵ) with respect to the best fit found by the iteration procedure. The amount of bath in the cell (w_{bath}) was found by,

$$w_{\text{bath}} = \frac{w_{\text{add}}}{c_{\text{start}} - c_{\text{bc}}} \quad [8-14]$$

where w_{add} is the weight of the element added. The area of the bath/metal interface (A) was given by Hydro Aluminium personnel. An industrial bath typically contains 11 wt% excess AlF_3 , 5 wt% CaF_2 and 2.5 wt% Al_2O_3 . By means of the data from Solheim (2000), the density of the bath (ρ_{bath}) was calculated to be 2100 kg m^{-3} at 965°C .

Table 8-10 Bath data and the resulting mass transfer coefficients of experiment ETE-Ia ($A = 30 \text{ m}^2$, $\rho_{\text{bath}} = 2100 \text{ kg m}^{-3}$).

Elem.	w_{add} kg	c_{bc} ppm	c_{start} ppm	ϵ %	w_{bath} kg	Avg. w_{bath} kg	kAV^{-1} h^{-1}	$10^6 \cdot k$ m s^{-1}
Fe	1.665	57	254	14	8478	6891	0.224	6.8
Si	0.419	4.4	83.4	12	5304		0.218	6.6

Table 8-11 Bath data and the resulting mass transfer coefficients of experiment ETE-Ib ($A = 30 \text{ m}^2$, $\rho_{\text{bath}} = 2100 \text{ kg m}^{-3}$).

Elem.	w_{add} kg	c_{bc} ppm	c_{start} ppm	ϵ %	w_{bath} kg	Avg. w_{bath} kg	kAV^{-1} h^{-1}	$10^6 \cdot k$ m s^{-1}
Fe	0.832	96	346	26	3325	5134	0.436	9.9
Si	0.209	21.0	56.5	3	5884		0.153	3.5
Ti	0.356	4.4	61.9	2	6192		0.126	2.9

Tables 8-10 and 8-11 show that the data obtained for iron, silicon and titanium gave different amounts of bath in the cells under investigation. For obvious reasons a cell can only have one bath volume at a given time, so the calculated bath weights were averaged.

As can be seen from Figures 8.5 and 8.6, the bath data for iron are scattered. This observation can probably be explained by the amount of iron added to the baths and the sampling device that was used. If larger batches of iron had been added, more reliable data would have been obtained, *i.e.* less influence of the fluctuating background concentration of iron. A pair of steel tongs was used as the sampling device. This could have given a random contribution to the iron concentration in the bath samples, and thereby it could account for some of the observed scatter.

The bath sampling as well as the addition of impurities was made at the same location. This means that there was no control of the distribution of the impurities in the bath,

and it was not known how long time was needed before the impurities were uniformly distributed.

Although there are several causes which undermine the results obtained in experiments ETE-Ia and ETE-Ib, the values of the obtained mass transfer coefficients seem to be reasonable, compared with the value reported for iron by Johansen *et al.* (1977), *i.e.* $k = 1.25 \times 10^{-5} \text{ m s}^{-1}$.

Apart from the possible sources of error mentioned above, the major parameters giving rise to uncertainty in the determined mass transfer coefficients are probably the area of the bath/metal interface and the bath volume. By measuring the side ledge profile, one can get a fairly good value for the area. It is expected that this profile may change somewhat during the period of one day and, thereby, cause some uncertainty in the determined area. However, the side profile was not measured in the period when these experiments were performed. A “typical” area, based on the experience of Hydro Aluminium personnel and earlier measurements, had, therefore, to be used in the calculations. An uncertainty of $\pm 1 \text{ m}^2$ in the value for the bath/metal interface area corresponds to a change in the thickness of the side ledge of more than $\pm 4 \text{ cm}$.

The uncertainty in the bath volume is probably even higher. It was assumed that the entire batch of impurity species ended up in the bath. This is probably not the case, as discussed in section 8.1. From equation [8-14] one sees that the calculated bath volumes will increase with decreasing proportion of the batch entering the bath. One can also assume, based on the information given in section 8.1, that different impurities would give different bath volumes due to different properties, such as volatility, dissolution mechanism *etc.* It is not possible to give an accurate estimate of the uncertainty in the bath volume, but it is likely to be 10 % or more. This value can probably be minimised by making larger additions.

Metal samples were collected shortly before and one day after the additions were made. Tables 8-12 and 8-13 show that the metal content of all the investigated species increased during this period of time. Based on the change in metal content and geometric data it is possible to estimate the fraction of the impurities added that co-deposited with the aluminium. Firstly, the weight of the aluminium metal ($w_{\text{metal}(1)}$) is calculated based on the metal analysis:

$$w_{\text{metal}(1)} = \frac{w_{\text{add}}}{c_{t \approx 1 \text{ day}} - c_{t < 0}} \quad [8-15]$$

$c_{t \approx 1 \text{ day}}$ is the element concentration in the metal approximately 24 hours after the element was added, while $c_{t < 0}$ is the element concentration before the batch was added. Secondly, the weight of the metal is calculated from the geometric data of the cell,

$$w_{\text{metal}(2)} = Ah_{\text{metal}} \rho_{\text{metal}} \quad [8-16]$$

where h_{metal} is the height of the metal pad and ρ_{metal} is the density of the aluminium produced. According to Grjotheim *et al.* (1982), aluminium metal at 965 °C, and with a purity of 99.75 %, has a density of 2300 kg m⁻³.

The fraction of impurity elements that co-deposits (x_{dep}) is then given by:

$$x_{\text{dep}} = \frac{W_{\text{metal}(2)}}{W_{\text{metal}(1)}} \quad [8-17]$$

The results of experiments ETE-Ia and ETE-Ib with regard to co-deposition of the impurity elements are given in Tables 8-12 and 8-13.

Table 8-12 Metal data and the resulting fraction of co-deposition of experiment ETE-Ia ($h_{\text{metal}} = 0.20 \text{ m}$, $A = 30 \text{ m}^2$, $\rho_{\text{metal}} = 2300 \text{ kg m}^{-3}$).

Elem.	W_{add} kg	$C_{t<0}$ ppm	$C_{t=1\text{ day}}$ ppm	$W_{\text{metal}(1)}$ kg	$W_{\text{metal}(2)}$ kg	x_{dep}
Fe	1.665	790	889	16800	13800	0.82
Si	0.419	336	362	16100		0.86

Table 8-13 Metal data and the resulting fraction of co-deposition of experiment ETE-Ib ($h_{\text{metal}} = 0.20 \text{ m}$, $A = 30 \text{ m}^2$, $\rho_{\text{metal}} = 2300 \text{ kg m}^{-3}$).

Elem.	W_{add} kg	$C_{t<0}$ ppm	$C_{t=1\text{ day}}$ ppm	$W_{\text{metal}(1)}$ kg	$W_{\text{metal}(2)}$ kg	x_{dep}
Fe	0.832	647	672	33300	13800	0.41
Si	0.209	324	335	19000		0.73
Ti	0.356	38	65	13200		1.05

Tables 8-12 and 8-13 indicate that this may be a method that yields little information. The fractions of iron and silicon that co-deposited in experiment ETE-Ia seem to be plausible, while the results of experiment ETE-Ib look more doubtful. A value of 0.41 for iron is highly unlikely, since Johansen *et al.* (1977) reported that in their experiments 85 to 90 % of the iron had entered the metal within 10 hours after being added. In view of the fact that Johansen *et al.* (1977) added between 10 and 20 kg of Fe₂O₃ or FeSO₄ to 105 kA cells, it follows that the batch of iron added in experiment ETE-Ib was too small. The same tendency is observed for silicon, the fraction co-deposited decreased when the addition was reduced to one half. The titanium result also seems strange, being above one. However, the amount of titanium that was added should be large enough, since it caused an increase of more than 70 % in the metal content.

Again, the assumption that the entire addition dissolved in the bath is likely to cause a too high metal volume when using equation [8-15], and, thereby, reducing the calculated fraction that was co-deposited. Another source of error is the metal height used in the calculations. Since aluminium is constantly produced, the metal height increases by 1.87 cm per day if $CE = 100\%$. Therefore, the value for the metal height used in the calculations had to be an average value. The uncertainty in the metal height was expected to be $\Delta h_{\text{metal}} = \pm 1$ cm. As discussed above, the uncertainty in the area of the metal was believed to be $\Delta A = \pm 1$ m². With the values for the uncertainty in the metal area and the metal height, one finds that the uncertainty in the metal volume based on geometry was almost 9 %.

8.4.1.2 Cell Type ETE-II

Two experiments were performed on a cell of the type ETE-II and with a time interval of three days. The impurities were added to the bath in position (A) (see Figure 8.3), while bath and metal samples were collected in positions (A) and (B). A sampling device made of brass was used in position (A), while a pair of steel tongs was used in position (B). Metal samples were collected with a steel ladle, and then poured into a brass-lined steel mould. Bath samples were analysed by ICP, while the content of the investigated elements in the metal samples was found with an optic emission spectrograph.

As can be seen from Table 8-8, the amounts of Fe_2O_3 and SiO_2 added were increased substantially compared to the experiments on the cell type ETE-I. This was done in order to reduce the influence of a varying background concentration.

Figures 8.7 and 8.8 show the bath and metal concentrations of the added species as a function of time for experiments ETE-IIa and ETE-IIb, respectively. It is noted that results are reported only for iron and titanium. The reason was that the ICP analysis failed to deliver reasonable data for silicon.

The bath data obtained and the corresponding mass transfer coefficients for experiments ETE-IIa and ETE-IIb are given in Tables 8-14 and 8-15, respectively. The mass transfer coefficients were determined in exactly the same way as described for the experiments with the cell type ETE-I.

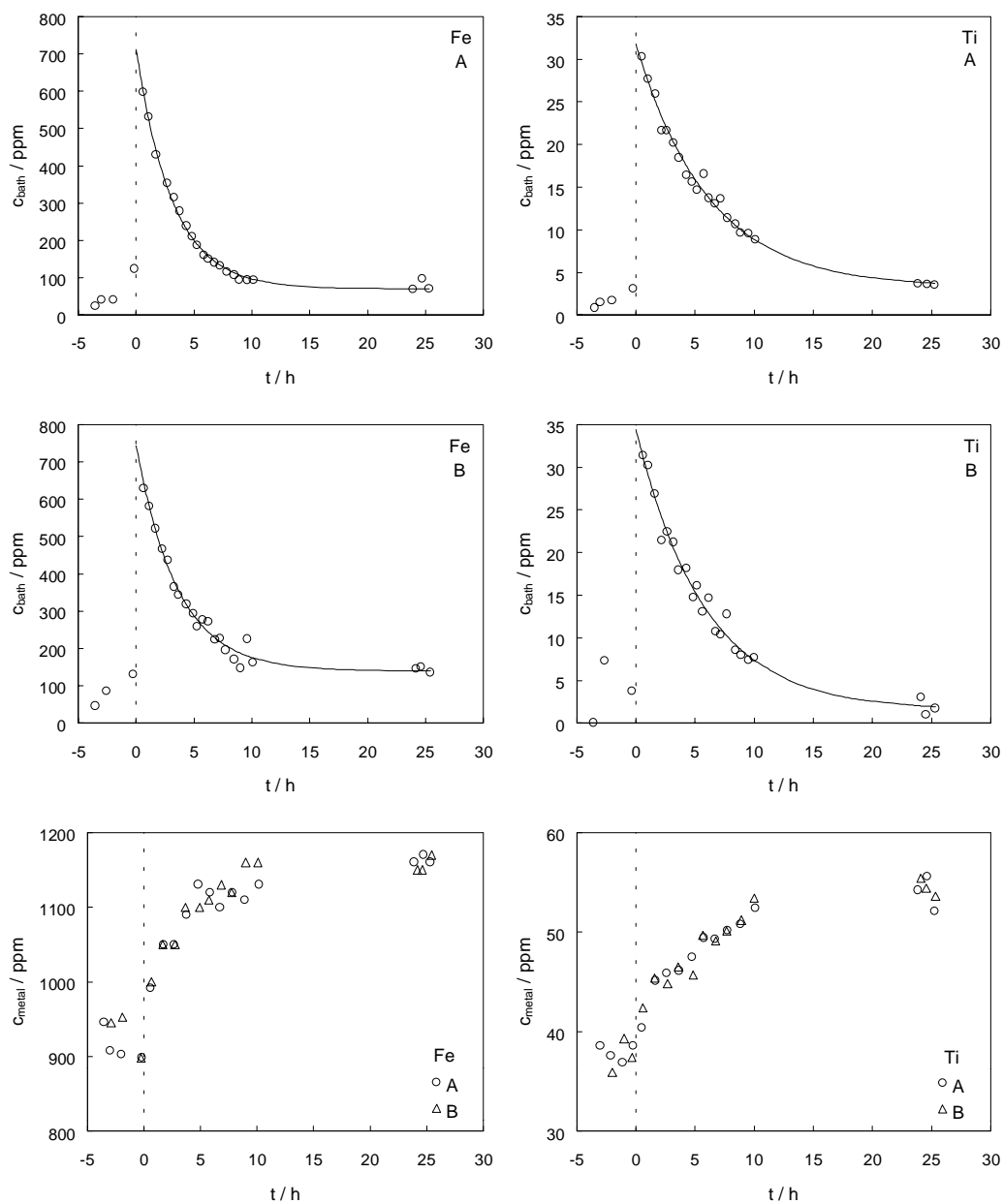


Figure 8.7 Concentrations of iron and titanium in the bath and metal as a function of time for experiment ETE-IIa. The batch added consisted of 6.698 kg Fe_2O_3 , 1.000 kg SiO_2 and 0.402 kg TiO_2 .

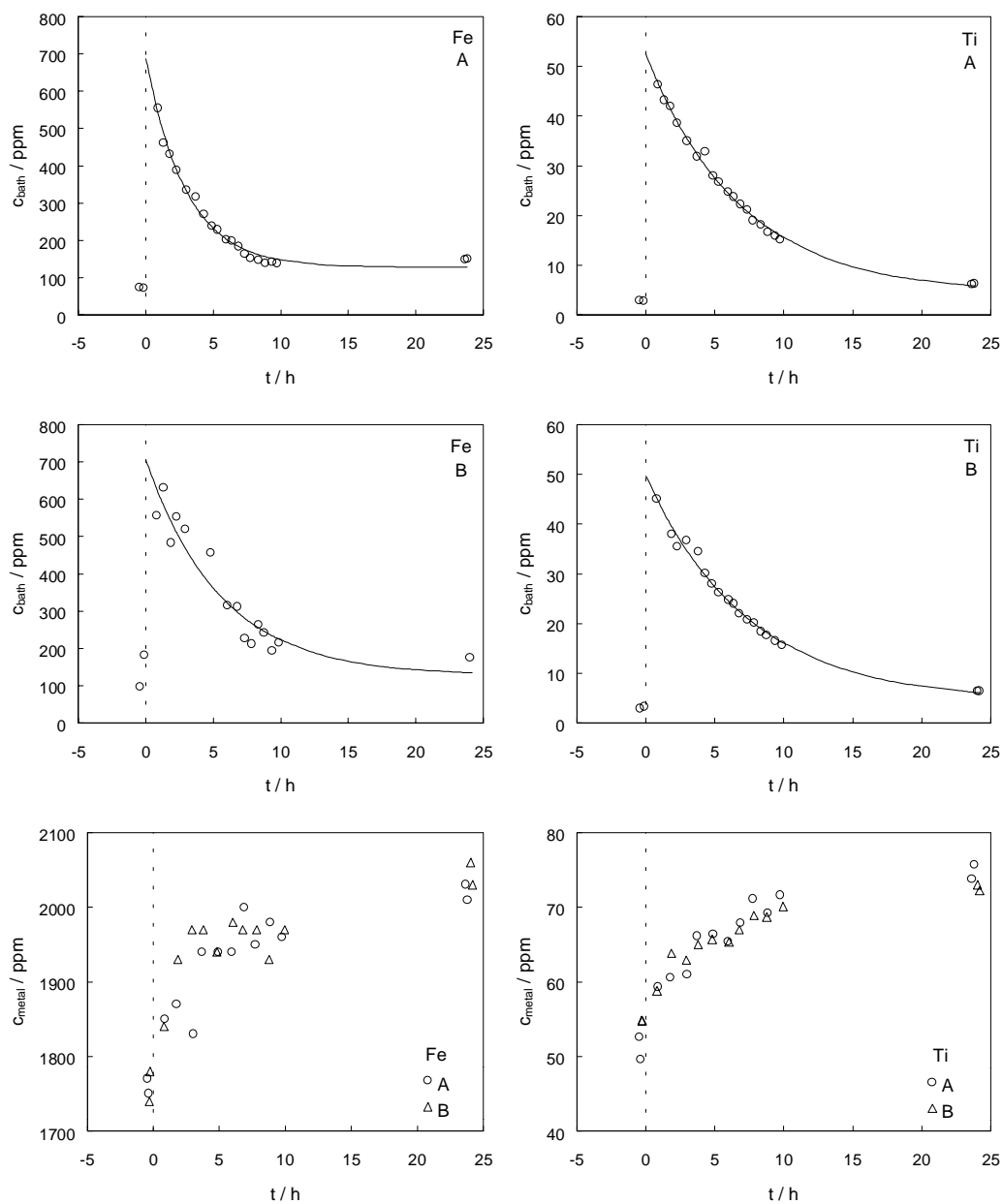


Figure 8.8 Concentrations of iron and titanium in the bath and metal as a function of time for experiment ETE-IIb. The batch added consisted of 6.196 kg Fe_2O_3 , 1.029 kg SiO_2 and 0.599 kg TiO_2 .

Table 8-14 Bath data and the resulting mass transfer coefficients of experiment ETE-IIa ($A = 31.5 \text{ m}^2$, $\rho_{\text{bath}} = 2100 \text{ kg m}^{-3}$).

Elem.	Pos.	w_{add}	c_{bc}	c_{start}	ϵ	w_{bath}	Avg. w_{bath}	kAV^{-1}	$10^6 \cdot k$
		kg	ppm	ppm	%	kg		h^{-1}	m s^{-1}
Fe	A	4.661	70	712	5	7266	7657	0.320	10
Fe	B	4.661	139	743	6	7716		0.281	9.0
Ti	A	0.239	3.3	31.8	4	8383		0.163	5.2
Ti	B	0.239	1.5	34.4	13	7262		0.173	5.6

Table 8-15 Bath data and the resulting mass transfer coefficients of experiment ETE-IIb ($A = 31.5 \text{ m}^2$, $\rho_{\text{bath}} = 2100 \text{ kg m}^{-3}$).

Elem.	Pos.	w_{add}	c_{bc}	c_{start}	ϵ	w_{bath}	Avg. w_{bath}	kAV^{-1}	$10^6 \cdot k$
		kg	ppm	ppm	%	kg		h^{-1}	m s^{-1}
Fe	A	4.312	128	687	6	7721	7608	0.336	11
Fe	B	4.312	127	705	12	7456		0.181	5.8
Ti	A	0.356	4.4	52.5	3	7401		0.146	4.7
Ti	B	0.356	4.4	49.7	3	7852		0.136	4.4

Tables 8-14 and 8-15 show that the bath weights found in experiments ETE-IIa and ETE-IIb were much more consistent than those obtained in the experiments with the cell type ETE-I. This is believed to be due to the increased additions of iron, thereby reducing the effect of the unknown variation in the background concentrations.

To check if the steel tongs influenced on the iron concentration in the bath samples, a sampling device made of brass was used in position (A). Figures 8.7 and 8.8 show that the data resulting from the bath samples collected with the brass tongs were less scattered than those obtained with the steel tongs. This implies that, if possible, the sampling device should be made of a material which does not contain one of the impurities under investigation in order to minimise random errors in the impurity concentration.

Since the addition was made in position (A) and the bath samples were collected in positions (A) and (B), one should be able to estimate the time of mixing, *i.e.* the time needed for the batch to be evenly distributed in the bath. In experiment ETE-IIa (Figure 8.7) the first bath samples were collected ~35 minutes after the addition was made, while in experiment ETE-IIb they were collected after ~53 minutes. In both experiments the element concentration in the bath turned out to be approximately the same in both position (A) and position (B). Based on these results the mixing time is believed to be well below an hour. This is supported by the findings of Tørklep *et al.*

(1997). According to them, the mixing time in the bath of a 155 kA end-to-end prebake is typically 30 - 40 minutes, while it is 8 - 10 minutes in the metal pad.

Except for the iron data collected in position (B) in experiment ETE-IIb, the results given in Tables 8-14 and 8-15 show that the obtained values for the mass transfer coefficient were consistent for both iron and titanium in the two experiments, *i.e.* $k_{\text{Fe}} = (10 \pm 1) \times 10^{-6} \text{ m s}^{-1}$ and $k_{\text{Ti}} = (5.0 \pm 0.5) \times 10^{-6} \text{ m s}^{-1}$. The value for iron that deviates from the given value is, as mentioned above, believed to be caused by the use of the steel tongs. The good agreement in the present experiments, compared with experiments ETE-Ia and ETE-Ib, is probably due to the larger additions of iron oxide.

The data resulting from the metal analysis and the corresponding fractions of the investigated elements that were co-deposited, are given in Tables 8-16 and 8-17 for the experiments ETE-IIa and ETE-IIb.

Table 8-16 Metal data and the resulting fraction of co-deposition of experiment ETE-IIa ($h_{\text{metal}} = 0.20 \text{ m}$, $A = 31.5 \text{ m}^2$, $\rho_{\text{metal}} = 2300 \text{ kg m}^{-3}$).

Elem.	w_{add}	$c_{t<0}$	$c_{t=1\text{day}}$	$w_{\text{metal}(1)}$	$w_{\text{metal}(2)}$	x_{dep}
	kg	ppm	ppm	kg	kg	
Fe	4.661	922 ± 25	1160 ± 9	19600	14500	0.74
Ti	0.239	38 ± 1	54 ± 1	14900		0.97

Table 8-17 Metal data and the resulting fraction of co-deposition of experiment ETE-IIb ($h_{\text{metal}} = 0.20 \text{ m}$, $A = 31.5 \text{ m}^2$, $\rho_{\text{metal}} = 2300 \text{ kg m}^{-3}$).

Elem.	w_{add}	$c_{t<0}$	$c_{t=1\text{day}}$	$w_{\text{metal}(1)}$	$w_{\text{metal}(2)}$	x_{dep}
	kg	ppm	ppm	kg	kg	
Fe	4.312	1760 ± 18	2033 ± 21	15800	14500	0.92
Ti	0.356	53 ± 2	74 ± 1	17000		0.85

The fractions of iron and titanium that co-deposited into the metal within one day, according to Tables 8-16 and 8-17, seem to be reasonable. The uncertainty in the determination of the geometrical metal volume is the same as discussed in section 8.4.1.1, *i.e.* $\Delta h_{\text{metal}} = \pm 1 \text{ cm}$ and $\Delta A = \pm 1 \text{ m}^2$. The uncertainty in the determination of the metal volume based on equation [8-15] was also discussed in section 8.4.1.1. However, Figures 8.7 and 8.8 show that the metal data obtained in the present experiments were somewhat scattered in the case of iron as well as titanium. This indicates that the scatter was not caused by the sampling equipment, *i.e.* steel ladle and brass-lined mould. As mentioned above, the mixing time in the metal was reported to be 8 - 10 minutes according to Tørklep *et al.* (1997). One would, therefore,

expect that there would be only small concentration gradients in the metal, and that these gradients would not cause such concentration fluctuations in the metal as shown in Figures 8.7 and 8.8. The observed scatter can, therefore, only be explained by random errors related to the metal analysis. The uncertainty of $c_{t<0}$ and $c_{t=1\text{day}}$ given in Tables 8-16 and 8-17 was taken as the standard deviation of the data used to calculate these parameters.

8.4.1.3 Cell Type SBS-I/SBS-II

Experiments were performed on cells of types SBS-I and SBS-II. In experiment SBS-Ia the impurity elements were added in positions (A) and (B), while bath samples were collected with a pair of steel tongs in position (A) and with a pair of brass tongs in position (B) (see Figure 8.4). In experiment SBS-IIa the additions were made in positions (A), (C), (D) and (E), while the bath sampling was performed in position (A) with a pair of steel tongs and with a pair of brass tongs in position (C). Metal samples were collected in position (A) in both experiments.

Due to the analytical problem with regard to silicon, an extra set of bath samples was collected so that analysis could be performed with both ICP and XRF. Metal samples were analysed as described earlier.

Since the cell types SBS-I and SBS-II were larger than those investigated above, the amounts of all the added impurity elements were increased.

The results of the experiment SBS-Ia are displayed in Figures 8.9 and 8.10, while Figures 8.11 and 8.12 show the results of the experiment SBS-IIa. The data obtained by ICP are given in Figures 8.9 and 8.11, while those determined by XRF are given in Figures 8.10 and 8.12, together with the results of the metal analysis.

ICP analysis did not provide any data on the silicon concentration in the bath in these experiments either.

The obtained bath data and the corresponding mass transfer coefficients for experiments SBS-Ia and SBS-IIa are given in Tables 8-18 and 8-19, respectively. The mass transfer coefficients were determined as described earlier.

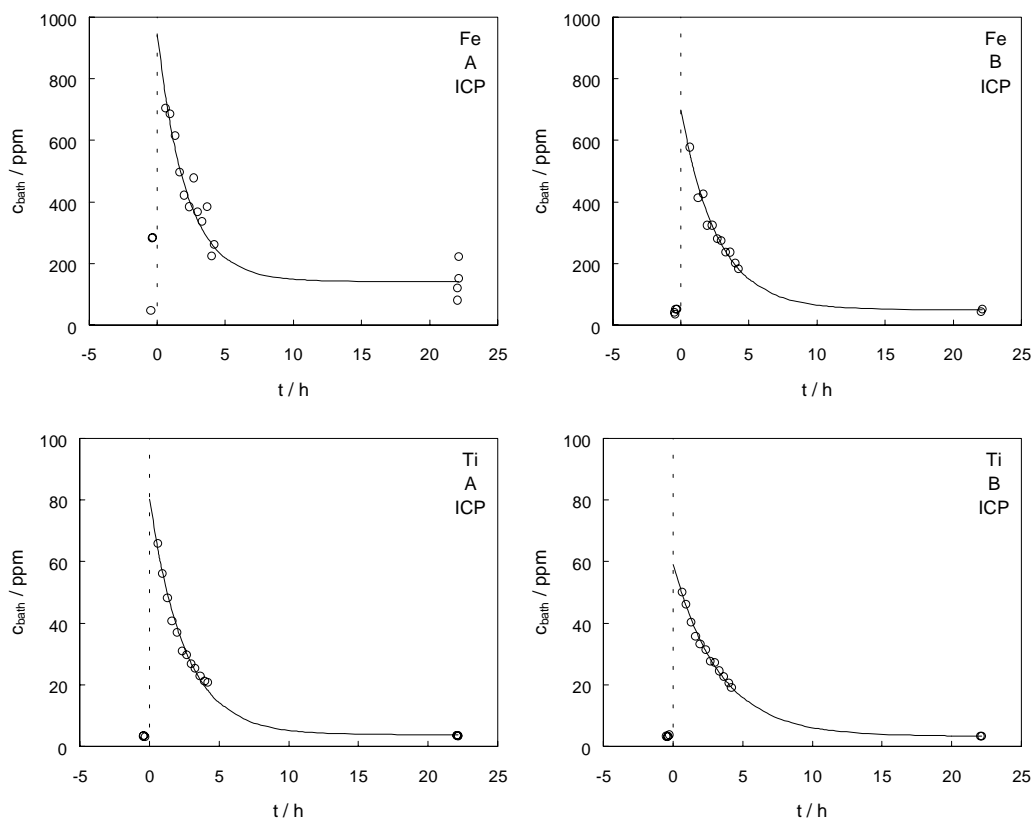


Figure 8.9 Concentrations of iron and titanium in the bath as a function of time for experiment SBS-Ia. Bath concentrations were determined by ICP. The batch added consisted of 7.609 kg Fe_2O_3 , 1.498 kg SiO_2 and 1.000 kg TiO_2 .

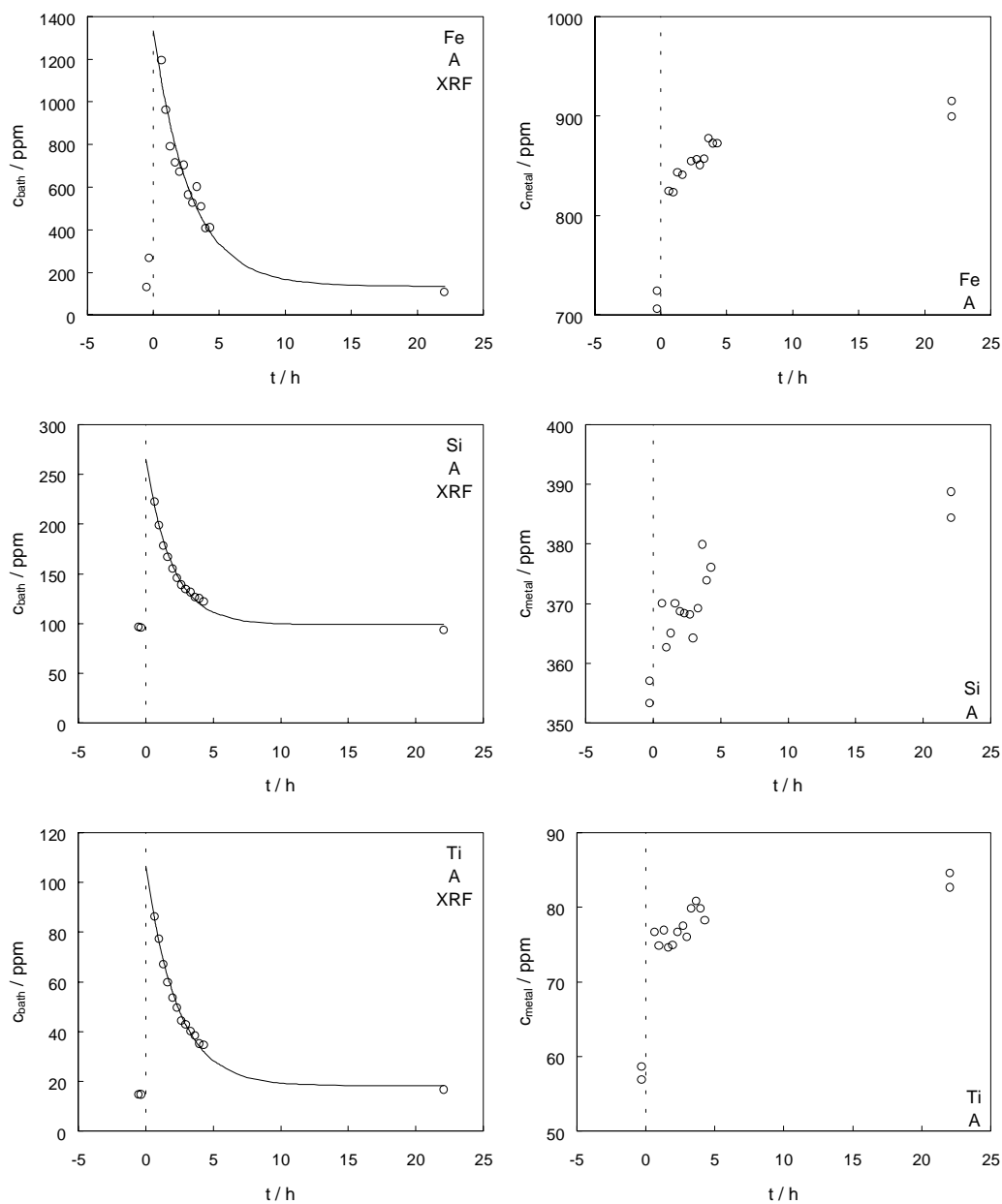


Figure 8.10 Concentrations of iron, silicon and titanium in the bath and metal as a function of time for experiment SBS-Ia. Bath concentrations were determined by XRF. The batch added consisted of 7.609 kg Fe_2O_3 , 1.498 kg SiO_2 and 1.000 kg TiO_2 .

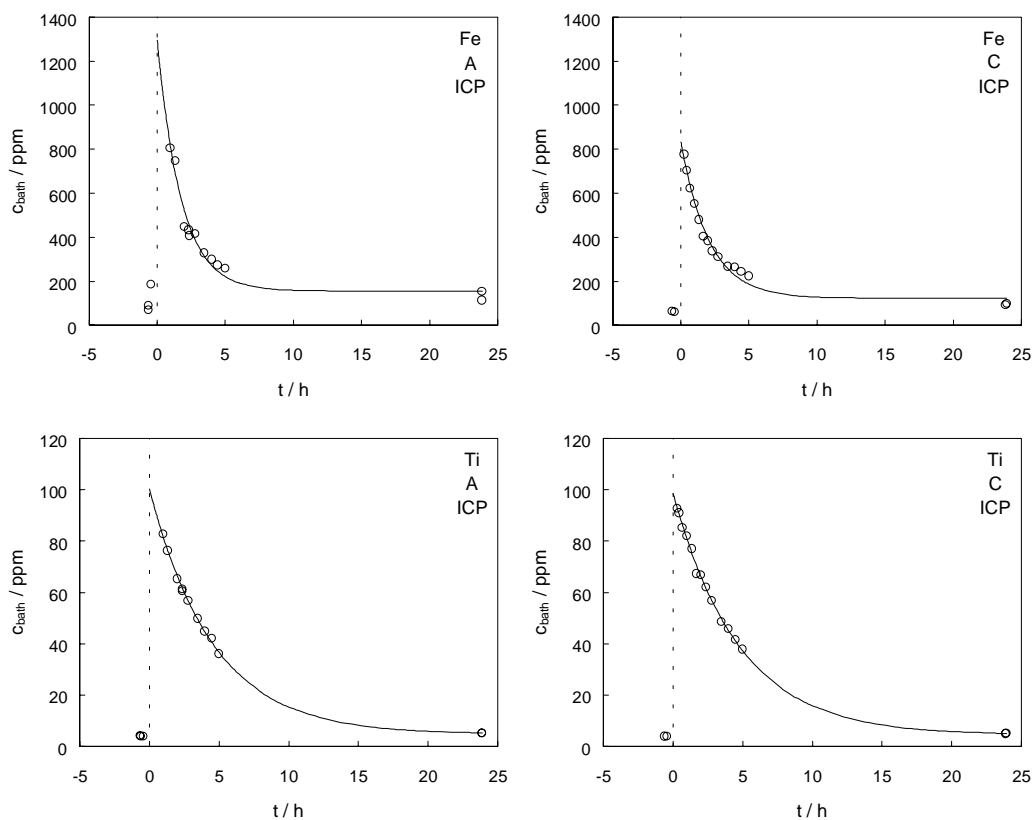


Figure 8.11 Concentrations of iron and titanium in the bath as a function of time for experiment SBS-IIa. Bath concentrations were determined by ICP. The batch added consisted of 7.391 kg Fe_2O_3 , 1.502 kg SiO_2 and 1.000 kg TiO_2 .

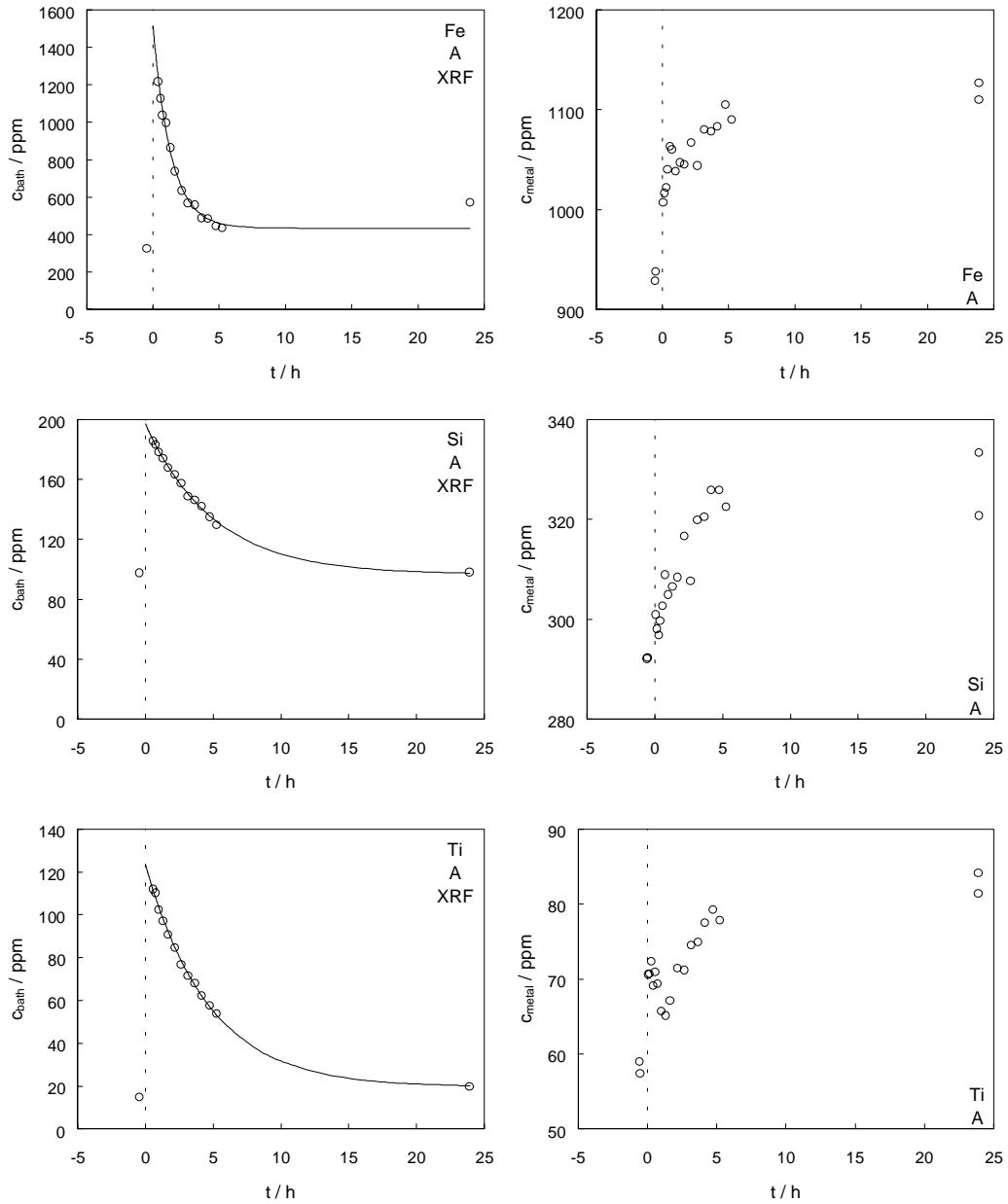


Figure 8.12 Concentrations of iron and titanium in the bath and metal as a function of time for experiment SBS-IIa. Bath concentrations were determined by XRF. The batch added consisted of 7.391 kg Fe_2O_3 , 1.502 kg SiO_2 and 1.000 kg TiO_2 .

Table 8-18 Bath data and the resulting mass transfer coefficients of experiment SBS-Ia ($A = 40.1 \text{ m}^2$, $\rho_{\text{bath}} = 2100 \text{ kg m}^{-3}$).

Elem.	Pos.	Anal. techn.	w_{add} kg	c_{bc} ppm	c_{start} ppm	ϵ %	w_{bath} kg	Avg. w_{bath} kg	kAV^{-1} h^{-1}	$10^6 \cdot k$ m s^{-1}
Fe	A	ICP	5.295	142	941	15	6629	8309	0.469	13
Fe	B	ICP	5.295	50	698	6	8175		0.374	10
Ti	A	ICP	0.594	3.8	80.2	7	7778		0.399	11
Ti	B	ICP	0.594	3.4	59.1	3	10655		0.299	8.2
Fe	A	XRF	5.295	135	1332	9	4424	5121	0.360	6.1
Si	A	XRF	0.697	99.0	264.8	2	4204		0.520	8.8
Ti	A	XRF	0.594	18.2	106.4	4	6735		0.432	7.3

Table 8-19 Bath data and the resulting mass transfer coefficients of experiment SBS-IIa ($A = 38.3 \text{ m}^2$, $\rho_{\text{bath}} = 2100 \text{ kg m}^{-3}$).

Elem.	Pos.	Anal. techn.	w_{add} kg	c_{bc} ppm	c_{start} ppm	ϵ %	w_{bath} kg	Avg. w_{bath} kg	kAV^{-1} h^{-1}	$10^6 \cdot k$ m s^{-1}
Fe	A	ICP	5.144	156	1295	11	4516	6076	0.571	12
Fe	C	ICP	5.144	123	832	9	7248		0.481	10
Ti	A	ICP	0.594	4.8	100.2	1	6224		0.219	4.6
Ti	C	ICP	0.594	4.4	98.5	2	6314		0.211	4.4
Fe	A	XRF	5.144	434	1513	3	4769	5816	0.744	15
Si	A	XRF	0.699	96.6	197.0	1	6962		0.199	4.0
Ti	A	XRF	0.594	19.5	123.4	1	5718		0.215	4.3

Table 8-18 shows that analyses by ICP and XRF resulted in substantially different bath volumes. This deviation was not observed in the data presented in Table 8-19. Tables 8-18 and 8-19 do also show that much higher element concentrations were obtained by XRF than by ICP. As can be seen from equation [8-14], this difference may lead to quite different bath volumes. However, the use of a pair of steel tongs could also influence the determination of the bath volume. As can be seen from the displayed results, the bath volumes calculated from iron data when the steel tongs was used, were in general lower than the average bath volumes. It is, therefore, likely that both the analytical technique in use and the sampling device could have influenced the determination of the bath volume.

The results show that the mass transfer coefficients obtained in experiment SBS-Ia were inconsistent. The ICP analysis indicates that the mass transfer coefficient of iron was somewhat higher than that of titanium. However, the XRF results indicate the opposite, the mass transfer of titanium being faster than that of iron. Another peculiar

observation was the fact that the impurity concentrations of both iron and titanium in position (A) were much higher than in position (B) right after the additions were made. In section 8.4.1.2 it was found that the mixing time was well below an hour when the addition was made in only one position. In this experiment additions were made in two positions, which should have given an even shorter mixing time. One can probably conclude that the results originating from bath analysis are of doubtful quality and that they should be used with caution.

Table 8-19 shows that the mass transfer coefficients of iron and titanium obtained in experiment SBS-IIa were relatively consistent, *i.e.* $k_{\text{Fe}} = (12 \pm 3) \times 10^{-6} \text{ m s}^{-1}$ and $k_{\text{Ti}} = (4.4 \pm 0.2) \times 10^{-6} \text{ m s}^{-1}$, and in good agreement with the findings in the experiments ETE-IIa and ETE-IIb. The value found for silicon also seems reasonable compared with the findings in experiments ETE-Ia and ETE-Ib (Tables 8-10 and 8-11).

The data resulting from the metal analysis and the corresponding fraction of the investigated elements that were co-deposited, are given in Tables 8-20 and 8-21 for the experiments SBS-Ia and SBS-IIa.

Table 8-20 Metal data and the resulting fraction of co-deposition of experiment SBS-Ia ($h_{\text{metal}} = 0.22 \text{ m}$, $A = 40.1 \text{ m}^2$, $\rho_{\text{metal}} = 2300 \text{ kg m}^{-3}$).

Elem.	W_{add}	$C_{t<0}$	$C_{t=1\text{day}}$	$W_{\text{metal}(1)}$	$W_{\text{metal}(2)}$	X_{dep}
	kg	ppm	ppm	kg	kg	
Fe	5.295	715 ± 13	907 ± 11	27600	20300	0.74
Si	0.697	355 ± 3	387 ± 3	21800		0.93
Ti	0.594	58 ± 1	84 ± 1	22800		0.89

Table 8-21 Metal data and the resulting fraction of co-deposition of experiment SBS-IIa ($h_{\text{metal}} = 0.22 \text{ m}$, $A = 38.3 \text{ m}^2$, $\rho_{\text{metal}} = 2300 \text{ kg m}^{-3}$).

Elem.	W_{add}	$C_{t<0}$	$C_{t=1\text{day}}$	$W_{\text{metal}(1)}$	$W_{\text{metal}(2)}$	X_{dep}
	kg	ppm	ppm	kg	kg	
Fe	5.144	933 ± 7	1118 ± 12	27800	19400	0.70
Si	0.699	292 ± 0.2	327 ± 9	20000		0.97
Ti	0.594	58 ± 1	83 ± 2	23800		0.82

Tables 8-20 and 8-21 show that the fraction of elements that co-deposited at the cathode within one day seems reasonable. Both experiments showed that silicon had the highest degree of co-deposition, while iron had the lowest. The uncertainty in the metal height and the metal area was set to be $\Delta h_{\text{metal}} = \pm 1 \text{ cm}$ and $\Delta A = \pm 1 \text{ m}^2$.

Figures 8.10 and 8.12 show that the metal data were somewhat scattered for all the investigated elements. This matter was discussed in section 8.4.1.2.

8.4.2 Effect of Current Interruption

One experiment was performed in a cell of type SBS-I by adding impurities in positions (A), (F) and (G) (see Figure 8.4). Bath samples were collected in position (A) with a sampling device made of brass, whereupon they were analysed by XRF. Metal samples were also collected in position (A), and analysed as described before.

It should be noted that Mn_2O_3 and Na_3PO_4 also were added to the bath in this experiment, but as a part of an investigation that is not included in this work.

The intention of this experiment was to see what happened with the impurity concentrations in the bath and in the aluminium metal when no current passed through the cell. Therefore, approximately two hours after the addition of impurities had taken place, a controlled power cut was performed. This power cut persisted for one hour before the electricity was turned on again.

Figures 8.13 and 8.14 show the concentration of the added impurities in the bath and in the aluminium metal, respectively, as a function of time.

Figure 8.13 shows that the impurity concentrations in the bath decreased as expected during the first two hours after the addition was made. In the period when no current passed through the cell, the drop in impurity concentration was even more pronounced, especially in the case of iron. When the power was turned on again, the impurity concentration in the bath first increased, followed by a drop again.

Figure 8.14 shows that the impurity content in the metal first increased, whereas it seemed to decrease somewhat in the cases of iron and silicon when no current passed through the cell. When the current was switched on again, things went back to normal.

When no current passes through the cell, the production of CO_2 stops. This will change the normal convection pattern, probably reducing the convection to a minimum. The movement of the metal pad will also be strongly reduced since the force caused by the current induced magnetic field will be terminated. The amount of dissolved aluminium in the bath will under these circumstances increase, since there is no CO_2 present in the bath to oxidise the aluminium. According to Grjotheim *et al.* (1982), the chemical solubility of aluminium is in the order of 0.1 wt%. The dissolved aluminium could have a strong tendency to react with more noble cations (*e.g.* Fe^{n+} , Si^{n+} and Ti^{n+}) present in the bath, in an exchange reaction similar to reaction [8-2]. The elementary metals (*e.g.* Fe, Si and Ti) resulting from these exchange reactions may end up on top of the metal pad due to sedimentation. At or close to the bath/metal interface, the

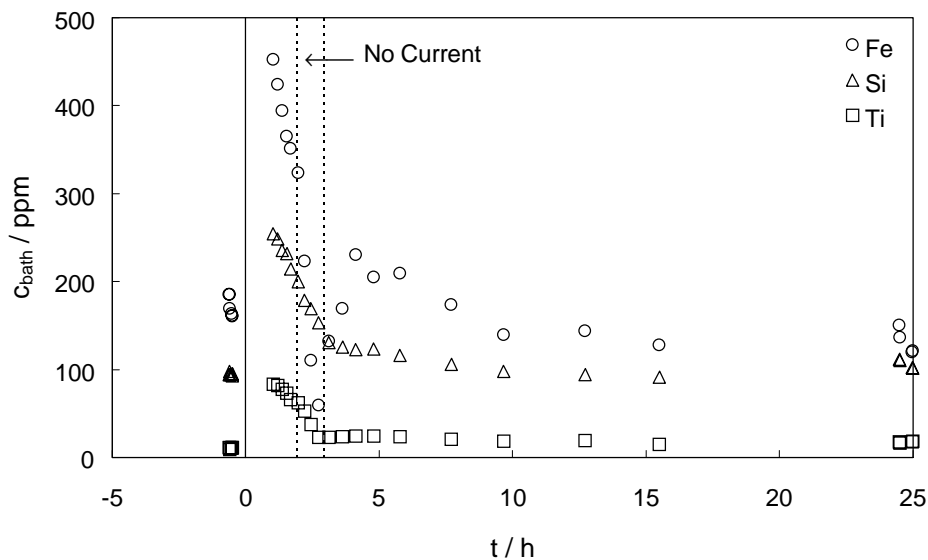


Figure 8.13 Concentrations of iron, silicon and titanium in the bath as a function of time for experiment SBS-Ib. The period in which no current passed through the cell is indicated in the figure. The batch added consisted of 10.150 kg Fe_2O_3 , 5.001 kg SiO_2 and 2.010 kg TiO_2 .

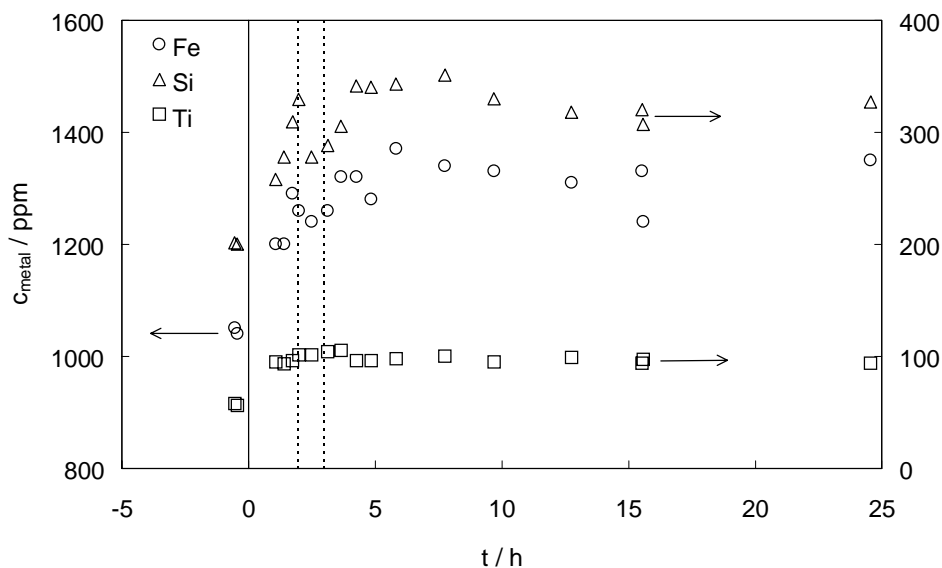


Figure 8.14 Concentrations of iron, silicon and titanium in the metal as a function of time for experiment SBS-Ib. No current passed through the cell in the period $2 \text{ h} < t < 3 \text{ h}$.

impurity species will be reduced to their elementary states, and may subsequently be alloyed with aluminium metal in accordance with reaction [8-2]. Both these phenomena, which are very similar, could explain a reduction in the bath concentration. However, the concentration decrease of all the elements in the bath was so steep during the current interruption, especially in the case of iron, that also other prevailing mechanisms were probably at play.

Thonstad (1999) suggested that metallic impurities might attach to the carbon particles, using them as nucleation sites. Such particles are dispersed all over the bath, but they tend to accumulate at the surface of the bath. The concept of impurities being attached to carbon particles was due to Sillinger and Horvath (1990) and others, who found that carbon dust and carbon particles in the bath had a higher iron content than the bath. Analysis by Sillinger and Horvath (1990) showed that iron was present as both iron oxide particles and as metallic iron at the surface of the carbon particles. The findings of Sillinger and Horvath (1990) were supported by the present work. Bath samples with carbon particles were found to have a much higher iron content than samples that did not contain any visible carbon. As pointed out by Thonstad (1999), the carbon particles will tend to accumulate at the surface of the bath. So when the convection decreases due to the stop in the CO₂ evolution, one can probably expect that even a larger fraction of the carbon particles will rise to the bath surface.

Another consequence of a current interruption will be a decrease in the cell temperature, and subsequently increased thickness of the side ledge (frozen bath). The frozen bath will mainly consist of cryolite, but it cannot be excluded that a small fraction of impurities will solidify together with the cryolite. However, as mentioned above, phosphorus was also added to the bath in this experiment. When comparing the bath concentration of phosphorus with that of iron, the data clearly demonstrated that those two elements followed the same trend. The relationship between iron and phosphorus is not understood.

When the current was switched on again, the iron concentration in the bath first increased before it started to decrease again (Figure 8.13). The question arises, where was the non-detectable iron located during the current interruption? Due to little or no convection, it is possible that large concentration gradients came into being both in the bath and in the metal. However, bath and metal samples were collected manually, *i.e.* at random heights, and it is therefore very unlikely that the data should have been so consistent if this had been the case. It is, therefore, believed that impurities ended up on top of the metal pad and/or at the bath surface attached to carbon particles.

Since the behaviour of the impurity elements during and after the current interruption is not understood, the mass transfer coefficient was determined based on the data obtained before the power cut. A somewhat different procedure was employed compared with the previous sections. The average bath concentration before the addition was made (c_{bc}) was subtracted from the measured concentrations in the bath after the addition (c_{bath}). As can be seen from equation [8-13], a plot of the natural

logarithm of this concentration difference *versus* time should give a straight line with slope equivalent to $-kAV^{-1}$. Such a plot is shown in Figure 8.15, and the corresponding results are given in Table 8-22.

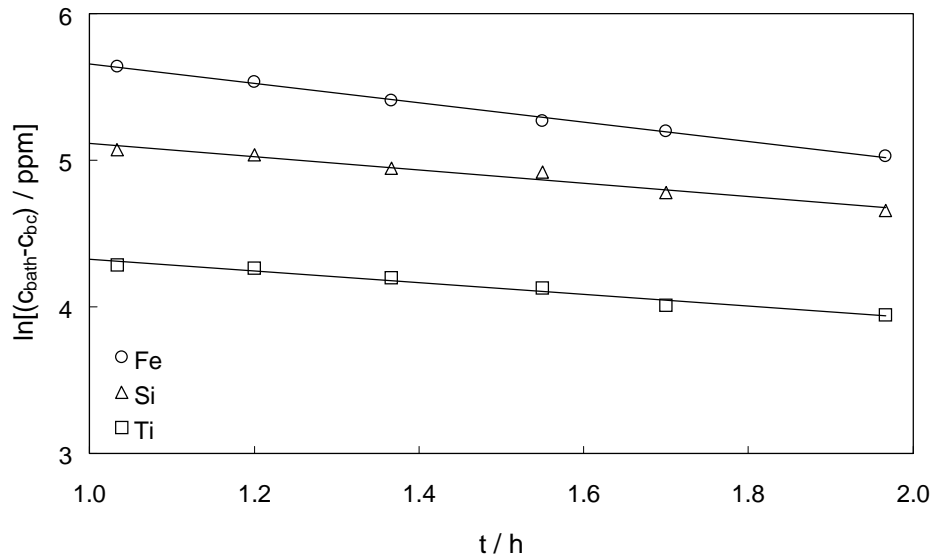


Figure 8.15 Plots of $\ln[c_{\text{bath}} - c_{\text{bc}}]$ for iron, silicon and titanium in the bath as a function of time (see text) for experiment SBS-Ib before current interruption.

Table 8-22 Bath data and the resulting mass transfer coefficients of experiment SBS-Ib before current interruption ($A = 40.4 \text{ m}^2$, $\rho_{\text{bath}} = 2100 \text{ kg m}^{-3}$).

Elem.	Pos.	w_{add} kg	c_{bc} ppm	c_{start} ppm	w_{bath} kg	Avg. w_{bath} kg	kAV^{-1} h^{-1}	$10^6 \cdot k$ m s^{-1}
Fe	A	7.064	171 ± 12	725 ± 17	12749	10744	0.662	23
Si	A	2.326	94.8 ± 1.5	356.4 ± 18	8894		0.453	16
Ti	A	1.193	10.9 ± 1.0	123.6 ± 6.6	10590		0.399	14

Figure 8.15 shows that good linear relationships were obtained for all the impurities in the period of interest. The resulting mass transfer coefficients, given in Table 8-22, also seem plausible, but perhaps somewhat high compared with the values obtained earlier in similar experiments (see Tables 8-18 and 8-19).

The metal data together with the fraction of impurity elements that co-deposited within one day are given in Table 8-23. Although the additions were rather large compared with earlier experiments, the results should be treated cautiously due to the rather mysterious data obtained on the concentration of impurities in the aluminium. Surprisingly, since titanium seemed to be the least influenced by the current interruption (see Figure 8.14), the titanium data gave a rather high and unrealistic metal volume.

Table 8-23 Metal data and the resulting fraction of co-deposition of experiment SBS-Ib ($h_{\text{metal}} = 0.22 \text{ m}$, $A = 40.4 \text{ m}^2$, $\rho_{\text{metal}} = 2300 \text{ kg m}^{-3}$).

Elem.	w_{add} kg	$c_{t<0}$ ppm	$c_{t=1\text{day}}$ ppm	$w_{\text{metal}(1)}$ kg	$w_{\text{metal}(2)}$ kg	x_{dep}
Fe	7.064	1045 ± 7	1350	23200	20400	0.88
Si	2.326	201 ± 1	327	18500		1.10
Ti	1.193	57 ± 1	94	32200		0.63

8.4.3 Effect of Interpolar Distance

The experiment was carried out on a cell of type SBS-I. Impurities were added to the bath in positions (A), (G) and (H) as indicated in Figure 8.4. Bath and metal samples were collected in position (A). A pair of brass tongs was used to collect the bath samples, whereupon they were analysed with XRF. The mould used for the metal samples was brass lined. Like in experiment SBS-Ib, the addition also contained Mn_2O_3 and Na_3PO_4 due to a parallel investigation.

The background for this study was to check how the mass transfer was affected when the distance between the anode and the cathode, *i.e.* the interpolar distance, was reduced by 1 cm. The interpolar distance was reduced by lowering the anodes by 1 cm 2.75 hours after the addition was made. Approximately 2 hours thereafter, the anodes were raised back to their normal positions. Figures 8.16 and 8.17 show the concentration of the added impurities in the bath and in the aluminium metal, respectively, as a function of time.

The convection in the bath is mainly caused by CO_2 evolution at the anodes. Since decreasing the interpolar distance reduces the space between the anodes and the cathode, one might expect an increase in the flow rate of CO_2 in this space. This increased flow rate of CO_2 will give rise to a stronger convection in the bath, and thereby a decrease in the thickness of the diffusion layer. Since the diffusion coefficient would remain approximately the same, it is easily seen from equation [8-5] that an increase in the mass transfer coefficient is expected under these conditions.

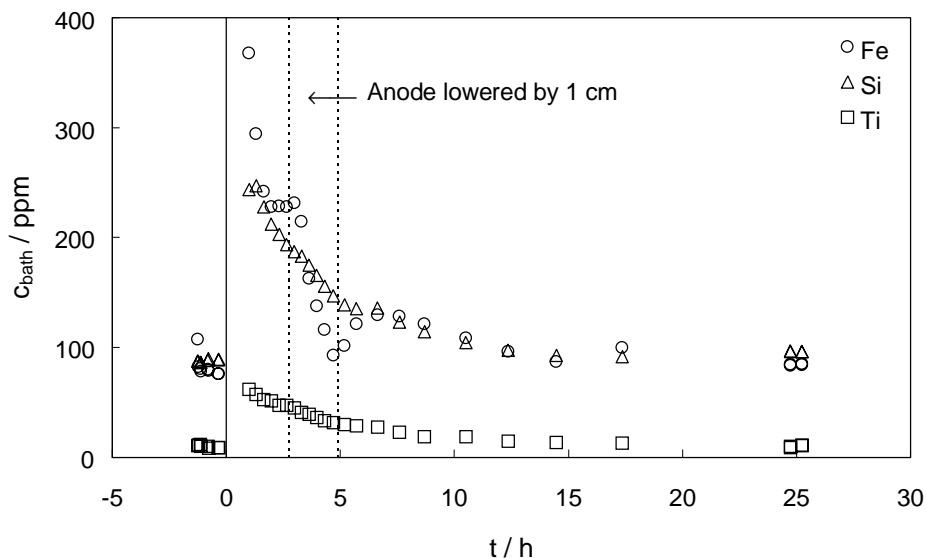


Figure 8.16 Concentrations of iron, silicon and titanium in the bath as a function of time for experiment SBS-Ic. The period during which the interpolar distance was reduced by 1 cm, is indicated in the figure. The batch added consisted of 10.571 kg Fe_2O_3 , 5.195 kg SiO_2 and 2.029 kg TiO_2 .

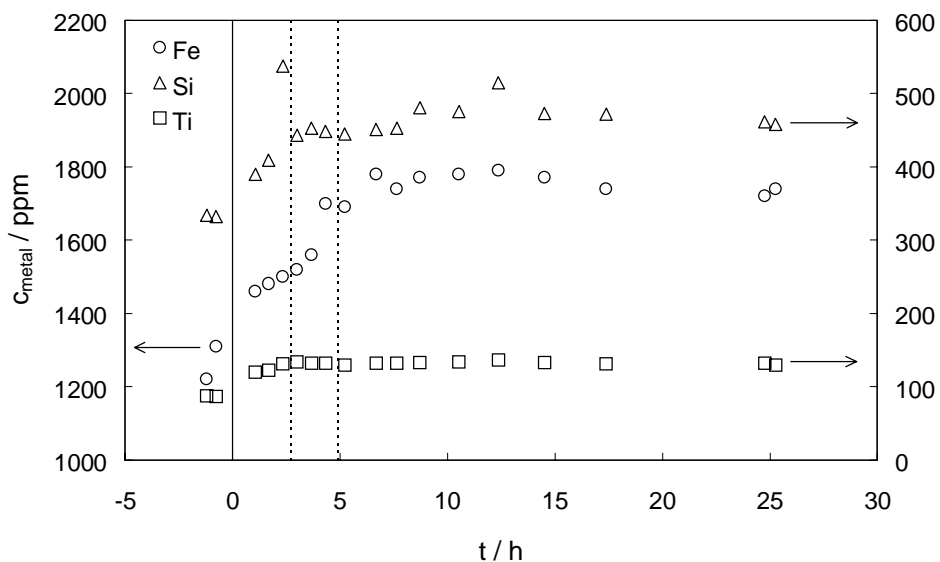


Figure 8.17 Concentrations of iron, silicon and titanium in the metal as a function of time for experiment SBS-Ic. The interpolar distance was reduced by 1 cm in the period $2.75 \text{ h} < t < 4.92 \text{ h}$.

From Figure 8.16 it is hard to tell if this is so for the case of silicon and titanium; both impurities seem to behave similarly to what they did in section 8.4.1.

In Figure 8.16, a strong reduction in the iron concentration is observed during electrolysis with reduced interpolar distance. For a short period just before the anodes were lowered, the iron concentration seemed to be independent of time, while it increased right after the anodes were raised again. This was followed by an apparently normal reduction in the concentration of iron in the bath. An explanation for this rather strange behaviour has not been found, but comparison with the phosphorous data showed that both elements behaved very similarly.

The metal data, which are displayed in Figure 8.17, show that the impurities behaved similar to what they did in section 8.4.1. Iron showed an increase during the period with reduced interpolar distance, corresponding to the decrease in the concentration in the bath.

The procedure described in section 8.4.2 was used to calculate the mass transfer coefficients of the elements iron, silicon and titanium. A plot of $\ln[c_{\text{bath}} - c_{\text{bc}}]$ versus time with the bath concentrations obtained before the interpolar distance was reduced, is shown in Figure 8.18. Bath data and the corresponding mass transfer coefficients are given in Table 8-24.

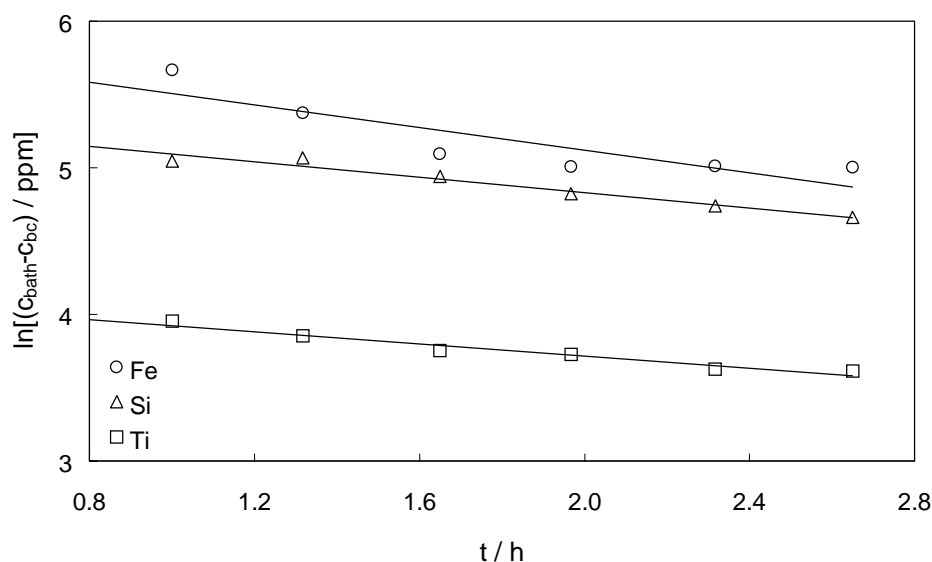


Figure 8.18 Semilogarithmic plot of concentrations of iron, silicon and titanium in the bath as a function of time for experiment SBS-Ic before the interpolar distance was reduced.

Table 8-24 Bath data and the resulting mass transfer coefficients of experiment SBS-Ic before reducing the interpolar distance ($A = 40.4 \text{ m}^2$, $\rho_{\text{bath}} = 2100 \text{ kg m}^{-3}$).

Elem.	Pos.	w_{add}	c_{bc}	c_{start}	w_{bath}	Avg. w_{bath}	kAV^{-1}	$10^6 \cdot k$
		kg	ppm	ppm	kg	kg	h^{-1}	m s^{-1}
Fe	A	7.357	79 ± 2	441 ± 81	20320	11389	0.386	14
Si	A	2.416	88.0 ± 1.4	300.1 ± 11.9	11389		0.263	9.8
Ti	A	1.204	9.9 ± 1.1	72.1 ± 2.7	19366		0.207	7.7

Figure 8.18 shows that, due to the rather unexpected behaviour of iron just before the anodes were lowered, the iron data were far from obeying a linear relationship on such a plot. As can be seen from Table 8-24, this resulted in an uncertainty of nearly 20 % in the estimated start concentration. The results also show that a very unlikely bath volume was obtained with the iron and titanium data. The bath volume obtained with the silicon data was therefore used in the calculation of the mass transfer coefficients. The resulting values are reasonable and in good agreement with those obtained previously.

To find the mass transfer coefficients of the added elements for the period when the interpolar distance was reduced, a plot similar to Figure 8.18 was made. The plot is shown in Figure 8.19, while the slope of the trend lines and the corresponding mass transfer coefficients are displayed in Table 8-25. The same procedure was applied for the data from the bath samples collected after the anodes were raised back to the normal position. That plot is shown in Figure 8.20, while the calculated mass transfer coefficients are given in Table 8-25. It should be noted that the bath volume found from Figure 8.18 was used in the calculation of the mass transfer coefficients displayed in Table 8-25.

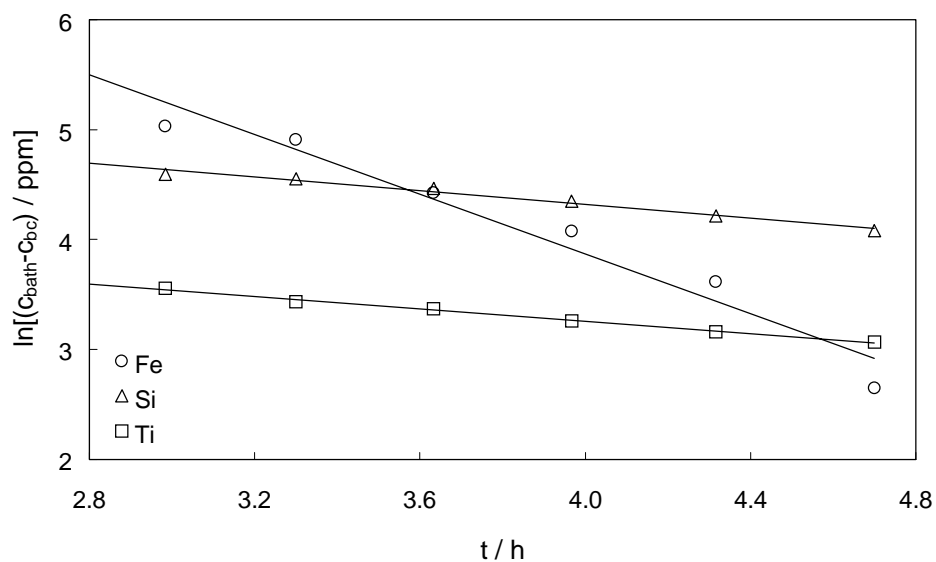


Figure 8.19 Semilogarithmic plot of concentrations of iron, silicon and titanium in the bath as a function of time for experiment SBS-Ic during the period in which the interpolar distance was reduced by 1 cm.

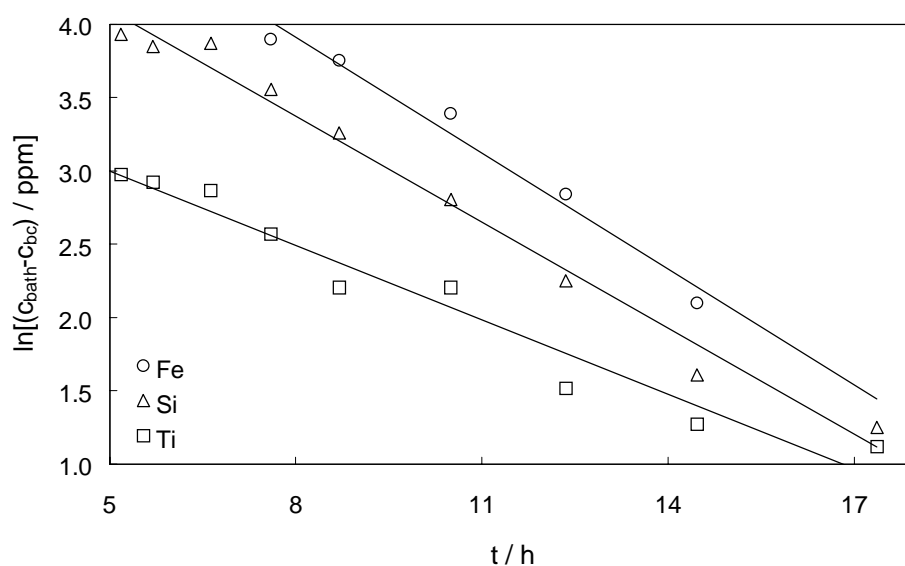


Figure 8.20 Semilogarithmic plot of concentrations of iron, silicon and titanium in the bath as a function of time for experiment SBS-Ic after the anodes were raised back to normal position.

Table 8-25 Mass transfer coefficients obtained at different interpolar distances for experiment SBS-Ic ($V_{bath} = 5.42 \text{ m}^3$, $A = 40.4 \text{ m}^2$, $\rho_{bath} = 2100 \text{ kg m}^{-3}$).

Element	Sampling Position	Anode Position	kAV^{-1} h^{-1}	$10^6 \cdot k$ m s^{-1}
Fe	A	–1 cm	1.358	51
Si	A	–1 cm	0.313	12
Ti	A	–1 cm	0.281	11
Fe	A	Normal	0.263	10
Si	A	Normal	0.241	9.0
Ti	A	Normal	0.169	6.3

Figures 8.19 and 8.20 show that good linear relationships were obtained for silicon and titanium. The iron data, however, did not correlate that well with a straight line, *i.e.* the trend of the data was slightly curved.

Table 8-25 shows that the mass transfer coefficients increased when the interpolar distance was reduced. When the anodes were raised back to their normal position, the value of the mass transfer coefficients decreased. The results show exactly what was expected, *i.e.* if the interpolar distance is reduced the mass transfer is enhanced due to an increased convection in the bath.

The metal data together with the fraction of the impurities that co-deposited within one day are given in Table 8-26.

Table 8-26 Metal data and the resulting fraction of co-deposition of experiment SBS-Ic ($h_{metal} = 0.22 \text{ m}$, $A = 40.4 \text{ m}^2$, $\rho_{metal} = 2300 \text{ kg m}^{-3}$).

Elem.	W_{add} kg	$C_{t<0}$ ppm	$C_{t \approx 1 \text{ day}}$ ppm	$W_{metal(1)}$ kg	$W_{metal(2)}$ kg	X_{dep}
Fe	7.357	1265 ± 63	1730 ± 14	15800	20400	1.29
Si	2.416	333 ± 1	460 ± 2	19000		1.07
Ti	1.204	89 ± 1	131 ± 1	28000		0.73

In this experiment some additional bath samples were collected with the purpose of determining the ratio of Fe(II) and Fe(III). These bath samples were analysed with respect to total Fe and Fe(II). The total concentration of iron was found by atomic absorption spectroscopy, while the concentration of divalent iron was found by photometric determination with o-phenanthroline. The analysis results are given in Table 8-27.

Table 8-27 Concentration of total dissolved iron and distribution of Fe(II) and Fe(III) in the bath of experiment SBS-Ic as a function of time after the addition of Fe_2O_3 was made. The total amount of iron was found by atomic absorption spectroscopy, while the amount of divalent iron was found by photometric determination.

Time h	Total Fe ppm	Fe(II) ppm	Fe(II) %	Fe(III) %
1.48	158	104	66	34
2.20	135	69	51	49
4.88	83	48	57	43
10.95	86	32	37	63
14.85	76	33	43	57

A comparison of the iron concentrations given in Table 8-27 with those displayed in Figure 8.16 shows that the latter were consistently higher. This is similar to what was observed in section 8.4.1, the ICP data were always lower than the XRF data. However, the analysis techniques used to determine the total amount of iron and the amount of Fe(II) were calibrated against each other so that the ratio Fe(II)/Fe(III) (or % Fe(II)) should be correct.

The results indicate that the fraction of Fe(II) decreased as the iron concentration in the bath decreased. The average ratio between Fe(II) and Fe(III) was found to be 51/49. Johansen *et al.* (1977) found the ratio between Fe(II) and Fe(III) to be 88/12 when FeSO_4 was added, while it was 70/30 when Fe_2O_3 was added. It should be noted that the values reported by Johansen *et al.* (1977) were obtained during the first three hours after FeSO_4 was added, and within 90 minutes when Fe_2O_3 was added (Johansen 1975). The value obtained within 90 minutes in the present work, *i.e.* 66 % Fe(II), corresponds well with the value reported by Johansen *et al.* (1977) after having added Fe_2O_3 , *i.e.* 70 % Fe(II).

8.4.4 Mass Transfer Coefficients

The present work shows that the transport of iron, silicon and titanium from bath to metal is mass transfer controlled. Some variation was observed in the obtained mass transfer coefficients. It was assumed that the batch dissolved completely in the bath, and that nothing escaped from the cell, neither during the addition nor under regular operation (dusting, evaporation *etc.*). As have been shown by Böhm *et al.* (1976) and in other works, this assumption is not fully correct. The implication will be that the bath volumes which were calculated were too large, and consequently the mass transfer coefficients would be estimated as being larger than they in reality were. The fraction that may have escaped during the experiments is difficult to estimate. If this fraction was the same for all the impurities, the obtained mass transfer coefficients for the

different impurities would be correct relative to each other, but in general too high. However, if let say the fraction of titanium escaping from the cell during regular operation was higher than that of silicon, and that both impurities had the same diffusion coefficient, then the bath concentration of titanium would decrease faster than that of silicon. The result would be that titanium appeared to have a higher mass transfer coefficient than silicon, even though the mass transfer between the bath and the aluminium metal was the same.

Furthermore it was assumed that the background concentration of the impurities remained constant throughout the experiments. Even though the batches were increased when secondary alumina was in use (SBS-I/SBS-II), it cannot be ruled out that the results were affected by fluctuations in the background concentration. Temperature effects such as freezing and melting of side ledge *etc.*, must also be taken into account. If impurities were partly trapped in the side ledge due to a temperature drop in the cell, the side ledge will have an impurity concentration much higher than the bath when it melted a few hours later.

An estimate of the uncertainty in the obtained mass transfer coefficients is difficult to give. Important factors in judging an experiment of this kind are the consistency of the obtained bath volumes and the scatter in the bath data obtained for the different impurity elements. In general the uncertainty in the mass transfer coefficients was probably as high as 20 %. However, if the results obtained under regular electrolysis are uncritically averaged, the following mass transfer coefficients were found:

$$k_{\text{Fe}} = (10 \pm 3) \times 10^{-6} \text{ m s}^{-1} \quad [8-18]$$

$$k_{\text{Si}} = (7 \pm 3) \times 10^{-6} \text{ m s}^{-1} \quad [8-19]$$

$$k_{\text{Ti}} = (5 \pm 2) \times 10^{-6} \text{ m s}^{-1} \quad [8-20]$$

The relationship between the investigated impurity elements therefore appears to be:

$$k_{\text{Fe}} > k_{\text{Si}} > k_{\text{Ti}} \quad [8-21]$$

Johansen *et al.* (1977) obtained a mass transfer coefficient of $12.5 \times 10^{-6} \text{ m s}^{-1}$ for iron in a 105 kA Söderberg cell. By using the relation given by equation [8-5], it was suggested that $2.5 \times 10^{-5} \text{ cm}^2 \text{ s}^{-1}$ and 0.02 cm would be appropriate values for the diffusion coefficient and the diffusion layer, respectively. In Chapter 5, the diffusion coefficient of Fe(II) in industrial melts at 965 - 970 °C was determined to be $D_{\text{Fe(II)}} = 3.5 \times 10^{-5} \text{ cm}^2 \text{ s}^{-1}$. Diep (1998) reported the diffusion coefficient of Fe(III) in cryolite at 1020 °C to be $D_{\text{Fe(III)}} = 1.7 \times 10^{-5} \text{ cm}^2 \text{ s}^{-1}$. Neither Johansen *et al.* (1977) nor the present work have suggested what the electroactive species is, but just concluded that the process was mass transfer controlled. If the average mass transfer coefficient of iron is used, *i.e.* $k_{\text{Fe}} = (10 \pm 3) \times 10^{-6} \text{ m s}^{-1}$, the thickness of the diffusion layer can be derived

to be $\delta_{\text{Fe(II)}} = 0.035$ cm for Fe(II) as the electroactive species, or to be $\delta_{\text{Fe(II)}} = 0.017$ cm for Fe(III) as the electroactive species. Both values are reasonable.

Frazer and Welch (1977) investigated the electrodeposition of silicon from SiO_2 dissolved in cryolite at 1020 °C. They concluded that the reduction mechanism involves the slow predissociation of a silica complex to form an electroactive species $\{\text{Si(IV)}\}$. The diffusion coefficient of the electroactive species was found to be $D_{\{\text{Si(IV)}\}} = 6.4 \times 10^{-5} \text{ cm}^2 \text{ s}^{-1}$. By combining this value with the average mass transfer coefficient for silicon, *i.e.* $k_{\text{Si}} = (7 \pm 3) \times 10^{-6} \text{ m s}^{-1}$, the thickness of the diffusion layer was calculated as $\delta_{\{\text{Si(IV)}\}} = 0.091$ cm. This value seems to be rather high, and may imply that the diffusion coefficient reported for silicon could be too high.

References to Chapter 8

- Augood, D. R. (1980): Impurities Distribution in Alumina Reduction Plants, in *Light Metals 1980*, C. J. McMinn, Editor, TMS, Warrendale, PA, p. 413.
- Böhm, E., L. Reh, V. Sparwald and G. Winkhaus (1976): Removal of Impurities in Aluminum Smelter Dry Gas Cleaning using the VAW/Lurgi Process, in *Light Metals 1976*, Vol. 2, S. R. Leavitt, Editor, TMS, New York, NY, p. 509.
- Chin, P., P. J. Sides and R. Keller (1996): The Transfer of Nickel, Iron, and Copper from Hall Cell Melts to Molten Aluminum, *Can. Met. Quart.*, **35**, 61.
- Diep, Q. B. (1998): Structure and Thermodynamics of Cryolite-Based Melts with Additions of Al_2O_3 and Fe_2O_3 , Doctoral Thesis 1998:28, Department of Electrochemistry, Norwegian University of Science and Technology, Trondheim, Norway, p. 79.
- Deininger, L. and J. Gerlach (1979): Stromausbeutemessungen bei der Aluminium-oxidreduktionselektrolyse in Laboratoriumszellen, *Metall*, **33**, 131.
- Goodes, C. G. and S. H. Algie (1989): The Partitioning of Trace Impurities between Aluminium, Cryolite and Air – a Laboratory Study, in *Light Metals 1989*, P. G. Campbell, Editor, TMS, Warrendale, PA, p. 199.
- Grjotheim, K. (1985): Nature and Origin of Impurities in the Hall-Héroult Electrolyte and their Effect on Metal Purity, *International Seminar on Refining and Alloying of Liquid Aluminium and Ferro-Alloys*, August 26 - 28, Trondheim, Norway.
- Grjotheim, K., C. Krohn, M. Malinovsky, K. Matiasovsky and J. Thonstad (1982): Aluminium Electrolysis – Fundamentals of the Hall-Héroult Process, 2nd Edition, Aluminium-Verlag GmbH, Düsseldorf, Germany.
- Frazer, E. J. and B. J. Welch (1977): A Galvanostatic Study of the Electrolytic Reduction Silica in Molten Cryolite, *Electrochim. Acta*, **22**, 1179.
- Ishihara, M. and K. Mukai (1965): Investigation of Small Amounts of Impurities and Non-Metallic Inclusions in Aluminium during its Production, *J. Metals*, **17**, 944.

- Ishihara, M. and K. Mukai (1966): Impurity Levels in Aluminium as Influenced by Raw Materials and Processing Methods, *Trans. Met. Soc. AIME*, **236**, 192.
- Johansen, H. G. (1975): Jern som forurensningselement i aluminiumelektrolysen, Doctoral Thesis, Department of Electrochemistry, Norwegian Institute of Technology, Trondheim, Norway.
- Johansen, H. G., J. Thonstad and Å. Sterten (1977): Iron as Contaminant in a VS Söderberg Cell, in *Light Metals 1977*, Vol. 1, K. B. Higbie, Editor, TMS, New York, NY, p. 253.
- Kobbeltvedt, O. (1997): Dissolution Kinetics for Alumina in Cryolite Melts – Distribution of Alumina in the Electrolyte of Industrial Aluminium Cells, Doctoral Thesis 1997:37, Department of Electrochemistry, Norwegian University of Science and Technology, Trondheim, Norway, p. 83.
- Metson, J. B. (1997): Impurity Distribution and Transport in Aluminium Reduction Cells, in *Proceedings of the 9th International Symposium on Light Metals Production*, J. Thonstad, Editor, August 18 - 21, Trondheim, Norway, p. 259.
- Sillinger, N. and J. Horvath (1990): Iron and Silicon Impurities in the Process of Aluminium Electrolysis, in *Light Metals 1990*, C. M. Bickert, Editor, TMS, Warrendale, PA, p. 369.
- Solheim, A. (2000): The Density of Molten NaF-LiF-AlF₃-CaF₂-Al₂O₃ in Aluminium Electrolysis, *Alum. Trans.*, **2**, 161.
- Sterten, Å., P. A. Solli and E. Skybakmoen (1998): Influence of Electrolyte Impurities on Current Efficiency in Aluminium Electrolysis Cells, *J. Appl. Electrochem.*, **28**, 781.
- Sturm, E. and G. Wedde (1998): Removing Impurities from the Aluminium Electrolysis Process, in *Light Metals 1998*, B. Welch, Editor, TMS, Warrendale, PA, p. 235.
- Thonstad, J. (1999): The Behaviour of Impurities in Aluminium Cells, in *Proceedings of the Tenth International Aluminium Symposium*, Stara Lesna, Slovakia, p. 5.
- Thonstad, J., F. Nordmo, S. Rolseth and J. B. Paulsen (1978): On the Transfer of some Trace Elements in Dry Scrubbing Systems, in *Light Metals 1978*, Vol. 2, J. J. Miller, Editor, TMS, New York, NY, p. 463.
- Tørklep, K., K. Kalgraf and T. Nordbø (1997): Alumina Distribution in Point-Fed Hall-Héroult Cells, in *Light Metals 1997*, R. Huglen, Editor, TMS, Warrendale, PA, p. 377.
- Øye, H. A. (1995): Impurities in Aluminium Smelting, *Fifth Australasian Aluminium Smelting Technology Workshop*, B. Welch and M. Skyllas-Kazacos, Editors, October 22 - 27, Sidney, Australia, p. 660.